TUDelft

Delft University of Technology

Tailoring the Hydrogen Detection Properties of Metal Hydrides

Boelsma, Christiaan

Important note
To cite this publication, please use the final published version (if applicable).
Please check the document version above.

Tailoring the
Hydrogen Detection Properties
of Metal Hydrides

Christiaan Boelsma

Tailoring the
Hydrogen Detection Properties
of Metal Hydrides

Proefschrift

ter verkrijging van de graad doctor
aan de Technische Universiteit Delft,
op gezag van de Rector Magnificus prof. ir. K.Ch.A.M. Luyben
voorzitter van het College voor Promoties,
in het openbaar te verdedigen op
vrijdag 10 maart 2017 om 12:30 uur

door

Christiaan BOELSMA
Master of Science (Natuurkunde)
geboren te Heerhugowaard

Dit proefschrift is goedgekeurd door promotor:
  Prof. dr. B. Dam

Samenstelling van promitiecommissie:
  Rector Magnificus   voorzitter
  Prof. dr. B. Dam   Technische Universiteit Delft

- Onafhankelijke leden:
  Prof. dr. J.J.C. Geerlings   Technische Universiteit Delft
  Prof. dr. P.E. de Jongh   Universiteit Utrecht
  Prof. dr. ir. B.J. Kooi   Universiteit Groningen
  Dr. A. Baldi   DIFFER (FOM), Eindhoven
  Dr. A. Borgschulte   Empa, Zwitserland
  Dr. C. Langhammer   Technische Universiteit Chalmers, Zweden

"Imagination is more important than knowledge."
– Albert Einstein

Table of Contents

i

Chapter 1

Introduction

1.1 H$_2$ Detection in a Sustainable Economy

Hydrogen plays an important role in many sectors of the industry.[1.1] It is, for example, necessary to produce ammonia (chemical industry),[1.2] it is a product of food ageing (e.g. food industry),[1.3] and it improves medical diagnostics (e.g. lactose intolerance).[1.4] Its impact on society will increase in the next decades as hydrogen will play an essential role as an energy carrier in the transition from an oil-based to a sustainable economy. This because the energy output of the combustion of $1\,\mathrm{kg}$ of hydrogen is 2.8 times higher than the combustion of $1\,\mathrm{kg}$ gasoline and the product is water. The simplest concept of a sustainable economy based on hydrogen is represented by the *hydrogen cycle* (see figure 1.1). Here, hydrogen is produced by the electrolysis of water powered by solar/wind energy while electricity is produced by combusting the hydrogen.[1.5] As a completely new infrastructure is necessary for an effective implementation of this cycle, the *synthetic fuel cycle* is a cost-effective alternative. This alternative cycle is based on the production of hydrocarbons (e.g. gasoline, kerosine) from captured CO_2 and hydrogen gas. It is cost-effective as the necessary infrastructure already exists.[1.5] However, major technology breakthroughs and improvements are required for an effective synthesis process.

The use of hydrogen is directly related to safety. As hydrogen is a colorless, odorless and tasteless gas and has a low ignition energy combined with a high energy output, hydrogen detection is essential. Although different approaches including gas chromatography, mass spectrometry, thermal conductivity, and laser gas analysis are available, the most common approach to detect hydrogen is solid-state based.[1.6] Usually catalytic resistors or electrochemical devices are used, where the resistivity of the material changes when being exposed to hydrogen.[1.7 − 1.9] Recent studies show that using the changing optical properties of thin film metal hydrides can also be viable to detect hydrogen.[1.10 − 1.15] The aim of this thesis is to study the application of thin film metal hydrides to detect hydrogen optically, and in particular how to tailor their sensing properties to improve their potential.
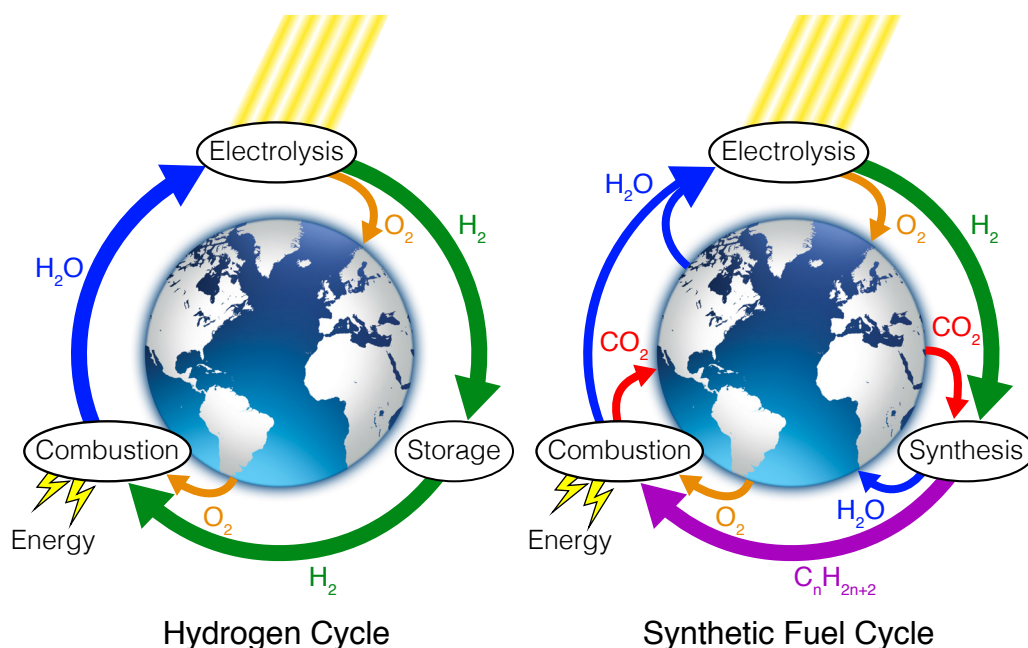
Figure 1.1 | **Hydrogen in a Sustainable Economy** – A sustainable energy economy represented by two cycles, the hydrogen cycle (left) and the synthetic fuel cycle (right). Each cycle includes the use of hydrogen.

1.2 The Basics of Hydrogen Detection

The essence of hydrogen detection is to receive a response when the partial hydrogen pressure (i.e. the amount of hydrogen in an area) exceeds a specific threshold. This response can be in form or an alarm or any other measure parameter (e.g. electric resistance, optical reflectance) that lead to an action. The relation between the hydrogen pressure and the response (i.e. isotherm) can be of different forms (see figure 1.2). It can be a step-function (threshold detector) or a continuous function (continuous sensor). With a continuous function one already receives a response when the pressure approaches the threshold. In this way additional information such as the speed of the pressure increase can be obtained.

To detect hydrogen effectively, the device must meet multiple requirements. These requirements can be divided into several categories, which are listed below. For each category we listed the general requirements, although they can be different depending on the application.[1.7 — 1.9]

- **response time** – the sensor/detector should response to a changing hydrogen pressure within a time ranging from a few seconds up to a few minutes.
- **resolution** – the response to a small hydrogen pressure change should be large while the read-out error should be low. In other words, the signal-to-noise ratio or resolution should be large. We define the resolution as the
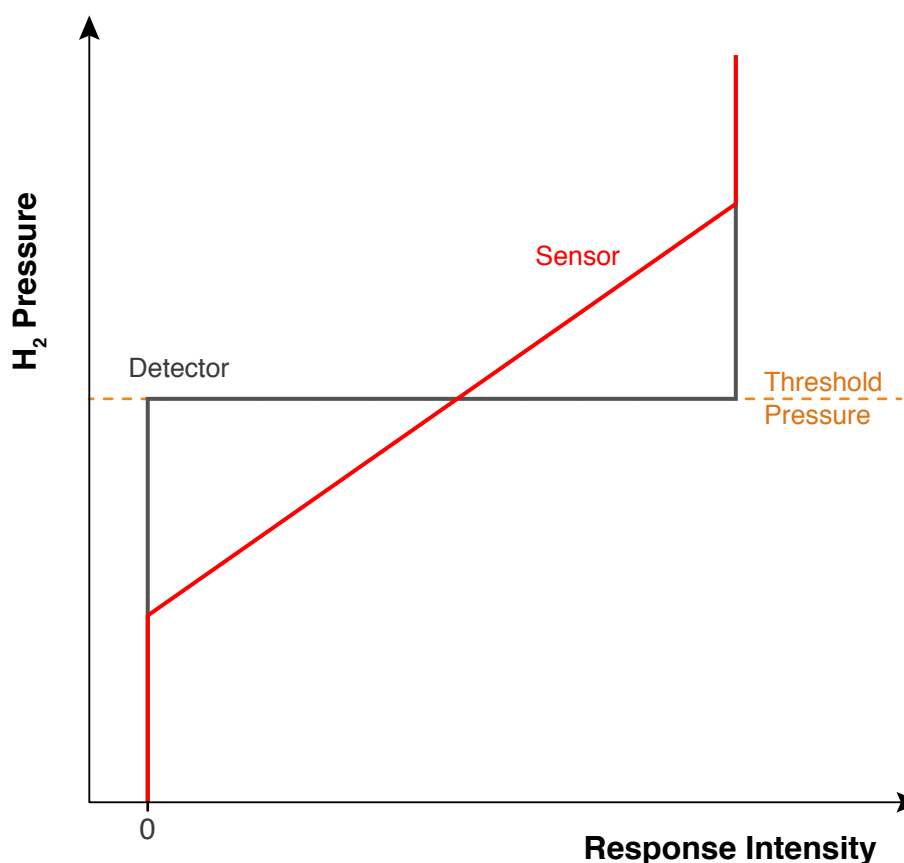
Figure 1.2 | **Detector *versus* Sensor** – Visualization of the difference between a threshold detector (black) and a continuous sensor (red), where the hydrogen pressure is plotted against the response/output at a constant temperature. Note that the relation between the pressure and the response in a sensor can be of any form, although the interpolation a linear relation is the most ideal.

smallest pressure change (on a logarithmic scale) that can be distinguished. The target resolution is often to be set below $<5\%$.

- **stability** – the response to a certain hydrogen concentration must be the constant for a lifetime of multiple years, often equivalent to more than >1000 exposures.
- **operating temperature** – the sensor/detector should be stable at ambient temperatures. The most common temperature range is from $-30°$C to $+100°$C.
- **cross-sensitivity** – other chemicals/species should not be affected by the response of the sensor/detector.

Important with respect to the accuracy/resolution is the presence of hysteresis. Hysteresis is a concept when a material describes two relations between the hydrogen

pressure and the response; one describing the response with increasing pressure and the other with decreasing pressure. As a result, a single response corresponds to two different hydrogen pressures causing an error and a smaller accuracy. Hysteresis is the result of a first-order phase transition upon hydrogenation. To detect hydrogen effectively, materials that remain in a single phase are therefore preferred.

Optical Hydrogen Detection
The disadvantages of solid-state based hydrogen detection devices are that they are bulky (in terms of dimensions), too expensive to be used in large quantities, and intrinsic unsafe.[1.10] As electric wires are present in the sensing unit, they can induce sparks that can lead to unsafe situations in explosive conditions. These disadvantages can be tackled by using optical fibers instead. Here hydrogen is detected by monitoring the optical reflection change of a material upon exposure to hydrogen, and this material is placed on the tip of the fiber. In this way the electronic components from the readout equipment can be mounted at the other end of the fiber (which can be hundreds of meters long) and be separated from the sensing points. In addition, optical fibers are small, flexible, and easy to combine with other in-situ probe measurements.[1.12,1.13,1.17 — 1.22] The most used material to detect hydrogen optically are thin film metal hydrides.

1.3 Thin film Metal Hydrides

Transition metals are, in a thin film geometry, very effective to detect hydrogen optically. When a thin film (transition) metal is exposed to hydrogen, the hydrogen enters the metal host and occupies the interstitial sites forming a *metal hydride*. The absorption of hydrogen induces a change of the electronic properties of the metal host, resulting in a lattice expansion and/or in a change of the dielectric functions/absorption coefficient. When thickness of the film is small enough, typically below <100 nm, these changes are reflected by a change of the optical transmission/reflection of the film. This is known as the switchable mirror effect, and it is observed in many transition metals.[1.23 — 1.27] The relation between the intensity of the transmitted light $\mathcal{T}$, the film thickness d and the absorption coefficient α:

$$ \ln\left(\frac{\mathcal{T}}{\mathcal{T}_0}\right) = -\alpha(\omega, x)\, d(x)\,. \tag{1.1} $$

Here $\mathcal{T}_0$ takes into account the transmission losses of the system, including the reflection at all interfaces. In this thesis we often focus on the transmission change of the film upon hydrogenation with respect to a reference state $\mathcal{T}_{\text{ref}}$, expressed by

$$ \ln\left(\frac{\mathcal{T}}{\mathcal{T}_{\text{ref}}}\right) = \ln\left(\frac{\mathcal{T}}{\mathcal{T}_0}\right) - \ln\left(\frac{\mathcal{T}_{\text{ref}}}{\mathcal{T}_0}\right)\,. \tag{1.2} $$

1.3.1   Thermodynamics of Metal Hydrides

An important aspect of a hydrogen detector/sensor is the detection pressure (range) and temperature range. As the temperature dependence of the detection pressure (range) is different for each material, the detection pressure (range) at a specific temperature can be different for each material. To find the operational detection pressure (range) within the desired temperature range, we use the Van 't Hoff relation. The Van 't Hoff relation describes the relation between the pressure and the temperature through an enthalpic and an entropic component:

$$\ln\left(\frac{P}{P_0}\right) = \frac{\Delta H}{R\,T} - \frac{\Delta S}{R}. \tag{1.3}$$

Here, the enthalpic term ΔH (in $\mathrm{kJ/mol\ H_2}$) is defined as the difference of the molar enthalpy between two hydrogen fractions (δx) with respect to the molar enthalpy of the hydrogen gas:

$$\Delta H = 2\frac{\bar{H}_{x+\delta x} - \bar{H}_x}{\delta x} - \bar{H}_{H_2}. \tag{1.4}$$

The entropic term ΔS (in $\mathrm{J/(K\ mol\ H_2)}$) is defined in a similar way:

$$\Delta S = 2\frac{\bar{S}_{x+\delta x} - \bar{S}_x}{\delta x} - \bar{S}_{H_2}. \tag{1.5}$$

While ΔH is commonly associated to the amount of energy that is released/needed to change the amount of hydrogen in the metal host, ΔS is associated with the change of disorder of the hydrogen atoms in the metal host when changing the amount of hydrogen in the metal host. In these equations the changing amount of hydrogen is indicated by the hydrogen fraction $x = H/M$, and is related to the response of the detector/sensor. The more hydrogen is absorbed by the metal host (i.e. large δx), the larger the response.

Not only can the Van 't Hoff relation be used as a tool to calibrate the temperature dependence of the detector/sensor, it gives also insight how to change the detection pressure (range) and its temperature dependence. Effects that change only ΔS causes the same shift of the detection pressure (range) for all temperatures (see figure 1.3a). As a result, the temperature dependence of the detection pressure (range) will not be affected. Changing the temperature dependence can be obtained by applying effects that ΔH. However, it also shifts the detection pressure (range) non-uniformly with temperature (see figure 1.3b). A change of ΔH and/or ΔS of thin film metal hydrides can be achieved by chemical deformation (e.g. alloying) and/or physical deformation (elastic clamping, interface energy).
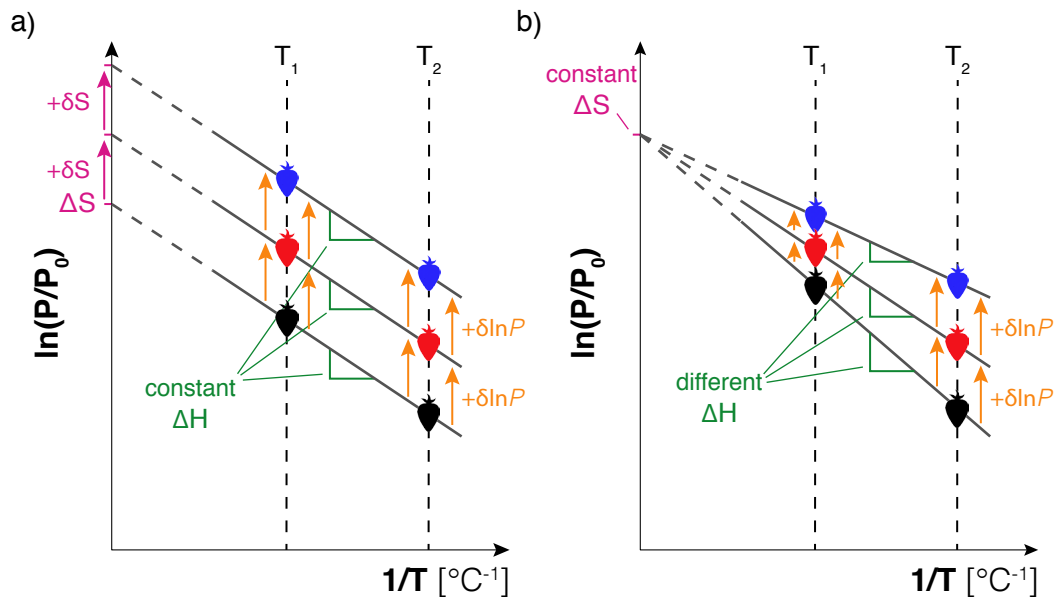
Figure 1.3 | Pressure Range and Thermodynamics – The effect of changing either **a)** ΔS or **b)** ΔH on the pressure at different temperatures. An uniform shift of the pressure (on a logarithmic scale) is obtained when changing only ΔS, while the temperature dependence of the pressure (slope of the line) remains constant. A different ΔH implies a different temperature dependence of the pressure and induces a pressure shift that depends on the temperature.

1.3.2   Examples of Effective Transition Metals

In literature, palladium hydride is considered to be an effective optical hydrogen detection material.[1.12,1.15 − 1.17,1.28,1.29] First, Pd acts as a catalyst for the hydrogen molecule dissociation process.[1.30] As a result, the response time to a changing hydrogen pressure ranges from a few seconds up to a minute at room temperature. Second, it can monitor fluctuations in the hydrogen pressures within a range of a few orders of magnitude. This behavior is only observed when the film is in the PdH_x low fraction α–phase. Here, hydrogen forms a solid solution with the crystalline Pd although the amount solved hydrogen is limited. At room temperature, the maximum solubility is $x = $ H/Pd ≈ 0.01. Nevertheless, a well-defined and hysteresis-free relation between the hydrogen pressure and the hydrogen fraction between $50 - 10^{+4}$ Pa at room temperature is observed.[1.17] The upper boundary of the pressure range is bound by the first order phase transition to the to the high fraction β–phase $(x > 0.60)$. As this transition induces a large change in the hydrogen fraction range, it can theoretically be used as a threshold detector. However, the practicality at room temperature is limited as the $\alpha \rightarrow \beta$ phase transition has an incoherent nature (being first order) and induces a hysteresis of approximately 1 order

of magnitude. It is also accompanied with a lattice expansion of approximately 11%, which reduces the stability as the formation of micro-cracks and micro-blisters are reported.[1.17,1.36] It is therefore recommended to avoid the $\alpha \to \beta$ phase transition.

Sieverts' Law

The well-defined relation between hydrogen pressure and the hydrogen fraction in the low fraction α–phase is well studied and its concept is well understood.[1.32 − 1.34] It obeys Sieverts' law, which is an empirical law that describes the solubility of diatomic gasses, including hydrogen, in metals. It follows from It states that the fraction x of dissolved hydrogen in a metal is proportional to the square root of the partial pressure in a thermodynamic equilibrium:

$$\frac{x}{r-x} = \sqrt{\frac{P}{P_0}} \times \exp(-\Delta G/R\,T)\,. \tag{1.6}$$

Here, r is the number of interstitial sites per metal atom and ΔG is the change of the Gibbs energy. As ΔG is related to ΔH and ΔS through

$$\Delta G = \Delta H + T\,\Delta S, \tag{1.7}$$

both ΔH and ΔS are a function of x. For $x << 1$, Sieverts' law is usually written as

$$\sqrt{P} = \frac{x}{\sqrt{K}}, \tag{1.8}$$

where is K the equilibrium constant. Sieverts' law obeys Henry's law (i.e. the amount of dissolved gas is proportional to its partial pressure of the gas) although two extra conditions have to be fulfilled. First, the hydrogen gas must be fully dissociated in the metal. Second, the hydrogen gas must be considered as ideal. Consequently, Sieverts' law implies that the dissolution is fully reversible and thus hysteresis free. Despite the fact that the Pd the solubility range is rather small $(x < 0.01)$, within the PdH$_x$ α–phase a $\sim 10\%$ change in both $\Delta H(x)$ and $\Delta S(x)$ is reported.[1.35] In this way, the pressure range strongly depends on the temperature. Nevertheless, PdH$_x$ is considered as a model system for hydrogen detection. It combines a simple relation between the pressure and the hydrogen fraction with a large pressure range, an absence of hysteresis, a great stability, and a fast response time. However, a larger solubility range is desired as it increases the optical response to hydrogen.

Increasing the Solubility Range in PdH$_x$

One way to increase the small solubility range in PdH$_x$ is to increase the temperature. Up to $294°\mathrm{C}$, the solubility range increases gradually with temperature to $x \approx 0.10$.[1.32,1.35] Above $294°\mathrm{C}$ the solubility range is much lager $(x \approx 0.25)$ as the

temperature exceeds the critical temperature of the non-stoichiometric $\alpha+\beta$ coexistence region. There is no distinction between the $\alpha-$ and the $\beta-$phase, and as a result steep hysteresis-free isotherms are obtained. However, the high operational temperature range reduces the applicability significantly.

The other way to increase the solubility range in PdH_x is to lower the critical temperature of the $\alpha+\beta$ coexistence region by chemical destabilization through alloying with Cu, Ta, Au, or Ag. With increasing alloy concentration the critical temperature decreases and for specific concentrations it can be lower than room temperature. As a result, steep and hysteresis-free isotherms with pressure ranges up to 10^{+6} Pa at room temperature are reported[1.36 − 1.39] while the optical response is at least doubled with respect to the α PdH_x phase.[1.11 − 1.13,1.29]

Magnesium Based Hydrides

Recent studies show that Pd capped Mg-based thin films are an interesting alternative to detect hydrogen optically.[1.16,1.29,1.40 − 1.42] Here steep isotherms are observed with different Mg alloys (such as MgTi, MgNi, and MgNiZr) with a pressure range of a few orders of magnitude. In addition, the optical response is up to 10 times larger than reported with Pd-based hydrides (in units of $\ln(T/T_{\mathsf{unl}})$).[1.29] The position/size of the pressure range depends on the alloy and the alloy concentration. For example, with $Mg_{60}Ti_{40}$ the isotherm describes a pressure range between $10^{+1} - 10^{+3}$ Pa at $90°C$,[1.29] while with $Mg_{52}Ni_{20}Zr_{28}$ a pressure range between $10^{-3} - 10^{+1}$ Pa is obtained at room temperature.[1.42] The steep isotherms are considered to be the result of many different structures, which each (de)hydrogenate at a slightly different pressure. The Pd capped MgNiZr is, for example, completely amorphous.[1.42] The steep isotherms found with Pd capped MgTi are explained through the presence of several crystalline Mg_yTi_{100-y} fcc configurations.[1.40].

Unfortunately, the isotherms are not hysteresis-free. Despite being alloyed, the transition from the MgH_x $\alpha-$phase ($x < 0.01$) to the MgH_x $\beta-$phase ($x \approx 2$) cannot be avoided without losing the hydrogen detection properties. This because above the critical temperature of the $\alpha+\beta$ coexistence region Mg does not form a hydride.[1.43] Note that the Pd capping layer is necessary to obtain reasonable response times and increase the cycle stability. As Mg is not a catalyst for the hydrogen dissociation process, its full hydrogenation can take up to weeks/months, even at elevated temperatures. With the addition of a Pd layer a switching time of a few seconds at elevated temperatures ($>90°C$) are obtained.[1.41] The cycle stability is improved as Pd protects the Mg-based thin film from oxidation and nitration. Both the response time and the cycle stability can be further improved by using a coating, such as PTFE or metal-organic-framework (MOF). In this way response time of a few seconds are obtained at $\sim 60°C$ while the cross-sensitivity to CO and CO_2 is also reduced.[1.44,1.45]
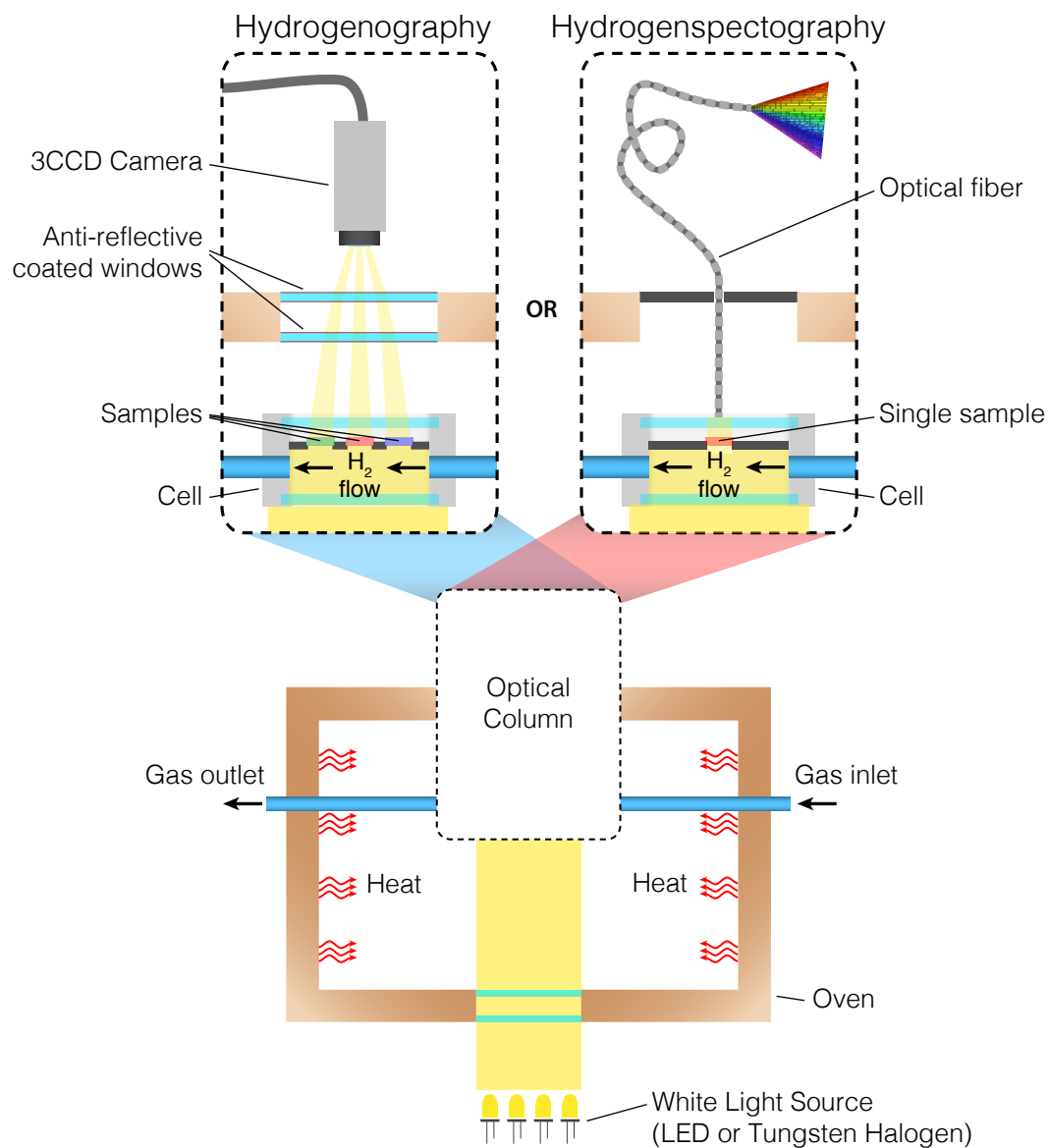
Figure 1.4 | Improved Hydrogenography – Schematic overview of the hydrogenography setup including its adjustments. The setup can either monitor the white light transmission of multiple thin films (left) or the transmission of a single film as a function of the wavelength between $400 - 1050\,\mathrm{nm}$ (**right**).

1.3.3 Hydrogenography

To study and characterize the optical sensing properties of metal hydrides we make use of hydrogenography. Hydrogenography is an optical technique to monitor the optical transmission of a thin film sample as a function of the time at a specific temperature, while the (partial) hydrogen pressure can be varied simultaneously.[1.28,1.29] Figure 1.4 shows a schematic illustration of the hydrogenation setup. In this setup we can vary the (partial) hydrogen pressure between $10^{-3} - 10^{+6}$ Pa using different H_2/Ar gas mixtures, while the temperature can be stabilized between $30 - 250°C$. The setup may contain up to 9 *square* samples $(10 \times 10 \text{ mm}^2)$, up to 3 *strip* samples $(70 \times 5 \text{ mm}^2)$, and up to 1 *wafer* sample $(3'' \text{ diameter})$. The 3CCD camera records the transmission of the samples as a function of time. Each sample can therefore consist of a composition gradient, as the 3CCD camera allows us to divide the sample surface into a 2D pixel matrix (a pixel represents a typical sample area of 0.02 mm^2). In this way each pixel may represent a different metal composition, allowing us to monitor the (de)hydrogenation of up to a few thousand metal compositions simultaneously. This also allow us to average pixels to improve the signal-to-noise ratio. For that reason, we use the *squares* to study single compositions, while only the *strips* and the *wafer* samples are commonly used to study gradient compositions in, respectively, one or two dimensions.

Hydrogenography is developed in the mid 2000s and is mainly used to study the hydrogen storage properties of thin film metal hydrides.[1.28,1.29,1.40] Recently, it has been shown that also the hydrogen detection/sensing properties of thin film metal hydrides can be studied.[1.11 — 1.13,1.16,1.41] However, to improve the limited resolution, to increase the continuous measurement time to more than 1 week, and to obtain spectral information, we upgraded the hydrogenography setup in several ways:

- we replaced the tungsten halogen light source by white light LEDs. This increased the lifetime of the white light source from from approximately 200 hrs (tungsten halogen) to $>25\,000 \text{ hrs}$ (LED). This allows us to monitor the transmission of the film for several weeks. To reduce fluctuations in the light intensity of the LED, we replaced the single halogen bulb by 5 LEDs. This also enables to use higher light intensities, reducing the signal-to-noise ratio. The effect of a different emission spectrum of LEDs with respect to the tungsten halogen bulb is also reduced by using higher intensities.[1.46] As we express the transmission change by $\ln(\mathcal{T}/\mathcal{T}_{\text{ref}})$, only at very low transmission intensities (close to the noise level) the difference is noticeable.

- we coated the two top sapphire windows of the optical column with an anti-reflection coating (red marked windows in figure 1.4). In this way we reduce internal reflections within the optical path, and therefore minimize their influence on the optical results (see figure 1.5).
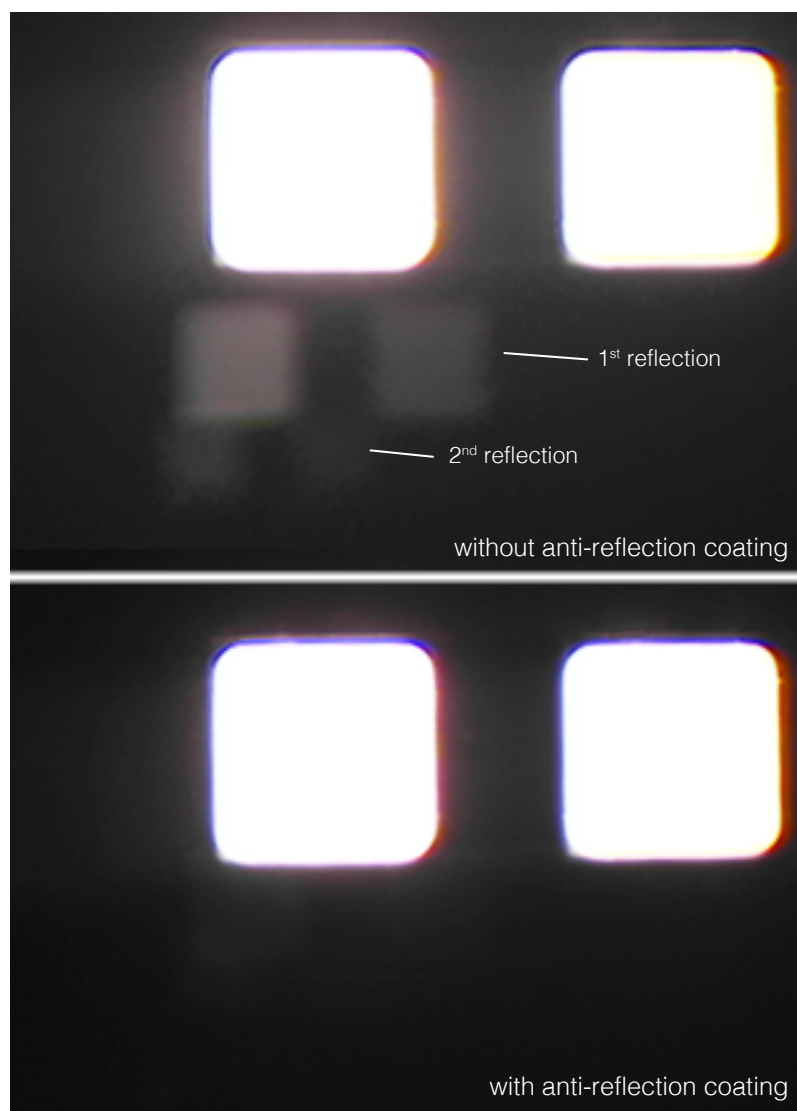
Figure 1.5 | Internal Reflections in Hydrogenography – Photographs of two *square* samples within the hydrogenography setup. The top photo includes the original windows (without an anti-reflection coating), showing two clear reflections. The bottom photo includes the windows with anti-reflection coating, showing no reflections. The reflections can influence the optical results when the transmission change is low.

- we built an extension of hydrogenography, called hydrogenspectrography, which enables to measure the optical transmission change of a thin film as a function of the wavelength (between $400 - 1050\,\mathrm{nm}$). For this we replaced the 3CCD camera and the top anti-reflective coated windows within the optical column by an optical fiber that is attached to a *Ocean Optics USB2000*® spectrometer. At the time of writing, the extension can only monitor the transmission change of a single thin film (see figure 1.4).

To improve the signal-to-noise ratio even more, we often include an aluminium reference sample during the measurement. This reference sample consists of an (oxidized) aluminium layer deposited on a quartz substrate. The thickness of the Al layer is selected in such a way that its transmission equals that of the sample of interest. We selected aluminium as a reference material as it is inert to hydrogen. In this way we are able to discard artifacts in the optical transmission of the sample of interest since the same artifacts will appear in the Al reference sample (see figure 1.6). All these improvements enable us to measure transmission changes (on a logarithmic scale) of $\delta \ln T = 10^{-3}$.
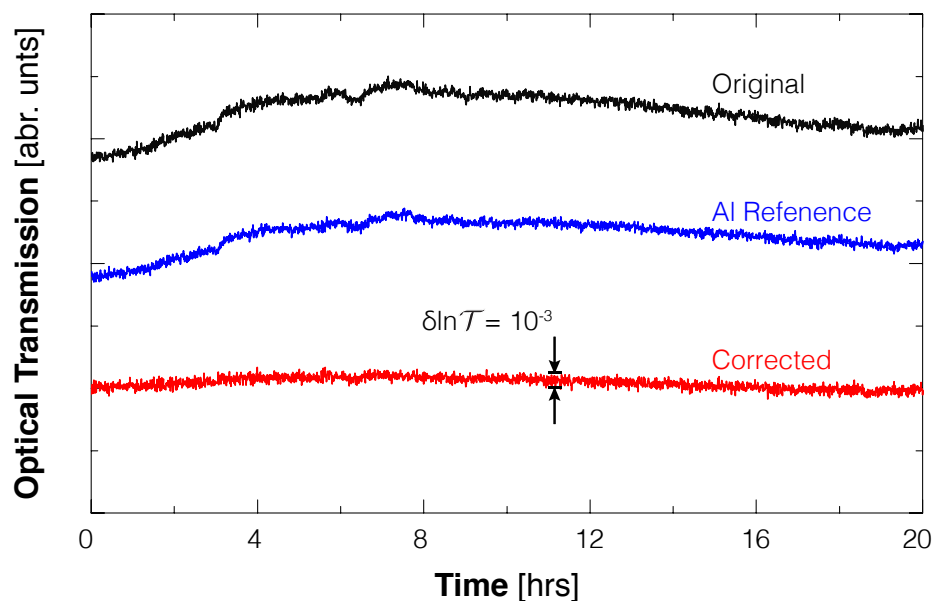
Figure 1.6 | **Correction of Light Source Fluctuations** – The optical transmission (on a logarithmic scale) of a Pd-capped Hafnium thin film (black) and an Al reference sample (red) as a function of time measured in hydrogenography at $120°\mathrm{C}$ at constant conditions. The corrected optical transmission (red) is obtained after subtracting Al reference signal from the original signal via $T_{\mathrm{cor}} = T_{\mathrm{org}} - aT_{\mathrm{Al}}$ where the coefficient a corrects for the thickness and absorption coefficient difference between the Hf and the Al reference sample.

1.4 This Thesis

This thesis describes the application of thin film metal hydrides as optical hydrogen sensing materials, and in particular how to tailor the sensing properties. It consists of two parts. In the first part (chapters 2 and 3) we focus on how to increase/shift the pressure range by studying effects that alter the hydrogenation thermodynamics of well-known thin film metal hydrides to detect hydrogen. In the second part (chapters 4 and 5) we focus on the sensing properties of two newly discovered sensing materials.

The effect of interface energy on the thermodynamics of a thin film metal hydride surrounded by another metal(hydride) is described in chapter 2. Interface energy describes the energy at the interface of two thin layers. Upon hydrogenation of (one of) the layers, the interface energy changes and results in a shift of the threshold pressure. As one of the few destabilization methods, it should shift the threshold pressure without inducing/increasing hysteresis. To demonstrate this experimentally, we study nano-structured MgH_2 surrounded by TiH_2. In two different configurations (thin films and nanodots) we find that by means of interface energy effects the threshold pressure can be shifted, although it is accompanied by plastic deformations. As a result, the shift is different for the hydrogenation and dehydrogenation pressure and a larger hysteresis is obtained.

In chapter 3 we focus on changing the pressure range through chemical destabilization. We study Ti doped MgH_2 and find that by changing the Mg/Ti ratio both the enthalpy ΔH and entropy ΔS of hydride formation changes. Both change in such a way that a plot of ΔH against ΔS as a function of the Ti/Mg ratio results in a straight line. This phenomenon is known as enthalpy-entropy compensation, which is not only found in other metal hydrides systems but also in a wide range of fields in chemistry, biology, and solid-state physics. Despite the abundant literature, there is no consensus about its origin. Many authors claim that it is induced by statistical and/or experimental errors and support this with several models. However, these models lack the description of how small these statistical and experimental errors have to be to exclude a statistical basis. In this chapter we present a new model with a direct link with the size of the statistical/experimental errors. We apply this model to the observed compensation effect in Ti doped MgH_2. Although existing models suggest that this compensation effect has a statistical basis, we find, however, that the experimental and statistical errors are too small for a statistical basis. We therefore conclude that the enthalpy-entropy compensation effect in Ti doped MgH_2 has a systematic basis.

In chapter 4 we show that, besides amorphous MgNiZr, also amorphous MgZr thin films can be used to sense hydrogen over a pressure range of about 4 orders of magnitude. This discovery shows that, in contrast to literature reports, the presence

of Ni is not essential. Besides the fact that the system becomes less complex, the absence of Ni also improves the relation between the hydrogen pressure and the optical transmission of the film. Instead of multiple kinks (MgNiZr) we find in MgZr thin films a highly linear relation between the optical transmission and the hydrogen pressure (on a log-log plot). We also show that we can extend the linear relation in both parameters by adding Ti or Hf to the alloy. The addition of Ti induces an increase of the optical contrast by a factor of 3 (without affecting the pressure range) while the addition of Hf an increase of the pressure range with at least 2 orders of magnitude (without affecting the optical transmission of the film).

Besides altering the sensing properties of TM doped Mg, we also discovered that Ti, Zr, and Hf are themselves effective hydrogen sensing materials. In chapter 5 we focus on HfH_x thin films as an optical hydrogen sensing material, which shows a simple relationship between the applied hydrogen pressure and the optical transmission over a pressure range of at least 6, possibly 10 orders of magnitude. This pressure range is without hysteresis while the optical transmission change per H of the film is of the same order as observed in Pd-alloy thin films with the same thickness. In addition, the films show great stability and good reproducibility. Besides discussing the sensing properties in great detail, we also discuss the origin of the anomalous large pressure range. Intriguingly, we find that adding hydrogen does not induce an enthalpy change. This not only means that the temperature dependence of the pressure range is highly linear, it also means that the pressure range is completely described by a large change in entropy. However, we cannot describe this large change in entropy by well-known contributions, such as the configurational, vibrational, and nearest-neighbour contributions. We therefore propose a contribution based on the elastic coupling between two structures. In the appendix we discuss the results by showing that also TiH_x, ZrH_x, and TaH_x are effective hydrogen sensing materials, each with a different pressure range. These discoveries suggest that more transition metals may be feasible for sensing hydrogen over a large pressure range.

References

[1.1] *T. Hübert, L. Boon-Brett, G. Black, and U. Banach.* **Hydrogen sensors - a review.** Sensors and Actuators B **157**, 329 – 352 (2011).

[1.2] *J.R. Jennings.* **Catalytic Ammonia Synthesis: Fundamentals and Practice. ISBN 978-1-4757-9594-3** Springer Science+Business (2013).

[1.3] *R.R.J. Maier, J.S. Barton, J.D.C. Jones, S. McCulloch, B.J.S. Jones, and G. Burnell.* **Palladium-based hydrogen sensing for monitoring of ageing materials.** Measurement Science and Technology **17**(5), 1118 – 1123 (2006).

[1.4] *T.H. Risby and S.F. Solga.* **Current status of clinical breath analysis.** Applied Physics B **85**, 421 – 426 (2006).

[1.5] *A. Züttel, A. Borgschulte, and L. Schlapbach.* **Hydrogen as a future energy carrier. ISBN 978-3-527-308170-0** Wiley-VCH (2011).

[1.6] *T. Hübert, L. Boon-Brett, G. Black, and U. Banach.* **Hydrogen sensors - a review.** Sensors and Actuators B **157**, 329 – 352 (2011).

[1.7] *L. Boon-Brett, J. Bousek, G. Black, P. Moretto, P. Castello, T. Hübert, and U. Banach.* **Identifying performance gaps in hydrogen safety sensor technology for automotive and stationary applications.** International Journal of Hydrogen Energy **35**, 373 – 384 (2010).

[1.8] *T. Hübert, L. Boon-Brett, V. Palmisano, and M.A. Bader.* **Developments in gas sensor technology for hydrogen safety.** International Journal of Hydrogen Energy **39**, 20474 – 20483 (2014).

[1.9] *V. Palmisano, E. Weidner, L. Boon-Brett, C. Bonato, F. Harskamp, P. Moretto, M.B. Post, R. Burgess, C. Rivkin, and W.J. Buttner.* **Selectivity and resistance to poisons of commercial hydrogen sensors.** International Journal of Hydrogen Energy **40**, 11740 – 11747 (2015).

[1.10] *M. Slaman, R.J. Westerwaal, H. Schreuders, and B. Dam.* **Optical hydrogen sensors based on metal-hydrides.** SPIE Proceedings **8368**, 836805 (2012).

[1.11] *R.J. Westerwaal, N. Duim, I. Nieuwenhuijse, C. Perrotton, A. Dabirian, J.M. van Leeuwen, V. Palmisano, and B. Dam.* **Thin film based sensors for a continuous monitoring of hydrogen concentrations.** Sensors and Actuators B **165**, 88 – 96 (2012).

[1.12] *R.J. Westerwaal, J.S.A. Rooijmans, I. Leclercq, D.G. Gheorge, T. Radeva, L.P.A. Mooij, T. Mak, L. Polak, M. Slaman, B. Dam, and T. Rasing.* **Nanostructured Pd-Au based fiber optic sensors for probing hydrogen concentrations in gas mixtures.** International Journal of Hydrogen Energy **38**, 4201 – 4212 (2013).

[1.13] *R.J. Westerwaal, S. Gersen, P. Ngene, D. Darmeveil, H. Schreuders, J. Middelkoop, and B. Dam.* **Fiber optic hydrogen sensor for a continuously monitoring of the partial hydrogen pressure in the natural gas grid.** Sensors and Actuators B **199**, 127 – 132 (2014).

[1.14] *P. Ngene, T. Radeva, M. Slaman, R.J. Westerwaal, H. Schreuders, and B. Dam.* **Seeing hydrogen in colors: low-cost and highly sensitive eye readable hydrogen detectors.** Advanced Functional Materials **24**(16), 2374 – 2382 (2014).

[1.15] *C. Wadell, S. Syrenova, and C. Langhammer.* **Plasmonic hydrogen sensing with nanostructured metal hydrides.** ACS Nano **8**(12), 11925 – 11940 (2014).

[1.16] *T. Mak, R.J. Westerwaal, M. Slaman, H. Schreuders, A.W. van Vugt, M. Victoria, C. Boelsma, and B. Dam.* **Optical fiber sensor for the continuous monitoring of hydrogen in oil.** Sensors and Actuators B **190**, 982 – 989 (2014).

[1.17] *C. Perrotton, N. Javahiraly, A. Kazemi, and P. Meyrueis.* **Review of optical fiber sensor technologies for hydrogen leak detection in hydrogen energy storage.** SPIE Proceedings **8026**, 802605 (2011).

[1.18] *R.C. Hughes, A.J. Ricco, M.A. Butler, and S.J. Martin.* **Chemical microsensors.** Science **254**, 7480 (1991).

[1.19] *M.A. Butler and R.J. Buss.* **Kinetics of the micromirror chemical sensor.** Sensors and Actuators B **11**, 161 – 166 (1992).

[1.20] *M.A. Butler.* **Micromirror optical fiber hydrogen sensor.** Sensors and Actuators B **22**, 155 – 163 (1994).

[1.21] *S.F. Silva, L. Coelho, O. Frazao, J.L. Santos, and F.X. Malcata.* **A review of palladium-based fiber-optic sensors for molecular hydrogen detection.** Sensor Journals **12**, 93 – 102 (2014).

[1.22] *N. Javahiraly and C. Perrotton.* **Hydrogen leak detection: a comparison between fiber optic sensors based on different designs.** SPIE Proceedings **9202**, 920206 (2014).

[1.23] *J.N. Huiberts, R. Griessen, J.H. Rector, R.J. Wijngaarden, J.P. Dekker, D.G. Groot, and N.J. Koeman.* **Yttrium and lanthanum hydride films with switchable optical properties.** Nature **380**, 231 – 234 (1996).

[1.24] *R. Griessen.* **Switchable mirrors.** Europhysics News (2001).

[1.25] *I.A.M.E. Giebels.* **Shining light on magnesium based switchable mirrors.** Doctoral thesis. VU University Amsterdam. ISBN 90-9018547-X (2004).

[1.26] *K. Von Rottkay, M. Rubin, F. Michalak, and R. Armitage.* **Effect of hydrogen insertion on the optical properties of Pd-coated magnesium lanthanides.** Electrochimica Acta **44**, 3093 – 3100 (1999).

[1.27] *D.E. Azofeifa, N. Clark, W.E. Vargas, H. Solós, G.K. Sólis, and B. Hjörvarsson.* **Temperature-and hydrogen-induced changes in the optical properties of Pd capped V thin films.** Physica Scripta **86**, 065702 1 – 11 (2012).

[1.28] *R. Gremaud, M. Slaman, H. Schreuders, B. Dam, and R. Griessen.* **An optical combinatorial method to determine the thermodynamics of hydrogen absorption and desorption in metals.** Applied Physics Letters **91**, 231916 (2007).

[1.29] *R. Gremaud.* **Hydrogenography. A thin film optical combinatorial study of hydrogen storage materials.** Doctoral thesis. VU University Amsterdam. ISBN/EAN 978-90-9023439-7 (2008).

[1.30] *M.A. Pick, J.W. Davenport, M. Strongin, and G.J. Dienes.* **Enhancement of hydrogen uptake rates for Nb and Ta by thin surface overlayers.** Physical Review Letters **43**(4), 286 – 289 (1979).

[1.31] *F.A. Lewis, K. Kandasamy, and X.Q. Tong.* **Palladium-hydrogen system.** Solid State Phenomena **73 – 75**, 268 – 502 (2000).

[1.32] *F.D. Manchester, A. San-Martin, and J.M. Pitre.* **The H-Pd (hydrogen-palladium) system.** Journal of Phase Equilibria **15**, 62 – 83 (1994).

[1.33] *J.R. Lacher.* **A theoretical formula for the solubility of hydrogen in palladium.** Proceedings of the Royal Society of London Series a-Mathematical and Physical Sciences **161**(A907), 525 – 545 (1937).

[1.34] *C. Labes and R.B. McLellan.* **Thermodynamic behavior of dilute palladium-hydrogen solid solutions.** Acta Metallurgica **26**, 893 – 899 (1978).

[1.35] *T.B. Flanagan and W.A. Oates.* **The palladium-hydrogen system.** Annual Review of Materials Science **21**, 269 – 304 (1991).

[1.36] *A. Armgarth and C. Nylander.* **Blister formation in Pd gate mis hydrogen sensors.** Electron Device Letters **3**(12), 384 – 386 (1982).

[1.37] *R.C. Hughes, T.E. Schubert, J.L. Zipperian, J.L. Rodriguez, and T.A. Plut.* **Thin-film palladium and silver alloys and layers for metal-insulator-semiconductor sensors.** Journal of Applied Physics **62**(3), 1074 – 1083 (1987).

[1.38] *M. Wang and Y. Feng.* **Palladium-silver thin film for hydrogen sensing.** Sensors and Actuators B **123**, 101 – 106 (2007).

[1.39] *L. Tang, G. Yu, X. Li, F. Chang, and C.J. Zong.* **Palladium-gold alloy nanowire-structured interface for hydrogen sensing.** ChemPlusChem **80**, 722 – 730 (2015).

[1.40] *R. Gremaud, A. Baldi, M. Gonzalez-Silveira, B. Dam, and R. Griessen.* **Chemical short-range order and lattice deformations in MgyTi1-yHx thin films probed by hydrogenography.** Physical Review B **77**, 144204 (2008).

[1.41] *M. Slaman, B. Dam, M. Pasturel, D.M. Borsa, H. Schreuders, J.H. Rector, and R. Griessen.* **Fiber optic hydrogen detectors containing Mg-based metal hydrides.** Sensors and Actuators B **123**, 538 – 545 (2007).

[1.42] *M. Victoria, R.J. Westerwaal, B. Dam, and J.L.M. van Mechelen.* **Amorphous metal-hydrides for optical hydrogen sensing: the effect of adding glassy Ni-Zr to Mg-Ni-H.** ACS Sensors **1**, 222 – 226 (2016).

[1.43] *A. San-Martin and F.D. Manchester.* **The H-Mg (hydrogen-magnesium) system.** Journal of Phase Equilibria **8**(5), 431 – 437 (1987).

[1.44] *P. Ngene, R.J. Westerwaal, S. Sachdeva, W.G. Haije, L.C.P.M. de Smet, and B. Dam.* **Polymer-induced surface modifications of Pd-based thin films leading to improved kinetics in hydrogen sensing and energy storage applications.** Angewandte Chemie International Edition **53**, 12081 – 12085 (2014).

[1.45] *P.A. Szilagyi, R.J. Westerwaal, R. van de Krol, H. Geerlings, and B. Dam.* **Metal-organic framework thin films for protective coating of Pd-based optical hydrogen sensors.** Journal of Materials Chemistry C **1**, 8146 – 8155 (2013).

[1.46] *R. Nomoto, J.F. McCabe, and S. Hirano.* **Comparison of halogen, plasma and LED curing units.** Operative Dentistry **29**, 287 – 294 (2004).

Interface Energy Controlled Thermodynamics

2.1 Introduction

The applicability of a continuous hydrogen sensor is mostly determined by its pressure range. This is defined by the nature of the material that interacts with hydrogen, and it can be altered by destabilizing the metal-hydrogen system. Here, we ignore the destabilization of the (de)hydrogenation reaction, as they do not affect the thermodynamics:

$$M + H_2 \rightarrow \text{constrained } MH_2 \rightarrow \text{deformations relaxed } MH_2 \rightarrow \text{relaxed } MH_2. \quad (2.1)$$

In this way, strain energies and (plastic) deformations act just as kinetic barriers. However, destabilization of the final product will be obtained when it remains constrained. We distinguish two types of destabilization. *Chemical* destabilization can be achieved by alloying the metal.[2.1] Here, both the non-hydrogenated and the hydrogenated state are destabilized. However, the improved properties mainly reflect the enhanced (de)hydrogenation kinetics[2.2 — 2.4] rather than the pressure range while the (optical) response to hydrogen strongly depends on the alloy concentration.[2.5] *Physical* destabilization is a more interesting option to change the pressure range, especially for nano-scaled structures. It mainly affects the hydrogenated state and can, in principle, be achieved via clamping[2.6] and/or interface energy.[2.7 — 2.10] The magnitude of both effects scales with the inverse thickness. For hydrogen detec-

tion destabilization through interface energy is preferred over clamping. This because (the change of) clamping affects the hydrogenation and the dehydrogenation process differently (asymmetric), while (the change of) interface energy influences these processes in the same manner. As a result, (the change of) clamping induces hysteresis (and increases it when already present) in contrast to (the change of) interface energy.

Until now, the destabilization through interface energy is only expected to occur from theory.[2.11 − 2.13] In this chapter we show that nano structured MgH_2 is destabilized by interface energy. For this we use Mg thin films with varying thicknesses between $1.5 - 10 \ \mathrm{nm}$, which show well-defined pressure plateaus. In this way we study the destabilization with high precision and find that the deduced interface energy change is in excellent agreement with the one obtained from first principle calculations. However, we also find that the observed destabilization can not be explained through only interface energy. We observe an increased hysteresis. Hence, we propose that the destabilization is the sum of interface energy and elastic clamping. Also using a different structure, we cannot separate interface energy from elastic clamping. Using Mg nanodots, the results suggest that the destabilization is the sum of interface energy, elastic clamping, and a volume strain. The latter is the result of the specific geometry of the nanodots, as in none of the dimensions the Mg dot cannot expand freely.

2.2   Interface Energy

The thermodynamics of non-constrained metal hydrides can be described by the sum of bulk and surface terms. The size of the terms depends on the structure dimensions. When the surface-to-volume ratio is small, the surface effects can be neglected. For structures below several tenths of nanometers, the surface effects have a significant effect on the (de)hydrogenation process. To deduce this mathematically, we assume that the hydrogenation of a metal M is of the form:

$$\mathrm{M} + \frac{x}{2}\,\mathrm{H}_2 \rightarrow \mathrm{MH}_x \tag{2.2}$$

where x is the hydrogen fraction. For bulk metals, the change in the Gibbs free energy for this reaction is:

$$\Delta_r G^0_\mathrm{bulk} = G_{\mathrm{MH}_x} - G_\mathrm{M} - \frac{x}{2} G_{\mathrm{H}_2} = \Delta_f G^0_{\mathrm{MH}_x}. \tag{2.3}$$

Here $\Delta_f G^0_{\mathrm{MH}_x}$ is the standard Gibbs free energy of MH_x formation form the elements. For nano-sized materials, we have to account for the surface effects in both the metal and the metal hydride phase:

$$\Delta_r G^0_\mathrm{nano} = (G_{\mathrm{MH}_x} + A_{\mathrm{MH}_x}\gamma_{\mathrm{MH}_x}) - (G_\mathrm{M} + A_\mathrm{M}\gamma_\mathrm{M}) - \frac{x}{2} G_{\mathrm{H}_2}. \tag{2.4}$$

Here A_i is the interface area and γ_i the surface energy of the respective phases i. Combining equations 2.3 and 2.4 results in:

$$\Delta_r G^0_{\mathsf{nano}} = \Delta_f G^0_{\mathsf{MH}_x} + A_{\mathsf{MH}_x} \gamma_{\mathsf{MH}_x} - A_{\mathsf{M}} \gamma_{\mathsf{M}}. \qquad (2.5)$$

Here we assume an uniform lattice orientation at the surface. Taken different lattice orientations into account, this leads to the anisotropy of the interface energies:

$$\Delta_r G^0_{\mathsf{nano}} = \Delta_f G^0_{\mathsf{MH}_x} + \sum_j \left(A_{\mathsf{MH}_x|j} \gamma_{\mathsf{MH}_x|j} - A_{\mathsf{M}|j} \gamma_{\mathsf{M}|j} \right). \qquad (2.6)$$

Here j indicates the different lattice orientations at the interface.

With the definition of the equilibrium constant K, we can relate the Gibbs free energy to the hydrogen pressure:

$$-\ln(K) = \ln\left(\frac{P_{\mathsf{eq}}}{P_0} \right) = \frac{\Delta_r G^0_{\mathsf{MH}_x}}{R\,T}. \qquad (2.7)$$

Here K is a function of P_{eq}, the equilibrium hydrogenation pressure of the metal, and P_0 the standard pressure $(10^{+5}\,\mathrm{Pa})$. For the hydrogen of a bulk metal this equations becomes:

$$\ln\left(\frac{P^{\mathsf{bulk}}_{\mathsf{eq}}}{P_0} \right) = \frac{\Delta_f G^0_{\mathsf{MH}_x}}{R\,T}. \qquad (2.8)$$

while for nano-sized materials it becomes:

$$\ln\left(\frac{P^{\mathsf{nano}}_{\mathsf{eq}}}{P_0} \right) = \frac{1}{R\,T} \left[\Delta_f G^0_{\mathsf{MH}_x} + \sum_j \left(A_{\mathsf{MH}_x|j} \gamma_{\mathsf{MH}_x|j} - A_{\mathsf{M}|j} \gamma_{\mathsf{M}|j} \right) \right]. \qquad (2.9)$$

When we subtract these to equations we find:

$$\ln\left(\frac{P^{\mathsf{nano}}_{\mathsf{eq}}}{P^{\mathsf{bulk}}_{\mathsf{eq}}} \right) = \frac{1}{R\,T} \left[\sum_j \left(A_{\mathsf{MH}_x|j} \gamma_{\mathsf{MH}_x|j} - A_{\mathsf{M}|j} \gamma_{\mathsf{M}|j} \right) \right]. \qquad (2.10)$$

Hence, the equilibrium pressure depends on the difference in the total surface energy of the metal and the metal hydride. A further derivation depends on the geometry of the nano-sized materials. Below we consider two extreme geometries, thin films and spherical particles.

2.2.1   Thin Films

We consider thin films as a multilayer system where the thin metal layer M is sandwiched between two layers SL of the same material (see figure 2.1). The sandwich layers SL are chosen in such a way that its surface properties do not change during

the hydrogenation of metal M. This implies that the change in surface (or interface) energy is only due to the hydrogenation of the metal M to form the metal hydride MH$_x$. As a result, we assume a single j lattice orientation at the surface of the metal. This reduces equation 2.10 to:

$$\ln\left(\frac{P_{\text{eq}}^{\text{nano}}}{P_{\text{eq}}^{\text{bulk}}}\right) = \frac{1}{R\,T}\left(A_{\text{MH}_x|\text{SL}}\gamma_{\text{MH}_x|\text{SL}} - A_{\text{M}|\text{SL}}\gamma_{\text{M}|\text{SL}}\right). \tag{2.11}$$

In a recent work on thin film samples, it has been showed by High Resolution Transmission Electron Microscopy (HRTEM) that the hydrogen induced volume expansion of a thin metal layer is fully converted to an expansion only in the direction perpen-
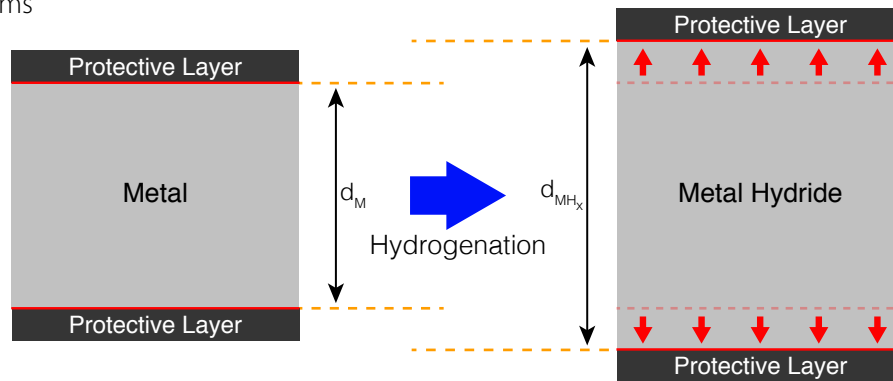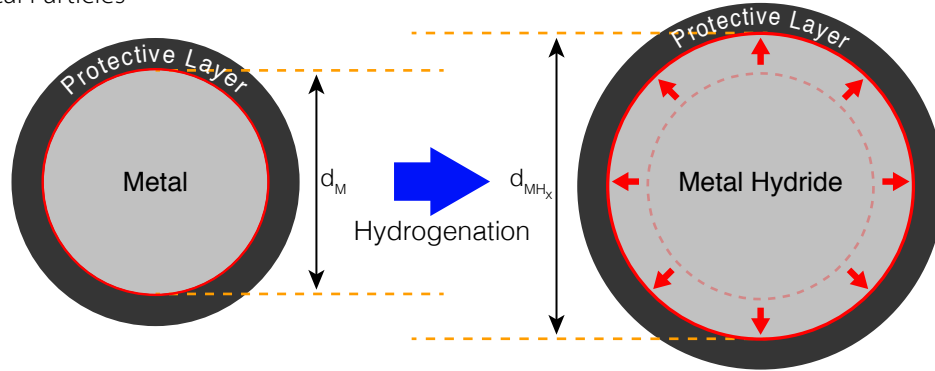
Figure 2.1 | Interface Area in Metal Thin Films and Spherical Particles – The effect of the geometry on the interface area (red) between the metal and the surrounding layer(s) when hydrogenate the metal. In thin films (top), the volume expansion due to hydrogen of the metal results only in the thickness expansion of the film (from d_{M} to d_{MH_x}). As a result, the interface area does not change. In spherical particles (bottom), the volume expansion due to the hydrogenation of the metal is uniform in all directions. Consequently, the interface area increases due to the increased diameter of the particle (from d_{M} to d_{MH_x}).

dicular to the substrate.[2.15] As a result, the interface area between the metal and the surrounding layers remains constant during hydrogenation:

$$A_{\mathsf{M|SL}} = A_{\mathsf{MH}_x\mathsf{|SL}} = A. \tag{2.12}$$

With $\Delta\gamma = \gamma_{\mathsf{MH}_x\mathsf{|SL}} - \gamma_{\mathsf{M|SL}}$ equation 2.11 reduces to

$$\ln\left(\frac{P_{\mathsf{nano}}}{P_{\mathsf{bulk}}}\right) = \frac{A}{R\,T}\Delta\gamma. \tag{2.13}$$

To relate the equilibrium pressure to the film thickness d, we express the surface area A to the film thickness d through the molar volume V_{M} of the metal by:

$$A = 2\frac{V_{\mathsf{M}}}{d}. \tag{2.14}$$

The factor 2 accounts for the two interfaces between the metal and the surrounding layers. With this relation we rewrite equation 2.13 to

$$\ln\left(\frac{P_{\mathsf{nano}}}{P_{\mathsf{bulk}}}\right) = 2\frac{V_{\mathsf{M}}}{R\,T\,d}\Delta\gamma. \tag{2.15}$$

In this way we find that P_{nano} scales with the inverse thickness and that a positive $\Delta\gamma$ results in the destabilization of the nano-sized hydride phase with respect to the bulk hydride $(d = \infty)$. We obtain $\Delta\gamma$ by measuring P_{nano} for various thicknesses. These measurements provide us also information about bulk, as the extrapolation to infinite thickness should be equal to the bulk equilibrium pressure of the metal hydride P_{bulk}. In this way the comparison of this extracted value with the reported values of P_{bulk} gives an indication of the legitimacy of equation 2.15 in thin films.

2.2.2   Spherical Particles

While the thin film geometry induces an expansion in one direction, the expansion in a spherical particle is homogeneous in all directions. This alters the derivation of the relation between the equilibrium pressure and the particle dimensions, as we have to take into account that surface area changes when the particle becomes hydrogenated. In the derivation, we consider the spherical particle as a core-shell system where the metal core is surrounded by a shell (see figure 2.1). In first approximation, we assume that the shell is highly elastic and exhibits no stiffness. As a result, the expansion of the metal core is not counteracted in any way by the surrounding layer. We also assume an isotropic surface energy for both the metal core and the surrounding layer: the surrounding layer does not form a hydride or has already formed a hydride when the metal core forms a hydride.

Our first step is to express the increase of the interface area between the metal core and the surrounding layer upon hydrogenation in terms of the uniform volume expansion of the metal core. The interface area between the metal and the surrounding layer is given by

$$A_{\mathsf{M|SL}} = \pi d_{\mathsf{M}}^2 \tag{2.16}$$

and increases to

$$A_{\mathsf{MH}_x|\mathsf{SL}} = \pi d_{\mathsf{MH}_x}^2 \tag{2.17}$$

upon hydrogenation. In both equations d indicates the diameter of the particle, in either the metal or the metal hydride state. Since the volume of a sphere is proportional to d^3, the expansion of the diameter $d_{\mathsf{M}} \rightarrow d_{\mathsf{MH}_x}$ can be rewritten in a volume expansion by

$$\frac{d_{\mathsf{MH}_x}}{d_{\mathsf{M}}} = \sqrt[3]{\frac{V_{\mathsf{MH}_x}}{V_{\mathsf{M}}}}. \tag{2.18}$$

This reduces equation 2.11 to

$$\ln\left(\frac{P_{\mathsf{eq}}^{\mathsf{nano}}}{P_{\mathsf{eq}}^{\mathsf{bulk}}}\right) = \frac{1}{R\,T}\left(\pi d_{\mathsf{MH}_x}^2 \gamma_{\mathsf{MH}_x|\mathsf{SL}} - \pi d_{\mathsf{M}}^2 \gamma_{\mathsf{M|SL}}\right) \tag{2.19a}$$

$$= \frac{1}{R\,T}\left(\pi d_{\mathsf{M}}^2 \left[\frac{V_{\mathsf{MH}_x}}{V_{\mathsf{M}}}\right]^{\frac{2}{3}} \gamma_{\mathsf{MH}_x|\mathsf{SL}} - \pi d_{\mathsf{M}}^2 \gamma_{\mathsf{M|SL}}\right) \tag{2.19b}$$

Converting the diameter of the metal core to its (molar) volume, we find

$$\ln\left(\frac{P_{\mathsf{eq}}^{\mathsf{nano}}}{P_{\mathsf{eq}}^{\mathsf{bulk}}}\right) = \pi \frac{V_{\mathsf{M}}}{R\,T\,d_{\mathsf{M}}}\left(\left[\frac{V_{\mathsf{MH}_x}}{V_{\mathsf{M}}}\right]^{\frac{2}{3}} \gamma_{\mathsf{MH}_x|\mathsf{SL}} - \gamma_{\mathsf{M|SL}}\right). \tag{2.20}$$

Similar to thin films, we find that the equilibrium pressure of nano-sized particles scales with the inverse diameter.

Unlike thin films, nano-sized spherical particles do not have an isotropic surface energy. This means that we have to take all surface orientations, including that of the shell, into account, both before and after hydrogenation. Despite that the number of orientations depends on the material of both the core and shell, each contribution scales with the surface/interface area, and therefore with d^{-1}. As a result, $P_{\mathsf{eq}}^{\mathsf{nano}}$ remains proportional to d^{-1}. This proportionality is maintained when we introduce a non-zero stiffness to the shell. Upon hydrogenation of the metal core, the corresponding volume expansion is constrained by the shell. The hydride phase becomes compressed and experiences a volume strain ε_V. Pasquini *et al.* show that such a compression give rise to an enthalpy change of:[2.14]

$$\delta(\Delta H) \approx -2B\,V_{\mathsf{H}}\,\varepsilon_V \tag{2.21}$$

where B is the bulk modulus and V_{MH_x} the partial molar volume of hydrogen in the hydride phase. The factor 2 is needed to express the enthalpy change per mol H_2. Since the volume strain is always negative, the enthalpy change $\delta(\Delta H)$ is always positive and destabilizes the hydride. Taken this effect into account results in an additional bias of $-2\,B\,V_H\,\varepsilon_V/R\,T$ with respect to equation 2.10:

$$\ln\left(\frac{P_{eq}^{nano}}{P_{eq}^{bulk}}\right) = \frac{1}{R\,T}\left[\sum_j \left(A_{MH_x|j}\gamma_{MH_x|j} - A_{M|j}\gamma_{M|j}\right)\right] - 2\frac{B\,V_H\,\varepsilon_V}{R\,T}. \qquad (2.22)$$

This means that a volume strain does not affect the linear relation between P_{eq}^{nano} and d^{-1}. Instead, it only induces a thermodynamical bias.

## 2.3 Interface Energy in Mg Thin Films

In the previous section we derived that the equilibrium pressure of ultra thin films scales with the inverse thickness of the layer through the interface energy $\Delta\gamma$ (see equation 2.15). To verify this relation experimentally, we measure the thermodynamics of Mg thin films with various thicknesses (between $1.5 - 10\,\text{nm}$) by means of hydrogenography. This is possible as, upon hydrogenation, the metal-to-insulator transition from Mg to MgH_2 causes a marked increase in optical transmission of the film at the equilibrium pressure P_{eq}.[2.6,2.15,2.18]

Mg thin films have also the advantage that they are highly textured, even after hydrogenation. It has been shown that Mg thin layers ($>20\,\text{nm}$) grows highly textured with the (002)-plane parallel to the substrate. After hydrogenation, the films are still textured with the MgH_2 (110)-plane parallel to the substrate.[2.15] Although no diffraction peak of MgH_2 could be seen for hydrogenated Mg layers below <20 nm, we assume the same texture. We also assume that the size of the nucleus of MgH_2 is larger than the Mg-layer surface. This means that at each time, also during hydrogenation, only a single lattice orientation is present at the interfaces.

To determine P_{eq}^{nano} as a function of the layer thickness d we use two different multilayer stacks of Mg and Ti (see sample preparation). The first stack consists of 6 Mg layers, each with a different thickness (1.5, 2, 3, 4, 7, and $10\,\text{nm}$). Each Mg layer is placed between two $5\,\text{nm}$ thin layers, which act as spacers. The Ti layers will be hydrogenated to form TiH_2 at pressures (far) below the hydrogenation pressure of Mg.[2.16] As a result, during the whole hydrogenation of Mg, the same textured fluorite TiH_2 (with the (111)-plane parallel to the surface) is present. The second stack has the same geometry, consists of only three Mg layers with a thickness of 2, 5, and $10\,\text{nm}$. On both types of stacks a Pd layer ($10\,\text{nm}$) is deposited to prevent the stacks from oxidation and to enhance the hydrogen dissociation process.[2.17]

Sample Preparation

The three thin film samples are composed of a stack of Ti and Mg layers. The first stack sample (left) consists of 6 Mg layers (red) of $10, 7, 4, 3, 2$, and 1.5 nm. The second stack sample (top right) consists of 3 Mg layers (red) of $10, 5$, and 2 nm. In both samples the Mg layers have a homogeneous thickness and are interlaced by 5 nm Ti layers. The third sample (bottom right) consists of a single Mg wedge layer, with a thickness gradient ranges from 1.7 to 10 nm. The Mg wedge layer is sandwiched between two 10 nm Ti layers. All samples are capped by a 10 nm Pd layer. The two stack samples are deposited on a 10×10 mm^2 polished quartz substrate (1 mm thick) by means of an ultra-high vacuum sputter system (base pressure of 10^{-10} Pa) in $3\,\mu$bar Ar (6N). The wedge sample is deposited on a 70×10 mm^2 polished quartz substrate (1 mm thick). The homogeneous thick layers are obtained by a rotating substrate during sputtering. Typical depositing rates are 0.7 Å/s (200 W DC) for Ti, 1.6 Å/s for Mg (150 W RF), and 1.2 Å/s for Pd (50 W DC), which are obtained by stylus profilometry (DEKTAK) recorded on thick layers (> 200 nm).
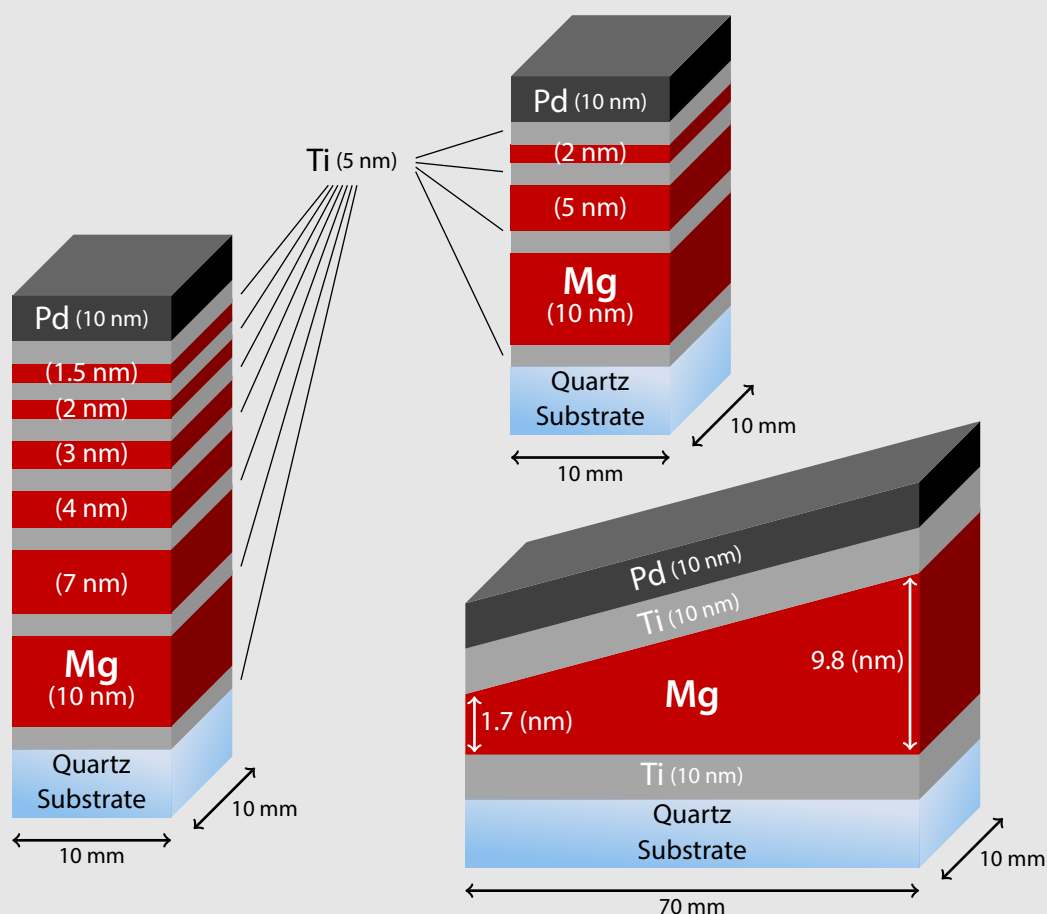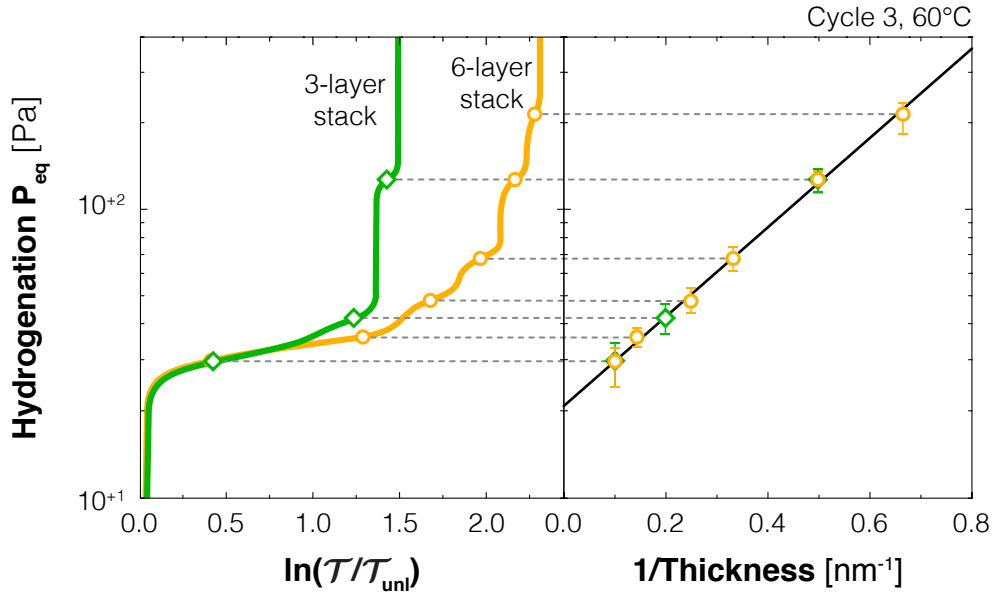
Figure 2.2 | Hydrogenation of Multi-layer Stack Mg – left: The third hydrogenation cycle isotherms of two Mg-Ti multilayer geometries measured at $60°\text{C}$. The three layer stack sample (green) consists of a stack in which Ti ($5\ \text{nm}$) is alternated by 10, 5, and $2\ \text{nm}$ thick Mg layers. In the six layer stack sample (orange) Mg layers with a thickness of 10, 7, 4, 3, and $2\ \text{nm}$ are interlaced by Ti layers ($5\ \text{nm}$). **right:** The equilibrium pressures as a function of the Mg layer thickness. The solid line represents the fit of equation 2.15, with $\Delta\gamma = 0.35\ \text{J m}^{-2}$ and $P_{\text{bulk}} = 20\ \text{Pa}$. The error bars indicate the pressure-span of the pressure plateaus.

After the initial exposure, the hydrogenation of Mg is reversible as the second and third absorption cycles perfectly overlap. We therefore use the third cycle absorption PTIs of the six- and three-layer stack samples measured at $60°\text{C}$ as shown in figure 2.2. Clearly, we find different plateau pressures indicating several distinctive thermodynamic equilibria. From the Lambert-Beer law it follows that the width of the pressure plateau (the change in transmission due to the transition from reflective, metallic Mg to insulating transparent MgH_2) is directly proportional to the thickness of the corresponding Mg layer.[2.18] Hence, we conclude that the thicker Mg layers absorbs hydrogen at lower pressures. This is verified by comparing the optical reflection from the substrate side to that from the top of the film.[2.6] By plotting the plateau pressure as a function of the inverse layer thickness, we find a clear linear dependence that is in perfect agreement with equation 2.15. Note that, while the pressure plateaus corresponding to the 7 and $10\ \text{nm}$ Mg layers are difficult to distinguish visually, their combined width exactly matches the plateau width of the completely hydrogenated three-layer sample (total thickness of $17\ \text{nm}$ Mg). Despite
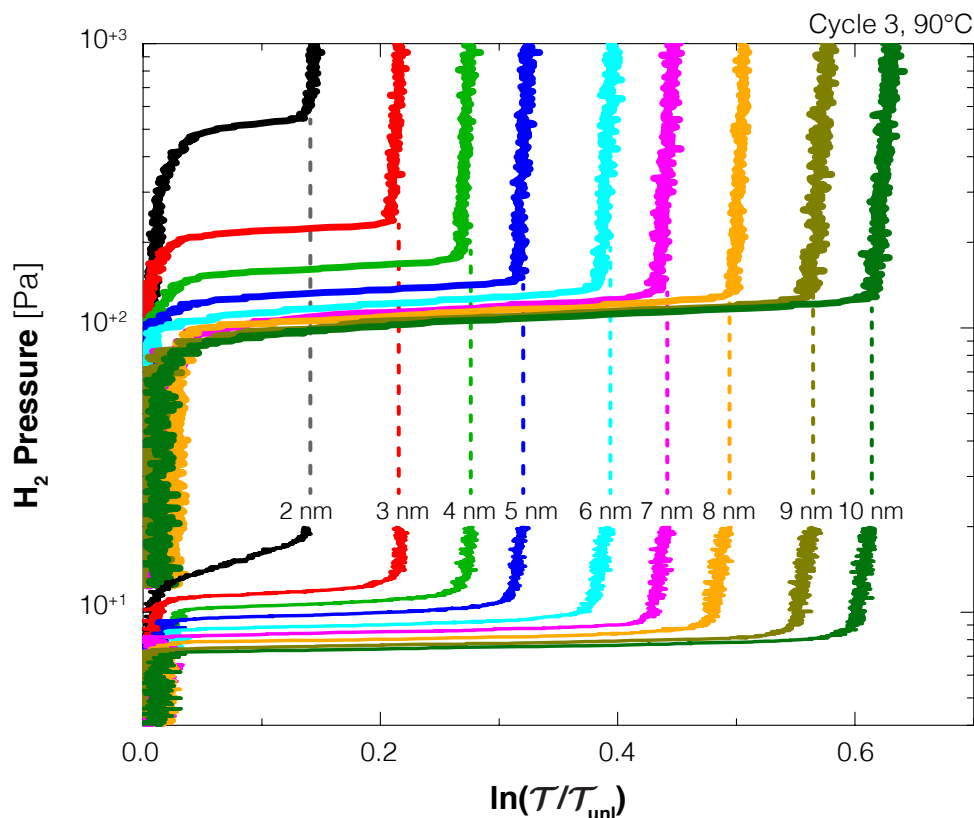
Figure 2.3 | Hydrogenation & Dehydrogenation Isotherms – Third hydrogenation and dehydrogenation pressure-optical transmission-isotherms (PTIs) for various Mg layer thicknesses using a Mg-wedge sample measured at $90°\text{C}$.

the different number of Mg layers, the results of both stack samples are consistent. We find that the 2 and $10\ \text{nm}$ Mg layers load at exactly the same pressure in both stacks. Despite that hydrogen (enters the sample from the top) has to overcome different kinetic barriers in the form of several layers of Mg and TiH_2, the thickest (and lowest) Mg layer hydrogenates first. This is strong indication for the thermodynamic nature of this effect.

Mg Wedge

To determine the change of interface energy $\Delta\gamma$ in the Mg thin films, we also have to consider the dehydrogenation of Mg. As with most other metal hydrides, the hysteretic behavior in Mg reflects the first order nature of a phase transition.[2.19] As the contribution of the interface energy to both the hydrogenation energy and the dehydrogenation energy should be the same, the effect of interface energy is equivalent to a thermodynamic bias. Therefore, on dehydrogenation we expect to find the same increase in pressure as a function of the thickness as observed on hydro-
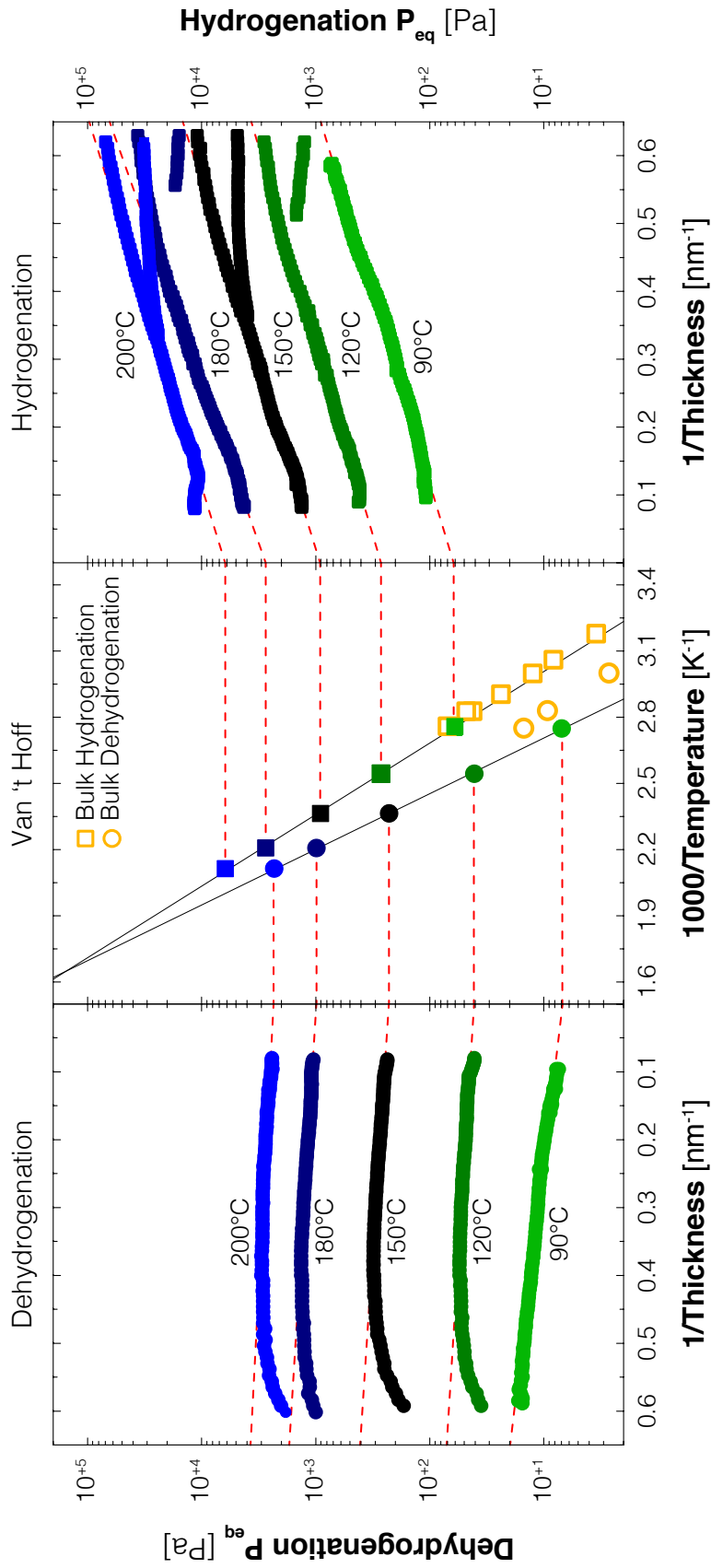
Figure 2.4 | Thickness Dependence of (de)Hydrogenation Pressure – The hydrogenation (right) and dehydrogenation (left) equilibrium pressure P_{eq} as a function of the thickness of the Mg layer ($1.6 - 9.8\,\mathrm{nm}$) in a wedge geometry, measured at different temperatures. Each temperature data corresponds to the second (de)hydrogenation. For this, a new sample is used for each temperature. The dashed lines in these indicates the fits through the data points for thicknesses larger than >3 nm. The middle plot shows the equilibrium pressures for bulk Mg as a function of the temperature (Van 't Hoff plot). Here the bulk values are obtained by extrapolating the nano-sized results to infinite thickness ($d^{-1} = 0$). The orange open points indicate the literature values for bulk Mg, extracted from *Kasemo et al.*[2.20]

genation. Since the dehydrogenation kinetics in the multilayer stacks are too slow to measure, we prepared single-layer Mg wedge samples. Here, a Mg wedge with a thickness gradient ranges from 1.6 to 10 nm is sandwiched between two 10 nm Ti layers (see sample preparation). With hydrogenography, we monitor the transmission change of the whole sample when we expose the sample to different hydrogen pressures. In this way we directly observe the pressure plateau of more than 600 Mg layer thicknesses simultaneously.

Figure 2.3 shows the pressure-optical transmission-isotherms measured at $90°C$ for a few thicknesses, by plotting the transmission $\ln(\mathcal{T}/\mathcal{T}_{\mathsf{unl}})$ against the applied hydrogen pressure. The same procedure is followed to construct the dehydrogenation isotherms. As with the stack sample, the hydrogenation and the dehydrogenation of Mg is reversible after the first exposure. In hydrogenation, we again find well-defined pressure plateaus. Even the pressure plateau of Mg layers as thin as 2 nm are clearly visible. In dehydrogenation, the pressure plateaus corresponding to Mg layers with a thickness below <3 nm have a visible slope. This is usually an indication of a kinetic limitation. However, this would also be reflected in the thicker MgH_2 layers. Instead of a slope, a flat pressure plateau are observed instead. As the rate of pressure decrease is for all thicknesses the same, the steep pressure plateaus for thickness below <3 nm are likely to have a thermodynamical character.

Because of the large amount of simultaneously recorded isotherms we determine $P_{\mathsf{eq}}^{\mathsf{nano}}$ as a function of the thickness in an automatic fashion, defining $P_{\mathsf{eq}}^{\mathsf{nano}}$ as the pressure where the slope of the isotherm is the smallest. As shown in figure 2.4 the plateau pressure increases in both the hydrogenation and the dehydrogenation isotherms with decreasing d. However, at $90°C$ the slope is found to be larger in hydrogenation ($\Delta\gamma_{\mathsf{abs}} = 0.44 \pm 0.02$ J/m^2) than in dehydrogenation ($\Delta\gamma_{\mathsf{abs}} = 0.17$ J/m^2). This behavior is not expected since the interface energy should act similarly on both branches of the hysteresis into the system (see figure 2.5). The hysteretic behavior of the ultra thin Mg films studied at other temperatures ($120°C$, $150°C$, $180°C$, and $200°C$) reveals that the hysteresis decreases with increasing temperature, the decrease (on a logarithmic scale) is the same for all thicknesses. This indicates that the interface energy remains the same and that the temperature dependence of the cause the hysteresis is the effect of plastic deformations, probably induced by a thermally activated process of the creation and removal of defects. We exclude the effect of residual stress between the hydrogenated Mg and TiH_2 layers as the out-of-plane expansion upon hydrogenation equals the theoretical bulk volumetric expansion of $\sim30\%$.[2.15]

Besides a temperature dependence, the results shown in figure 2.3 also indicate that the plastic deformations should also have a thickness dependence. While the results show an increasing hysteresis with decreasing thickness, interface energy
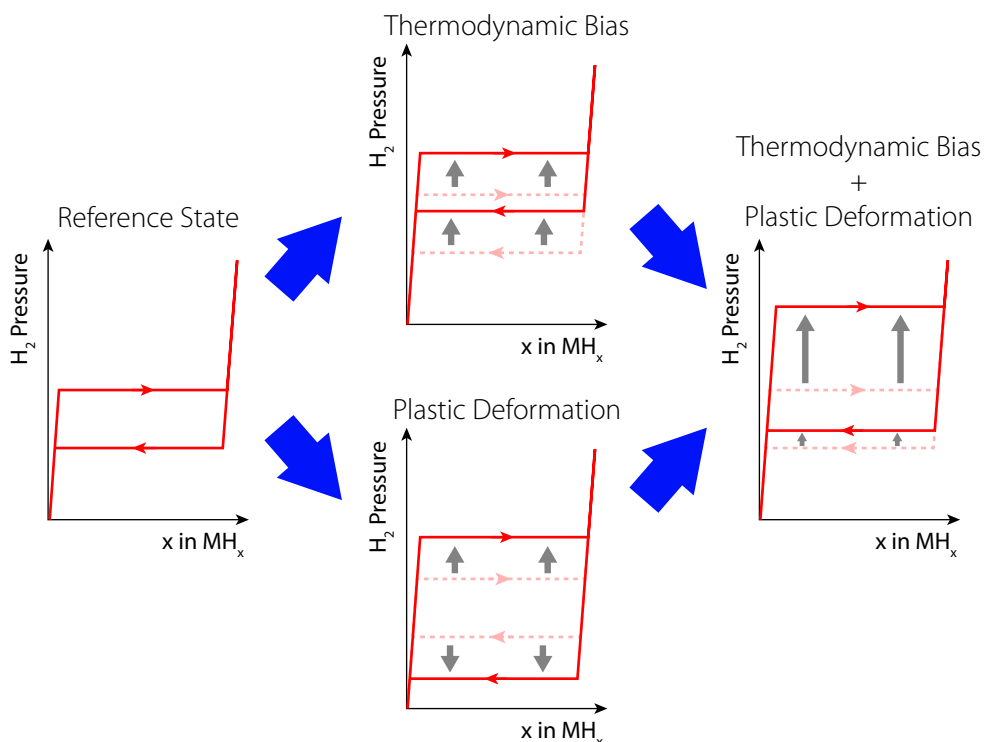
Figure 2.5 | Influence Mechanisms on (De)Hydrogenation Isotherms –
The influence of plastic deformations and/or a thermodynamic bias on
the hysteresis of a reference state (left). Compared to the reference state
(dashed), a thermodynamic bias (e.g. interface energy) results in an uni-
form shift of the hydrogenation and dehydrogenation pressure plateau
(middle, top). There is no increase of hysteresis. A plastic deformation re-
sults in an increase the hysteretic effect, as the hydrogenation pressure
plateau increases while the dehydrogenation pressure plateau decreases
(symmetric) in pressure (middle, bottom). The combination of the two
effects results in an increased hysteretic effect, where the shift of the hy-
drogenation pressure plateau is much larger compared to the shift of the
dehydrogenation pressure plateau (right).

effects predicts a constant (on a logarithmic scale) hysteresis as a function of the
thickness. Consequently, the increasing size of the hysteretic component with the
inverse thickness suggests that the amount of plastic deformations is proportional
to the interface area, which is the same for all thicknesses. This points at the for-
mation of misfit dislocations upon hydrogenation at the interface to accommodate
the misfit between MgH_2 and TiH_2.[2.22] As the amount of misfit dislocations formed
per unit volume of Mg increases with inverse thickness, so will the energy that is re-
quired to form these dislocations. Assuming that the process is symmetric, we can
now separate the interface energy from the plastic deformation. Only the average

of the hydrogenation and dehydrogenation slope of $P_{\text{eq}}^{\text{nano}}$ versus d^{-1} provides the thermodynamical bias. From this average we deduce an interface energy difference of $\Delta\gamma = 0.33 \pm 0.01$ J m^{-2}.

The assumption that plastic deformations have the same effect on the hydrogenation and dehydrogenation of thin films is questioned by Mooij *et al.*[2.23] Their experimental study on Mg thin films indicates that the structural relaxation of the surrounding Ti layers occurs on a larger timescale than the dehydrogenation of the film. This suggests that during the dehydrogenation, porous Mg is formed along with voids. This means that separate interfaces are created, each with a different interface energy. If present, this means it is difficult to separate the interface energy from the plastic deformation. Nevertheless, we expect that the interface energy difference between Mg|TiH$_2$ and MgH$_2$|TiH$_2$ will not be significantly different from the deduced value of $\Delta\gamma = 0.33 \pm 0.01$ J m^{-2}.

Finally, we compare our experimental results with calculations based on first principles. Theoretical calculations on Mg nano-particles in vacuum have revealed a destabilization of MgH$_2$ at the nanoscale due to an increase in interface energy on hydrogenation.[2.11] Furthermore, recent calculations revealed the stabilization of fluorite MgH$_2$ compared to rutile MgH$_2$ with decreasing thickness.[2.24] SAED patterns showed the presence of only the rutile phase in Mg(4 nm)/ Ti(2 nm) multi-layers.[2.15] We calculated the difference in excess energy associated with coherent interfaces without introducing elastic energy of periodic regions of TiH$_2$ (111) and MgH$_2$ (110), as compared with those of TiH$_2$ (111) and Mg (001) using the plane wave basis VASP code.[2.25] This implements the generalized gradient approximation (GGA). The resulting interface energies of these calculations are $\gamma_{\text{Mg|TiH}_2} = 0.196$ eV Å^{-2} and $\gamma_{\text{MgH}_2|\text{TiH}_2} = 0.163$ eV Å^{-2}. This leads to difference of $\Delta\gamma = 0.033$ eV Å^{-2}, which equals $\Delta\gamma = 0.53$ J m^{-2}. This value, calculated for perfectly coherent and flat interfaces, matches the value determined experimentally on ultra thin Mg layers.

Thermodynamics of Bulk from Nanosized Mg

A second way to legitimate our interpretations is to extract the thermodynamics of bulk Mg from the experimental results shown in figure 2.4. According to equation 2.15 the extrapolation of the linear relation found between $P_{\text{eq}}^{\text{nano}}$ (on a logarithmic scale) and the inverse thickness to $d^{-1} = 0$ (see figure 2.4) should be equal to the equilibrium pressure of a Mg layer with an infinite thickness $P_{\text{eq}}^{\text{bulk}}$. Plotting $P_{\text{eq}}^{\text{bulk}}$ as a function of the temperature we find that the hydrogenation values are in excellent agreement with the low temperature data for Mg particles with a diameter between $0.5 - 1$ μm, reported by Kasemo *et al.* (see figure 2.4).[2.20] Our results indicate that $\Delta H_{\text{abs}} = -59.1 \pm 1.2$ kJ/mol H$_2$ and $\Delta S_{\text{abs}} = -101.0 \pm 2.9$ J/(K mol H$_2$), while Kasemo *et al.* reports $\Delta H_{\text{abs}} = -57.8 \pm 1.1$ kJ/mol H$_2$ and $\Delta S_{\text{abs}} = -98.7 \pm 3.3$

	ΔH_{des} [kJ/mol H$_2$]	ΔS_{des} [J/(K mol H$_2$)]
This study	-75.5 ± 0.9	-128.5 ± 2.3
Krozer[2.20]	-57.6 ± 2.6	-142.8 ± 7.4
Stampfer[2.26]	-75.6 ± 0.2	-136.1 ± 0.2
Reilly[2.27]	-77.4 ± 4.2	-138.3 ± 2.9
Tanguy[2.28]	-77.0 ± 2.0	-138.1 ± 3.2
Pedersen[2.29]	-70.6 ± 0.8	-127.2 ± 1.2
Friedlmeier[2.30]	-74.3 ± 0.5	-136.0 ± 1.0
Bogdanovic[2.31]	-76.2 ± 0.3	-136.6 ± 0.5

Table 2.1 | Dehydrogenation Enthalpy and Entropy of Bulk Mg – The comparison of the enthalpy and entropy values of bulk Mg (Mg with an infinite thickness) extrapolated from nanosized Mg layers with the reported values for bulk Mg.

$J/(K \text{ mol } H_2)$.[2.20]

The extrapolated dehydrogenation pressures for an infinite thick Mg layer do not match the partial dehydrogenation pressures of the Mg particles reported by Kasemo *et al.*: $\Delta H_{\text{des}} = -75.5 \pm 0.9 \text{ kJ/mol } H_2$ and $\Delta S_{\text{des}} = -128.5 \pm 2.3 \text{ J/(K mol } H_2)$ versus $\Delta H_{\text{des}} = -57.6 \pm 2.6 \text{ kJ/mol } H_2$ and $\Delta S_{\text{des}} = -142.8 \pm 7.4 \text{ J/(K mol } H_2)$ reported by Kasemo *et al.*[2.20] However, our results do match the values extracted from other studies on Mg particles ranging from a few hundreds of nanometers to hundred μm (see table 2.1).

Ultra thin Mg: Interalloying Effects

The isotherms of nano-sized Mg studied at $120°C$, $150°C$, $180°C$, and $200°C$ indicates the presence of Mg-Ti interalloying effects in ultra-thin Mg layers. Instead of a single pressure plateau, we find for layers below 3 nm that the hydrogenation isotherms consist of two pressure plateaus. This results in two relations between the equilibrium pressure and the Mg layer thickness, represented by two branches in figure 2.4. The relation corresponding to the *upper* branch is very similar to equation 2.15. The equilibrium pressure increases with decreasing thickness, although at very small layer thicknesses ($<1.8 \text{ nm}$) the increase is less than described by equation 2.15 with $\Delta \gamma_{\text{abs}} = 0.44 \text{ J/m}^2$. The *lower* branch describes on the other hand a completely different relation. In this branch the equilibrium pressure does not depend on the thickness of the Mg layer. Note that in figure 2.4 for some temperatures this branch is not plotted continuously. The two pressure plateaus in the corresponding isotherms

are not distinct enough to extract the corresponding equilibrium pressure by means of the automatic extraction script.

The presence of two pressure plateaus in a Mg-Ti multilayer system is also observed by Baldi *et al.*[2.15] While for Mg layer thicknesses above $>4\,\mathrm{nm}$ a single pressure plateau is observed in the hydrogenation isotherms measured at $90°\mathrm{C}$, two plateaus are observed at thicknesses below $<4\,\mathrm{nm}$. The origin of this second plateau is assigned to the presence of MgTi alloys at the Mg-Ti interfaces due to the effect of cumulative roughness of the substrate. The lower formation enthalpy of TiH_2 with respect to MgH_2 results in a lower hydrogenation pressure and therefore in a lower pressure plateau.[2.32] Compared to our results this study suggests that also in our Mg-Ti multilayer system MgTi alloys at the Mg-Ti interfaces are present. Also in our system the origin is likely to be found in the substrate roughness. The constant equilibrium pressure (with Mg layer thickness) suggests that the MgTi interalloys have a constant composition and thickness, indicating that the roughness is homogeneous. This means that the interalloys should be formed at all thicknesses, although they become significant only at thickness below $<3\,\mathrm{nm}$.

While the MgTi interalloying effects partially affects the hydrogenation process of the Mg layer at layer thicknesses below $<3\,\mathrm{nm}$, it affects the dehydrogenation of the whole Mg layer at the same thicknesses. Similar to layer thicknesses above $3\,\mathrm{nm}$, the dehydrogenation isotherms of the Mg-Ti multilayer system consist of only a single pressure plateau below $3\,\mathrm{nm}$. In contrast to Mg layers above $>3\,\mathrm{nm}$, below $<3\,\mathrm{nm}$ the equilibrium pressure decreases with decreasing layer thickness. The difference with the fitted equation 2.15 with $\Delta\gamma_{\mathsf{des}} = 0.17\ \mathrm{J/m^2}$ therefore increases with decreasing thickness, and equals the difference between the fitted relation and the *lower* branch upon hydrogenation. This indicates that the MgTi interalloys obstructs the contraction of the Mg lattice during dehydrogenation, that is associated with a 32% volume decrease.

That the interalloying effects are due to the substrate roughness is supported by the experimental results shown in figure 2.4. Here we observe that the thickness dependence of the equilibrium pressure studied at $120°\mathrm{C}$, $150°\mathrm{C}$, $180°\mathrm{C}$, and $200°\mathrm{C}$ show a clear difference between the (de)hydrogenation of a Mg layer below or above $3\,\mathrm{nm}$, while at $90°\mathrm{C}$ there is no difference. As at each temperature the data set is obtained with a new sample (from the same batch), each temperature data set can correspond to a different substrate roughness. Although not verified, the results indicate that the substrate roughness used at $90°\mathrm{C}$ is smaller (and below a critical value) than at the other temperatures.

The two nanodot samples are prepared by a three-step procedure. First, ultra-thin alumina membranes are prepared by a two-step anodization process on quartz substrates, which allows for a precise adjustment of the pore shape, the pore diameter d, the interpore distance l, and the pore height h. We considered two types of templates, each with a different shape. ND60 represents a template of circular pores with $d = 60$ nm, $l = 150$ nm, and $h = 300$ nm. ND320 represents a template of square pores with $d = 320$ nm, $l = 400$ nm, and $h = 700$ nm. The templates cover an area of about 2 cm^2. The substrates are then put in ultra-high vacuum conditions ($P \approx 10^{-11}$ Pa) and let outgassing for 2 days. The Mg-based nanodots are fabricated by means of Molecular Beam Epitaxy apparatus (MBE), depositing a homogeneous thick Mg layer (30 nm), a homogeneous thick Ti layer (5 nm), and a homogeneous thick Pd layer (10 nm) (base pressure of 10^{-11} Pa). The growth rates were 0.3 Å/sec for Mg, 0.1 Å/sec for Ti, and 0.1 Å/sec for Pd, monitored by a quartz crystal microbalance. After deposition, the alumina membranes were removed by using the tape lift-off method. The three step procedure is illustrated below.
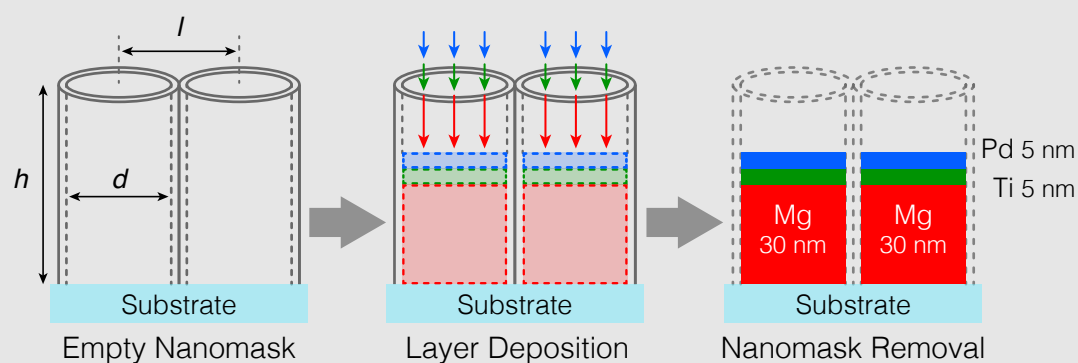
2.4 Thermodynamics of Mg Nanodots

The experiments on Mg thin films show that the (de)hydrogenation of nano-sized Mg can be described by interface energy and plastic deformations. With respect to hydrogen sensors, changing the geometry from thin films to, for example, nanodots can be interesting in order to reduce response time by increasing the ratio between the surface and the volume. A different geometry can induce different effects, for example elastic constrains. For spherical samples the protective layer(s) can induce a compression of the metal hydride phase. This results in an additional thermodynamical bias, as described by equation 2.22. The question is whether this elastic strain has a significant influence on the thermodynamics of a metal hydride.

Here we study the hydrogenation and dehydrogenation thermodynamics of multilayer Mg nanodots. We consider two sets of samples, consisting of an array of nan-
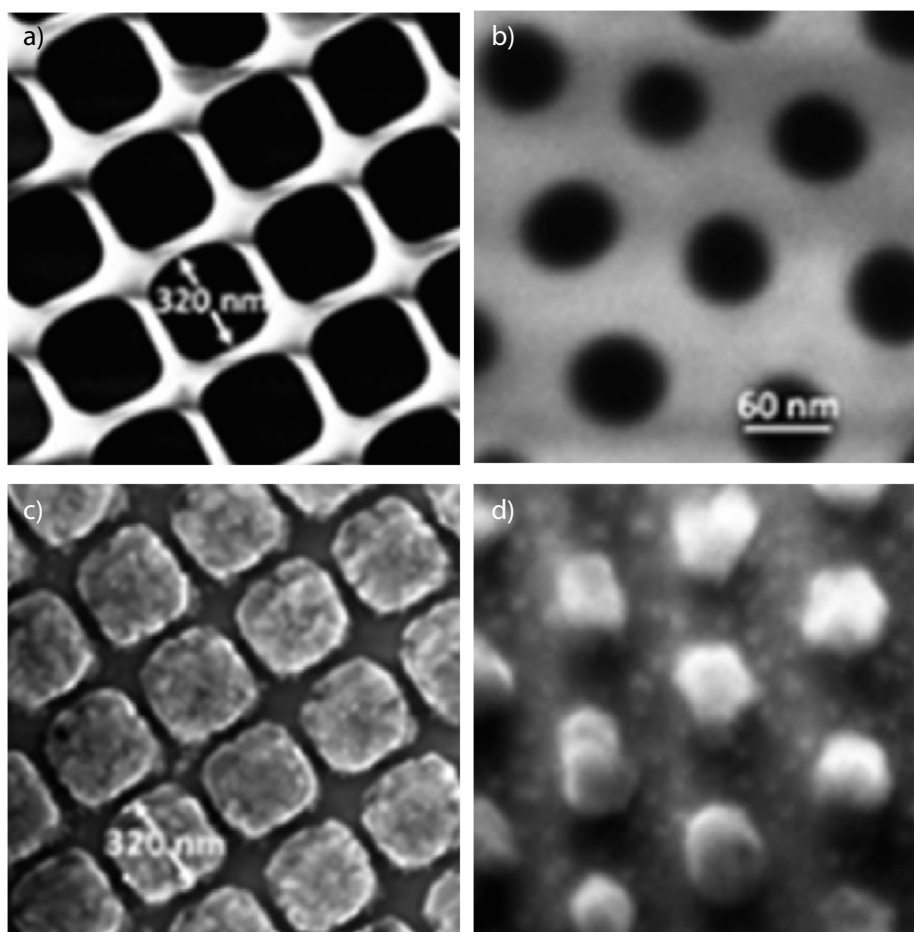
Figure 2.6 | FESEM Images of Fabricated Nanodots – FESEM images of the two templates before (**a** & **b**) and after (**c** & **d**) the removal of the alumina nano-membranes. The square nanodots (**a** & **c**) have diameter $d \approx 320$ nm and interpore distance of $l \approx 400$ nm, the circular nanodots (**b** & **d**) have $d \approx 60$ nm and $l \approx 150$ nm. All nanodots have a height of 45 nm.

odots, each with a diameter of 60 and 320 nm. Each nanodot consists of a Mg-Ti-Pd multilayer with a constant Mg thickness of 30 nm. From now on, we will name these samples as ND60 and ND320. Note that due to the preparation technique, the lateral surface of the nanodots is not covered by the Ti and Pd protective layers. Consequently, the exposure of the samples to air causes the formation of thin $(4-5\,\text{nm})$ MgO lateral layers. The FESEM images shown in figure 2.6 confirm the successful fabrication of the nanodots with different diameters.

To study whether the interface energy has can destabilize MgH_2 through the nanodot diameter, we studied the optical transmission as a function of the hydrogen pressure of ND60 and ND320 at $90°C$ and $120°C$. From the pressure-optical transmission-isotherms shown in figure 2.7 we observe that, despite the same Mg thickness,
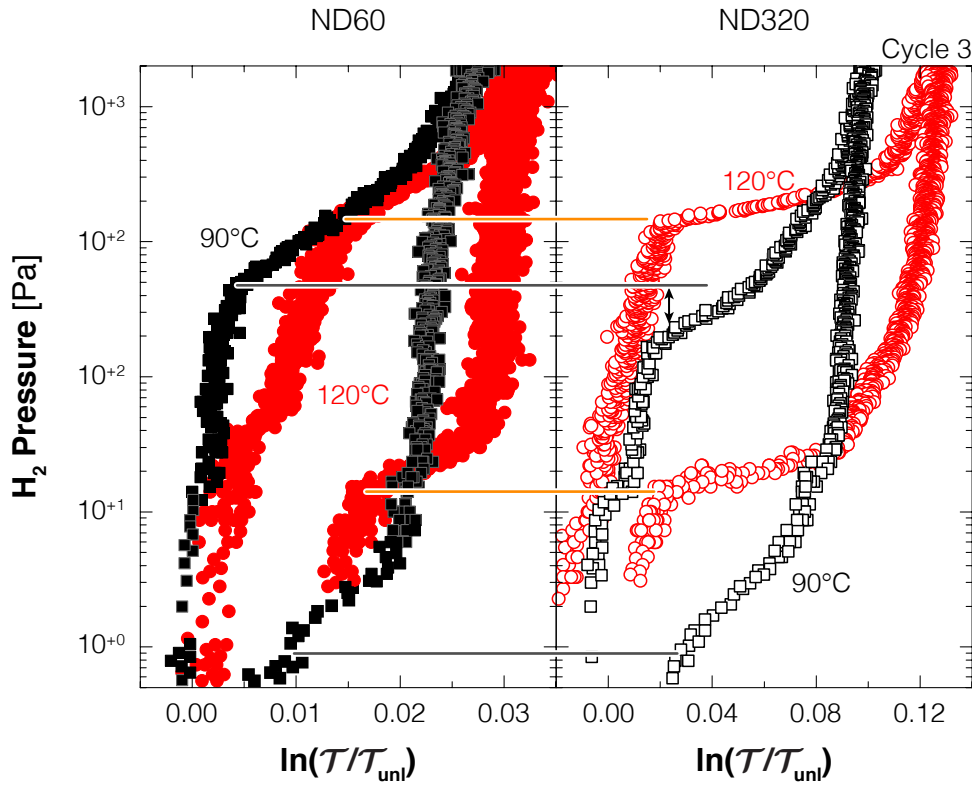
Figure 2.7 | Nanodots Pressure-Optical Transmission-Isotherms – The pressure-optical transmission-isotherms of the Mg-Ti-Pd ND60 (left, filled symbols) and ND320 (right, open symbols) measured at $90°$C (black) and $120°$C (red). Note that a different horizontal scale is used for the two samples for better visualization. The dashed lines are a visual guide to compare the start-plateau pressures of the two samples.

the optical transmission change is different for ND60 and ND320. Nevertheless, it is much smaller than expected from Lambert-Beer law ($\ln(T/T_{unl}) \sim \alpha\,d$) as it is comparable with the optical transmission change of a $2\,\text{nm}$ thick Mg thin film. Nevertheless, the isotherms show clear hydrogenation and dehydrogenation pressure plateaus. They exhibit a certain slope, despite the slow pressure sweeps of more than $5\,\text{hrs}$. Also in pressure we observe difference between the nanodots. The pressure plateaus of the ND60 isotherms are steeper than the ND320 isotherms. The pressure plateaus do not show large differences, although the hydrogenation pressure of ND60 is higher than ND320 at $90°$C. As a result, the hysteresis is increased.

As illustrated in figure 2.8 the Mg nanodot core is encapsulated by several phases. At the bottom there is a Mg|SiO$_2$ interface. At the top there is a Mg|TiH$_2$ interface (Ti will be hydrogenated before Mg will be hydrogenated). In the lateral direction there are two Mg|MgO interfaces. Because the Mg layer thickness is the same for ND60 and ND320, the Mg|SiO$_2$ and the Mg|TiH$_2$ interfaces should be the same and should not depend on the diameter of the nanodots. On the other hand, the effect
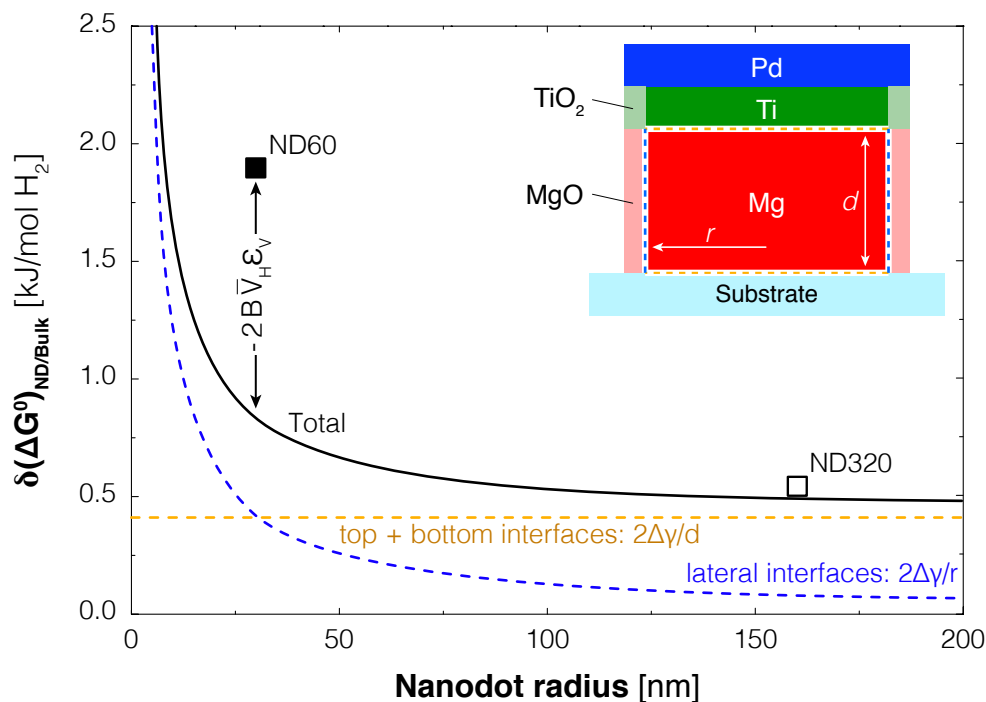
Figure 2.8 | Size-Dependent Thermodynamic Bias – The contributions of thermodynamical effects to the free energy changes $\delta(\Delta G^0)$ with respect to the value (black squares) derived from the experimentally observed pressure difference between nanodots and bulk at $90°C$. The blue dotted line represents the calculated contribution of the Mg|SiO$_2$ and the Mg|TiH$_2$ interfaces at the top and bottom of the Mg core upon hydrogenation. The red dashed-dotted line represents the calculated contribution of the two lateral Mg|MgO interfaces. The black solid line indicates the sum of all interfaces. The arrow indicates the contribution of the elastic constrain energy to the thermodynamical bias of ND60.

of the lateral Mg|MgO interfaces should depend on the diameter of the nanodots. For simplicity, we assume that the Mg|MgO and MgH$_2$|MgO interface energies are of the same order of the previously calculated interface energies between Mg|TiH$_2$ and MgH$_2$|TiH$_2$: $\Delta\gamma = 0.33$ J m^{-2}. In addition, we also have to take into account that the interface areas increase upon hydrogenation. For a spherical geometry, it would be about 22% assuming a volume expansion of 32%. In the nanodots it depends on the relative radial and axial expansion. Ideally, the Mg can expand freely in all directions and the lateral MgO layers do not counteract this expansion. In this case the expansion of the interface areas will be around 20%. This number reduces when the Mg cannot expand freely in all directions.

Figure 2.8 shows that the scenario of a free expansion of the Mg core can only partially describe the experimental results. Only for ND320 the contributions of the lateral and the parallel interfaces matches the experimental results. For ND60, the

Gibbs free energy difference calculated from the hydrogenation of the nanodots is more than twice as large as described by the free expansion scenario ($0.85\,\mathrm{kJ/mol}$ $\mathrm{H_2}$ *vs* $1.9\,\mathrm{kJ/mol}$ $\mathrm{H_2}$). This suggests that the lateral MgO layers constrain the expansion of the Mg core, resulting in a deformation of the Mg|TiH$_2$ interface. This would increase the interface area between the two layers, however, it will be of the same order as in the free expansion scenario. We therefore expect that the thermodynamical bias of about $1.1\,\mathrm{kJ/mol}$ $\mathrm{H_2}$ be the result of elastic compressive strain.

To calculate the magnitude of the elastic compressive strain, we are using equation 2.21. Using $B = 35.9\,\mathrm{GPa}$ being the Mg bulk modulus and $V_\mathrm{H} = 2.24\,\mathrm{cm^3/mol}$ being the partial molar volume of hydrogen in MgH$_2$,[2.14] we obtain an elastic compressive strain of $\varepsilon_v = -0.8\%$. This number is rather small compared to the compressive volume strain of $\varepsilon_v = -16.5\%$ upon hydrogenation of a spherical Mg core of 30 nm embedded in a $5\,\mathrm{nm}$ thick MgO shell.[2.14] Even when we take the difference in geometry into account, we find a compressive volume strain of $\varepsilon_v = -11.5\%$ upon hydrogenation.[2.33] This number corresponds to a thermodynamical bias of about $23\,\mathrm{kJ/mol}$ $\mathrm{H_2}$, more than a magnitude higher than experimentally observed. This suggests that the volume of the hydrogenated nanodots is almost the same as in the unconstrained situation. However, instead of an expansion in all directions we suggest that the core's volume expansion develops only in the direction perpendicular to the substrate (similar to thin films). An expansion in all directions should result in a plastic deformation in the radial direction of the nanodots. Such a permanent shape change is not observed after hydrogenation (see figure 2.9).
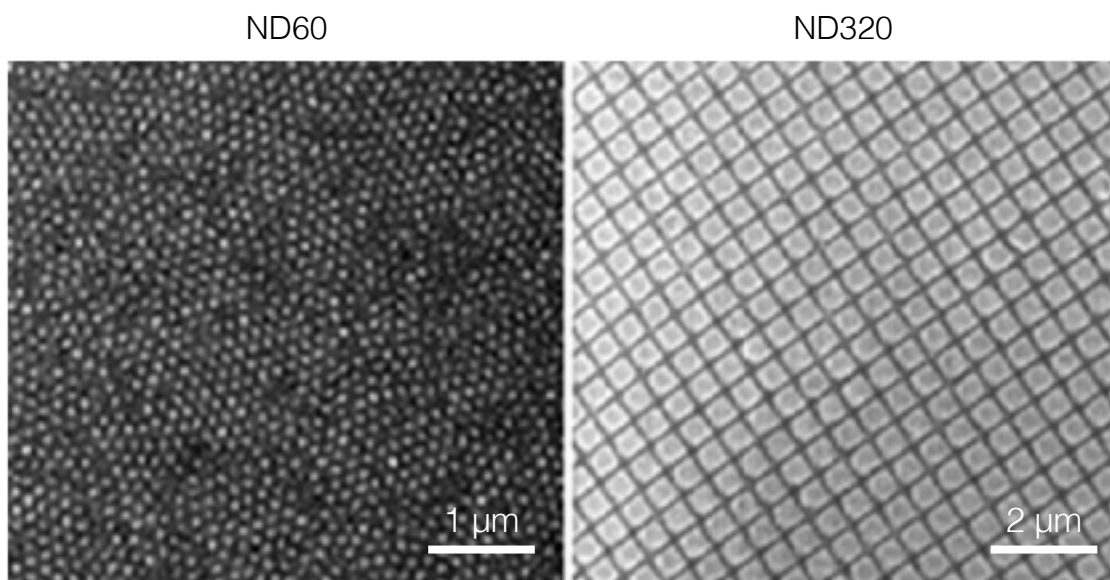
Figure 2.9 | Dehydrogenated Nanodots – Low magnification SEM images of ND60 (left) and ND320 (right) taken after dehydrogenation.

A perpendicular expansion induces a small residual yield stress through deformation of the capping layers. The yield stress σ can be estimated from the additional mechanical work required for a (de)hydrogenation cycle. This additional work is equal to the extrinsic hysteresis compared to that of bulk:[2.21]

$$\Delta G^{\text{hys}} = R\,T \ln\left(\frac{P_{\text{abs}}^{\text{nano}}/P_{\text{des}}^{\text{nano}}}{P_{\text{abs}}^{\text{bulk}}/P_{\text{des}}^{\text{bulk}}}\right) = V_{\text{M}} \oint \boldsymbol{\sigma} \cdot d\varepsilon. \tag{2.23}$$

Assuming that the plastic deformations only in the directions parallel to the substrate ($\sigma_y = \sigma_x$, $\sigma_z = 0$), the right-hand side of equation 2.23 reduces to $0.32\sigma_y$. From the isotherms measured at $90°\text{C}$ we find a hysteresis of $P_{\text{abs}}^{\text{nano}}/P_{\text{des}}^{\text{nano}} = 107$ for ND60 and $P_{\text{abs}}^{\text{nano}}/P_{\text{des}}^{\text{nano}} = 37$ for ND320. Using $P_{\text{abs}}^{\text{bulk}}/P_{\text{des}}^{\text{bulk}} = 2.5$ for bulk Mg, we obtain a yield stress of about 2.6 and $1.9\,\text{GPa}$ for ND60 and ND320, respectively. These numbers are matches the reported yield stress of about $1.4\,\text{GPa}$ in Mg-Ta-Pd thin films and about $1.5\,\text{GPa}$ in Pd-Ti thin films on glass substrates.[2.21,2.34]

2.5   Conclusions

We have experimentally shown for the first time the possibility to tailor the thermodynamics of a metal-hydrogen system by means of interface energy. Using thin films as a model system, we find an energy difference of $0.33\,\text{J m}^{-2}$ between the MgH$_2$|TiH$_2$ and Mg|TiH$_2$ interfaces. Assuming an isotropic interface energy implies that a Mg layer with a thickness of $1.8\,\text{nm}$ experiences an order of magnitude increase in the equilibrium pressure at $120°\text{C}$ compared to bulk Mg. Depending on the material and the interaction with the surrounding matrix an even stronger destabilization should be possible. This means that interface energy can be a tool to tailor the pressure range of a metal hydride based hydrogen sensor.

The experimental results on the two different geometries show that in of Mg-Ti-Pd multilayers the interface energy is associated with plastic deformations. For hydrogen detection the presence of plastic deformations is not desired, as it induces that a different hydrogenation and dehydrogenation pressure (hysteresis) and, if already present, increases the difference. Our results suggest that these plastic deformations are induced by a substrate roughness in thin films and by oxide layers in nanodots. It is, however, not known whether it is possible to minimize the plastic deformations and induce only interface energy effects in multilayer systems. Nevertheless, this is essential to be able to tailor the hydrogen detection pressure (range) without hysteresis.

References

[2.1] *J.J. Vajo, F. Mertens, C.C. Ahn, R.C. Bowman, and B. Fultz.* **Altering hydrogen storage properties by hydride destabilization through alloy formation: LiH and MgH2 destabilized with Si.** Journal of Physical Chemistry B **108**(37), 13977 – 13983 (2004).

[2.2] *R. Janot, L. Aymard, A. Rougier, G.A. Nazri, and J.M. Tarascon.* **Enhanced hydrogen sorption capacities and kinetics of Mg2Ni alloys by ball-milling with carbon and Pd coating.** Journal of Materials Research **18**, 1749 – 1752 (2003).

[2.3] *D. Kyoi, T. Sato, E. Ronnebro, N. Kitamura, A. Ueda, M. Ito, S. Katsuyama, S. Hara, D. Noreus, and T. Sakai.* **A new ternary magnesium-titanium hydride Mg7TiHx with hydrogen desorption properties better than both binary magnesium and titanium hydrides.** Journal of Alloys and Compounds **372**, 213 – 217 (2004).

[2.4] *W.P. Kalisvaart, C.T. Harrower, J. Haagsma, B. Zahiri, E.J. Luber, C. Ophus, E. Poirier, H. Fritzsche, and D. Mitlin.* **Hydrogen storage in binary and ternary Mg-based alloys: a comprehensive experimental study.** International Journal of Hydrogen Energy **35**, 2091 – 2103 (2010).

[2.5] *R. Gremaud, C.P. Broedersz, A. Borgschulte, M.J. van Setten, H. Schreuders, M. Slaman, B. Dam, and R. Griessen.* **Hydrogenography of MgyNi1-yHx gradient thin films: Interplay between the thermodynamics and kinetics of hydrogenation.** Acta Materialia **58**, 658 – 668 (2010).

[2.6] *A. Baldi, M. Gonzalez-Silveira, V. Palmisano, B. Dam, and R. Griessen.* **Destabilization of the Mg-H system through elastic constraints.** Physical Review Letters **102**, 226102 1 – 4 (2009).

[2.7] *K.J. Jeon, H.R. Moon, A.M. Ruminski, B. Jiang, C. Kisielowski, R. Bardhan, and J.J. Urban.* **Air-stable magnesium nanocomposites provide rapid and high-capacity hydrogen storage without using heavy-metal catalysts.** Nature Materials **10**, 286 – 290 (2011).

[2.8] *K.F. Aguey-Zinsou and J.R. Ares-Fernandez.* **Synthesis of colloidal magnesium: A near room temperature store for hydrogen.** Chemistry of Materials **20**, 376 – 378 (2008).

[2.9] *S.B. Kalidindi and B.R. Jagirdar.* **Highly monodisperse colloidal magnesium nanoparticles by room temperature digestive ripening.** Inorganic Chemistry **48**(10), 4524 – 4529 (2009).

[2.10] *R. Bogerd, P. Adelhelm, J.H. Meeldijk, and K.P. de Jong.* **The structural characterization and H2 sorption properties of carbon-supported Mg1-xNix nanocrystallites.** Nanotechnology **20**(20), 204019 1 – 9 (2009).

[2.11] *K.C. Kim, B. Dai, J.K. Johnson, and D.S. Sholl.* **Assessing nanoparticle size effects on metal hydride thermodynamics using the Wulffconstruction.** Nanotechnology **20**(20), 204001 1 – 7 (2009).

[2.12] *V. Berube, G. Radtke, M. Dresselhaus, and G. Chen.* **Size effects on the hydrogen storage properties of nanostructured metal hydrides: a review.** International Journal of Energy Research **31**, 637 – 663 (2007).

[2.13] *M. Fichtner.* **Properties of nanoscale metal hydrides.** Nanotechnology **20**(20), 204009 1 – 4 (2009).

[2.14] *L. Pasquini, M. Sacchi, M. Brighi, C. Boelsma, L.P.A. Mooij, S. Bals, L. Polak, T. Perkisas, and B. Dam.* **Hydride destabilization in core–shell nanoparticles.** International Journal of Hydrogen Energy **39**, 2115 – 2123 (2014).

[2.15] *A. Baldi, G.K. Palsson, M. Gonzalez-Silveira, H. Schreuders, M. Slaman, J.H. Rector, G. Krishnan, B.J. Kooi, G.S. Walker, M.W. Fay, B. Hjorvarsson, R.J. Wijngaarden, B. Dam, and R. Griessen.* **Mg/Ti multilayers: structural and hydrogen absorption properties.** Physical Review B **81**(22), 224203 1 – 10 (2010).

[2.16] *A. San-Martin and F.D. Manchester.* **The H-Ti (hydrogen-titanium) system.** Bulletin of Alloy Phase Diagrams **8**(1), 30 – 42 (1987).

[2.17] *M.A. Pick, J.W. Davenport, M. Strongin, and G.J. Dienes.* **Enhancement of hydrogen uptake rates for Nb and Ta by thin surface overlayers.** Physical Review Letters **43**(4), 286 – 289 (1979).

[2.18] *A. Baldi, V. Palmisano, M. Gonzalez-Silveira, Y. Pivak, M. Slaman, H. Schreuders, B. Dam, and R. Griessen.* **Quasifree Mg-H thin films.** Applied Physics Letters **95**(7), 071903 1 – 3 (2009).

[2.19] *R.B. Schwarz and A.G. Khachaturyan.* **Thermodynamics of open two-phase systems with coherent interfaces: Application to metal-hydrogen systems.** Acta Materialia **54**(2), 313 – 323 (2006).

[2.20] *A. Krozer and B. Kasemo.* **Hydrogen uptake by Pd-coated Mg: absorption-decomposition isotherms and uptake kinetics.** Journal of the Less-Common Metals **160**, 323 – 342 (1990).

[2.21] *Y. Pivak, H. Schreuders, M. Slaman, R. Griessen, and B. Dam.* **Thermodynamics, stress release and hysteresis behavior in highly adhesive Pd-H films.** International Journal of Hydrogen Energy **36**(6), 4056 – 4067 (2011).

[2.22] *A. Pundt.* **Hydrogen in nano-sized metals.** Advanced Engineering Materials **6**, 11 – 12 (2004).

[2.23] *L.P.A. Mooij and B. Dam.* **Hysteresis and the role of nucleation and growth in the hydrogenation of Mg nanolayers.** Physical Chemistry Chemical Physics **15**(8), 2782 – 2792 (2013).

[2.24] *S.X. Tao, P.H.L. Notten, R.A. van Santen, and A.P.J. Jansen.* **Fluorite transition metal hydride induced destabilization of the MgH2 system in MgH2/TMH2 multilayers (TM=Sc, Ti, V, Cr, Y, Zr, Nb, La, Hf).** Physical Review B **82**(12), 125448 1 – 5 (2010).

[2.25] *L.P.A. Mooij, A. Baldi, C. Boelsma, K. Shen, M. Wagemaker, Y. Pvak, H. Schreuders, R. Griessen, and B. Dam.* **Interface energy controlled thermodynamics of nanoscale metal hydrides.** Advanced Energy Materials **1**, 754 – 758 (2011).

[2.26] *J.F. Stampfer, C.E. Holley, and J.F. Suttle.* **The magnesium-hydrogen system.** Journal of the American Chemical Society **82**, 3504 – 3508 (1960).

[2.27] *J.J. Reilly and R.H. Wiswall.* **The reaction of hydrogen with alloys of magnesium and nickel and the formation of Mg2NiH4.** Inorganic Chemistry **7**, 2254 – 2256 (1968).

[2.28] *B. Tanguy, J.L. Soubeyroux, M. Pezat, and J. Portier.* **Amelioration des conditions de synthese de l'hydrure de magnesium a l'aide d'adjuvants.** Materials Research Bulletin **11**, 1441 – 1448 (1976).

[2.29] *A.S. Pedersen, J. Kjoller, B. Larsen, and B. Vigeholm.* **Magnesium for hydrogen storage.** International Journal of Hydrogen Energy **8**(3), 205 – 211 (1983).

[2.30] *G.M. Friedlmeier and J.C. Bolcich.* **Production and characterization of Mg-10 wt% Ni alloys for hydrogen storage.** International Journal of Hydrogen Energy **13**(8), 467 – 474 (1988).

[2.31] *B. Bogdanovic, K. Bohmhammel, B. Christ, A. Reiser, K. Schlichte, R. Vehlen, and U. Wolf.* **Thermodynamic investigation of the magnesium-hydrogen system.** Journal of Alloys and Compounds **282**, 84 – 92 (1999).

[2.32] *R. Gremaud, A. Baldi, M. Gonzalez-Silveira, B. Dam, and R. Griessen.* **Chemical short-range order and lattice deformations in MgyTi1-yHx thin films probed by hydrogenography.** Physical Review B **77**, 144204 (2008).

[2.33] *A. Molinari, F. D'Amico, M. Calizzi, Y. Zheng, C. Boelsma, L.P.A. Mooij, Y. Lei, L. Polak, H. Hahn, B. Dam, and L. Pasquini.* **Interface and strain effects on the H-sorption thermodynamics of size-selected Mg nanodots.** International Journal of Hydrogen Energy **41**, 9841 – 9851 (2016).

[2.34] *Y. Pivak, H. Schreuders, and B. Dam.* **Thermodynamic properties, hysteresis behavior, and stress-strain analysis of MgH2 thin films, studied of a wide temperature range.** Crystals **2**, 710 – 729 (2012).

Chapter 3

Enthalpy-Entropy Compensation
— in metal hydrides —

3.1   Introduction

The thermodynamics of a metal hydride is an important concept with respect to its hydrogen detection pressure (range). Not only can it be used to describe the pressure (range) as a function of the response and its temperature dependence, it give also insight how to change these dependencies. The thermodynamics is commonly expressed by an enthalpic ΔH and a entropic ΔS term. The relation between the hydrogen pressure P, the temperature T, ΔH, and ΔS is described by the Van 't Hoff relation:

$$\ln\left(\frac{P}{P_0}\right) = \frac{\Delta H}{R\,T} - \frac{\Delta S}{R}. \tag{3.1}$$

From this relation we find that a change in ΔS results in a shift of the pressure (range), while ΔH also changes the temperature dependence. Effects that affects these parameters are, for example, alloying the metal,[3.1,3.2] changing the film thickness[3.3], or by changing the film interfaces.[3.4] In principle, tuning ΔH should not affect ΔS, or vice versa. However, this is not a matter of course. In fact, in most cases a simultaneous change of ΔH and ΔS is obtained.[3.2,3.3,3.5 — 3.7,3.9] Interestingly, the change in ΔH is often found to be linearly related to the change in ΔS. In literature, this phenomenon is known as enthalpy-entropy compensation.

Enthalpy-entropy compensation is not only associated to metal hydride systems. It is also found in a wide range of fields in chemistry,[3.10 — 3.14] biology,[3.15 — 3.18] and solid-state physics.[3.19 — 3.22] It is, for example, found while comparing the denaturation of similar proteins and while studying the conduction of (organic) semiconductors. Although the effect is known by different names (e.g. isokinetic relationship or Meyer-Nelder rule), the concept is the same: it describes a linear relation

---

This chapter is based on: C. Boelsma, R. Griessen, H. Schreuders, and B. Dam. Verification of the enthalpy-entropy compensation effect in metal hydrides (under review, 2017).

between two thermodynamic parameters in a series of similar reactions. The effect is characterized by a single parameter, the compensation temperature T_{comp}, which is defined as the slope of the linear relation between ΔH and ΔS. Interestingly, the compensation temperature is often found to be close to the mean experimental temperature $(T_{\mathsf{comp}} \approx T_{\mathsf{mean}})$.

Although enthalpy-entropy compensation has been observed and studied for more than a century, the mechanism behind it is not understood. In fact, there is even no consensus about whether the effect has a systematic basis. Many authors claim that statistical and/or experimental errors induce compensation effects with $T_{\mathsf{comp}} \approx T_{\mathsf{mean}}$.[3.6,3.23 — 3.30] Although these claims are supported by statistical models, it is unclear when a T_{comp} should be considered to be close enough to T_{mean} to attribute a compensation effect to a statistical basis. To be able to discern whether a compensation effect has a statistical or a physical origin is of great importance. In the field of hydrogen detection a physical compensation effect implies that a shift of the detection pressure (range) cannot be decoupled from the temperature dependence of this pressure (range). In the field of hydrogen storage enthalpy-entropy compensation is an interesting feature. It allows us to reduce the large heat produced during hydrogen loading $(\sim \Delta H)$ without changing the hydrogenation pressure.

In the present chapter we show that the existence of a well-defined T_{comp} is not a sufficient condition to determine the nature of a compensation effect, independent of how accurate T_{comp} is determined. To do so, we require an additional characterization parameter, called the *order coefficient* ρ. This parameter quantifies the degree of correlation of the measured quantity (e.g. hydrogenation pressure) within the experimental temperature range. From this we present a step-by-step guide to determine the nature of the compensation effect in a particular experiment. In this way find a well-defined T_{comp}– and ρ–range in where a systematic and a statistical basis cannot be discriminated from each other. As a result, a compensation effect may have a systematic basis even in cases where $T_{\mathsf{comp}} \approx T_{\mathsf{mean}}$. On the other hand we find that compensation effects can have a statistical basis even in cases where T_{comp} is (far) outside the temperature range. To decide whether it is possible to exclude a statistical basis, it is important to determine the T_{comp} and ρ with the highest accuracy.

We illustrate our verification method by analyzing compensation effects found in thin film metal hydrides. However, the verification method is developed in such a way that it also can be used to analyze analogue effects in other systems. We choose to analyze the compensation effect found in the Ti doped MgH_2, a simple and well-studied system.[3.1,3.2,3.7,3.31 — 3.37] This system shows very well-defined pressure plateaus, which allows us to determine T_{comp} and ρ with a high precision. The observed $T_{\mathsf{comp}} = 154°\mathrm{C}$ is very close mean temperature of the experiments $(138°\mathrm{C})$.

According to the existing models, this suggests a statistical basis. However, by including the systematic variation of the pressure with temperature through the *order coefficient* ρ we find there must be a systematic basis for this compensation effect.

3.2 $T_{\textbf{comp}}$ from Random Fluctuations

In order to identify the nature (statistical/systematic) of a composition induced enthalpy-entropy compensation effect, one commonly uses the compensation temperature T_{comp} as the distinctive parameter. From the definition of this compensation temperature, $T_{\text{comp}} = \Delta H / \Delta S$, it follows from the Van 't Hoff relation that in metal hydrides at $T = T_{\text{comp}}$ the (de)hydrogenation equilibrium pressures of all compositions must coincide. Griessen *et al.* uses this feature to show that two enthalpy-entropy compensations observed in the hydrogen absorption/desorption isotherms of Pd particles by Bardhan *et al.*[3.8] with different dimensions (both with $T_{\text{comp}} \approx T_{\text{mean}}$) are very likely to be a consequence of systematic errors induced by the normalization of the isotherms, resulting that at each temperature the *same* pressure
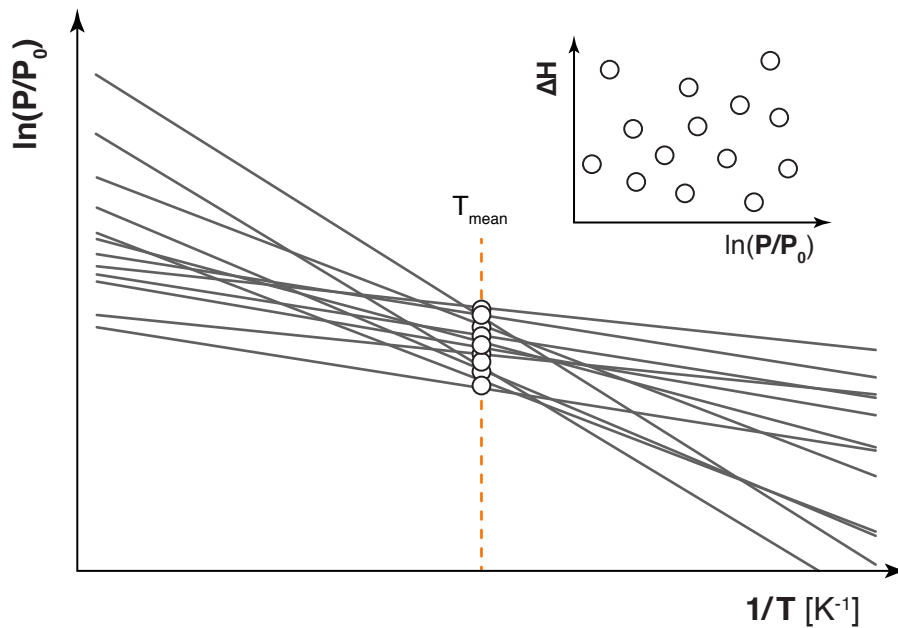
Figure 3.1 │ Literature Models – A schematic representation of the models presented in literature[3.6,3.23 − 3.30] to generate enthalpy-entropy compensation effects. Here random ΔH values are assigned to random pressure values, which are generated at T_{mean} (see inset). From this the corresponding ΔS values can be obtained by means of the Van 't Hoff construction (lines). Consequently, these models lead to compensation temperatures close to the mean experimental temperature: $T_{\text{comp}} \approx T_{\text{mean}}$.

point corresponds to a different hydrogen fraction.[3.9] At $T = T_{\mathsf{comp}}$ they do not find any evidence that the equilibrium pressures coincide nor signs that such a temperature exists. Although this approach is straightforward, it lacks a criterium with respect to the experimental error margins. Experimental uncertainties do not only result in an error in T_{comp}, they also imply that at each temperature, including T_{comp}, it is not possible to exclude a non-zero distribution of the pressure. The question *how large these experimental uncertainties are allowed to be to still be able to exclude a statistical basis* is therefore very relevant.

Existing models do not give an indisputable answer to this question, as they do not include all experimental uncertainties. In these models the uncertainties are introduced in one of the thermodynamical parameters (ΔH or ΔS) and in the experimental parameter (e.g. equilibrium pressure P), which is only evaluated at the mean experimental temperature T_{mean} (see figure 3.1).[3.6,3.27 − 3.30] As a result, the models generate compensation temperatures close to the mean experimental temperature: $T_{\mathsf{comp}} \approx T_{\mathsf{mean}}$. From this the authors conclude that compensation temperatures with $T_{\mathsf{comp}} \approx T_{\mathsf{mean}}$ must have a statistical basis.

Instead of introducing fluctuations in (one of) the thermodynamic parameters, it is more logical to introduce them only in the actual experimental variables (e.g. the temperature T and the plateau pressure P). Here, we develop a statistical model using this basis. Thus at each experimental temperature T_j we allow a certain (logarithmic) pressure range $\delta \mathrm{ln}P$ for all pressure data observed at that temperature. Furthermore, we include a statistical error $\delta \mathrm{T}$ representing the error in the experimental temperature. For simplicity, we take the same $\delta \mathrm{ln}P$ and $\delta \mathrm{T}$ for all temperatures (see figure 3.2). We match the number of compositions and temperatures in the simulation to that of the experimental data set. As another input we calculate $\langle P\left(T_j\right)\rangle$, the average of all pressures measured at each temperature T_j.

$$\langle P\left(T_j\right)\rangle = \frac{1}{N}\sum_{n=1}^{N} P_{j,n} \tag{3.2}$$

where N is the total number of compositions. Our next step is to generate computational *data sets*, each corresponding to unique reaction composition n, evaluated at each temperature T_j. We do this by generating a random pressure $P_{j,n}$

$$\mathrm{ln}(P_{j,n}) = \mathrm{ln}\langle P\left(T_j\right)\rangle + r_P\,\delta \mathrm{ln}P \tag{3.3}$$

at each temperature $T_{j,n}$

$$T_{j,n} = T_j + r_T\,\delta T, \tag{3.4}$$

where both r_P and r_T are random numbers in the interval $[-1/2,+1/2]$. The next step is to determine the corresponding ΔH_n and ΔS_n from a fit to

$$\ln(P_{j,n}) = \frac{\Delta H_n}{R\,T_{j,n}} - \frac{\Delta S_n}{R}. \tag{3.5}$$

This is repeated N times, representing the number of compositions of the experimental data set. In this way, we obtain N pairs of $(\Delta H_n, \Delta S_n)$. As shown in figure 3.3a, quite surprisingly, a plot of ΔH_n versus ΔS_n is a straight line where the slope equals the characteristic compensation temperature T_{comp}. This is not exceptional. Every new generation of N pairs $(\Delta H_n, \Delta S_n)$ using the same model parameters results in a compensation effect, although the slope T_{comp} may be different. This results in a distribution of the T_{comp}'s around T_{mean} (see figure 3.3b). Note that the shape of the distribution depends on the number of compositions. The distribution is Lorentzian
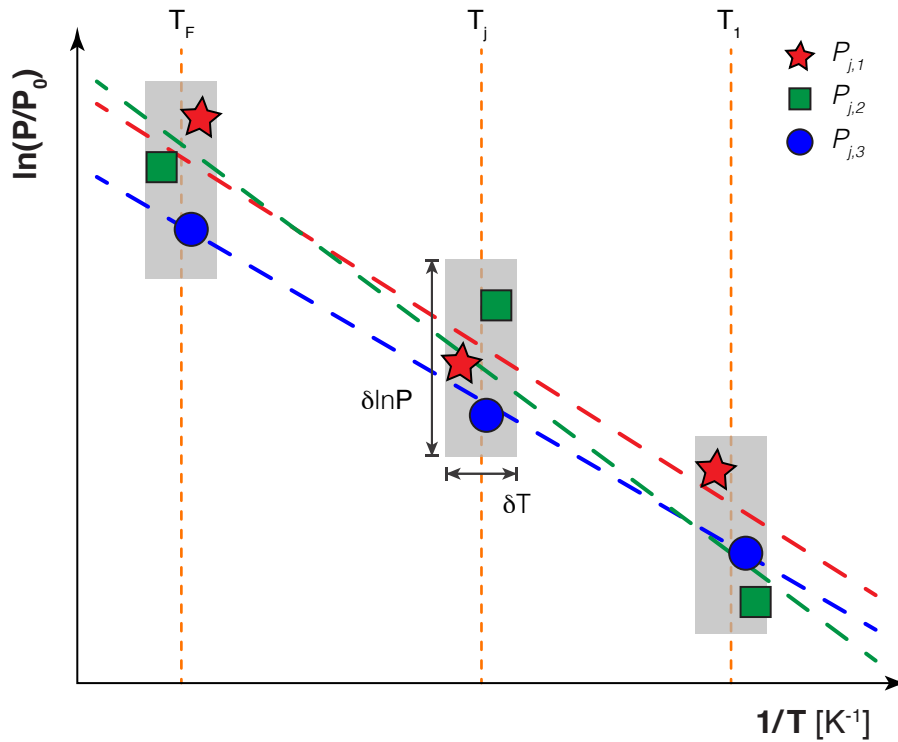
Figure 3.2 | Generating Random Pressures – Schematic overview of $N = 3$ measurements simulated by generating at each temperature T_j with $1 \leq j \leq F$ a random quantity $P_{j,n}$ within the interval $\delta\ln P$ and δT (grey area). The colored dashed lines represent the fit of equation 3.5 through the points. The slope of each line is proportional to ΔH_n, the intersect at infinite temperature to ΔS_n.

for a small number of compositions

$$\text{Counts}(T_{\text{comp}}; T_{\text{mean}}; \sigma) = \frac{\sigma}{4\pi \left(\left[T_{\text{comp}}^{-1} - T_{\text{mean}}^{-1} \right]^2 + \sigma^2 \right)} \quad \text{for } N > 2, \qquad (3.6)$$

while the distribution is Gaussian when the number of compositions is large

$$\text{Counts}(T_{\text{comp}}; T_{\text{mean}}; \sigma) = \frac{1}{\sigma\sqrt{2\pi}} e^{-\left(\left[T_{\text{comp}}^{-1} - T_{\text{mean}}^{-1} \right] / \sqrt{2}\sigma \right)^2} \quad \text{for } N >> 2 \qquad (3.7)$$

For both distributions σ is the standard deviation of the distribution. This allows us to define a temperature range of 2σ where we can expect computationally enthalpy-entropy compensation effects originating from random fluctuations.

Although we introduce a non-zero $\delta\ln\text{P}$ and δT, their values do not change the probability of generating computationally a well-defined T_{comp} nor its value. This we can understand from the definition of $\delta\ln\text{P}$. Note that we see the error δT as an additional $\delta\ln\text{P}$ as the error in the temperature can be converted into the error in pressure through equation 3.5. $\delta\ln\text{P}$ is defined as the range in where a $P_{j,n}$ can be generated computationally at a temperature T_j. Thus at each T_j $\delta\ln\text{P}$ fixes the minimum and maximum value of $P_{j,n}$ that can be generated. As equation 3.5 relates $P_{j,n}$ to ΔH_n and ΔS_n, $\delta\ln\text{P}$ also fixes the possible values of these thermodynamic parameters. A larger $\delta\ln\text{P}$ results only in a larger range of possible ΔH_n and ΔS_n values. It does not change the linear dependence between ΔH_n and ΔS_n nor the distribution of the corresponding compensation temperatures. This is illustrated in figure 3.4 where we vary the value of $\delta\ln\text{P}$ while keeping the other variables constant.

The conclusion that having a well-defined T_{comp} does not depend on the size of the experimental errors indicates the limitations of using T_{comp} as characterization parameter. Using it can result in false conclusions. Finding a T_{comp} close to T_{mean} suggests that the compensation effect is merely a statistical artifact. However, in section 3.5 we present an experimental data set where T_{comp} is close to T_{mean} while the pressure varies systematically as a function of the composition at each temperature. This suggests a compensation effect with a systematic basis instead of a statistical one. A theoretical way to check the validity is to determine whether the pressures at $T = T_{\text{comp}}$ indeed coincide. However, the non-zero experimental uncertainties always imply random fluctuations. Since we demonstrated that random fluctuations lead to a well-defined T_{comp}, the question then arises how large the experimental uncertainties are allowed to be in order to be able to exclude a statistical basis of the compensation effect. To overcome these limitations, we now introduce an additional characterization parameter, the order coefficient ρ (see next section). It turns out that this additional parameter is essential to determine/verify the basis of an enthalpy-entropy compensation effect.
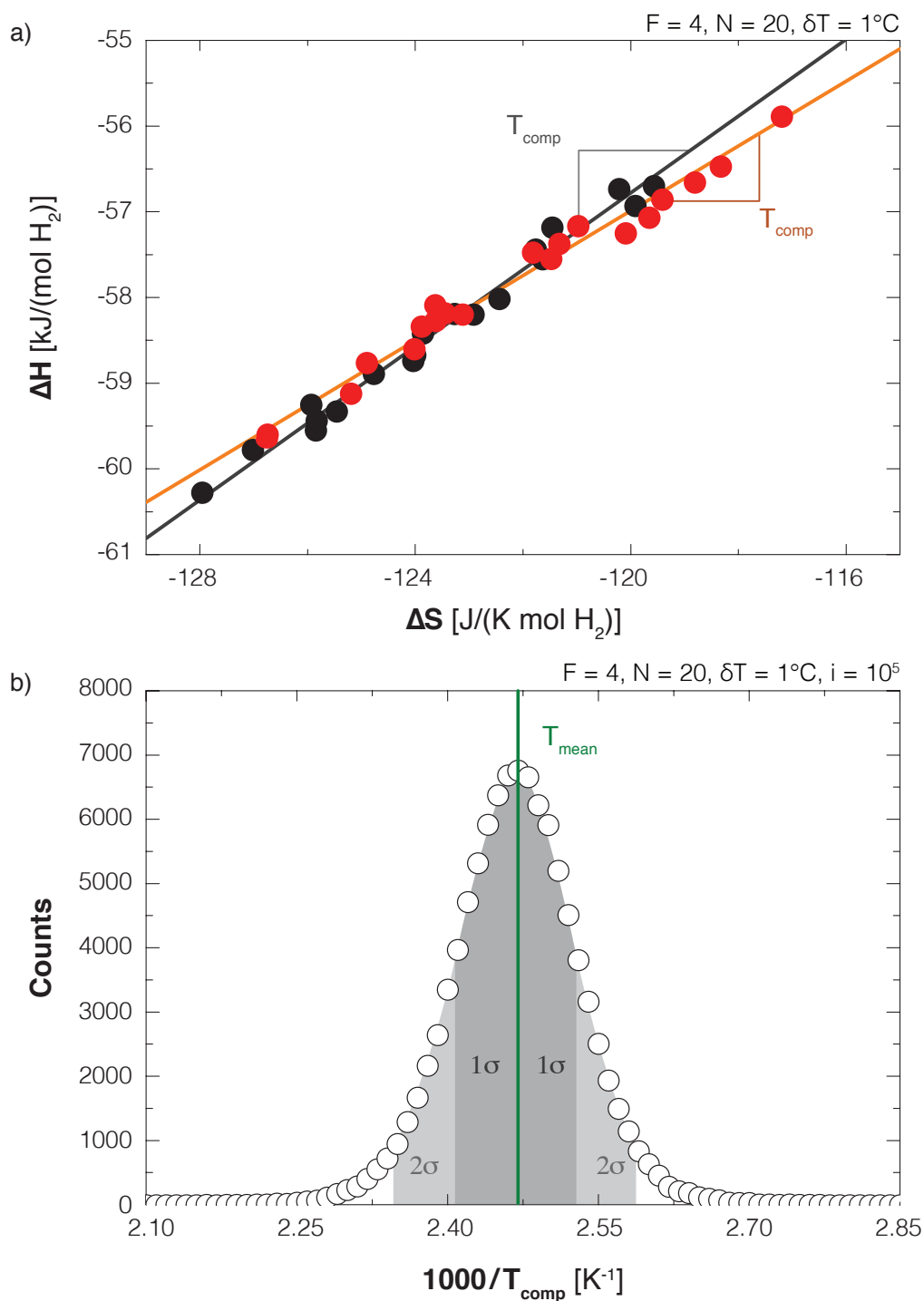
Figure 3.3 | Generated Compensation Effects – a) Two (red and black) *generated* correlations between ΔH_n and ΔS_n obtained through equations 3.2-3.5, each with a different slope T_{comp}. **b)** The distribution *generated* compensation temperatures T_{comp}, obtained from $i = 10^5$ simulation runs. Both figures represent the simulation of the same measurement (with $N = 20$, $\delta \ln P = 0.30$, $\delta T = 1°C$, $T_1 = 75°C$, $T_2 = 110°C$, $T_3 = 165°C$, and $T_4 = 200°C$)

3.3 The Order Coefficient ρ

In the previous section we showed that a well-defined compensation temperature T_{comp} does not capture all necessary features of a data set to determine the basis of the corresponding compensation effect. Its main limitation is that it does not include whether the pressure varies systematically or randomly with the composition as a function of the temperature. To capture this feature we introduce an additional parameter: the *order coefficient ρ*. We distinguish two situations, each resulting in a different expression for ρ. First, we discuss the simple case where the variation of pressures at the lowest (T^{min}) and highest (T^{max}) temperatures are representative for all measurement temperatures. Second, we present the expression for ρ where we consider variations in pressure at all relevant temperatures. In section 3.4 we show how we can use ρ to verify/determine the nature of an enthalpy-entropy compensation effect.

a)
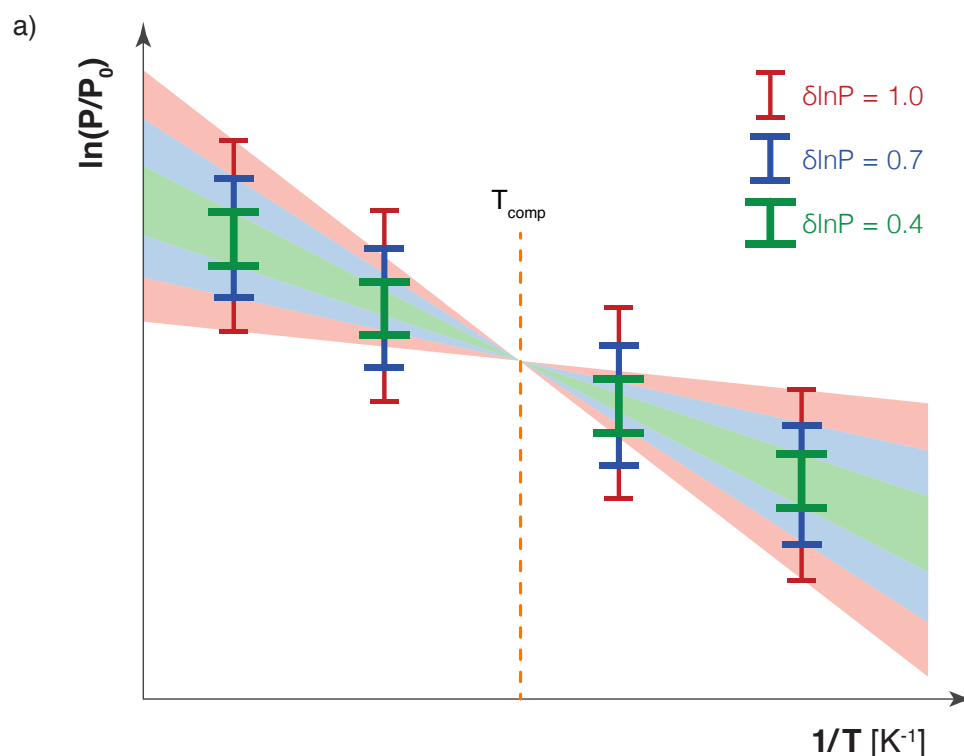
Figure 3.4 | Influence of δlnP on T_{comp} – a) Schematic illustration to show that the value of δlnP has no influence on the value of T_{comp}. This is confirmed by the simulations. A larger δlnP results in a larger range of ΔH_n and ΔS_n values (see **b)**, next page). Nevertheless, the value of δlnP does not influence the linear relation between ΔH_n and ΔS_n nor the distribution of T_{comp}'s (see **c)**, next page).

b) F = 4, N = 20, δT = 1°C

c) F = 4, N = 20, δT = 1°C, i = 10⁵
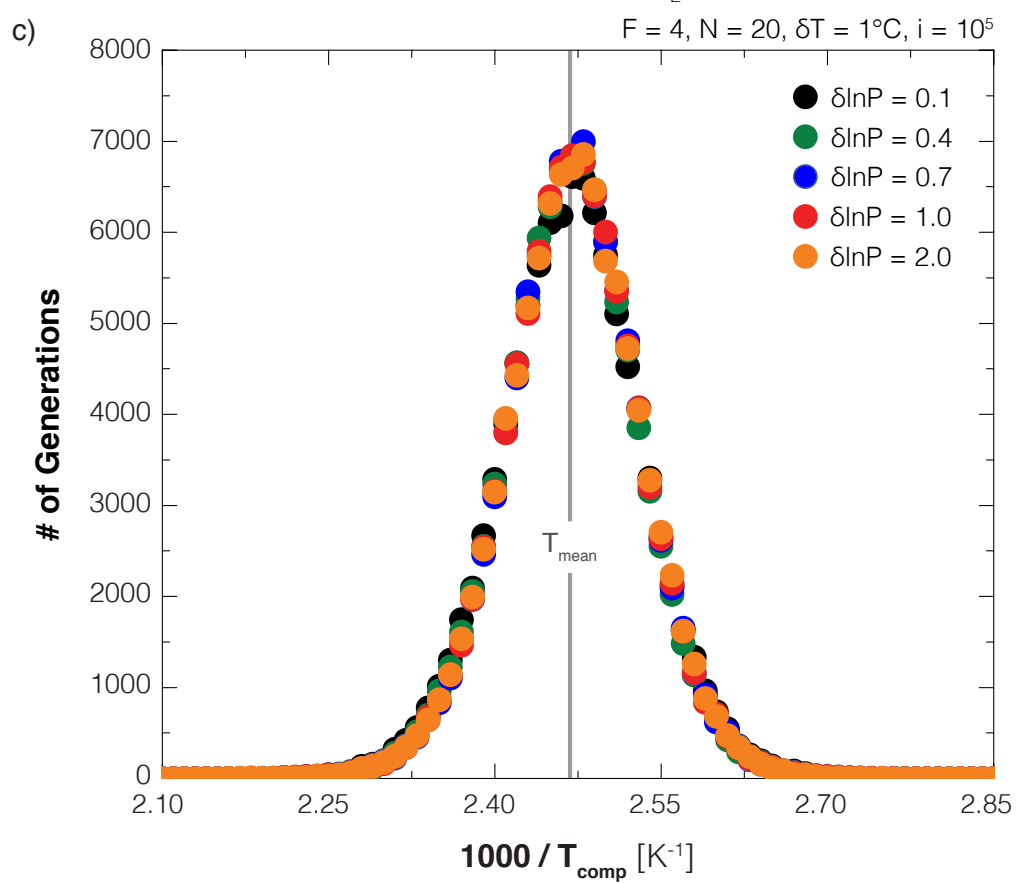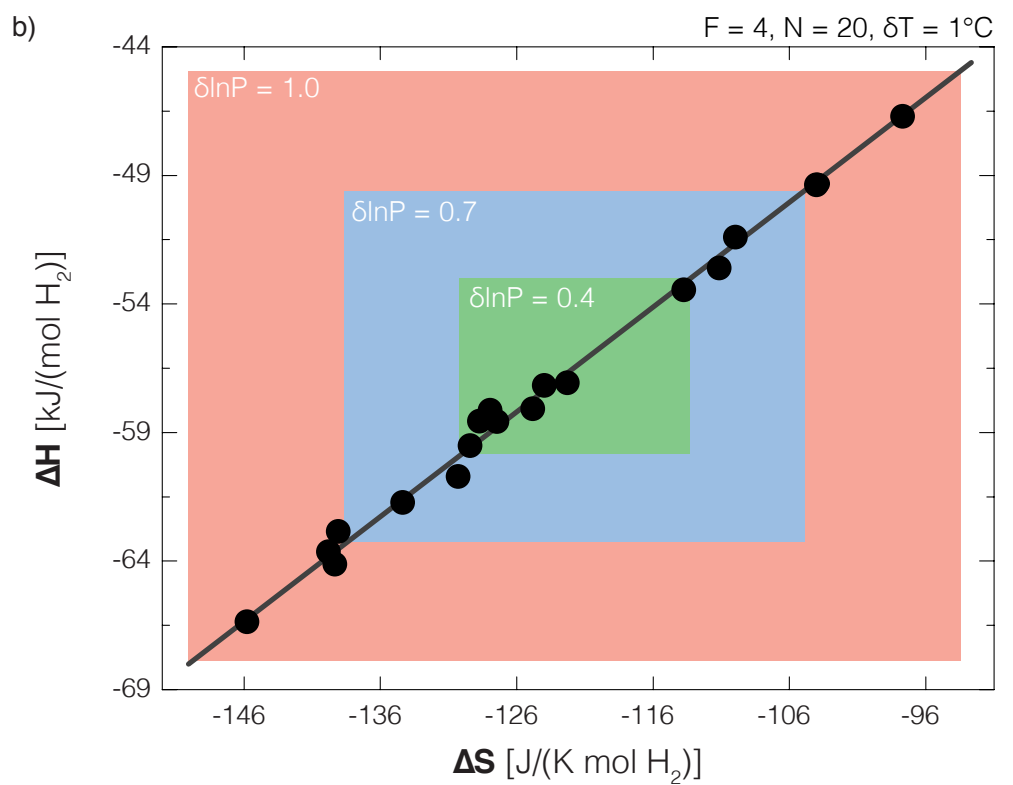
Simple Version: Two Temperature Representation

The assumption that the variation of the pressures at T^{min} and T^{max} are representative for all measurement temperatures implies that the variation of the pressures at temperatures close to T^{min} and to T^{max} are very similar to that at T^{min} and T^{max}. It also implies that when the variation at T^{min} is opposite to that at T^{max} there is a gradual change of pressure variation at temperatures between T^{min} and T^{max}. With these conditions in mind, we express ρ as

$$\rho = \frac{\sum_{n=1}^{N}\left\{\delta_n^{\mathsf{min}} \times \delta_n^{\mathsf{max}}\right\}}{\sqrt{\sum_{n=1}^{N}\left\{\delta_n^{\mathsf{min}}\right\}^2}\sqrt{\sum_{n=1}^{N}\left\{\delta_n^{\mathsf{max}}\right\}^2}} \qquad (3.8)$$

with

$$\delta_n^{\mathsf{min}} = \ln\left(P_n^{\mathsf{min}}\right) - \ln\left\langle P\left(T^{\mathsf{min}}\right)\right\rangle \qquad (3.8a)$$

$$\delta_n^{\mathsf{max}} = \ln(P_n^{\mathsf{max}}) - \ln\langle P\left(T^{\mathsf{max}}\right)\rangle. \qquad (3.8b)$$

In short, ρ captures the difference in variation of P with the composition between the lowest T^{min} and highest T^{max} measurement temperature. From this definition we distinguish three distinct situations, which can been interpreted as *thought experiments*, each expressed by a different value of ρ:

- The ***fully correlated*** situation ($\rho = +1$) where the sequence of $P_{j,n}$ as a function of the composition n does not change within the temperature range: it is the same at both T^{min} and T^{max}. In this situation the compositional pressures at each temperature are distributed in the same manner.

- The ***random*** situation ($\rho = 0$) where there is a random sequence and position of $P_{j,n}$ as a function of n at all temperatures.

- The ***fully anti-correlated*** situation ($\rho = -1$), which is similar to the *fully correlated* situation although the sequence of $P_{j,n}$ reverses within the temperature range. Also, the compositional pressures at each temperature are distributed in the same manner but mirrored below and above T_{comp}.

The fully (anti-)correlated situation implies that there is one temperature where all pressures should coincide. For a *correlated* distribution, this temperature is predicted to be outside the temperature range (see figure 3.5). For an *anti-correlated* distribution, it should be within the temperature range. The exact value of this temperature (i.e. T_{comp}) can be determined from the property that, when $\rho = +1$, the

a) $\rho = +1, \alpha > +1$

b) $\rho = +1, 0 < \alpha < +1$

c) $\rho = -1, -1 < \alpha < 0$

d) $\rho = -1, \alpha < -1$

e) $\rho = +1, \alpha = +1$

f) $\rho \approx 0$

g) $-1 < \rho < 0$

h) $0 < \rho < +1$
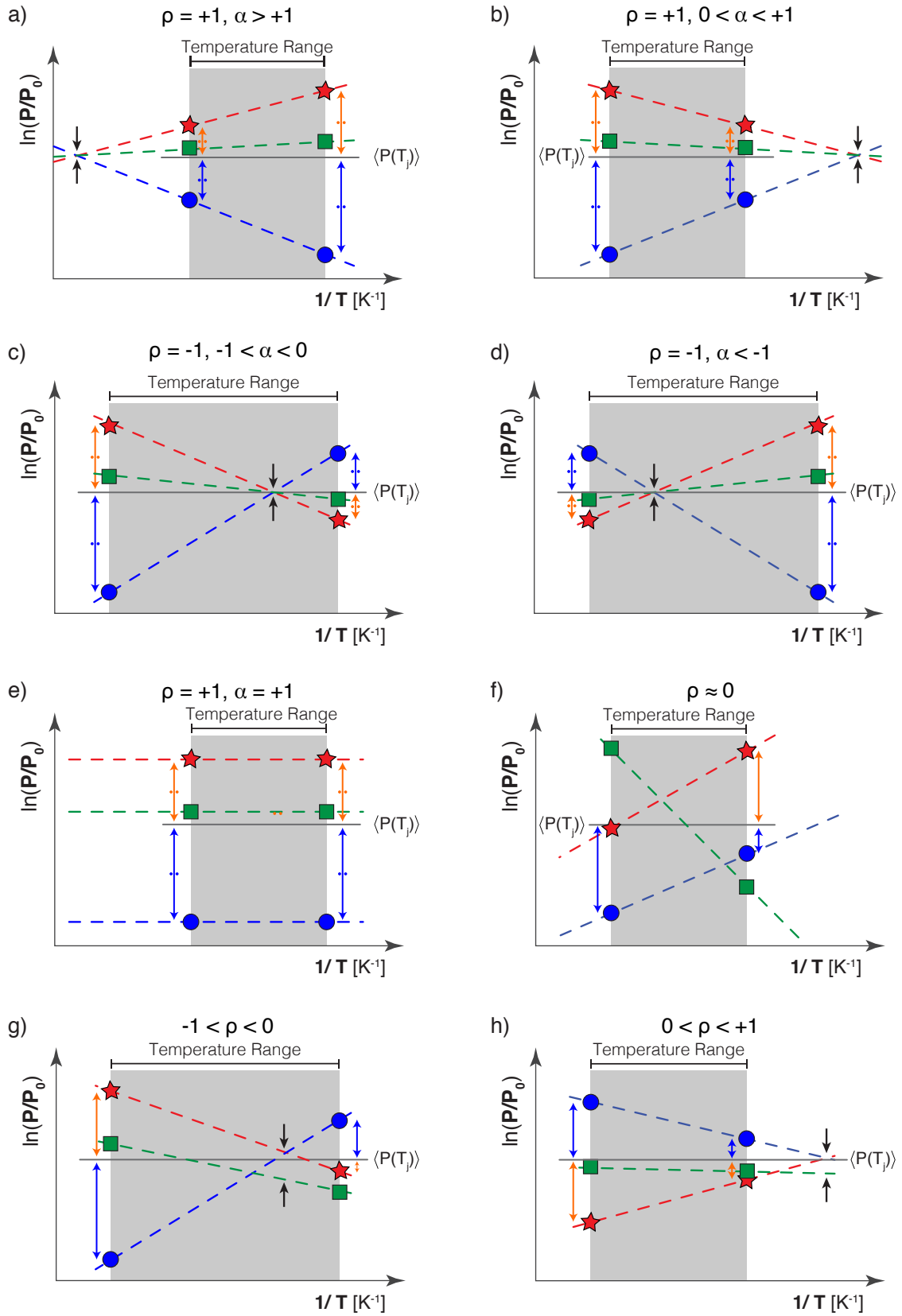
Figure 3.5 | (Previous Page) Order Coefficient ρ & the Position of T_{comp} – Schematic illustration of the position of the compensation temperature T_{comp} for different distributions of the pressure $P_{j,n}$ at the minimum T_{min} and maximum T_{max} temperature. In all panels the black arrows indicate the temperature where the distribution of $P_{j,n}$ is minimum (i.e. T_{comp}) and the dotted arrows indicate that the distribution scales with temperature. **a)** reflects the situation of a *fully correlated* ($\rho = +1$) distribution of $P_{j,n}$ with $\alpha > +1$. **b)** reflects the situation of a *fully correlated* ($\rho = +1$) distribution of $P_{j,n}$ with $0 < \alpha < +1$. **c)** reflects the situation of a *fully anti-correlated* ($\rho = +1$) distribution of $P_{j,n}$ with $-1 < \alpha < 0$. **d)** reflects the situation of a *fully anti-correlated* ($\rho = +1$) distribution of $P_{j,n}$ with $\alpha < -1$. For these situations the exact position of T_{comp} as a function of α is given by equation 3.10. When the distribution of $P_{j,n}$ is *fully correlated* ($\rho = +1$) with $\alpha = +1$ or is *random* ($\rho = 0$), the position of T_{comp} is undetermined (see **e)** and **f)**). **g)** and **h)** illustrate situations where the distribution of of $P_{j,n}$ behave in less ordered fashion ($-1 \leq \rho \leq 0$ or $0 \leq \rho \leq +1$).

compositional order/distribution of $P_{j,n}$ at $T = T^{\text{min}}$ and at $T = T^{\text{max}}$ are the same (reversed when $\rho = -1$):

$$\delta_n^{\text{min}} = \alpha\, \delta_n^{\text{max}}. \tag{3.9}$$

Here α is a scalar and the same for all n. In this way the position of T_{comp} only depends on α:

$$T_{\text{comp}} = \frac{\alpha - 1}{\alpha^{1/T^{\text{max}}} - 1/T^{\text{min}}}. \tag{3.10}$$

From this we can draw some general conclusions of the position of T_{comp} with respect to the temperature range:

- For compensation effects with a *fully correlated* distribution of $P_{j,n}$ ($\rho = +1$), α can only be positive. We distinguish two situations:
  - when $\alpha > 1$ the compensation temperature is above the temperature range: $T_{\text{comp}} \geq T^{\text{max}}$ (see figure 3.5a), and
  - when $0 \leq \alpha < 1$ the compensation temperature is below the temperature range: $T_{\text{comp}} \leq T^{\text{min}}$ (see figure 3.5b).
- For compensation effects with a *fully anti-correlated* distribution of $P_{j,n}$ ($\rho = -1$), α can only be negative. Here, the compensation temperature is always within the temperature range although
  - when $-1 \leq \alpha \leq 0$, T_{comp} is closer to T^{min} than to T^{max} (see figure 3.5c).
  - when $\alpha \leq -1$, T_{comp} is closer to T^{max} (see figure 3.5d).

Special situations occur when $\alpha = -1$ (T_{comp} is exactly in the middle of the (inverse) temperature range), $\alpha = \pm\infty$ (T_{comp} equals T^{max}), $\alpha = 0$ (T_{comp} equals T^{min}), and
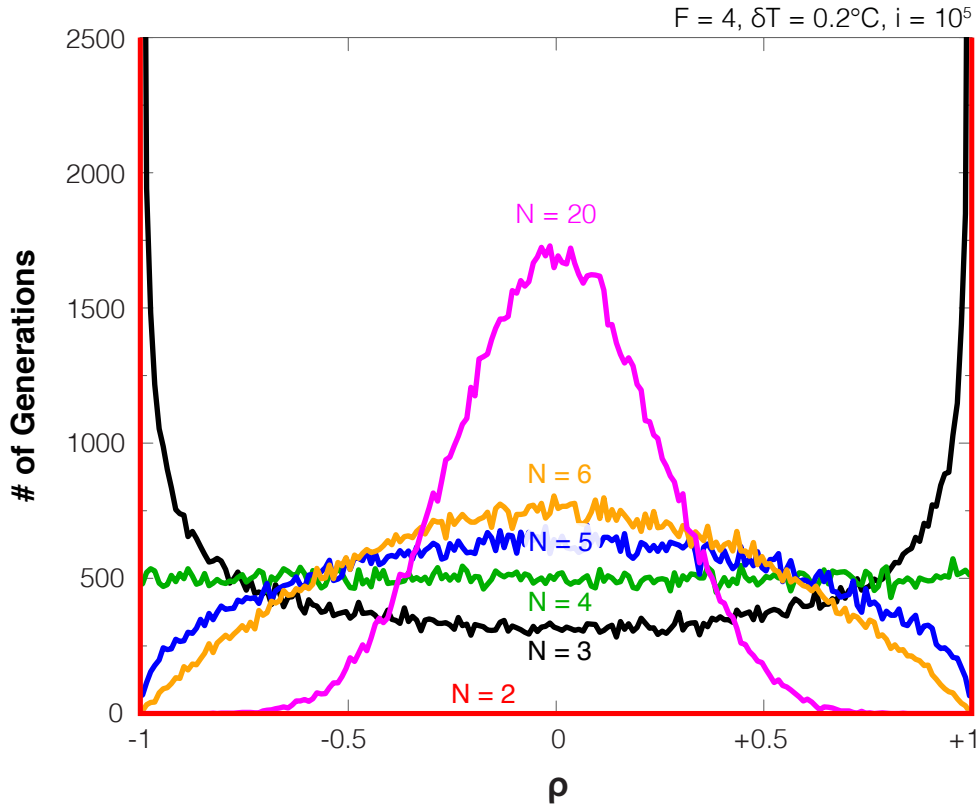
Figure 3.6 | Composition Dependence of the Order Coefficient ρ – The number of generated (total $i = 10^5$) compensation effects as a function of the order coefficient ρ with a varying number of composition N evaluated at two temperatures (at $T_1 = 25°C$, and $T_2 = 37°C$), with a constant parameters: $\delta\ln P = 0.15$, $\delta T = 0.2°C$. Note that with $N = 2$ (red) only two values are possible: $\rho = -1$ or $\rho = +1$.

when $\alpha = 1$ (T_{comp} is infinite, see figure 3.5e). Note that the interpretation is the same for $\rho \approx \pm 1$, although the mathematical expression given in equation 3.10 is not exact anymore. The use of ρ as additional verification parameter shows that it is possible to have compensation effects with a statistical basis when $T_{comp} \gg T_{mean}$ or $T_{comp} \ll T_{mean}$, while it also be possible to have compensation effects with a systematic basis when $T_{comp} \approx T_{mean}$.

Of course, $P_{j,n}$ may behave in a less orderly fashion. This results in an order coefficient between $-1 \leq \rho \leq 1$. For these situations it is not possible to relate a value of ρ to only one nature. This because there is no temperature where all pressures coincide when $-1 \leq \rho \leq 1$. Instead, there is a temperature where the distribution width of the pressures shows a minimum. The size of distribution depends on the value of ρ (see figures 3.5g and 3.5h). However, it is not directly clear whether a similar distribution of pressures cannot be due to random fluctuations.

Whether we can assign a compensation effect to either statistical or systematic effects also depends on the total number of temperatures and compositions. For example, it is more likely to generate computationally a compensation effect with $\rho = -0.5$ with only four compositions ($N = 4$) than with twenty ($N = 4$) (see figure 3.6). Even when the order coefficient equals $\rho = -1$ or $\rho = +1$, we cannot directly exclude a statistical basis. Although these situations imply that there must be a temperature where the pressures should coincide, it is possible to generate computationally such a situation when only two compositions ($N = 2$) and two temperatures ($F = 2$) are considered (see figure 3.6). In these cases, studying more different compositions and/or at more temperatures will give a more conclusive answer.

The Extended Version: All Temperatures

The limitation of using equation 3.8 as the definition for ρ is that the variation of $P_{j,n}$ at the lowest and highest measurement temperature must be representative for all temperatures. When this is not the case, for example when the variation of $P_{j,n}$ is completely random, it still gives the same ρ. However, we would expect a different value of ρ. To handle these cases, we introduce an expression for the order coefficient ρ that includes the variation at all temperatures.

Since the correlation can be calculated up to two independent data sets, a simply extension of equation 3.8 by adding adding δ_n^j for all temperature combinations does not reflect all properties of a data set. We can use this approach only when the variation of $P_{j,n}$ has a temperature history. However, it is more realistic to consider the variation of $P_{j,n}$ at each temperature as an independent data set. We therefore take a different approach by introducing a new definition for ρ:

$$\rho = \rho_{\text{Hoff}} \times R_{\text{Points}}. \tag{3.11}$$

Here ρ_{Hoff} captures the *general* variation of P with the composition as a function of the temperature by making use of the Van 't Hoff construction. R_{Points} is included to correct for the possible difference between the pressures obtained from the Van 't Hoff construction and the actual pressures, as they will not necessarily coincide.

Our first step is to calculate the *Van-'t-Hoff* pressures $P_{j,n}^{\text{Hoff}}$, using the Van 't Hoff relation (equation 3.1 or equation 3.5) and the corresponding ΔH_n and ΔS_n values obtained from the data set. As a result, we have for each composition a set of pressures $P_{j,n}^{\text{Hoff}}$, each corresponding to a different temperature. Note that these *predicted* or *Van-'t-Hoff* pressures $P_{j,n}^{\text{Hoff}}$ do not necessarily coincide with the data pressures $P_{j,n}$. In order to calculate ρ_{Hoff}, we only uses the *Van-'t-Hoff* pressures at the lowest

and highest temperature: $P_{\mathsf{min},n}^{\mathsf{Hoff}}$ and $P_{\mathsf{max},n}^{\mathsf{Hoff}}$. From this we calculate ρ_{Hoff} through

$$\rho_{\mathsf{Hoff}} = \frac{\displaystyle\sum_{n=1}^{N}\left\{\delta_n^{\mathsf{min}} \times \delta_n^{\mathsf{max}}\right\}}{\sqrt{\displaystyle\sum_{n=1}^{N}\left\{\delta_n^{\mathsf{min}}\right\}^2}\sqrt{\displaystyle\sum_{n=1}^{N}\left\{\delta_n^{\mathsf{max}}\right\}^2}} \qquad (3.12)$$

with

$$\delta_n^{\mathsf{min}} = \ln\left(P_{\mathsf{min},n}^{\mathsf{Hoff}}\right) - \ln\left\langle P_{\mathsf{min}}^{\mathsf{Hoff}}\right\rangle_n \qquad (3.12a)$$

$$\delta_n^{\mathsf{max}} = \ln\left(P_{\mathsf{max},n}^{\mathsf{Hoff}}\right) - \ln\left\langle P_{\mathsf{max}}^{\mathsf{Hoff}}\right\rangle_n \qquad (3.12b)$$

where δ_n^{min} and δ_n^{max} are defined as, for each composition, the difference between the predicted Van 't Hoff pressure $P_{j,n}^{\mathsf{Hoff}}$ and the mean predicted pressure $\langle P^{\mathsf{max}}{}_n\rangle$ at the lowest and highest measurement temperature, respectively. In this way ρ_{Hoff} captures how the distribution of $P_{\mathsf{min},n}^{\mathsf{Hoff}}$ changes with temperature. Because the expressions for ρ_{Hoff} and ρ in the simple form (see equation 3.8) are similar, they have the same interpretation and possible values. This means that ρ_{Hoff} varies between -1 and $+1$ and basically indicates how correlated Van 't Hoff constructions are.

The second part of equation 3.11, R_{Points}, corrects for the difference between *Van-'t-Hoff* pressures $P_{j,n}^{\mathsf{Hoff}}$ and the data pressures $P_{j,n}$ (see figure 3.7). We define it as

$$R_{\mathsf{Points}} = \frac{\displaystyle\sum_{j}^{F}\sum_{n}^{N}\left\{\exp\left[-\frac{\left\{\ln(P_{j,n}) - \ln\left(P_{j,n}^{\mathsf{Hoff}}\right)\right\}^2}{2\,\delta\mathrm{lnP}^2}\right]\right\}}{F \times N}. \qquad (3.13)$$

Recall that here $\delta\mathrm{lnP}$ is the (fixed) pressure range where all data pressures are (expected to be) found. By means of this expression we convert for each composition and at each temperature the difference between $P_{j,n}$ and $P_{j,n}^{\mathsf{Hoff}}$ to a Gaussian or normal distribution. This also allows us to express the difference between 0 (the difference between $P_{j,n}$ and $P_{j,n}^{\mathsf{Hoff}}$ is larger than $\delta\mathrm{lnP}$) and $+1$ (no difference between $P_{j,n}$ and $P_{j,n}^{\mathsf{Hoff}}$). The summation and normalization over all temperatures and all compositions allows us to minimize the influence of a single large difference, for example due to a measurement error.

By combining ρ_{Hoff} and R_{Points} we end up with an expression for the order coefficient ρ with the same characteristics as presented in the previous section (simple case). It varies between $-1 \leq \rho \leq +1$, where $\rho = -1$, $\rho = 0$, and $\rho = +1$ represents respectively the *anti-correlated*, the *random*, and the *correlated* situation. In the next section we discuss in detail how to use ρ to determine the basis of an enthalpy-entropy compensation effect.
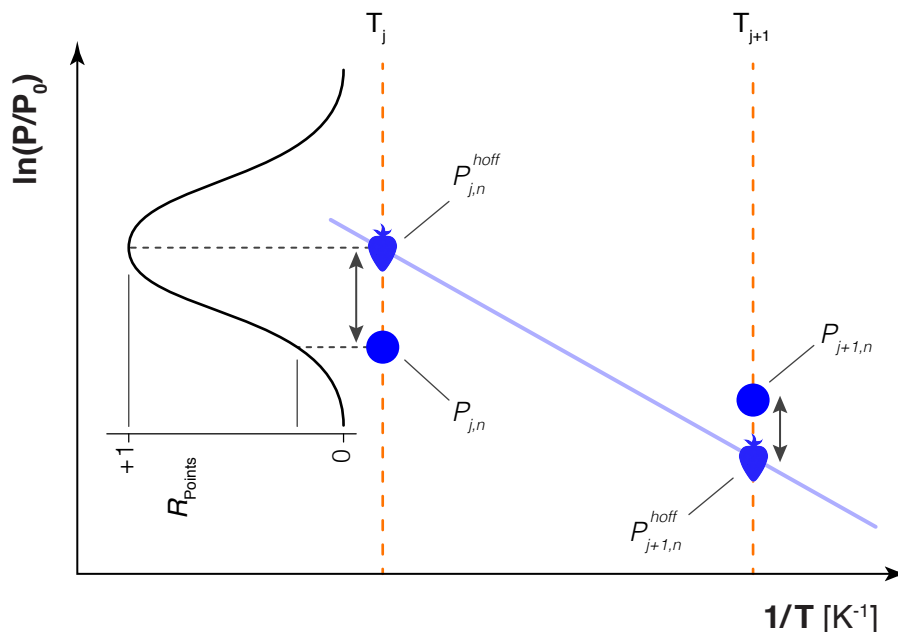
Figure 3.7 | Definition of R_{Points} – Schematic overview of how to obtain R_{Points}. At each temperature T_j, we calculate the difference (on logarithmic scale) between the data pressure and the Van 't Hoff pressure, the pressure obtained from the fitted Van 't Hoff relation (equation 3.1). The difference is translated into a value between 0 and $+1$ through a Gaussian/normal distribution. R_{Points} is the average of this value for all compositions and all temperatures.

3.4   Verification Procedure

In section 3.2 we showed that the compensation temperature T_{comp} as the only verification parameter cannot distinguish compensation effects with a statistical basis from compensation effects with a systematic basis. To correct this, we introduced an additional verification parameter, the order coefficient ρ (see the previous section). We now show that the combination of T_{comp} and ρ can be used to determine/verify the basis of an enthalpy-entropy compensation effect.

Our approach to conclude whether an enthalpy-entropy compensation effect has a systematic basis is to exclude the possibility that statistical methods (i.e. random fluctuations) can produce the same compensation effect. We do this by making use of the model presented in section 3.2. Using the same number of compositions and temperatures, and by extracting the average of all pressures $\langle P\left(T_j\right)\rangle$ at each temperature T_j, the temperature error δT, and the (fixed) range $\delta \ln \text{P}$, a large number of compensation effects can be generated computationally. For each generated compensation effect we determine the corresponding T_{comp} and ρ. This results in a

distribution of $(T_{\mathsf{comp}}, \rho)$ combinations with a specific standard deviation σ. We determine/verify the basis of a compensation effect by comparing the experimental combination of T_{comp} and ρ from the selected compensation effect with the combinations we are able to generate computationally. If the experimental combination does not lie within the 2σ-range of the generated distribution, there cannot be a statistical basis for the compensation effect: it must have a systematic basis. Otherwise, it is not possible to exclude a statistical basis. In steps, the procedure to determine/verify the nature of a compensation effects is:

- Calculate T_{comp} and ρ (and their error margin) from the experimental data set.
- Compute the distribution of T_{comp}'s and ρ's by means of the model presented in section 3.2. We recommend to stay as close as possible to the experimental data set. This means that we recommend to use the same temperatures, use the same number of compositions and extract the parameters $\langle P(T_j) \rangle$, $\delta \ln \mathrm{P}$, and $\delta \mathrm{T}$ from the experimental data set.
- Determine whether the experimental combination of T_{comp} and ρ (including their error margin) can be reproduced with a statistical significance: is the combination T_{comp} and ρ within the 2σ-range of the computational generated distribution? If not, the compensation effect has a systematic of genuine basis. Otherwise, it is not possible to exclude a systematic basis.

As the method relies on the overlap of the statistical distribution and the margin of the experimental $(T_{\mathsf{comp}}, \rho)$-pair, it is essential to determine T_{comp} and ρ with the highest precision.

## 3.5 Compensation Effect in Mg$_y$Ti$_{100-y}$H$_x$

We now demonstrate the power of the verification method described in the previous section to determine the nature of the compensation effect we observed in the Ti doped MgH$_2$ thin films. This is a simple and well-studied system.[3.1,3.2,3.7,3.31 — 3.37] We produced Mg$_y$Ti$_{100-y}$ films with a composition gradient between $57 \leq y \leq 90$ (see sample preparation for more details). By means of hydrogenography we monitored the optical transmission change upon hydrogenation for all composition *simultaneously* between $75°\mathrm{C}$ and $200°\mathrm{C}$ (see experimental details). From this we construct for each composition at each temperature a pressure-optical trans-mission-isotherm (PTI), which is analogue to PCIs.[3.38,3.39] The PTIs for the Mg$_y$Ti$_{100-y}$H$_x$ films are shown in figure 3.8c.

We develop an automatic procedure to extract from each PTI the corresponding pressure plateau P (see plateau pressure extraction procedure). By means of the Van 't Hoff relation (see equation 3.1) we find for each composition y the values of ΔH and ΔS from the temperature dependence of P. In this way we find that both ΔH and

Sample Preparation

The thin film samples are composed (from bottom to top) of a Fe layer, a gradient Mg$_y$Ti$_{100-y}$ ($57 \leq y \leq 90$) layer, a Fe layer and of a Pd capping layer. The Fe layers (10 nm) are used to reduce clamping effects from the substrate on the Mg$_y$Ti$_{100-y}$ and to prevent the mixing of Pd and Mg/Ti. The thickness of the Mg$_y$Ti$_{100-y}$ is between $45 - 55$ nm, depending on the composition. The layers are deposited on a 50×5 mm^2 polished quartz substrate (1 mm thick) by means of an ultra-high vacuum sputter system (base pressure of 10^{-10} Pa) in 3 μbar Ar (6N). Fe and Pd layers have a homogeneous thickness, which are obtained by a rotating substrate during sputtering. The composition range of the Mg$_y$Ti$_{100-y}$ ($57 \leq y \leq 90$) layer is obtained by co-sputtering Mg and Ti. The composition range is only present in the long axis of the sample, and is obtained by aligning this axis with the opposite configuration of the Mg and Ti targets. Typical depositing rates are 0.7 Å/s (200 W DC) for Ti, 1.6 Å/s for Mg (150 W RF), 1.2 Å/s for Pd (50 W DC), and 0.6 Å/s for Fe (100 W DC), which are obtained by stylus profilometry (DEKTAK) recorded on thick layers (> 200 nm). The same technique is used to obtain the fraction range $57 \leq y \leq 90$. All considered samples (one for each temperature) are sputtered simultaneously, and are therefore identical to each other.
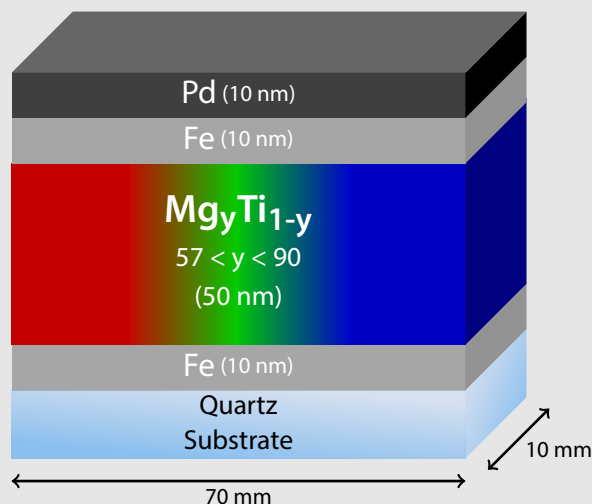
ΔS are strongly related to y. The relationship that draws our attention the most is the linear relation between $77 \leq y \leq 82$. Despite the small composition change, both ΔH and ΔS change with approximately 7% (see figure 3.8b). From this the question arise whether this linear dependence is the signature of a physical process or just a statistical accident? The fact that the compensation temperature ($T_{\text{comp}} = 154°\text{C}$) is very close to mean experimental temperature ($T_{\text{mean}} = 132°\text{C}$) suggest the latter. However, figure 3.8c shows that the plateau pressure varies systematically with the alloy composition y. This rather suggest a physical nature.

Experimental Details

The pressure-optical transmission-isotherms (PTIs) are obtained with hydrogenography. Here, the optical transmission of a film is monitored by means of a white light source in combination with a 3CCD camera (see section 1.xx). The optical transmission of every spot (expressed in pixels) of the gradient sample is recorded by a 3CCD camera. The transmission data is averaged in direction perpendicular to the composition gradient. The hydrogen pressure is gradually increased exponentially in more than 200 steps between min. 10^{-2} and max. $200 \, \mathrm{kPa}$, depending on the temperature. For this purpose, 4% H$_2$/Ar gas mixture and pure (100%) H$_2$ gas are used with a gas flow set to $20 \, \mathrm{sccm}$. The time to increase of the hydrogen pressure by one order of magnitude for the three lowest $(75°\mathrm{C}, 110°\mathrm{C}, \text{and } 165°\mathrm{C})$ temperatures is approximately $8 \, \mathrm{hrs}$, twice as high compared to the highest $(200°\mathrm{C})$ temperature $(\sim 4 \, \mathrm{hrs})$. During each pressure step, the transmission of the film is recorded at least 10 times to check whether the system reached equilibrium.

Plateau Pressure Extraction Procedure

The plateau pressures are extracted from the recorded PTIs by means of an automatic (MATLAB®) extraction procedure. Here the plateau pressure is chosen to be the pressure where the slope of the pressure plateau is the smallest. Instead of having limits of the slope between 0 (pressure plateaus) and ∞ (no change in hydrogen content), we rotate the PTI by $45°$ in order to limit the slope profile between -1 and 1, respectively. To reduce the data handling (a typical PTI consist of several hundred to a few thousand measurement points), we automatically quantify a rotated PTI by 50 points equally distributed over the rotated PTI. The slope profile is obtained by fitting a linear relation through each five points in a row. A quadratic relation fitted through every five points in a row in the slope profile results in the position on the rotated PTI where the slope is the closest to -1. Converting to the non-rotated situation, this point represents the pressure P where the slope of the PTI is the smallest.

To determine the nature of the compensation effect we proceed in two steps. First we show that a compensation effect with the same T_{comp} as in the experiment can be generated computationally by random fluctuations in the plateau pressure. Second we show that the order coefficient ρ is a reliable discriminator to establish the *systematic* compensation effect in Mg$_y$Ti$_{100-y}$H$_x$. Note that due to the small composition change we assume that the same single fcc hydride phase is reached and that the same hydrogen fraction (change). In this way we avoid the possibility that equilibrium pressures related different hydrogen fractions causes a (statistical) compensation effect, as observed by Griessen *et al.*[3.9]

To compare the experimentally observed T_{comp} with the computationally gen-
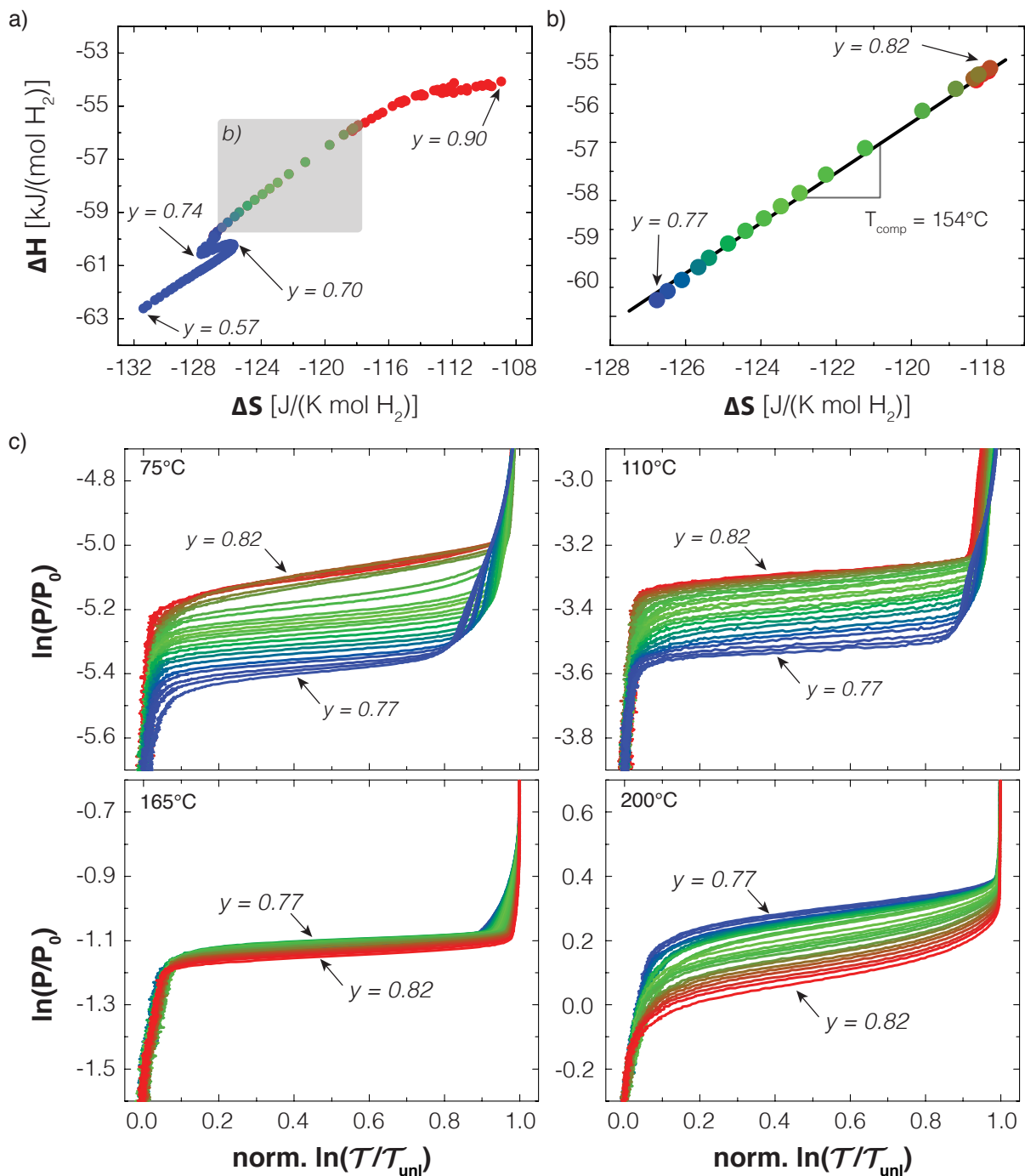
Figure 3.8 | Enthalpy-Entropy Compensation in Mg$_y$Ti$_{100-y}$H$_x$ – a) ΔH versus ΔS as a function of Mg$_y$Ti$_{100-y}$H$_x$ alloys with $57 \leq y \leq 90$ (1st hydrogenation). **b)** Close-up of the linear relation between ΔH and ΔS for $77 \leq y \leq 82$ with a slope $T_{comp} = 154°$C. **c)** Normalized pressure-optical transmission-isotherms (PTIs) for $77 \leq y \leq 82$ monitored at $T_1 = 75°$C, $T_2 = 110°$C, $T_3 = 165°$C, and $T_4 = 200°$C by means of hydrogenography.

erated T_{comp}'s, we stay as closely as possible to the experimental parameters. Hence, we generate computationally the same number of plateau pressures as the number of metal alloy compositions ($N = 20$) at the same temperatures as used in the measurements: $T_1 = 75°C$, $T_2 = 110°C$, $T_3 = 165°C$, and $T_4 = 200°C$ ($F = 4$). As we ignore the information about the known alloy composition, the range of allowed pressure values equals the maximum spread in plateau pressure in our experiments ($\delta\ln P = 0.3$). Although the PTIs of all compositions are, at each temperature, measured simultaneously by means of hydrogenography, we might expect a small gradient in the sample temperature ($\delta T = 1°C$). Furthermore, we describe the temperature dependence of $\langle P(T_j) \rangle$ through equations 3.1 and 3.2 and find $\langle \Delta H \rangle = -58$ kJ/mol H$_2$ and $\langle \Delta S \rangle = -121$ J/(K mol H$_2$). These values equal the average value of the experimentally obtained ΔH and ΔS shown in figure 3.8b. Figure 3.3a shows an example of two runs of computationally *generated* sets of (ΔH,ΔS) using these parameters, each with a different compensation temperature T_{comp}.

After $i = 10^5$ simulations we find that the distribution of T_{comp}, described by equation 3.7, is centered at $1000/T_{\text{mean}} = 2.47\,\text{K}^{-1}$ with a standard deviation $\sigma = 5.9 \times 10^{-2}\,\text{K}^{-1}$ (see figure 3.3b). The experimentally observed compensation temperature $1000/T_{\text{comp}} = 2.34\,\text{K}^{-1}$ is very close to $1000/T_{\text{mean}}$. At first glance, this suggests a *statistical* origin of the compensation effect. However, we find that this conclusion is premature when we include the systematic variation of the plateau pressure with composition, which we obtain from the normalized PTIs shown in figure 3.8c. This picture immediately confirms the value of $T_{\text{comp}} = 154°C$ since at $T_3 = 165°C$ all alloy compositions almost coincide. In addition, we recognize that the sequence of the plateau pressures as a function of alloy composition is reversed when comparing temperatures $T_1 = 75°C$ and $T_4 = 200°C$. This suggests $\rho \approx -1$.

At all temperatures and for all alloy compositions we find well-defined pressure plateaus. Since the pressure distribution changes gradually with temperature, it is very likely that the pressure distributions at $T = T^{\text{min}}$ and at $T = T^{\text{max}}$ are representative for all temperatures. To prove this, we calculate ρ by the two different definitions including only two (equation 3.8) or all (equation 3.11) temperatures. As the optical change of each composition is studied under exactly the same conditions, the automatic pressure plateau extraction procedure allows us to determine the plateau pressure and therefore the *experimental* order coefficient ρ with the highest degree of accuracy. For Mg$_y$Ti$_{100-y}$H$_x$ we find that $\rho = -0.978$ using only two temperatures, and $\rho = -0.912$ ($\rho_{\text{Hoff}} = -0.956$, $R_{\text{Points}} = 0.954$) when we include all temperatures. This indeed shows that the data set can be represented by only two temperatures while it also shows that the pressure distribution is indeed strongly *anti-correlated*.

Although $\rho = -0.978$ is far away from zero and the number of compositions is high ($N = 20$), we use our simulations to decide whether the a *statistical* reason for
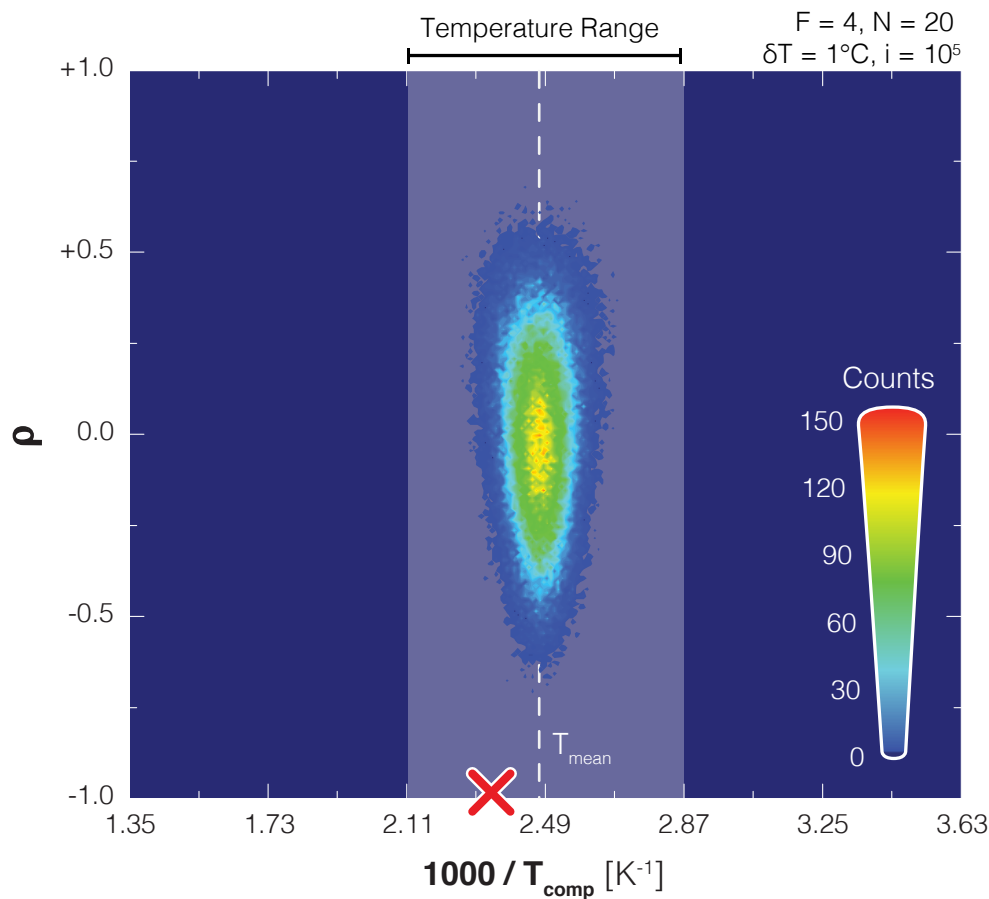
Figure 3.9 | Verificiation of Compensation Effect in Mg$_y$Ti$_{100-y}$H$_x$ – Contour plot of generated T_{comp} and ρ from $i = 10^5$ simulations using parameters $N = 20$, $\delta\ln P = 0.30$, $\delta T = 1°C$, $T_1 = 75°C$, $T_2 = 110°C$, $T_3 = 165°C$, and $T_4 = 200°C$ $(F = 4)$. Red indicates a high number of generated combinations, blue a low number of generated combinations. The parameters used in the simulation corresponds to those of the enthalpy-entropy compensation observed in Mg$_y$Ti$_{100-y}$H$_x$. The red cross indicates the combination of T_{comp} and ρ experimentally observed in Mg$_y$Ti$_{100-y}$H$_x$, which cannot be generated by the simulations.

the compensation effect observed in Mg$_y$Ti$_{100-y}$H$_x$ really can be excluded. From the same dataset as previously used to determine the temperature range of *statistically* feasible T_{comp}'s, we now determine for each compensation effect the corresponding order coefficient ρ using only two temperatures. Figure 3.9 shows the distribution of the computationally produced T_{comp}'s and ρ's. We find that the distribution lies within the experimental temperature range and is centered at $T_{comp} = T_{mean}$ and $\rho = 0$. From the simulations of the experiments we only find compensation effects with $|\rho| < 0.70$, independent of T_{comp}. Thus by using only two temperatures, we already

can conclude that the characterization parameters of the observed compensation effect in $Mg_yTi_{100-y}H_x$ ($T_{\text{comp}} = 154°C$, $\rho = -0.978$) cannot be reproduced by means of random pressures. This excludes a *statistical* origin. Hence, we conclude on the basis of the available sets of plateau pressures at the four temperatures that there must be a *systematic* basis for the compensation effect in $Mg_yTi_{100-y}H_x$.

3.6 Discussion

The discovery that the compensation effect in Ti doped MgH_2 thin films must have a *systematic* origin gives rise to one of the most intriguing question in the field of enthalpy-entropy compensation, *what causes it?* Although the Mg-T-H system is very well studied, it provides us no direct answer. Nevertheless, we briefly discuss effects that might play a role. Note that these effects can play a role in other systems where enthalpy-entropy compensation (or analogue effects) is observed.

It is unlikely that the temperature dependence of the enthalpy and/or the entropy plays a role. This temperature dependence is only significant at high temperatures and for large temperature differences. In addition, in the Mg_yTi_{100-y} thin films we have to deal with the difference between the heat capacity of the α and β-phase, which is even a smaller number. The entropy on the other hand is basically determined by the transition of hydrogen from the gas phase to the metal lattice. In metal hydrides configurational and vibrational effects are considered two most important contributions to the entropy. However, we assume that the variation of these effects is neglectable within the relatively narrow composition range of the compensation effect ($77 \leq y \leq 82$). We expect that in this range the amount of hydrogen uptake and the structure of the films are the same. The latter is supported by Borsa *et al.*, where the presence of a single *fluorite* or fcc MgH_2 phase with embedded TiH_2 is reported in this range.[3.34] EXAFS studies show that the hydrides are partially segregated and form a structurally coherent phase.[3.37] That a different structure can influence the thermodynamics is observed at higher compositions. For $y > 82$ a mixed *rutile* MgH_2/fcc TiH_2 structure is reported.[3.31,3.34] In this range we find a non-linear relation between ΔH and ΔS where ΔH converges to a constant value equal to the enthalpy of formation of *rutile* MgH_2 reported by Krozer *et al.*[3.40]

An answer might be found plastic and/or elastic deformations within the film, as both deformations can have a strong composition and temperature dependence. The presence of a well-defined pressure plateau in the PTIs of $Mg_yTi_{100-y}H_x$ is a direct consequence of the hydrogen-hydrogen interaction.[3.41] In large extent this mechanism is of elastic origin. However, during hydrogenation clamping effects and stresses and constrains may build up within the films. Multiple studies show that these effects can strongly affect the plateau pressure of the first hydrogenation.[3.42 — 3.44]

Another possible effect might be the hydrogen solubility in the parent phases of MgH_x and TiH_x. In chapter 5 we find within the solubility range of HfH_x a significant change of the entropy. A recent study shows that the hydrogen solubility ranges within nanostructured MgH_x and TiH_x are increased compared to the bulk compounds.[3.46] We can therefore not exclude that a changing ratio of MgH_x and TiH_x domains affects the hydrogen solubility, including the thermodynamics.

Also the effects of nucleation and growth on the hydrogenation of nano-structured materials cannot be excluded. Recently, Mooij *et al.* showed the presence of nucleation barriers and the removal of these barriers results in a lower plateau pressure of MgH_2 formation.[3.45] Consequently, these effects may contribute to the $\Delta H - \Delta S$ compensation we observed in $Mg_yTi_{100-y}H_x$. However, further research is necessary to see whether these plastic/elastic deformations are actually capable of producing the observed correlation. Studying a compensation effect in a single composition system is preferable, as it will reduce the number of possible contributions.

3.7 Conclusions

We conclude that the enthalpy-entropy compensation in metal hydrides can have a systematic nature. For this we developed a verification method where we determine whether we can generate the experimental observed compensation effect from random fluctuations. In this way we decide whether we can exclude a statistical basis for the compensation effect. In contrast to other models, we introduce random fluctuations in the actual experimental parameters (the pressure and temperature). In this way we stay as close as possible to the experiments.

The key ingredient of the verification is the introduction of the order coefficient. In this way we can capture the systematic change of the pressure with temperature. The characterization by T_{comp} alone is not sufficient to determine the nature of a compensation effect. We show that compensation effects with or without a systematic change of the pressure with temperature can have the same T_{comp}. In this way we show that random fluctuations cannot reproduce the enthalpy-entropy compensation effect in Ti doped MgH_2 thin films.

We stress that our method can be applied to any system where a compensation effect (or analogue effect) is observed. Only a few simple symbol definition changes are necessary. It is however crucial to determine the compensation temperature and the order coefficient with the highest degree of accuracy. A combinatorial technique such as hydrogenography to determine the experimental measure of many reaction compositions simultaneously may be essential to achieve this. The broad applicability of the verification method paves the way towards a general understanding of enthalpy-entropy compensation and analogue effects.

References

[3.1] *R. Gremaud, A. Baldi, M. Gonzalez-Silveira, B. Dam, and R. Griessen.* **Chemical short-range order and lattice deformations in MgyTi1-yHx thin films probed by hydrogenography.** Physical Review B **77**, 144204 (2008).

[3.2] *R. Gremaud.* **Hydrogenography. A thin film optical combinatorial study of hydrogen storage materials.** Doctoral thesis. VU University Amsterdam. ISBN/EAN 978-90-9023439-7 (2008).

[3.3] *C. Boelsma.* **Enthalpy-entropy compensation studied in two metal hydrides.** Master thesis. VU University Amsterdam. (2011).

[3.4] *L.P.A Mooij, A. Baldi, C. Boelsma, K. Shen, M. Wagemaker, Y. Pivak, H. Schreuders, R. Griessen, and B. Dam.* **Interface energy controlled thermodynamics of nanoscale metal hydrides.** Advanced Energy Materials **1**(5), 754 – 758 (2011).

[3.5] *Y. Pivak.* **Validation of Hydrogenography for the search of promising hydrogen storage materials.** Doctoral thesis. VU University Amsterdam & Delft University of Technology. ISBN/EAN 978-94-6108-260-2 (2012).

[3.6] *A. Andreasen, T. Vegge, and R.A. Grieger.* **Compensation effect in the hydrogenation/dehydrogenation kinetics of metal hydrides.** The Journal of Physical Chemistry B **109**, 3340 – 3344 (2005).

[3.7] *A. Anastasopol, T.B. Pfeiffer, J. Middelkoop, U. Lafont, R.J. Canales-Perez, A. Schmidt-Ott, F. Mulder, and S.W.H. Eijt.* **Reduced enthalpy of metal hydride formation for Mg-Ti nanocomposites produced by spark discharge generation.** Journal of the American Chemical Society **135**, (21) 7891 – 7900 (2013).

[3.8] *R. Bardhan, L.O. Hedges, C.L. Pint, A. Javey, and S. Whitelam.* **Uncovering the intrinsic size dependence of hydriding phase transformations in nanocrystals.** Nature Materials **12**, 905 – 912 (2013).

[3.9] *R. Griessen, N. Strohfeldt, and H. Giessen.* **Thermodynamics of the hybrid interaction of hydrogen with palladium nanoparticles.** Nature Materials **15**, (3) 311 – 318 (2015).

[3.10] *E. Cremer.* **The compensation effect in heterogeneous catalysis.** Advanced Energy Catalysis **7**, 75 (1955).

[3.11] *M.C. Wilson and A.K Galwey.* **Compensation effect in heterogeneous catalytic reactions including hydrocarbon formation on clays.** Nature **243**, 402 – 404 (1973).

[3.12] *D. McPhail and A. Cooper.* **Thermodynamics and kinetics of dissociation of ligand-induced dimers of vancomycin antibiotics.** Journal of the Chemical Society, Faraday Transactions **93**, 2283 – 2289 (1977).

[3.13] *L. Liu and Q.X. Guo.* **Isokinetic relationship, isoequilibrium relationship, and enthalpy-entropy compensation.** Chemical Reviews **101**(3), 673 – 696 (2001).

[3.14] *T. Bligaard, K. Honkala, A. Logadottir, J.K. Nørskov, S. Dahl, and C.J.H. Jacobsen.* **On the compensation effect in heterogeneous catalysis.** The Journal of Physical Chemistry B **107**, 9325 – 9331 (2003).

[3.15] *R. Lumry and S. Rajender.* **Enthalpy-entropy compensation phenomena in water solutions of proteins and small molecules: An ubiquitous properly of water.** Biopolymers **9**, 1125 – 1227 (1970).

[3.16] *B. Rosenberg, G. Kemery, R.C. Switcher, and T.C. Hamilton.* **Quantitative evidence for protein denaturation as the cause of thermal death.** Nature **232**, 471 – 473 (1973).

[3.17] *J. Petruska and M.F. Goodman.* **Enthalpy-entropy compensation in DNA melting thermodynamics.** Journal of Biological Chemistry **270**, 746 – 750 (1995).

[3.18] *L. Liu, C. Yang, and Q. Guo..* **A study on the enthalpy-entropy compensation in protein unfolding.** Biophysical Chemistry **84**, 239 – 251 (2000).

[3.19] *J.A. Schwarz and L.E. Felton.* **Compensating effects in electromigration kinetics.** Solid-State Electronics **28**, 669 – 675 (1985).

[3.20] *U. Lubianiker and I. Balberg.* **Two Meyer-Neldel rules in porous silicon.** Physical Review Letters **78**, 2433 – 2436 (1997).

[3.21] *R. Widenhorn, L. Mündermann, A. Rest, and E. Bodegom.* **Meyer-Neldel rule for dark current in charge-coupled devices.** Journal of Applied Physics **89**, 8179 – 8182 (2001).

[3.22] *M. Ullah, T.B. Singh, A. Rest, H. Stifler, and N.S. Sariciftci.* **Meyer-Neldel rule in fullerene field-effect transistors.** Applied Physics A **97**, 521 – 526 (2009).

[3.23]   *O. Exner.*   **Concerning the isokinetic relationship.** Nature   **201**,   488 – 490 (1964).

[3.24]   *O. Exner.*   **Determination of the isokinetic temperature.** Nature   **227**, 366 – 367 (1970).

[3.25]   *B.E.C. Banks, V. Damjanovic, and C.A. Vernon.*   **The so-called thermodynamic compensation law and thermal death.** Nature   **240**, 147 – 148 (1972).

[3.26]   *G. Kemeny and B. Rosenberg.*   **Compensation law in thermodynamics and thermal death.** Nature   **243**, 400 – 401 (1973).

[3.27]   *P.S. Harris.*   **Compensation effect and experimental error.** Nature   **243**, 401 – 402 (1973).

[3.28]   *R.R. Krug, W.G. Hunter, and A.S. Pedersen.*   **Statistical interpretation of enthalpy-entropy compensation.** Nature   **261**, 566 – 567 (1976).

[3.29]   *A. Cornish-Bowden.*   **Enthalpy-entropy compensation: a phantom phenomenon.** Journal of Biosciences **27**, 121 – 126 (2002).

[3.30]   *J.P. Barrie.*   **The mathematical origins of the kinetic compensation effect.** Physical Chemistry Chemical Physics **14**, 318 – 336 (2012).

[3.31]   *P. Vermeulen, R.A.H. Niessen, and P.H.L. Notten.*   **Hydrogen storage in metastable MgyTi(1-y) thin films.** Electrochemistry Communications **8**, 27 – 32 (2006).

[3.32]   *D.M. Borsa, A. Baldi, M. Pasturel, H. Schreuders, B. Dam, R. Griessen, P. Vermeulen, and P.H.L. Notten.*   **Mg-Ti-H thin films for smart solar collectors.** Applied Physics Letters **88**, 241910 (2006).

[3.33]   *W.P. Kalisvaart, J.H. Wondergem, F. Bakker, and P.H.L. Notten.*   **Mg-Ti based materials for electrochemical hydrogen storage.** Journal of Materials Research **22**, 1640 – 1649 (2007).

[3.34]   *D.M. Borsa, R. Gremaud, A. Baldi, H. Schreuders, J.H. Rector, B. Kooi, P. Vermeulen, P.H.L. Notten, and B. Dam.* R. Griessen **Structural, optical, and electrical properties of MgyTi1-yHx thin films.** Physical Review B **75**, 205408 (2007).

[3.35]   *R. Gremaud, D.M. Borsa, A. Borgschulte, P. Mauron, H. Schreuders, J.H. Rector, B. Dam, and R. Griessen.*   **Hydrogenography: an optical combinatorial method to find new light-weight hydrogen storage materials.** Advanced Materials **19**, 2813 (2007).

[3.36] *A. Baldi, D.M. Borsa, H. Schreuders, J.H. Rector, T. Atmakidis, M. Bakker, H.A. Zondag, W.G.J. van Helden, and B. Dam.* R. Griessen **Mg-Ti-H thin films as switchable solar absorbers.** International Journal of Hydrogen Energy **33**, 3188 – 3192 (2008).

[3.37] *A. Baldi, R. Gremaud, D.M. Borsa, C.P. Balde, A.M.J. van der Eerden, G.L. Kruijtzer, P.E. de Jongh, B. Dam, and R. Griessen.* **Nanoscale composition modulations in MgyTi1-yHx thin film alloys for hydrogen storage.** International Journal of Hydrogen Energy **34**, 1450 – 1457 (2009).

[3.38] *A. Borgschulte, W. Lowstroh, R.J. Westerwaal, H. Schreuders, J.H. Rector, B. Dam, and R. Griessen.* **Combinatorial method for the development of a catalyst promoting hydrogen uptake.** Journal of Alloys and Compounds **404-406**, 699 – 705 (2005).

[3.39] *R. Gremaud, M. Slaman, H. Schreuders, J.H. Rector, B. Dam, and R. Griessen.* **An optical combinatorial method to determine the thermodynamics of hydrogen absorption and desorption in metals.** Applied Physics Letters **91**, 231916 (2007).

[3.40] *A. Krozer and B. Kasemo.* **Hydrogen uptake by Pd-coated Mg: absorption-decomposition isotherms and uptake kinetics.** Journal of the Less Common Metals **160**, 323 – 342 (1990).

[3.41] *H. Wagner and H. Horner.* **Elastic interaction and the phase transition in coherent metal-hydrogen systems.** Advances in Physics **23**, (4) 587 – 637 (1974).

[3.42] *Y. Pivak, R. Gremaud, K. Gross, M. Gonzalez-Silveira, A. Walton, D. Book, H. Schreuders, B. Dam, and R. Griessen.* **Effect of the substrate on the thermodynamic properties of PdHx films studied by hydrogenography.** Scripta Materialia **60**, 348 – 351 (2009).

[3.43] *Y. Pivak, H. Schreuders, M. Slaman, B. Dam, and R. Griessen.* **Thermodynamics, stress release and hysteresis behavior in highly adhesive Pd-H films.** International Journal of Hydrogen Energy **36**, 4056 – 4067 (2011).

[3.44] *Y. Pivak, H. Schreuders, and B. Dam.* **Thermodynamic properties, hysteresis behavior and stress-strain analysis of MgH2 thin films, studied over a wide temperature range.** Crystals **2**, 710 – 729 (2012).

[3.45] *L.P.A. Mooij and B. Dam.* **Hysteresis and the role of nucleation and growth in the hydrogenation of Mg nanolayers.** Physical Chemistry Chemical Physics **15**, 2782 – 2792 (2013).

[3.46] *L.J. Bannenberg, H. Schreuders, L. van Eijck, J.R. Heringa, N.J. Steinka, R. Dalgliesh, B. Dam, F.M. Mulder, and A.A. van Well.* **Impact of Nanostructuring on the Phase Behavior of Insertion Materials: The Hydrogenation Kinetics of a Magnesium Thin Film.** The Journal of Physical Chemistry C **120**(19), 10185 – 10191 (2016).

Mg(Ti)ZrH$_x$

— an Optical Hydrogen Sensing Material —

4.1   Introduction

An effective optical hydrogen detection material shows a large monotonously increase of the optical response within a large hydrogen pressure range without hysteresis. Pd-based thin films are considered to be effective, with a pressure range spanning a few orders of magnitude.[4.1] However, its optical response is small compared to the hydrogenation of Mg thin films.[4.2]

Mg thin films are, however, not suitable for hydrogen detection over a large pressure range. Mg has a very small hydrogen solubility range ($\delta x < 0.01$) where the optical properties do not change. The large optical response is only induced by the incoherent transition from metallic Mg to insulating MgH$_2$, which occurs at a well-defined pressure. As a result the corresponding isotherm shows only a flat pressure plateau, not an inclined one, and is accompanied by a hysteresis (i.e. the hydrogenation and the dehydrogenation isotherms are different from each other) of approximately 1 order of magnitude. However, it is possible to introduce an inclined pressure plateau by alloying the Mg. Gremaud *et al.* found that for a range of MgTi alloys an inclined pressure plateau rather a flat one.[4.3] However, the pressure range is only 1 order of magnitude, the optical response is significantly reduced with respect to MgH$_2$, and the large hysteresis not reduced.

Recently, it is found that creating amorphous Mg-based materials by adding NiZr results in steep hydrogenation isotherms. The pressure range is found to be up to 4 orders of magnitude while the optical response is close to that of pure MgH$_2$.[4.4] The presence of Ni is considered to be essential and combines the properties of

---

This work resulted in allocation of the patent application: C. Boelsma, and B. Dam. Large pressure range hydrogen sensor. PCT Patent PCT/NL2014/050805. Filling date: 27 Nov 2014. Publication date: 4 Jun 2015.

two well-known alloys. First, the amorphous NiZr alloys are known to have steep isotherms although they do not exhibit a large optical response during hydrogenation (i.e. the alloys remain metallic).[4.5 — 4.7] Second, MgNiH$_x$ shows a similar large optical response as MgH$_x$.[4.8 — 4.10] However, the MgNiZr isotherms show multiple inclinations which makes it difficult to describe mathematically (see figure 4.1).

In this chapter we show that the presence Ni is not essential in the MgNiZr alloys to have steep isotherms. It is possible to make amorphous MgZr structures with steep isotherms. These steep isotherms show only one inclination with a pressure range that is larger than observed with MgNiZr (5 orders versus 4). The optical response of these alloys is smaller compared to pure MgH$_x$, although we can increase the optical response by replacing Zr partially by Ti without changing the amorphous structure nor the pressure range. In addition, we are also able to increase the pressure range by replacing Zr partially by Hf. Nonetheless, the Mg(Ti/Hf)Zr alloys demonstrate the particular although not understood role of Zr in creating amor-
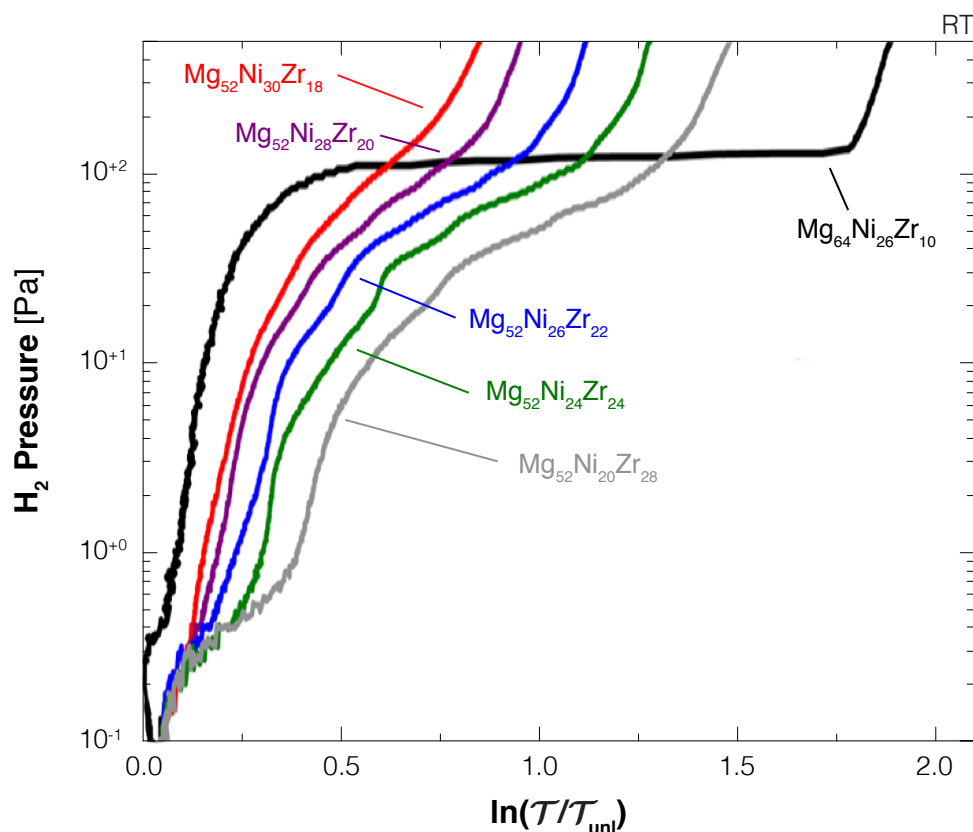
Figure 4.1 | Mg-Ni-Zr Isotherms – Pressure–optical transmission– isotherms (PTIs) of the hydrogenation of various MgNiZr alloys measured at room temperature, adapted from Victoria *et al.*[4.4] The isotherms are obtained using Pd covered MgNiZr gradient thin films with a typical thickness of $\sim$60 nm.

phous alloys. They also indicate the potential of amorphous structures as optical hydrogen detection materials, although hysteresis is still observed.

4.2 Results

In this section we discuss the results of our study on MgZr-based thin films as an optical hydrogen sensing material. However, this study was not intentionally and the sensing properties of MgZr were discovered by surprise. Instead, our original goal was to study the influence of the thin film interfaces on the thermodynamics of MgTi. In this section we first present chronological steps that led to discovery of the sensing capabilities of MgZr. This is followed by a detailed discussion of the sensing properties. In the final part we discuss the effects on the sensing properties when replacing Zr partially by Ti or Hf.

4.2.1 Amorphous MgTiZr from Crystalline Zr-MgTi-Zr

In chapter 2 we demonstrate that the hydrogen absorption pressure of Mg can be changed significantly through interface energy.[4.11] This means that the interface energy can be used to alter the thermodynamics of metal hydrides, although it is unknown whether it affects both the entropy and the entropy of formation or only one of them. To study this we used MgTi thin films as a basis. Since the hydrogenation of MgTi sandwiched between two Fe layers is reflected by clear pressure plateaus, it en-

Sample Preparation

The Mg_yTi_{100-y} multilayer thin films are composed (from the bottom to the top) of a Zr layer $(10\,\text{nm})$, a Mg_yTi_{100-y} layer $(50\,\text{nm})$, a Zr layer $(10\,\text{nm})$, and a Pd capping layer $(10\,\text{nm})$. Each film consist of an uniform Mg-Ti composition between $75 < y < 85$. The films are prepared by means of an ultra-high vacuum sputter system (base pressure of $10^{-10}\,\text{Pa}$) in $3\,\mu\text{bar}$ Ar (6N). The deposited on a $10 \times 10\,\text{mm}^2$ polished quartz substrate. The Pd layer protects the underlying layers from oxidation and also improves the hydrogen dissociation process.[4.12] All layers have an uniform thickness, obtained by a rotating substrate during sputtering. The layer thicknesses and the atomic ratio of the Mg_yTi_{100-y} layer is determined by means of a sputter-rate, obtained by stylus profilometry (DEKTAK) on bulk samples $(>400\,\text{nm})$.

Pd (10nm)

Zr (10nm)

Mg_yTi_{100-y}
$75 < y < 85$
(50 nm)

Zr (10nm)

Quartz Substrate

10mm

10mm
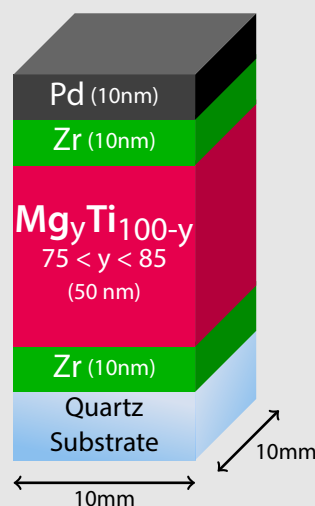
ables us to determine the thermodynamics with high precision (see chapter 3). We therefore chose to studio the effect of the interface energy on the thermodynamics of various MgTi alloys by sandwich them between Zr instead of Fe (see sample preparation). We selected Zr as it is immiscible with both Mg and Ti and we therefore reduce the alloy formation at the interfaces.[4.13,4.14]

Figure 4.2 shows the pressure-optical transmission-isotherms (PTIs) of a Pd-capped $Mg_{80}Ti_{20}$ thin film $(50 \, \text{nm})$ sandwiched between two layers of Zr $(10 \, \text{nm})$ upon full hydrogenation/dehydrogenation cycles. All isotherms are measured at $165°C$ by means of hydrogenography, and the film is not exposed to oxygen between each measurement. The first hydrogenation isotherm shows very similar behavior as found with Fe sandwiched $Mg_{80}Ti_{20}$. Up to $2 \times 10^{+4} \, \text{Pa}$ we observe almost no op-
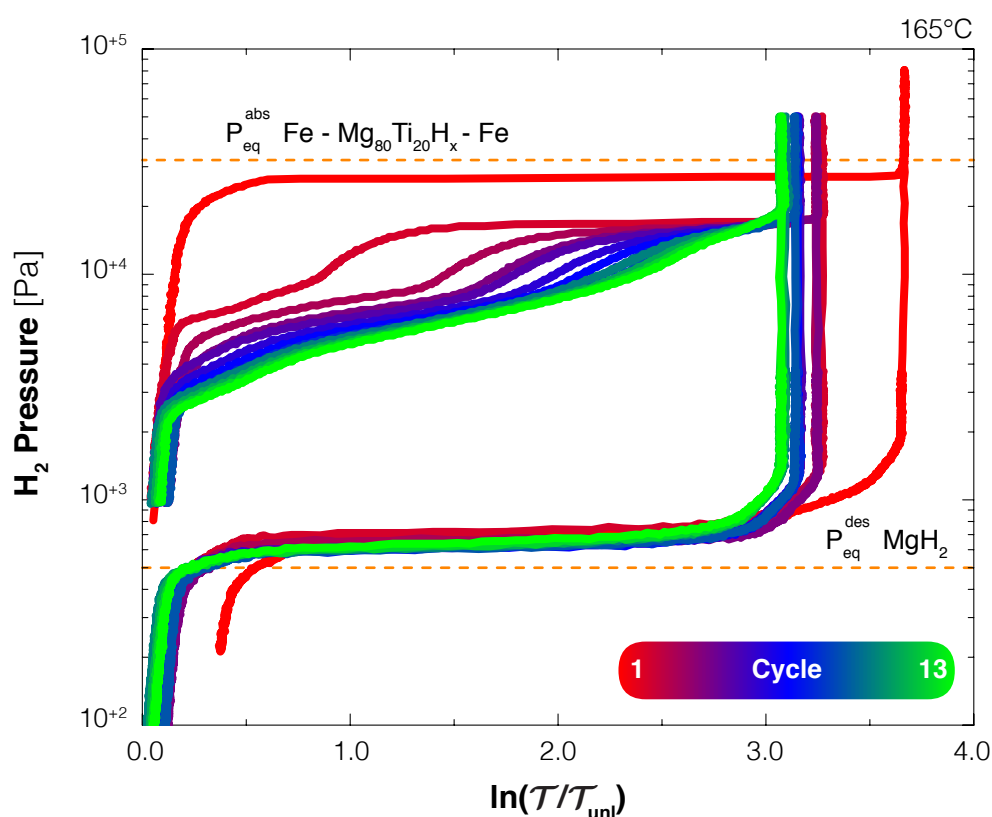
Figure 4.2 | Cycle Stability of a Zr Sandwiched $Mg_{80}Ti_{20}$ Thin Film – Pressure–optical transmission–isotherms (PTIs) at $T = 165°C$ of a Pd-capped $Mg_{80}Ti_{20}$ thin film $(50 \, \text{nm})$ sandwiched between two layers of Zr $(10 \, \text{nm})$ upon complete hydrogenation/dehydrogenation cycles. Note that for each cycle the zero transmission level corresponds to the stable unloaded state reached during the previous cycle. The orange dashed lines indicate the absorption pressure of $Mg_{80}Ti_{20}H_x$ sandwiched between Fe layers $(3.2 \times 10^{+4} \, \text{Pa} \, @ \, 165°C)$ and the desorption pressure of MgH_2 $(5.0 \times 10^{+2} \, \text{Pa} \, @ \, 165°C)$, respectively.

tical response to an increasing hydrogen pressure. At $2.5 \times 10^{+4}$ Pa a flat pressure plateau is found, most probably resulting from the hydrogenation of Mg-Ti, which is slightly lower than the first hydrogenation pressure of Fe sandwiched $Mg_{80}Ti_{20}$ ($5.0 \times 10^{+2}$ Pa @ 165°C). This suggests that the different interface does indeed alter the hydrogenation pressure and therefore the thermodynamics of $Mg_{80}Ti_{20}H_x$.

The second hydrogenation of the $Mg_{80}Ti_{20}$ thin film alters the shape of the isotherm. Instead of a flat pressure plateau we observe that from $6 \times 10^{+3}$ Pa the optical response of the film starts to increase gradually with pressure. At $1.7 \times 10^{+4}$ Pa the gradually increase stops and a pressure plateau is observed. This pressure is lower than the pressure plateau observed during the first hydrogenation, most probably due to the release of stress built up during the film's deposition. The width of the pressure plateau equals approximately 50% of the total optical transmission change after the second hydrogenation of the film. With cycling the width of this flat plateau reduces without changing its pressure. Consequently, the inclined pressure plateau becomes more prominent with each cycle. Remarkable, the slope does not change with cycling. Therefore, the pressure where the inclined pressure starts decreases with each cycle. After approximately 13 cycles the inclined pressure plateau equals the whole transmission contrast change and starts already at $2.5 \times 10^{+3}$ Pa. The result is an almost linear relation between the optical transmission and the pressure (on a log-log scale) for a pressure range of approximately 1 order of magnitude while the optical response is still close to that of MgH_2: $\ln(\mathcal{T}/\mathcal{T}_{unl}) = +3.1$.

The transformation from a flat to an inclined pressure plateau is most likely due to Zr. Although Mg and Ti have a positive enthalpy of mixing, $Mg_{80}Ti_{20}$ forms a coherent crystalline structure in both its metallic and hydrogenated state and is considered to be meta-stable.[4.3,4.15 — 4.23] Each hydrogenation is therefore reflected by a flat pressure plateau. Knowing that many metallic glasses with inclined/steep isotherms are Zr-based,[4.6 — 4.8,4.24] the optical results shown in figure 4.2 suggest that Zr has penetrated the MgTi layer. As with each hydrogenation more and more of the flat pressure plateau is converted into an inclined one, Zr penetrates further into the $Mg_{80}Ti_{20}$ layer and converting more of this layer into a MgTiZr alloy (see figure 4.3). Since Zr forms a hydride at much lower pressures than MgTi alloys,[4.25,4.26] the results suggest that the mobility of ZrH_2 must be high within the (partially) hydrogenated MgTi layer. This is remarkable as Zr-hydride forms a crystalline structure while metallic Mg, Ti, and Zr have a positive enthalpy of mixing.[4.13,4.14]

Interestingly, the dehydrogenation isotherms are not affected by the presence of Zr. Instead of an inclined pressure plateau, we observe flat pressure plateaus for each consecutive dehydrogenation with a pressure very close to the desorption pressure of MgH_2 ($5.0 \times 10^{+2}$ Pa). This suggests that once fully hydrogenated, all interstitial sites have (almost) the same energy equivalent to that of MgH_2.
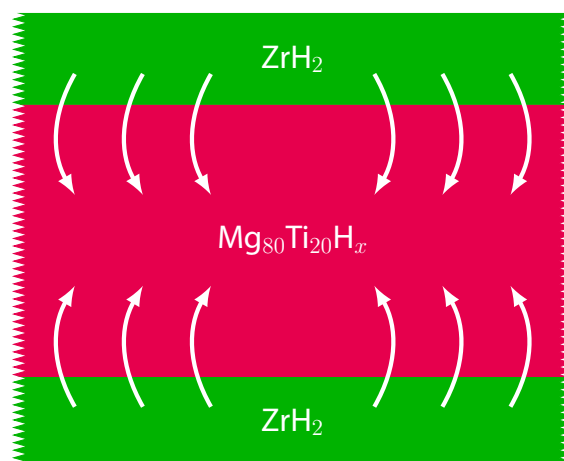
Figure 4.3 | Penetration of Zr into crystalline Mg$_{80}$Ti$_{20}$ – Illustration of the penetration of ZrH$_2$ from the separate layers into the sandwiched Mg$_{80}$Ti$_{20}$ layer with each hydrogenation. This causes a transformation of the coherent crystalline Mg$_{80}$Ti$_{20}$H$_x$ layer in a(n) (distribution of) amorphous MgTiZr-H$_x$ alloy(s).

4.2.2 Reproducing the Amorphous MgTiZr Structure

The optical results of Zr sandwiched MgTi thin films shown in figure 4.3 do not clarify whether the steep isotherms are the result of one specific amorphous MgTiZr alloy, with a distribution of site-energies, or that they are the result of a range of MgTiZr alloys, each with a different hydrogenation pressure. In addition, the (local) Zr fraction within the Mg-Ti layer is also unknown. To find out, we produce a ternary gradient sample creating thousands different Mg-Ti-Zr alloys (see sample preparation). With hydrogenography, we are able to study the hydrogenation of all these compositions at the same time and under the exact same conditions.

Figure 4.4 shows for three Mg$_y$Ti$_z$Zr$_{100-y-z}$ alloys the corresponding isotherms measured at $100°$C. The isotherms of these alloys represents the hydrogenation of all studied alloys:

- for **Mg-rich** alloys $(y \approx 80, z \approx 10)$ the isotherms show two flat pressure plateaus, connected by a small inclination. The lower pressure plateau is more prominent at higher Zr fractions, the higher pressure plateau at higher Ti fractions. The optical transmission change matches that of Mg$_{80}$Ti$_{20}$, indicating that the addition of Zr does not change the optical properties.

- for **Ti-rich** alloys $(y \approx 60, z \approx 25)$ the isotherms do not show pressure plateaus. Instead, we observe steep although curved (on a log-log plot) isotherms spanning a pressure range of approximately 1 order of magnitude. The optical

transmission change is significantly lower compared to Mg-rich alloys, mainly due to the lower Mg fraction.

- for **Zr-rich** alloys ($y \approx 50, z \approx 20$) the isotherms are steep and highly linear (on a log-log plot). The isotherms span a pressure range of approximately 2 order of magnitude, while the optical transmission change is even lower than observed in the Ti-rich alloys.


Sample Preparatie

The Mg-Ti-Zr wafer sample (left) and the $Mg_{51}Ti_{22}Zr_{27}$ single composition sample (right) are prepared by means of an ultra-high vacuum sputter system (base pressure of 10^{-10} Pa) in 3 μbar Ar (6N). The wafer sample consist of (from the bottom to top) a gradient Ti_kZr_{100-k} layer $(8 - 16$ nm$)$, a gradient $Mg_yTi_zZr_{100-y-z}$ layer $(25 - 70$ nm$)$, another layer gradient Ti_kZr_{100-k} layer $(8 - 16$ nm$)$, and of a Pd capping layer. The Ti_kZr_{100-k} layers are used to reduce the clamping effects from the substrate on the $Mg_yTi_zZr_{100-y-z}$ layer and to prevent the mixing of Pd and Mg/Ti/Zr, the gradient profile is chosen in such a way that at each position of the waver the atomic fraction between Ti and Zr is the same as in the $Mg_yTi_zZr_{100-y-z}$ layer: $k = 100z/(100 - y)$. The Mg, Ti, and Zr atomic fraction ratios ranges from $0.44 \leq y \leq 0.88$, $0.05 \leq z \leq 0.32$, and $0.05 \leq 100 - y - z \leq 0.32$. The single composition sample consist of the same stack of layers, only with a fixed composition: $y = 51$, $z = 22$, and $h = 45$. The atomic fraction ratios are obtained by co-sputtering Ti, Zr, and/or Mg. The layer thicknesses and composition is determined by means of a sputter-rate, obtained from stylus profilometry (DEKTAK) on bulk samples (>400 nm).
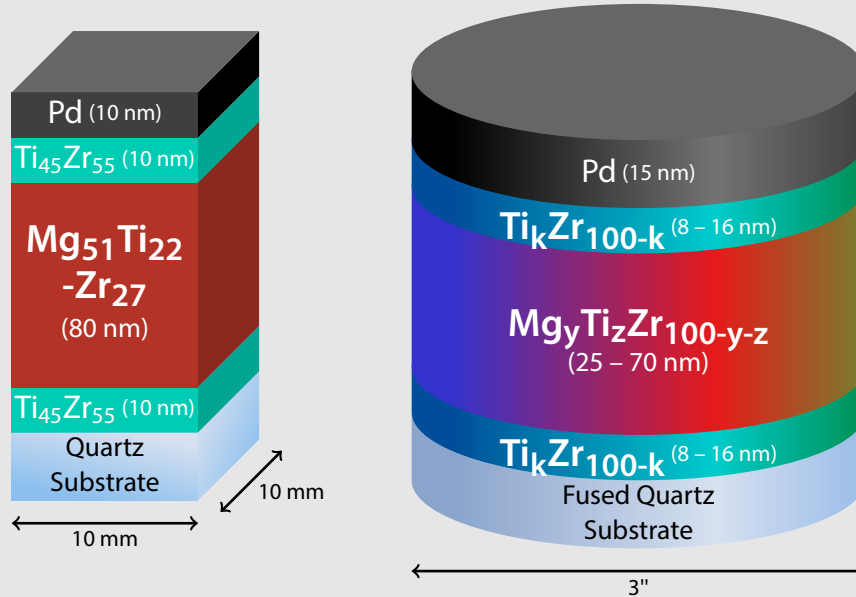
Note that these observations are based on the second hydrogenation of the alloys, as the during the first hydrogenation usually stresses are still present within the film resulting in a different hydrogenation isotherm. Furthermore, the layer thickness strongly depends on the composition. Mg-rich alloys has the highest layer thickness ($\sim$70 nm), Ti-rich alloys the lowest ($\sim$25 nm).

Figure 4.4 shows that the isotherms with a linear (on a log-log plot) relation between the hydrogen pressure and the optical transmission as found in the previous subsection can be reproduced by depositing a Zr-rich MgTiZr alloy. This means that there is indeed a driving force that converts a Zr sandwiched MgTi thin film into a MgTiZr alloy. This raised the question what the driving force for this behavior is. Adding Zr to $Mg_{80}Ti_{20}$ does not result in an alloy with the most optimum linear
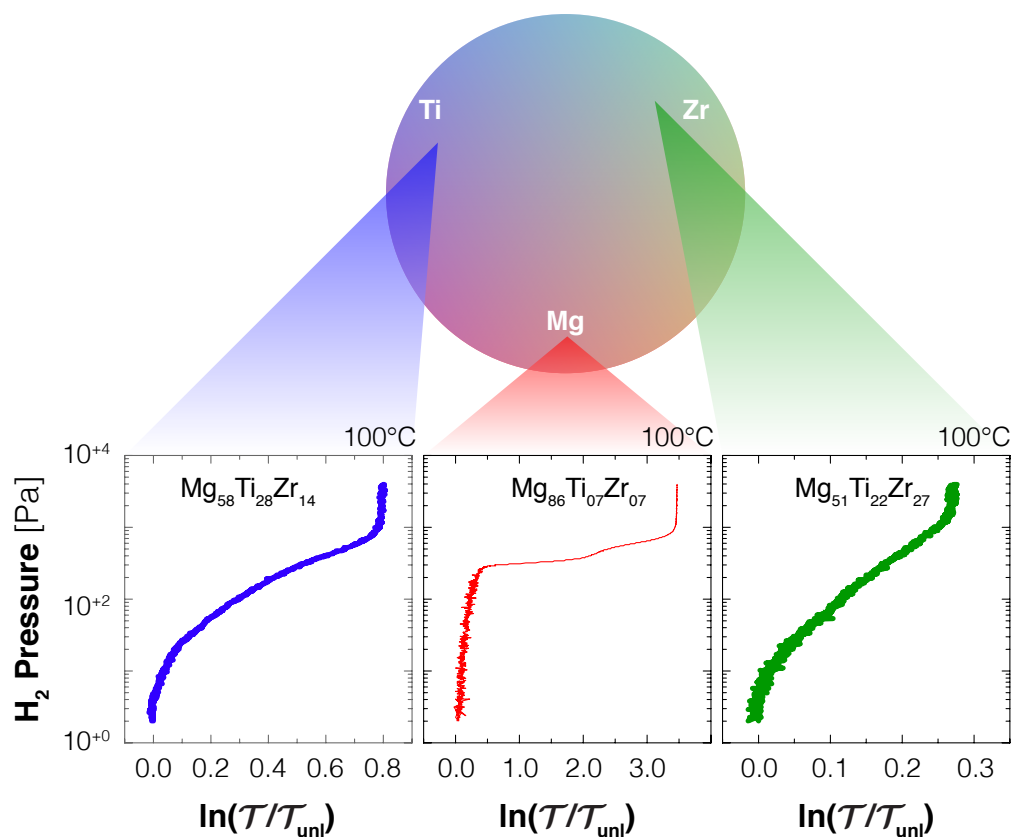
Figure 4.4 | MgTiZr Alloy Isotherms – The pressure-optical transmission-isotherms (PTIs) of three MgTiZr alloys, representing the isotherms of all studied $Mg_y Ti_z Zr_{100-y-z}$ alloys ($0.44 \leq y \leq 0.88$, $0.05 \leq z \leq 0.32$, and $0.05 \leq 100 - y - z \leq 0.32$). The Ti-rich alloys show steep although curved (on a log-log plot) isotherms (left). The Mg-rich alloys show two flat pressure plateaus (middle). The Zr-rich alloys show steep and highly linear (on a log-log plot) isotherms (right).

isotherm. Instead, we find that $Mg_{51}Ti_{22}Zr_{27}$ shows the most linear isotherm spanning the highest pressure range (more than two orders of magnitude). In the next section we show that the small optical contrast can be improved by increasing the layer thickness.

4.2.3 $Mg_{51}Ti_{22}Zr_{27}$: Single Composition Sample

The next step was to demonstrate the full potential of $Mg_{51}Ti_{22}Zr_{27}$ thin films as an optical hydrogen sensing material. To do so, we investigated in detail its optical and structural properties by means of a $Mg_{51}Ti_{22}Zr_{27}$ single composition sample (see sample preparation). Compared to the wafer sample, we increased the thickness from $36\,\mathrm{nm}$ to $80\,\mathrm{nm}$ in order to increase the optical contrast.

First Hydrogenation

Exposing the $Mg_{51}Ti_{22}Zr_{27}$ single composition thin film sample for the first time to an increasing hydrogen pressure, we first observe a gradual increase of the optical transmission (see figure 4.5). This behavior is also observed with the wafer sample. However, instead of a single linear relation we observe above $10^{+2}\,\mathrm{Pa}$ that the pressure-optical transmission-isotherm (PTI) consist of three inclined pressure plateaus, each with a different slope. None of the inclined pressure plateaus are directly related to the hydrogenation of pure Mg, Ti, or Zr. The hydrogenation pressure (at $120°\mathrm{C}$) of $4.0\,\mathrm{Pa}$ for Mg, $10^{-6}\,\mathrm{Pa}$ for Ti, $10^{-13}\,\mathrm{Pa}$ for Zr, are all orders of magnitude lower than the inclined pressure plateaus.[4.25,4.27,4.28]

The presence of pressure plateaus suggest that the as-deposited film is crystalline before hydrogenation and undergoes a phase transition. This is confirmed by x-ray diffraction (see figure 4.6). Here we find that the intensity peaks are not related to the individual elements. Instead, they are related to a MgTiZr alloy. The intensity peaks at $41.44°$ and at $43.68°$ coincides with the respectively (002) and (101) calculated reflections of $Mg_{51}Ti_{22}Zr_{27}$, assuming Vegard's law. Vegard's law states that the lattice parameters of a solid solution is approximately equal to weighted mean of the lattice parameters of the individual elements. In our situation, we used the lattice parameters of pure Mg, Ti, and Zr[4.25,4.27,4.28] while using the atomic fraction ratio as weighted mean:

$$a_{Mg_yTi_zZr_{100-z}} = (1 - \frac{y}{100})a_{Mg} + (1 - \frac{z}{100})a_{Ti} + (1 - \frac{y}{100} - \frac{z}{100})a_{Zr}. \qquad (4.1)$$

Note that the intensity peak at $46.9°$ coincides with the (111) lattice reflection reported for Pd.[4.29]

Consecutive Hydrogenation Cycles

The first exposure to hydrogen alters the structural properties of the $Mg_{51}Ti_{22}Zr_{27}$
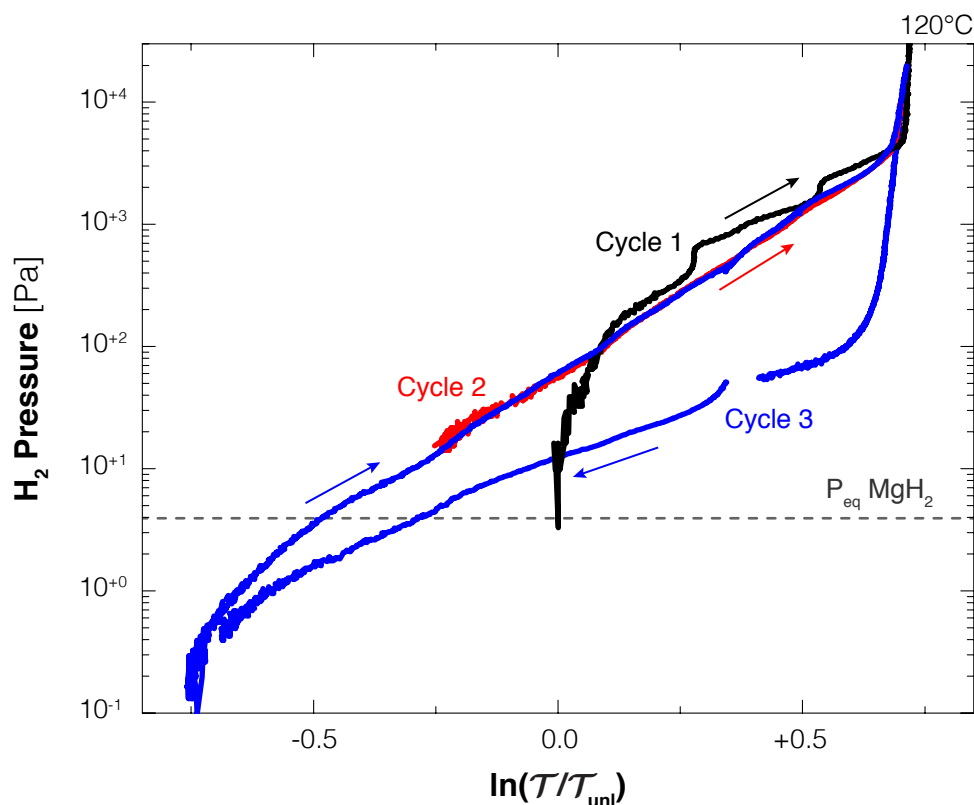
**Figure 4.5 | Mg$_{51}$Ti$_{22}$Zr$_{27}$** – Pressure-optical transmission-isotherms (PTIs) of the first three hydrogenations and the third dehydrogenation of a Mg$_{51}$Ti$_{22}$Zr$_{27}$ thin film (80 nm, single composition) measured at $120°$C. The optical transmission $\mathcal{T}$ of the film is compared to the transmission intensity $\mathcal{T}_{unl}$ of the as-deposited film. The kink and the gap in the third hydrogenation/dehydrogenation isotherm at $\ln\left(\mathcal{T}/\mathcal{T}_{unl}\right) \approx +0.35$ is the result of the change from a 0.1% to a 4% H$_2$/Ar gas-mixture. The dashed line indicates the absorption equilibrium pressure of MgH$_2$ (4.0 Pa).

thin film drastically. The crystalline structure of the as-deposited film reflected by the intensity peaks found at $41.44°$ and at $43.68°$ have vanished. Instead we find an asymmetric and broad intensity peak at $38.8°$. Interestingly, we cannot relate this peak to any reflections of Mg$_{51}$Ti$_{22}$Zr$_{27}$ nor to metallic Ti$_{45}$Zr$_{55}$ (intermediate layers) assuming Vegard's law. The broad width the intensity peak suggests that the crystalline structure consists of a distribution of lattice parameters, while its small intensity (compared to the as-deposited film) suggests that only a small part of the sample is crystalline. Possibly, this crystalline intensity peak is the reflection of TiZrH$_x$. For Ti it is known that it remains (partially) hydrogenated despite being exposed to oxygen.[4.30]

The large structural change of the first exposure to is also observed optically. When we reduce the partial hydrogen pressure from 10^{+4} to 10^{+1} Pa the optical
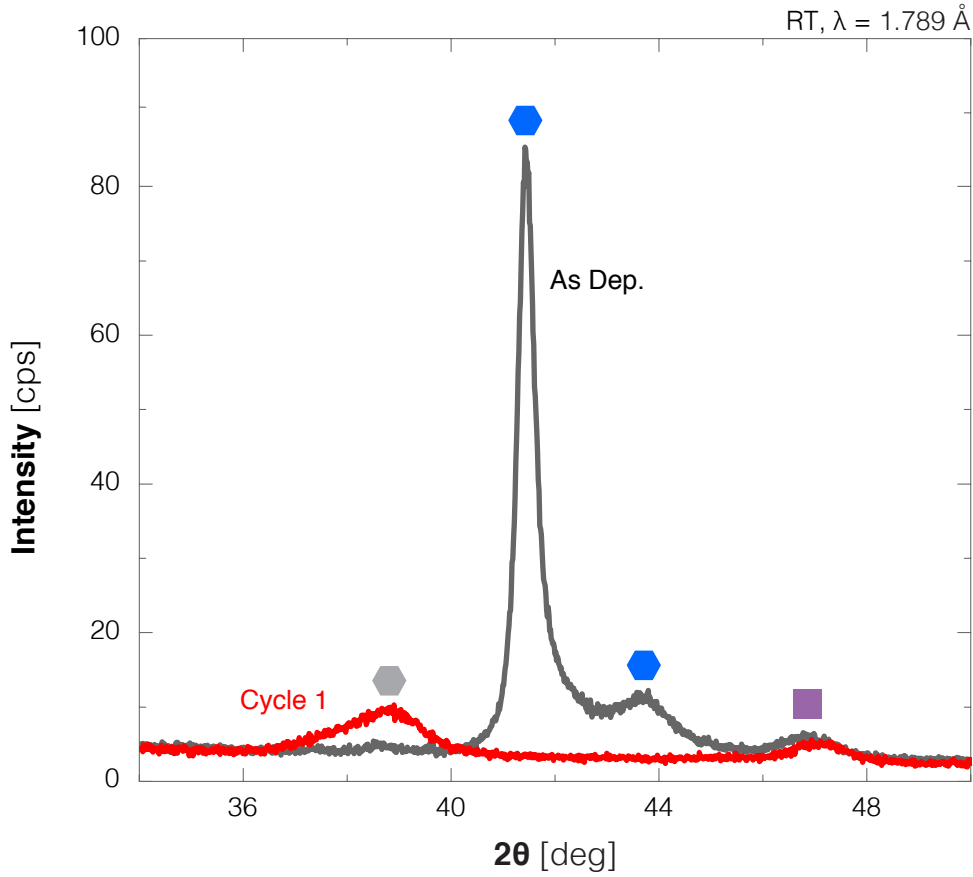
Figure 4.6 | From Crystalline to Amorphous Mg$_{51}$Ti$_{22}$Zr$_{27}$ – Two x-ray diffraction patterns measured before and after the first hydrogenation/dehydrogenation cycle of a Mg$_{51}$Ti$_{22}$Zr$_{27}$ thin film (80 nm, single composition) thin film at room temperature. The symbols above the intensity peaks indicate the corresponding lattice reflections of different compounds. ⬡ at $41.44°$ and at $43.68°$ indicates, respectively, the calculated (101) and (002) lattice reflections of Mg$_{51}$Ti$_{22}$Zr$_{27}$, assuming Vegard's Law. ⬡ at $38.8°$ indicates the lattice reflection of a possible (partially) hydrogenated TiZr alloy, with unknown composition and hydrogen fraction. ◼ at $46.9°$ indicates the (111) lattice reflection of Pd.

transmission of the film does not return to its original level. Instead, we find that tit becomes lower than before hydrogenation: $\ln(\mathcal{T}/\mathcal{T}_{\mathsf{unl}}) = -0.25$ (see figure 4.5). Increasing the pressure again (2nd cycle) we find a steep isotherm with only one slope spanning a pressure range of 2 orders of magnitude.

When we study the optical response of the Mg$_{51}$Ti$_{22}$Zr$_{27}$ thin film at lower pressures we find that the linear relation between hydrogen pressure and the optical transmission spans a larger pressure range of 4 orders of magnitude, starting already from a partial hydrogen pressure of 3×10^{-1} Pa. This is combined with a

large optical transmission change, much larger than observed with the wafer sample (same composition). Between 10^{-1} and 10^{+4} Pa the optical contrast increases from $\ln(\mathcal{T}/\mathcal{T}_{unl}) = -0.75$ to $\ln(\mathcal{T}/\mathcal{T}_{unl}) = +0.70$, while we found with the wafer sample only a transmittance difference of $\ln(\mathcal{T}/\mathcal{T}_{unl}) = +0.27$. This difference cannot only be assigned to the film thickness increase from 36 to 80 nm. Also the increased pressure range (from 2 to 4 orders of magnitude) with respect to the wafer sample is not to be likely an effect of the thickness increase. It therefore must be related to the structural changes within this thicker film.

During the dehydrogenation we find a similar relation between the pressure and the optical transmission, albeit with a different slope (see figure 4.7). This results in an asymmetric hysteresis. While the difference between the hydrogenation and the dehydrogenation isotherm at high optical transmission intensities $(\ln(\mathcal{T}/\mathcal{T}_{unl}) \sim +0.70)$ is almost 2 orders of magnitude, it reduces with decreasing optical transmission intensity. At low optical transmission intensities $(\ln(\mathcal{T}/\mathcal{T}_{unl}) \sim -0.75)$ the hysteresis is not observed anymore.
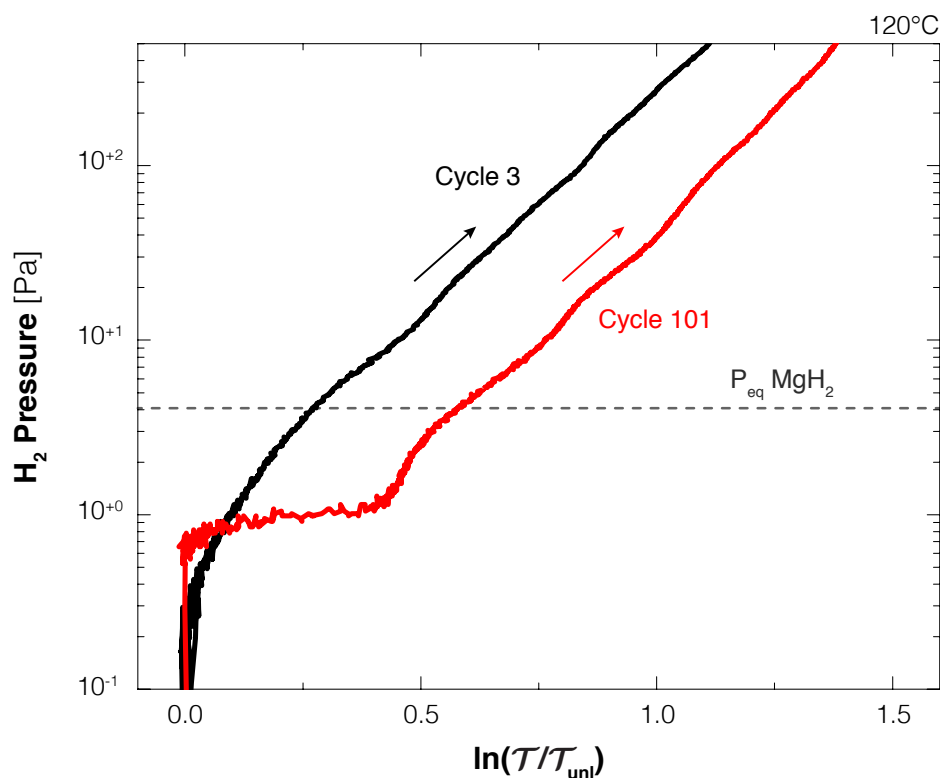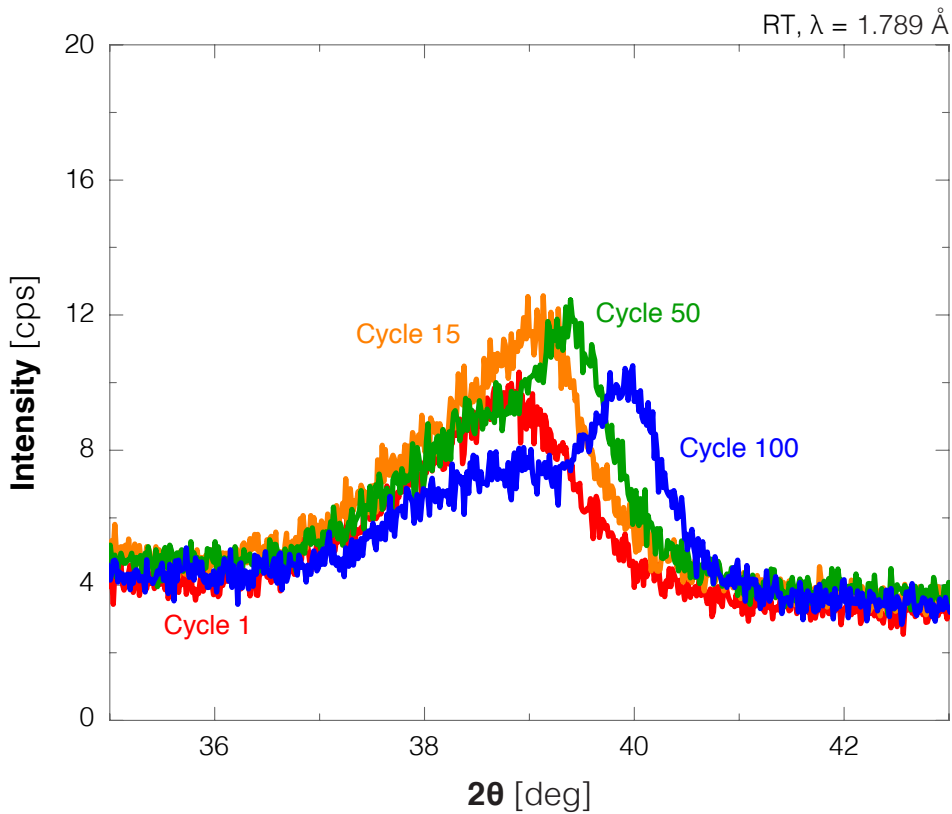

Figure 4.7 | Mg$_{51}$Ti$_{22}$Zr$_{27}$: Optical Instability – Pressure-optical transmission-isotherms (PTIs) of the 3rd (black) and the 101st (red) hydrogenation of a Mg$_{51}$Ti$_{22}$Zr$_{27}$ thin film (80 nm, single composition) thin film. The dashed line indicates the hydrogenation pressure of MgH$_2$ at $120°$C (4.0 Pa).

Stability

Besides the presence of hysteresis, the cycle instability is another downside of Mg_{51}-$Ti_{22}Zr_{27}$ with respect to sensing hydrogen. Optically, after 100 hydrogenation/dehydrogenation cycles the hydrogenation isotherm shows a pressure plateau at approximately $1 \, \mathrm{Pa}$ (see figure 4.7). The width of this pressure plateau $(\ln(\mathcal{T}/\mathcal{T}_{\mathsf{unl}}) \sim +0.5)$ is significant. Since the hydrogenation of Zr and Ti occurs at pressures far below $1 \, \mathrm{Pa}$ at $120°\mathrm{C}$[4.25,4.28] and only induces a small optical transmission change (see chapter 5), it is highly likely that this pressure plateau originates from the hydrogenation of (clamped) Mg. For free-standing thin films of Mg ($10 - 100 \, \mathrm{nm}$, sandwiched between Ti thin layers) a hydrogenation pressure of $4.0 \times 10^{-1} \, \mathrm{Pa}$ at $120°\mathrm{C}$ is reported.[4.11]

Interestingly, after 100 cycles we still observe a linear relation (on a log-log plot) between the hydrogen pressure and the optical transmission above $1 \, \mathrm{Pa}$. This suggests that an amorphous structure is still present, although it is unlikely that its composition equals $Mg_{51}Ti_{22}Zr_{27}$. This is confirmed by structural analysis. While the strong crystalline intensity peaks observed in the as-deposited film are still absent


Figure 4.8 | $Mg_{51}Ti_{22}Zr_{27}$: Structural Instability – X-ray diffraction patterns obtained from a $Mg_{51}Ti_{22}Zr_{27}$ thin film ($80 \, \mathrm{nm}$, single composition) thin film measured after 1 (red), 15 (orange), 50 (green), and 100 (blue) hydrogenation/dehydrogenation cycles, all at room temperature.

after 100 hydrogenation/dehydrogenation cycles, with cycling the broad asymmetric peak found at $2\theta = 38.8°$ broadens towards higher angles (i.e. lower lattice parameters). After 100 cycles a clear symmetric intensity peak is found at $2\theta = 39.9°$, very close to the (002) lattice reflection ($2\theta = 40.2°$) reported for pure Mg. This suggests that within the $Mg_{51}Ti_{22}Zr_{27}$ film hydrogen induces the segregation of crystalline Mg domains within the layer. However, it is not clear whether these domains grow until all Mg atoms is clustered together or that a stable MgTiZr composition (with lower Mg fraction) is formed that would maintain the linear relation between the hydrogen pressure and the optical transmission of the film.

4.2.4 $Mg_{51}Zr_{49}$

The creation of amorphous MgTiZr alloys indicates that Zr, and not Ni, is essential to create steep isotherms. To demonstrate this, we replaced Ti in the MgTiZr thin films by additional Zr to create a $Mg_{51}Zr_{49}$ alloy. In addition, the Ti in the interme-
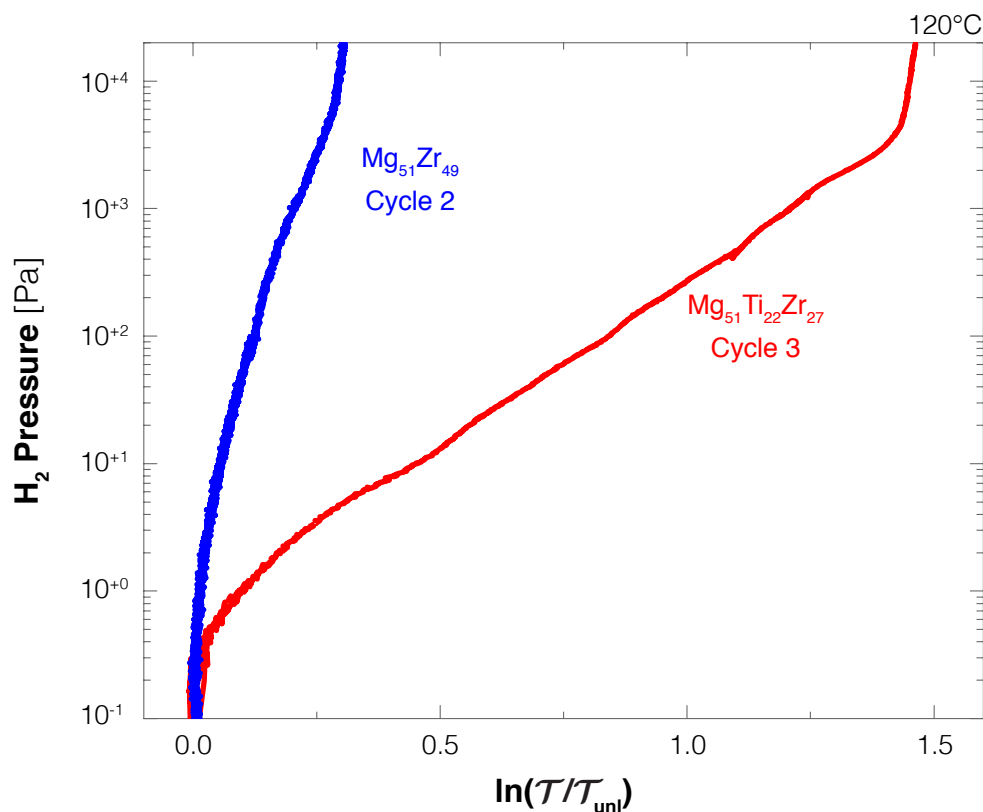
**Figure 4.9 | $Mg_{51}Ti_{22}Zr_{27}$ *versus* $Mg_{51}Zr_{49}$** – Pressure-optical transmission-isotherms (PTIs) of a $Mg_{51}Zr_{49}$ (2nd cycle, blue) and a $Mg_{51}Ti_{22}Zr_{27}$ (3rd cycle, red) thin film measured at $120°C$. Both films have the same layer thicknesses, indicating that Ti has a positive influence on the optical transmission change with hydrogenation of the film.

diate/sandwich layers are also replaced by Zr (see sample preparation). The layer thicknesses are kept constant. In this way we find that the relation between hydrogen pressure and the optical transmission is also with $Mg_{51}Zr_{49}$ (on a log-log plot) highly linear (see figure 4.9). It describes the same pressure range of 4 orders of magnitude (from 3×10^{-1} to $7 \times 10^{+3}$ Pa). The replacement of Ti by Zr reduces, however, the optical transmission change significantly. The optical contrast reduces from $\ln(\mathcal{T}/\mathcal{T}_{unl}) = +1.45$ with $Mg_{51}Ti_{22}Zr_{27}$ to $\ln(\mathcal{T}/\mathcal{T}_{unl}) = +0.3$ with $Mg_{51}Zr_{49}$. Since the layer thickness is kept the same, Lambert-Beer $(\mathcal{T} = \mathcal{T}_0 \exp(-\alpha/d))$ law suggests that Ti has a positive influence on electronic structure (i.e. dielectric function/absorption coefficient) of the alloy. This means that we can use ratio Ti/Zr to alter the optical contrast of the film without changing the pressure range. This is difficult to understand since in both Ti-TiH_2 and Zr-ZrH_2 the optical absorption increases on hydrogenation (see chapter 5).

Sample Preparatie

The $Mg_{51}Zr_{49}$ (left) and the $Mg_{51}Hf_{22}Zr_{27}$ (right) single composition samples are prepared by means of an ultra-high vacuum sputter system (base pressure of 10^{-10} Pa) in 3 μbar Ar (6N). The $Mg_{51}Zr_{49}$ sample consist of a $Mg_{51}Zr_{49}$ layer (80 nm), sandwiched between two Zr layers (10 nm). The $Mg_{51}Hf_{22}Zr_{27}$ sample consist of a $Mg_{51}Hf_{22}Zr_{27}$ layer (80 nm), sandwiched between two $Hf_{45}Zr_{55}$ layers (10 nm). Both samples are covered by a Pd capping layer (10 nm). The atomic fraction ratios are obtained by co-sputtering Ti, Zr, and/or Mg. The layer thicknesses and composition is determined by means of a sputter-rate, obtained from stylus profilometry (DEKTAK) on bulk samples (>400 nm).
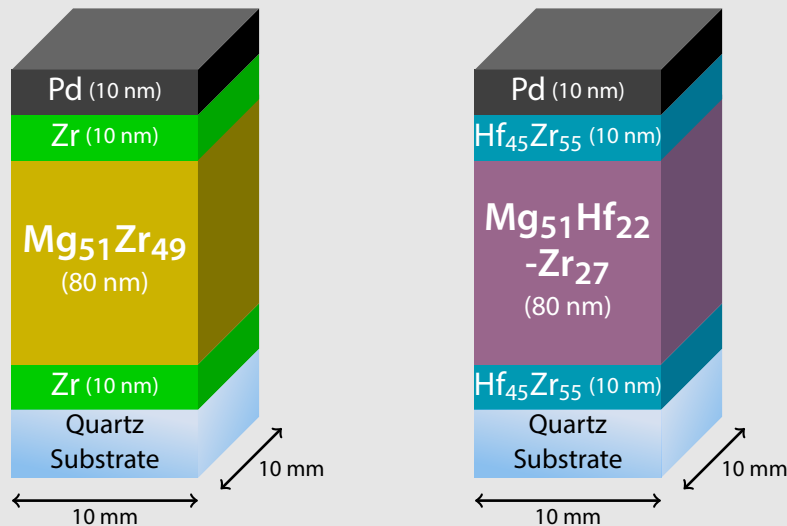
4.2.5   Mg$_{51}$Hf$_{22}$Zr$_{49}$

The results shown above indicate that the addition of Zr to Mg creates an amorphous structure resulting in steep isotherms. The optical contrast of the film can be improved by replacing Zr partially with Ti, without changing the pressure range. Since Zr and Ti are both group IV elements of the periodic table, the question arises *what is the result when we replace Zr in Mg$_{51}$Zr$_{49}$ partially with Hf (also a group IV element)? Will it changes the optical contrast and/or the pressure range?*

Figure 4.10 shows the pressure-optical transmission-isotherm of the fourth hydrogenation of a Mg$_{51}$Hf$_{22}$Zr$_{27}$ thin film $(80\,\mathrm{nm})$ at $120°C$ (see sample configuration). We find that the addition of Hf reduces the optical contrast. While Mg$_{51}$Zr$_{49}$ shows an optical transmission change of $\ln(\mathcal{T}/\mathcal{T}_{\mathsf{unl}}) = +0.3$ between 10^{-1} and 10^{+4} Pa, we find in Mg$_{51}$Hf$_{22}$Zr$_{27}$ an optical transmission change of $\ln(\mathcal{T}/\mathcal{T}_{\mathsf{unl}}) = +0.17$ within the same pressure range. However, the addition of Hf also increases the pressure range to higher pressures. Ignoring the pressure plateau observed at 10^{+4} Pa that is
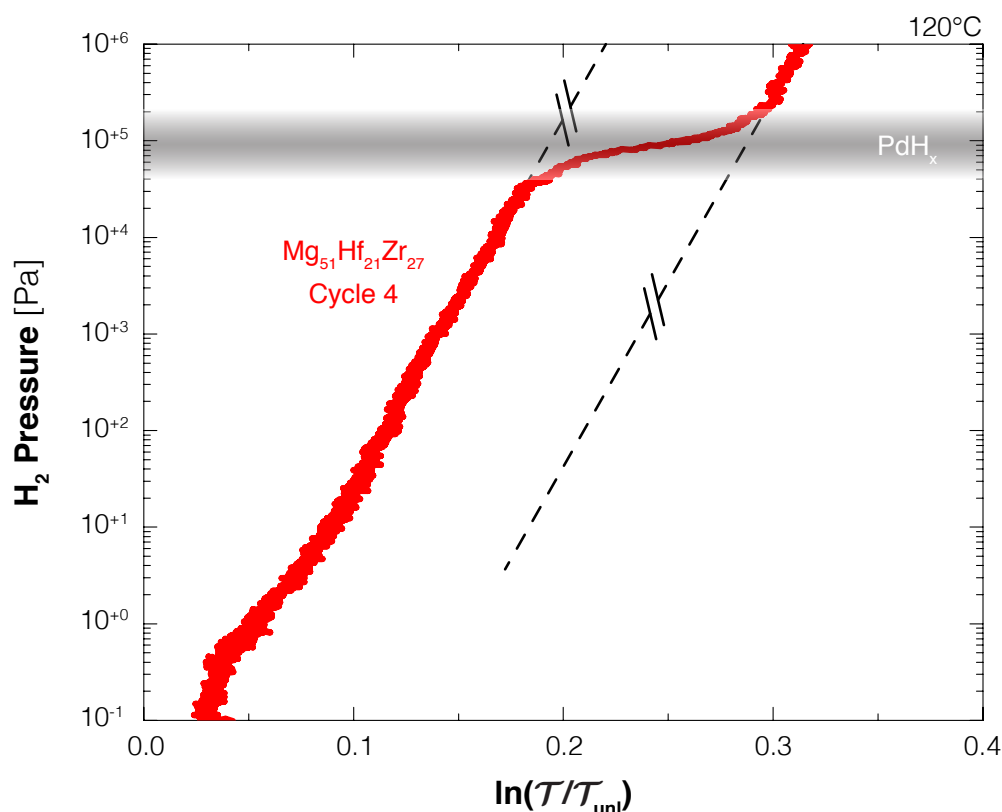
Figure 4.10 | Increased Pressure Range with Mg$_{51}$Hf$_{22}$Zr$_{27}$ – Pressure-optical transmission-isotherm (PTI) of a Mg$_{51}$Hf$_{22}$Zr$_{27}$ (80 nm, 2$^{\text{nd}}$ cycle) thin film measured at $120°C$. The addition of Hf to Mg$_{51}$Zr$_{27}$ results in an increase of the pressure range towards higher pressures, ignoring the pressure plateau at 10^{+5} due to the hydrogenation of the Pd caplayer.

due to the hydrogenation of the Pd caplayer, we observe a linear relation between the hydrogen pressure and the optical transmission from 10^{-1} Pa up to 10^{+6} Pa. The pressure range is likely to be larger, as at 10^{+6} Pa (the upper experimental limit of the hydrogenography setup) we do not observe any indications of a deviation of the linear relation. Further research is necessary to confirm this.

4.3   Discussion

The discovery of amorphous MgZr based alloys shows that not Ni but Zr is essential for creating a Mg-based alloy with steep isotherms. The creation of an amorphous structure suggests the presence of a large distribution of unique MgZr unit cells within the whole film, each with a different hydrogenation energy (i.e. interstitial site energy). However, the question is however *why does Zr creates an amorphous structure and what is the role of hydrogen with this?* Since the first exposure to hydrogen of an as-deposited $Mg_{51}Ti_{22}Zr_{27}$ thin film changes the structure from a crystalline to amorphous one, it is clear that hydrogen plays an essential role in this transformation. Our results on sandwiching a MgTi layer between two Zr-layers suggest that there is a large driving force to mix sufficient hydrogenated Zr to mix with MgTi and make it amorphous. This is difficult to understand since metallic Mg, Ti, and Zr have a positive enthalpy of mixing. Possibly, the MgTiZr alloy consist of a coherently coupled mixture of nano-phases.

Although the addition of small fractions of Zr to Mg may result in a reduction of the MgTi hydrogenation plateau pressure, the crystallinity is not changed. An opposite effect is obtained when alloying Y (yttrium) with low fractions of Zr. In that case the compound remains highly crystalline while the plateau pressure of the $YH_{2.1}$ to $YH_{3.1}$ significantly increases (orders of magnitude) with a small increase of the Zr fraction.[4.31] This suggest that there are many unique interactions between Zr and the metal hydride host. Further study on this is necessary to capture all the unique effects, and to find a possible common origin for these effects.

Equally interesting is the fact that we are able to improve the optical contrast of the MgZr film without changing the pressure range by adding Ti. On the other hand by adding Hf we are able to increase the pressure range by multiple orders of magnitude without any change in optical contrast. Although Ti, Zr, and Hf are group IV elements of the periodic table and all are immiscible with Mg and each other, indicating that the electronic structure of the elements are the same, each element creates a different effect with respect to the optical hydrogen sensing properties. Not only opens this the possibility to optimize the sensing properties by adjusting the atomic fractions of Mg, Hf, Ti, Zr within the alloy, it also led us to study the optical response to hydrogen of these elements alone in much more detail (see chapter 5).

Conclusions

We conclude that it is possible to create amorphous Mg-based alloys with steep isotherms without the presence of Ni. Instead, we find that the presence of Zr is essential. The relation between the hydrogen pressure and the optical transmission of the thin film is strongly related to atomic ratio between Mg and Zr. At low Zr fractions ($< 10\%$) a flat pressure plateau is observed, making these compounds only suitable for being used in a threshold detector, instead of begin used in a hydrogen sensor. At higher Zr fractions steep although curved (on a log-log plot) isotherms are observed. With $Mg_{51}Zr_{49}$ a highly linear relation between the hydrogen pressure and the optical transmission of the film is observed spanning 4 orders of magnitude in pressure, making it very easy to interpolate.

The optical contrast and/or the pressure range can be improved by a partial replacement of Zr by Ti and/or Hf. Adding Ti increases the optical contrast by a factor or 3, while adding Hf increases the pressure range towards higher pressures with at least 2 orders of magnitude. Despite having the same electronic structure, these elements have a different effect on the Mg-Zr host. We finally conclude that amorphous MgZr based alloys show a great potential for being used in an optical hydrogen sensor as they combine the large optical contrast of MgH_x (significantly larger than obtained with Pd-based sensing materials) with a large pressure range (equally large and possibly larger than obtained with Pd-based sensing materials).

References

[4.1] *R.J. Westerwaal, J.S.A. Rooijmans, I. Leclercq, D.G. Gheorge, T. Radeva, L.P.A. Mooij, T. Mak, L. Polak, M. Slaman, and B. Dam.* **Nanostructured Pd-Au based fiber optic sensors for probing hydrogen concentrations in gas mixtures.** International Journal of Hydrogen Energy **38**, 4201 – 4212 (2013).

[4.2] *A. Baldi, G.K. Palsson, M. Gonzalez-Silveira, H. Schreuders, M. Slaman, J.H. Rector, G. Krishnan, B.J. Kooi, G.S. Walker, M.W. Fay, B. Hjorvarsson, R.J. Wijngaarden, B. Dam, and R. Griessen.* **Mg/Ti multilayers: structural and hydrogen absorption properties.** Physical Review B **81**(22), 224203 1 – 10 (2010).

[4.3] *R. Gremaud, D.M. Borsa, A. Borgschulte, P. Mauron, H. Schreuders, J.H. Rector, B. Dam, and R. Griessen.* **Hydrogenography: an optical combinatorial method to find new light-weight hydrogen storage materials.** Advanced Materials **19**, 2813 (2007).

[4.4] *M. Victoria, R.J. Westerwaal, B. Dam, and J.L.M. van Mechelen.* **Amorphous metal-hydrides for optical hydrogen sensing: the effect of adding glassy Ni-Zr to Mg-Ni-H.** ACS Sensors **1**, 222 – 226 (2016).

[4.5] *G.G. Libowitz, H.F. Hayes, and T.R.P. Gibb.* **The system zirconium-nickel and hydrogen.** Journal of Physical Chemistry **62**(1), 76 – 79 (1958).

[4.6] *K. Aoki, M. Kamachi, and M. Tsuyoshi.* **Hydrogen sorption by the metallic-glass Ni64zr36 and by related crystalline compounds.** Scripta Metallurgica **61 – 62**(10), 222 – 226 (1980).

[4.7] *E. Batalla, J.O. Strom-Olsen, Z. Altounian, D. Boothroyd, and R. Harris.* **Hydrogen in amorphous Ni-Zr: pressure concentration isotherms, site occupation, and binding energies.** Journal of Materials Research **1**(6), 765 – 773 (1986).

[4.8] *J.L.M. van Mechelen, B. Noheda, W. Lohstroh, R.J. Westerwaal, J.H. Rector, B. Dam, and R. Griessen.* **Mg-Ni-H films as selective coatings: tunable reflectance by layered hydrogenation.** Applied Physics Letters **84**(18), 3651 – 3653 (2004).

[4.9] *R. Gremaud, J.L.M. van Mechelen, H. Schreuders, M. Slaman, B. Dam, and R. Griessen.* **Structural and optical properties of MgyNi1-yHx gradient thin films in relation to the as-deposited metallic state.** International Journal of Hydrogen Energy **34**(21), 8951 – 8957 (2009).

[4.10] *R. Gremaud, C.P. Broedersz, A. Borgschulte, M.J. van Setten, H. Schreuders, M. Slaman, B. Dam, and R. Griessen.* **Hydrogenography of MgyNi1-yHx gradient thin films: interplay between the thermodynamics and kinetics of hydrogenation.** Acta Materialia **58**, 658 – 668 (2010).

[4.11] *L.P.A. Mooij, A. Baldi, C. Boelsma, K. Shen, M. Wagemaker, Y. Pvak, H. Schreuders, R. Griessen, and B. Dam.* **Interface energy controlled thermodynamics of nanoscale metal hydrides.** Advanced Energy Materials **1**, 754 – 758 (2011).

[4.12] *M.A. Pick, J.W. Davenport, M. Strongin, and G.J. Dienes.* **Enhancement of hydrogen uptake rates for Nb and Ta by thin surface overlayers.** Physical Review Letters **43**(4), 286 – 289 (1979).

[4.13] *J.L. Murray.* **The Ti-Zr (titanium-zirconium) system.** Bulletin of Alloy Phase Diagrams **2**(2), 197 – 201 (1981).

[4.14] *H. Okamoto.* **Mg-Zr (magnesium-zirconium).** Journal of Phase Equilibria and Diffusion **28**(3), 305 – 306 (2007).

[4.15] *P. Vermeulen, R.A.H. Niessen, and P.H.L. Notten.* **Hydrogen storage in metastable MgyTi(1-y) thin films.** Electrochemistry Communications **8**, 27 – 32 (2006).

[4.16] *D.M. Borsa, A. Baldi, M. Pasturel, H. Schreuders, B. Dam, R. Griessen, P. Vermeulen, and P.H.L. Notten.* **Mg-Ti-H thin films for smart solar collectors.** Applied Physics Letters **88**, 241910 (2006).

[4.17] *W.P. Kalisvaart, J.H. Wondergem, F. Bakker, and P.H.L. Notten.* **Mg-Ti based materials for electrochemical hydrogen storage.** Journal of Materials Research **22**, 1640 – 1649 (2007).

[4.18] *D.M. Borsa, R. Gremaud, A. Baldi, H. Schreuders, J.H. Rector, B. Kooi, P. Vermeulen, P.H.L. Notten, B. Dam, and R. Griessen.* **Structural, optical, and electrical properties of MgyTi1-yHx thin films.** Physical Review B **75**, 205408 (2007).

[4.19] *R. Gremaud, A. Baldi, M. Gonzalez-Silveira, B. Dam, and R. Griessen.* **Chemical short-range order and lattice deformations in MgyTi1-yHx thin films probed by hydrogenography.** Physical Review B **77**, 144204 (2008).

[4.20] *R. Gremaud.* **Hydrogenography. A thin film optical combinatorial study of hydrogen storage materials.** Doctoral thesis. VU University Amsterdam. ISBN/EAN 978-90-9023439-7 (2008).

[4.21] *A. Baldi, D.M. Borsa, H. Schreuders, J.H. Rector, T. Atmakidis, M. Bakker, H.A. Zondag, W.G.J. van Helden, B. Dam, and R. Griessen.* **Mg-Ti-H thin films as switchable solar absorbers.** International Journal of Hydrogen Energy **33**, 3188 – 3192 (2008).

[4.22] *A. Baldi, R. Gremaud, D.M. Borsa, C.P. Balde, A.M.J. van der Eerden, G.L. Kruijtzer, P.E. de Jongh, B. Dam, and R. Griessen.* **Nanoscale composition modulations in MgyTi1-yHx thin film alloys for hydrogen storage.** International Journal of Hydrogen Energy **34**, 1450 – 1457 (2009).

[4.23] *A. Anastasopol, T.B. Pfeiffer, J. Middelkoop, U. Lafont, R.J. Canales-Perez, A. Schmidt-Ott, F. Mulder, and S.W.H. Eijt.* **Reduced enthalpy of metal hydride formation for Mg-Ti nanocomposites produced by spark discharge generation.** Journal of the American Chemical Society **135**, (21) 7891 – 7900 (2013).

[4.24] *T. Himitliiska and T. Spassov.* **Hydrogen in amorphous TM33Zr66 (TM = Fe, Co, Ni) alloys.** Journal of Thermal Analysis and Calorimetry **96**(2), 347 – 351 (2009).

[4.25] *E. Zuzek, J.P. Abriata, A. San-Martin, and F.D. Manchester.* **The H-Zr (hydrogen-zirconium) system.** Bulletin of Alloy Phase Diagrams **11**(4), 385 – 395 (1990).

[4.26] *A. Aladjem.* **Zirconium-hydrogen.** Solid State Phenomena **49 – 50**, 281 – 330 (1996).

[4.27] *A. San-Martin and F.D. Manchester.* **The H-Mg (hydrogen-magnesium) system.** Journal of Phase Equilibria **8**(5), 431 – 437 (1987).

[4.28] *A. San-Martin and F.D. Manchester.* **The H-Ti (hydrogen-titanium) system.** Bulletin of Alloy Phase Diagrams **8**(1), 30 – 42 (1987).

[4.29] **JCPDS-International Centre for Diffraction Data** (1998).

[4.30] *L.J. Bannenberg, H. Schreuders, L. van Eijck, J.R. Heringa, N.J. Steinka, R. Dalgliesh, B. Dam, F.M. Mulder, and A.A. van Well.* **Impact of Nanostructuring on the Phase Behavior of Insertion Materials: The Hydrogenation Kinetics of a Magnesium Thin Film.** The Journal of Physical Chemistry C **120**(19), 10185 – 10191 (2016).

[4.31] *P. Ngene, R.J. Westerwaal, and B. Dam.* In private communication (2016).

Chapter 5

Hafnium-Hydride

— an Optical Hydrogen Sensing Material —

5.1 Introduction

In literature, palladium thin films are considered as effective (optical) hydrogen detectors.[5.1 — 5.3] Besides the stability, the drawback of PdH_x is, however, the small solubility range ($\delta x < 0.01$) at room temperature.[5.4] As a result, both the optical response and the hydrogen pressure range is limited.[5.4 — 5.6] The solubility range can be increased by increasing the temperature ($\delta x \approx 0.1$ @ $290°C$), although this limits the applicability of Pd as a hydrogen detection material.

In this chapter we describe the discovery of Pd-capped HfH_x thin films as an (very) effective optical hydrogen detection material. It exhibits a simple relation between the pressure and the optical transmission over a pressure range of at least 6 (possibly 10) orders of magnitude. In addition, it is stable for more than hundred cycles, it can (potentially) detect partial hydrogen pressures of at least 5 orders of magnitude lower than Pd, and no hysteresis is observed. The question arising from this discovery is *why HfH_x is an effective optical hydrogen sensing material with sensing properties that are superior to Pd-based materials?* This question becomes more intriguing knowing that HfH_x show some unique properties:

- the hydrogen solubility range is large ($\delta x \sim 0.65$),
- the system undergoes a phase transition, *and*
- the temperature dependence is highly linear.

Understanding the mechanism becomes even more relevant as we discovered that, besides Pd-capped hafnium, also Pd-capped tantalum shows similar hydrogen detection properties. In addition, we have strong indications that the same is true for Pd-capped titanium and zirconium (see appendix).

To understand why HfH$_x$ (thin film) is an effective (optical) hydrogen detection material we first give a short background of the interaction between hafnium and hydrogen reported for bulk samples (see section 5.2). After this, in section 5.3, we describe the optical interaction between Hf thin films and hydrogen. Here we mainly focus on the optical response in the visible part of the spectrum, although we also observe a response in the near-infrared (>700 nm) and the high-ultraviolet part of the spectrum (<400 nm). In (sub)section 5.3.1 we discuss the sensing properties (stability, resolution, and reproducibility) in more detail.

In section 5.4 we discuss the structural properties of the Pd-capped HfH$_x$ thin films. Here we find that Hf in a thin film configuration behaves differently than in bulk. For example, we find that solubility range of the fcc hydride phase is almost twice as large in thin films than in bulk and also the nature of the fcc-fct phase transition is different. As a result, the pressure range and the optical response of Pd-capped HfH$_x$ thin films are significantly larger than expected from bulk studies. In this section we also the link the structural and the optical properties by means of the dielectric function, calculated for different HfH$_x$ states. In section 5.5 we focus on the origin of the large pressure range, induced by a seemingly unphysical large entropy change. We will investigate this through both the thermodynamics and the optical properties (i.e. the dielectric function). In the appendix we present the results of our study on the sensing properties of some other transition metal-hydrides.

5.2   Background: Phase Behavior of Bulk HfH$_x$

The interaction between hafnium and hydrogen is hardly studied. Most studies are based on bulk (powder and rods) samples and date from more than half a century ago. Recently, the system regained some interest as it was discovered that the hydrides of hafnium are good neutron moderators in neutron reactors.[5.7] However, the properties of HfH$_x$ are only studied at non-ambient conditions (above $250°$C and at pressures from 10^{+2} Pa up to several bars). These studies show that three stable hydride phases can be formed (see figure 5.1):

- the **hcp**–phase, a solution of hydrogen $(x < 0.01)$ in a hexagonal closed-packed (hcp) hafnium structure.

- the **fcc**–phase. HfH$_x$ $(1.62 \leq x \leq 1.78)$ with a face-centered cubic (fcc) structure where the hydrogen atoms occupy the tetrahedral interstitial sites. Within this phase the reported volume expansion is 6% per H.[5.8]

- the **fct**–phase. HfH$_x$ ($1.86 \leq x \leq 2.00$) with a face-centered tetragonal (fct) structure. The fct hydride phase is considered to be a tetragonal distortion of the fcc hydride phase, where the in-plane ($x - y$ axis) lattice parameter a is larger than the off-plane (z axis) lattice parameter c. In HfH$_x$ the ratio c/a reduces to 0.889 within the fct-phase.[5.8]

Note that no data is available for temperatures below $300°$C. Therefore the boundaries of the phases for $T < 300°$C are only given as indications based on high temperature measurements.
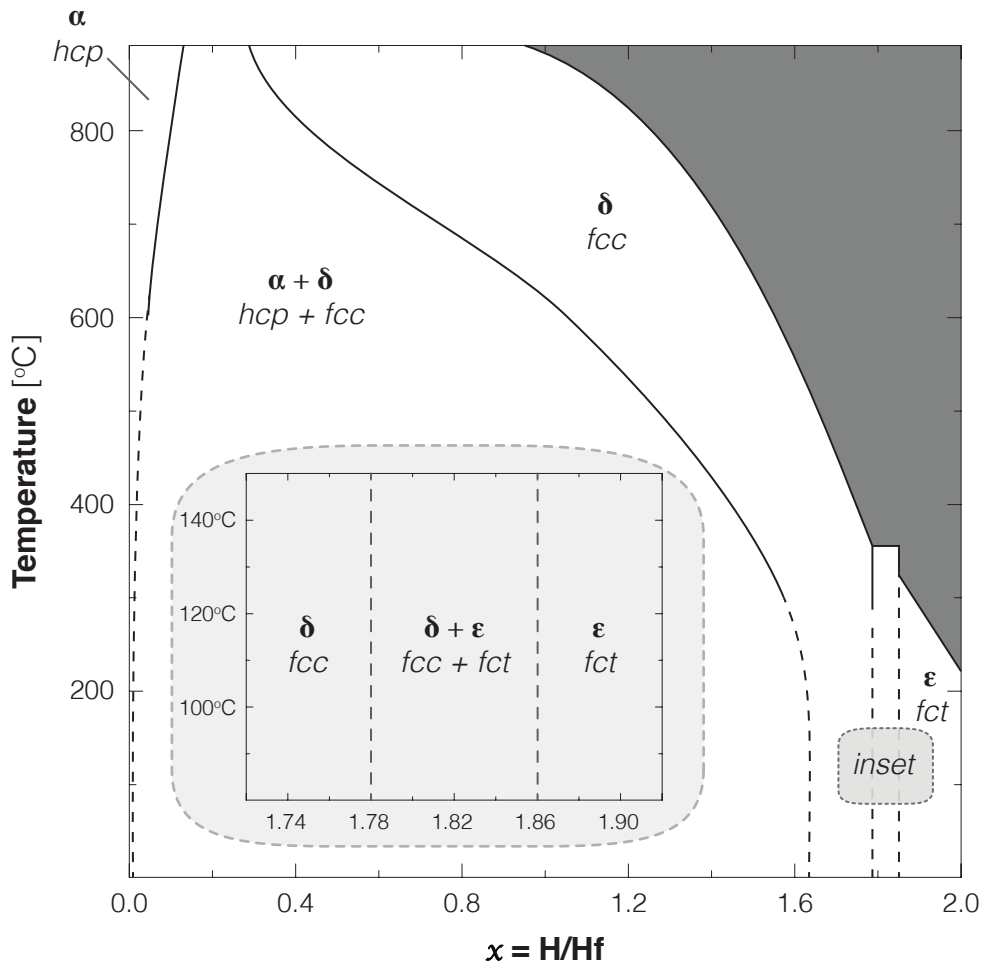
Figure 5.1 | Hafnium-Hydrogen Phase Diagram – Non-isobaric (up to 1 atm.) phase diagram of the hafnium-hydrogen system adapted from Mintz.[5.8] The dashed lines are indications of the phase boundaries based on high temperature data (solid lines). The shaded area indicates the unexplored region where the hydride formation pressure exceeds 1 atm. The inset shows the diagram between $1.72 \leq x \leq 1.92$ between $80 - 150°$C in more detail.

The three phases are connected by two coexistence regions.[5.8 — 5.11] The hcp and the fcc phases coexists between $0.01 \leq x \leq 1.62$. This region is reflected by a pressure plateau in the corresponding pressure-composition-isotherms (PCIs), indicating that the hcp -> fcc phase transition is first order (see figure 5.2a).[5.9] It is remarkable that no hysteresis is observed at this transition. Edwards *et al.* observed at $827°C$ identical absorption and desorption pressure plateaus, although the reversibility has not been studied at lower temperatures.[5.9] Also the transition from the fcc to the fct phase is reported to be first order as a coexistence region of both phases is observed between $1.78 \leq x \leq 1.86$.[5.10,5.11] In contrast to the hcp-fcc transition, this transition is not reflected by a pressure plateau in the corresponding isotherms. Instead, around $x \approx 1.79$ the PCIs show only an inflection that becomes more prominent at lower temperatures (see figure 5.2c).[5.9] This might be due to a critical temperature of the fcc-fct phase transition below $250°C$, although it is not supported by experimental results.

There is no concession about the origin for the fcc-fct phase transition in HfH$_x$. In similar systems, TiH$_x$ and ZrH$_x$, this transition is attributed to be a consequence of the Jahn-Teller effect.[5.12] It describes the splitting of the energy levels of the in-plane and the off-plane interstitial sites within the fcc lattice when a certain amount of interstitial sites are occupied. At a low occupancy rate, there is no energy difference when a hydrogen atom occupy an in-plane or an off-plane interstitial site. As a result, the energies levels of the in-plane and off-plane interstitial sites are the same (the levels are double degenerated). Above a specific occupancy rate it becomes energetically more favorable to occupy the in-plane interstitial sites than the off-plane sites (or vice versa). The result is an asymmetric transformation of the fcc lattice where the in-plane lattice parameter a expands and the off-plane parameter c contracts. However, Quijano *et al.* show by means of band-structure calculations that within the fcc-phase there are no double degenerated energy-levels present.[5.13] As a result the tetragonal distortion cannot be attributed to the Jahn-Teller effect. Instead, a different electron-driven mechanism – a sharp reduction of the number of electron states – is suggested as alternative cause.[5.14,5.15]

Thermodynamics of Bulk Samples

In both the hcp and the fcc phases a simple relation between the applied pressure and the hydrogen fraction in HfH$_x$ (rods) is observed. Within the hcp phase, the system behaves as a *dilute* system and the solubility of hydrogen in the Hf lattice is described by Sieverts' law: $\sqrt{P/P_0} \propto x$ (see figure 5.2b).[5.9] At high temperatures, the hydrogen solubility is relatively large ($\delta x < 0.13$). However, as in PdH$_x$, it strongly reduces with decreasing temperature ($\delta x < 0.04$ @ $595°C$). As a result, the pressure range has a strong temperature component and is limited to a few orders of magni-
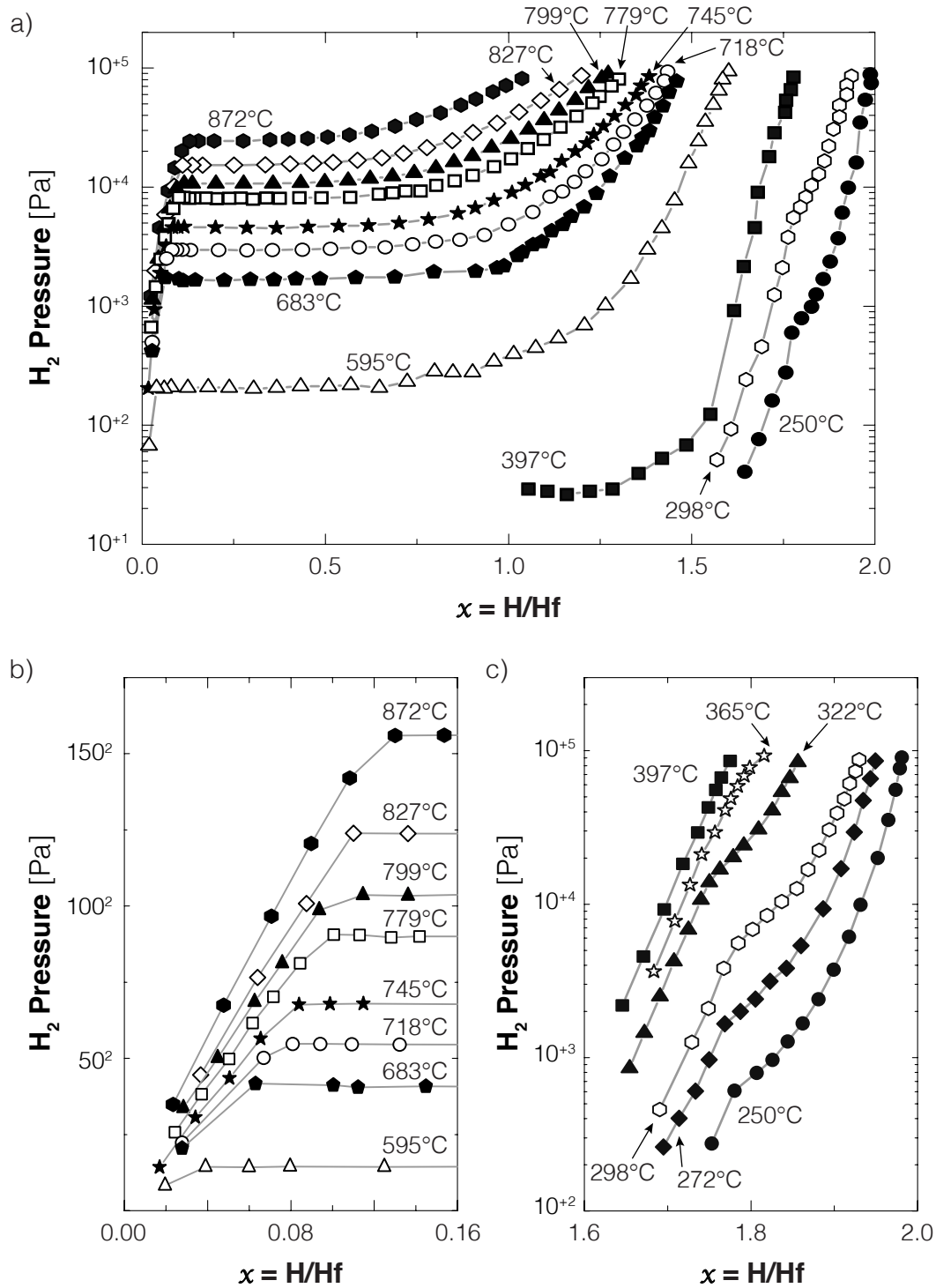
Figure 5.2 | Bulk Pressure-Composition-Isotherms – a) High temperature pressure-composition-isotherms (PCIs) of bulk hafnium $(0.25\ \mathrm{mm\ thick})$ adapted from Edwards *et al.*[5.9] **b)** Close-up of $0.00 < x < 0.16$. Here, the hydrogen pressure is plotted on a square root scale. **c)** Close-up for $1.6 < x < 2.0$. In all figures, the same symbol corresponds to the same temperature.

tude.

Within the fcc phase, Edwards *et al.* suggest that the relation between the applied pressure and the hydrogen fraction at high temperatures ($>250°C$) is described by $\ln\sqrt{P/P_0} \propto \ln(x/(x+1))$.[5.9] However, the isotherms do not exclude a linear relation between P (on a logarithmic scale) and x (see figure 5.2c). The relation spans a hydrogen fraction range of $\delta x = 0.17$ and a pressure range of approximately 4 orders of magnitude. The upper limit of this pressure range is marked by the (small) inflection in the corresponding PCIs, which originates from the transition to the fct phase.[5.9] The measurements performed at both $250°C$ and $827°C$ show no difference between the absorption and desorption PCIs. Remarkable is that in this fcc phase the temperature dependence of the pressure range is highly linear. By means of the Van 't Hoff relation (see equation 5.2) it is found that the enthalpy of the system is constant over the whole compositional range: $\Delta H(x = 1.62) = \Delta H(x = 1.79) = -112.1\,\text{kJ/mol H}_2$.[5.8] This implies that the pressure increase as a function of x should be completely due to the a decrease of the entropy from $\Delta S(x = 1.62) = -82.8\,\text{J/(K mol H}_2)$ to $\Delta S(x = 1.79) = -173\,\text{J/(K mol H}_2)$. The origin of the constant ΔH and the large ΔS change within the fcc phase has not been addressed in literature.[5.8,5.9]

The diffusion of hydrogen within bulk hafnium is slow. The temperature dependence of the hydride front velocity U of two types of bulk samples (a polycrystalline rod and a crystal bar) was studied by Levitin *et al.*[5.16] Despite the difference in grainsize ($10 - 30$ μm for the polycrystalline rod, $1 - 3\,\mu m$ for the crystal bar), between $250 - 450°C$ the hydrogen diffusion in both samples could be described by:

$$\ln(U) = -5.45 \times 10^3/T + 13.45. \tag{5.1}$$

Here U is given in $\mu m/\min$ while this relation is obtained by exposing the samples to a hydrogen pressure of approximately 10^{+5} Pa at temperatures between $250 - 450°C$. At $250°C$, it takes only a few seconds to hydrogenate a $1\,\mu m$ thick sample. The extrapolation to room temperature and to a $40\,\text{nm}$ thin film suggests a response time of $5\,\text{mins}$.

5.3 Optical Properties of HfH$_x$ Thin Films

In this section we discuss the optical interaction between hydrogen and hafnium thin films. Similar to many other thin film metal hydrides (e.g. PdH$_x$, MgH$_x$, and VH$_x$)[5.17 — 5.21] we find that also HfH$_x$ thin films respond optically (in the visual spectrum) when we expose them to hydrogen. We find that the optical response is only partly reversible. Here, the thin films show extraordinary hydrogen detection properties. These properties are discussed in the second part of this second.

Sample Preparation

The hafnium thin films are prepared by means of an ultra-high vacuum sputter system (base pressure of $10^{-10}\,\mathrm{Pa}$) in $3\,\mu\mathrm{bar}$ Ar (6N). For this we used a hafnium target (MaTecK, lot.no. 13012101) with a purity of 99.9%, with zirconium as main impurity. The films are deposited on a $10 \times 10\,\mathrm{mm}^2$ polished quartz substrate and are capped by a palladium layer. The Pd layer protects the Hf layer from oxidation and also improves the hydrogen dissociation process.[5.22] All layers have an uniform thickness, obtained by a rotating substrate during sputtering. The thickness of the hafnium layer is $40\,\mathrm{nm}$, indicated otherwise. This thickness is determined by means of a sputter-rate, obtained by stylus profilometry (DEKTAK) on bulk samples ($>400\,\mathrm{nm}$). The Pd-capping layer has a thickness of $10\,\mathrm{nm}$ and no intermediate layers are used.

Pd (10nm)

Hf
(40 nm)

Quartz
Substrate

10mm

10mm
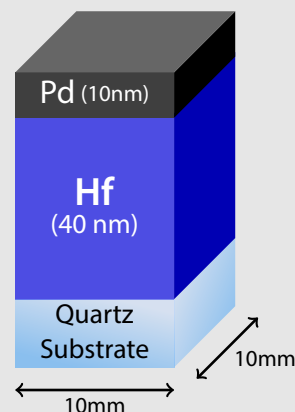
Experimental Details

The optical transmission of the HfH$_x$ thin films is monitored by hydrogenography. Here, the optical transmission of a film is monitored by means of a LED white light source (Philips MR16 MASTER LEDs (10/50W) with a color temperature of $4000\mathrm{K}$ and a beam angle of $24°$) in combination with a 3CCD camera. The transmission intensity change is monitored for only an area that covers $\sim 20\%$ of the total film (centered in the middle). This prevents artificial transmission changes such as the movement of the film due to vibrations or bumps. Due to the homogeneous composition of the film, the transmission data of each individual pixel is averaged in order to increase the signal-to-noise ratio. During a measurement, the hydrogen pressure is gradually (>5 steps per order of magnitude) varied between $10^{-3} - 10^{+4}\,\mathrm{Pa}$. Higher pressures are avoided in order to prevent the hydrogenation of the Pd capping layer ($P_{\mathrm{eq}} \sim 10^{+4}\,\mathrm{Pa}$ @ RT).[5.23,5.24] The pressure range is reached by using different gas mixtures of $1\mathrm{ppm}$, 0.1%, 4%, and 100% H$_2$ in Ar. The gas flow within the setup is set to $20\,\mathrm{sccm}$ during the absorption, and $200\,\mathrm{sccm}$ during the unloading. The pressure steps are increasing/decreasing linearly on a logarithm scale. The hafnium films are usually recorded along with a $30\,\mathrm{nm}$ thick aluminium layer deposited on a $10 \times 10\,\mathrm{mm}^2$ polished quartz substrate. We used this *reference* sample (aluminium is inert to hydrogen at low pressures) to correct for the light fluctuations in the (white) light source.

First Exposure

Exposing an as-deposited, Pd-capped Hf thin (40 nm) film to hydrogen results in a particular optical response of the film (see figure 5.3). From its as-prepared transmission level $\mathcal{T}_{\text{prep}}$, we observe that the transmittance first increases. After 3 hours (at $120°\text{C}$), however, it decreases and reaches a stable level after approximately 6 hours (see figure 5.3a). This optical behavior is partially reversible. Exposing the hydrogenated film first to vacuum $(10^{-4} \text{ Pa } \text{H}_2)$ and later to oxygen $(10^{+5} \text{ Pa } \text{H}_2/\text{Ar})$ results only in an increase of the transmission. The transmission of the film does not return to $\mathcal{T}_{\text{prep}}$. Instead, the transmission converges to the maximum transmission level, defined as $\mathcal{T}_{\text{unl}}$, reached during the first exposure to hydrogen (see figure 5.3a). This non-reversible optical behavior suggests that the film still contains hydrogen while being in the *unloaded* state. This is confirmed by x-ray diffraction and neutron reflectometry, where we observed that this state corresponds to $\text{HfH}_{1.43}$ with a fcc structure (see section 5.4).

The decrease of the transmission when exposing the Pd-film to hydrogen is rare, but not unique. We also observe it when we exposed a Pd-capped titanium or zirconium thin film to hydrogen (see appendix), while it is also been observed using Pd-capped yttrium[5.25 − 5.28] and vanadium[5.21,5.29] thin films. For VH_x thin films it has been shown that the dehydrogenation (within the dihydride state) results in a change of the dielectric function (imaginary part) that causes an increase of the visible light absorption.[5.21]

Sensing Behavior

The negative transmission change upon hydrogenation is not bound to pressures below $<0.4 \text{ Pa}$. Applying higher pressures results in a further decrease of the film transmission. Remarkable, a pressure step results in a very distinct optical transmission change (see figure 5.3b). The levels are not only very stable over time, they are also hysteresis free: applying the same pressure results in the same transmission level, independent of the history of the sample.

In figure 5.4 we plot the optical transmission between $\mathcal{T}_{\text{unl}}$ and $\mathcal{T}_{\text{sat}}$ as a function of the hydrogen pressure at various temperatures, resulting in so-called pressure-(optical) transmission-isotherms (PTIs). Here, each data point obtained from stepwise measurements where, similar to figure 5.3b, the optical transmission of the film is monitored as a function of distinct pressure steps. At each temperature, we find that below $|\ln(\mathcal{T}/\mathcal{T}_{\text{unl}})| < 0.201$ the PTIs describes a linear relation between the transmission and the pressure (both on a logarithmic scale). We define this optical level as $\mathcal{T}_{\text{lin}}$. As the PTIs are shifted in pressure with temperature, the pressure range spanned by the linear relation changes with temperature. At $90°\text{C}$ we find that the linear relation spans a pressure range between $10^{-3} - 1.05 \times 10^{-1} \text{ Pa}$, at $120°\text{C}$ between
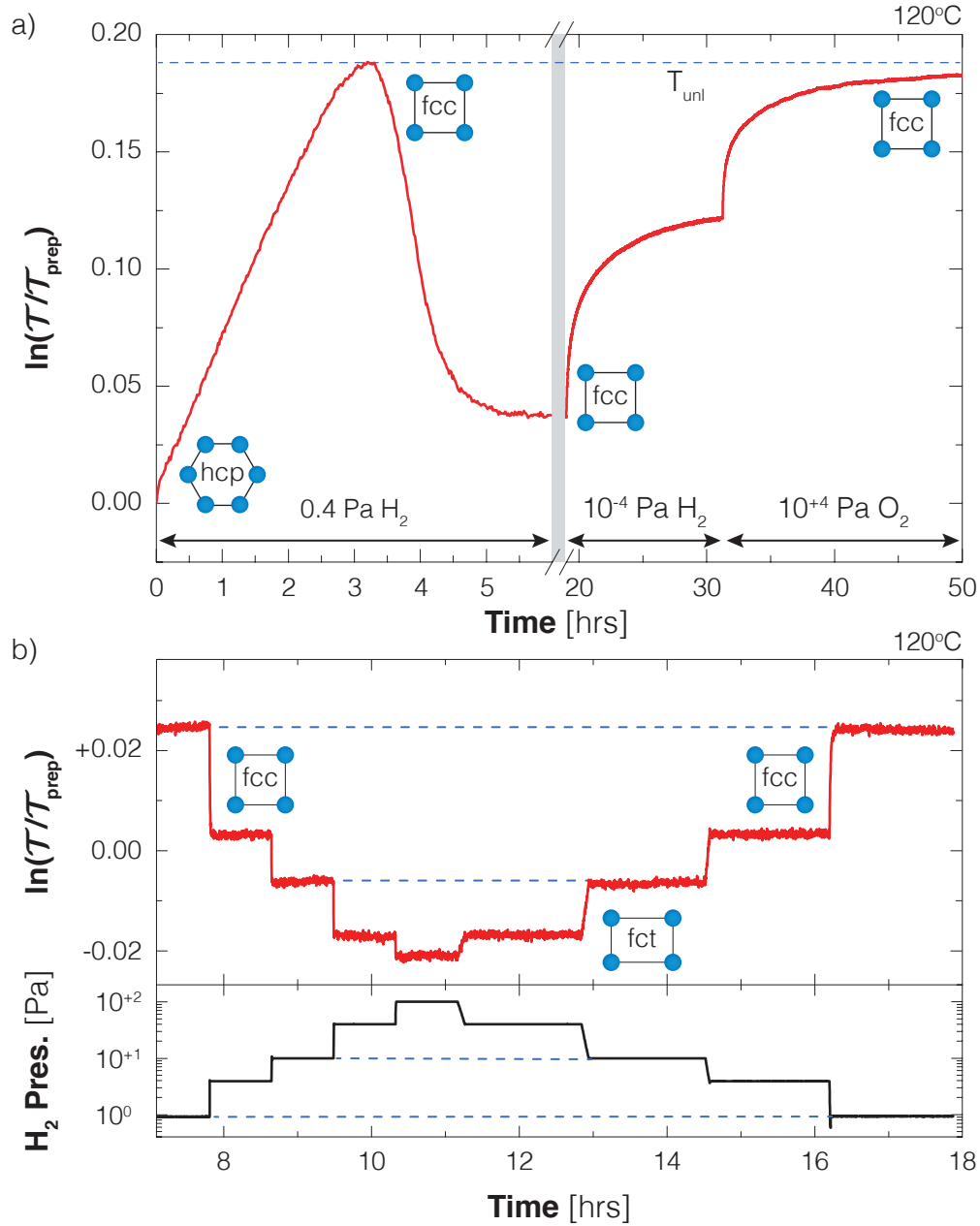
Figure 5.3 | Optical Resonse to Hydrogen – The (white light) optical transmission change $\ln(\mathcal{T}/\mathcal{T}_{\text{prep}})$ of a Pd-capped Hf film $(40\,\text{nm})$ as a function of time, where the film is exposed to different (hydrogen) pressures at $120°\text{C}$. The dashed line in **a)** indicates the maximum reached transmission defined as $\mathcal{T}_{\text{unl}}$, obtained by exposing the sample to oxygen after the hydrogenation. The dashed lines in **b)** indicate the levels of the same transmission and pressure. Indicated in both graphs are symbols that corresponds to the structures of HfH$_x$ obtained by x-ray diffraction (see section 5.4).

10^{-3} – 30 Pa, and at 150°C between 10^{-3} – $2.2 \times 10^{+2}$ Pa. Here, the lower limit of 10^{-3} Pa is defined by the hydrogenography setup, which prevent us from studying the optical properties at equilibrium conditions below 10^{-3} Pa. Nevertheless, the results indicate that pressures below 10^{-3} Pa should in principle be detectable. At this pressure we find that the transmission of the film equals $|\ln(\mathcal{T}/\mathcal{T}_{\mathsf{unl}})| = 0.13$ at 90°C, $|\ln(\mathcal{T}/\mathcal{T}_{\mathsf{unl}})| = 0.095$ at 120°C, and $|\ln(\mathcal{T}/\mathcal{T}_{\mathsf{unl}})| = 0.07$ at 150°C. Extrapolating the linear relations to $|\ln(\mathcal{T}/\mathcal{T}_{\mathsf{unl}})| = 0$ suggest that hydrogen pressures as low as 1.3×10^{-8} Pa at 90°C, 2.8×10^{-7} Pa at 120°C, and 3.7×10^{-6} Pa at 150°C should be observable. We justify these extrapolations by the fact that these pressures coincide with the equilibrium pressure of the hcp $\rightarrow$ fcc phase transition calculated from the bulk thermodynamics ($\Delta S^{\mathsf{bulk}} = -82.7$ J/(K mol H$_2$) and $\Delta H^{\mathsf{bulk}} = -112.1$ kJ/mol H$_2$): 2.2×10^{-8} Pa at 90°C, 4.4×10^{-7} Pa at 120°C, and 5.6×10^{-6} Pa at 150°C.[5.8] The extrapolations are also justified by neutron reflectometry (see section 5.4).

Above $>|\mathcal{T}_{\mathsf{lin}}|$, the optical transmission continues to decrease with increasing pressure. However, the transmission change reduces significantly with increasing pressure (see figure 5.4) and finally saturates towards a level of $|\ln(\mathcal{T}/\mathcal{T}_{\mathsf{unl}})| = 0.218$. We define this *saturated* transmission level by $\mathcal{T}_{\mathsf{sat}}$. Neutron reflectometry shows that the hydrogen fraction is also saturated: $x = 1.98(2)$ (see section 5.4). At 120°C, $\mathcal{T}_{\mathsf{sat}}$ is reached at 10^{+3} Pa. This means that the Hf films show an optical response over a pressure range of at least 6 (experimentally observed) and potential, using the extrapolation, of 10 orders of magnitude. A similar (potential) range is observed at 90°C and 150°C.

Thermodynamics

The PTIs shown in figure 5.4 reveal an uniform shift to higher pressures as a function of the temperature. Note that this is for a hydrogen detection material very desirable, as it allow us to use a simple relation to describe the temperature dependence of the optical response to the pressure. To relate this temperature dependence to the thermodynamics of the system, we use the Van 't Hoff relation:

$$\ln\left(\frac{P}{P_0}\right) = \frac{\Delta H(x)}{R\,T} - \frac{\Delta S(x)}{R}. \tag{5.2}$$

In general, both ΔH and ΔS are a function of the hydrogen fraction x.[5.30] A change in the enthalpy as a function of x should imply that at each temperature the isotherm has a different slope. However, figure 5.4 shows that each isotherm has the same slope. This indicates a constant ΔH, which is confirmed in figure 5.5a. Here, ΔH and ΔS are plotted as a function of $\ln(\mathcal{T}/\mathcal{T}_{\mathsf{unl}})$ (e.g. x). The values of these parameters are obtained by means of the Van 't Hoff construction (see figure 5.5b). Through this construction we find that ΔH equals -117.9 kJ/mol H$_2$, which is close to the
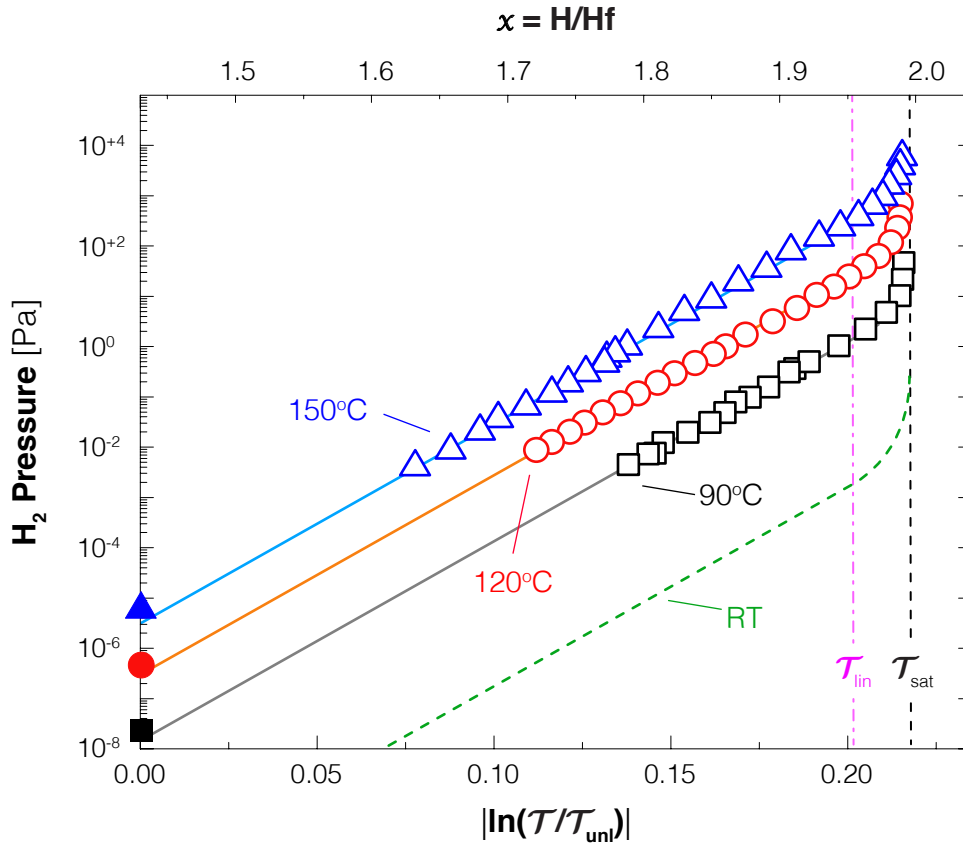
Figure 5.4 | **HfH$_x$:** **Partial Optical Transmission Isotherms** – Partial pressure-optical transmission-isotherms (PTIs) of a Pd-capped hafnium thin film $(40\,\mathrm{nm})$ measured at $90°\mathrm{C}$ (■), $120°\mathrm{C}$ (●), and $150°\mathrm{C}$ (▲), after reaching the *unloaded* state (i.e. $|\ln(\mathcal{T}/\mathcal{T}_{\mathsf{unl}})| = 0$). **Note that $\ln(\mathcal{T}/\mathcal{T}_{\mathsf{unl}})$ is decreasing with increasing hydrogen fraction**. The open symbols are thin film data optically measured by hydrogenography, while the closed symbols are the HfH$_x$ hcp $\rightarrow$ fcc phase transition pressures (equilibrium) for bulk calculated from high temperature data.[5.8] The solid lines are extrapolations of the measured thin film data below $\mathcal{T}_{\mathsf{lin}}$ (magenta dot-dashed line). The black vertical dashed line indicates the saturated transmission level $\mathcal{T}_{\mathsf{sat}}$. The green dashed line indicates the excepted behavior at room temperature, predicted from the temperature data through the thermodynamics. The hydrogen fraction $x = $ H/Hf as a function of the pressure and $|\ln(\mathcal{T}/\mathcal{T}_{\mathsf{unl}})|$ is obtained by neutron reflectometry (see section 5.4).
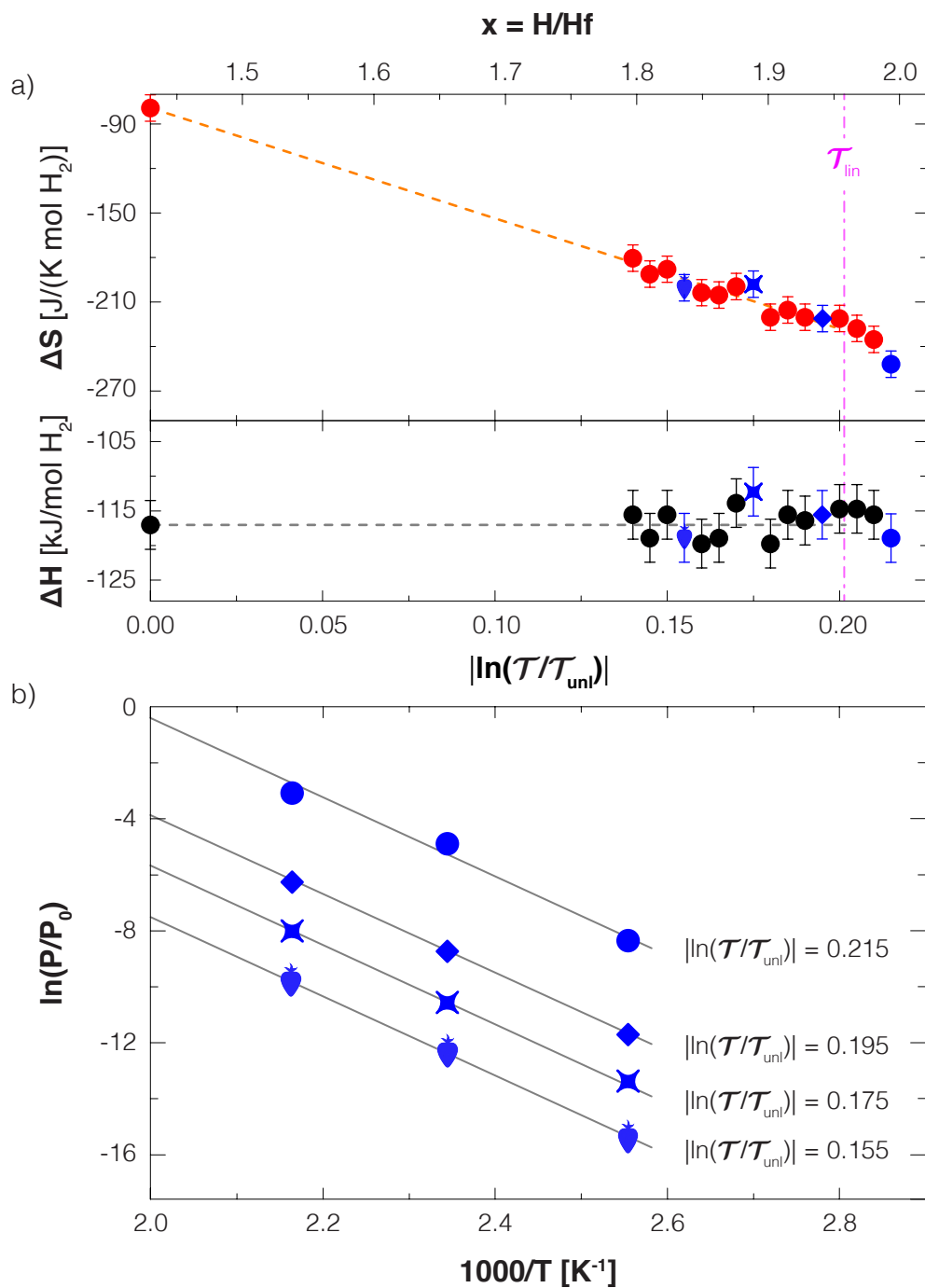
Figure 5.5 | Thermodynamics of HfH$_x$ Thin Films – a) The thermodynamical parameters ΔH and ΔS as a function of the optical transmission $|\ln(\mathcal{T}/\mathcal{T}_{unl})|$ (bottom) and hydrogen fraction x (top) obtained from the optical transmission isotherms at $90°C$, $120°C$, and $120°C$ through the Van 't Hoff construction. **b)** The Van 't Hoff construction for $|\ln(\mathcal{T}/\mathcal{T}_{unl})| = 0.155$ (●), $|\ln(\mathcal{T}/\mathcal{T}_{unl})| = 0.175$ (✹), $|\ln(\mathcal{T}/\mathcal{T}_{unl})| = 0.195$ (◆), and $|\ln(\mathcal{T}/\mathcal{T}_{unl})| = 0.215$ (●). The solid lines represents the fit of the Van 't Hoff relation (equation 5.2).

reported value ($\Delta H^{\mathsf{bulk}} = -112.1 \ \mathrm{kJ/mol} \ \mathrm{H}_2$) for HfH_x hcp $\rightarrow$ fcc phase transition obtained from bulk samples at high temperatures.[5.8]

Given the fact that the enthalpy remains constant, we conclude that the pressure range is fully determined by the entropy. As shown in figure 5.5a, we find that the experimentally determined entropy decreases from $\Delta S(\mathcal{T} = \mathcal{T}_{\mathsf{unl}}) = -79.9 \ \mathrm{J/(K\ mol}$ $\mathrm{H}_2)$ to $\Delta S(\mathcal{T} = \mathcal{T}_{\mathsf{lin}}) = -228.0 \ \mathrm{J/(K\ mol\ H}_2)$ and to $\Delta S(\mathcal{T} = \mathcal{T}_{\mathsf{sat}}) = -251.7 \ \mathrm{J/(K\ mol}$ $\mathrm{H}_2)$. This entropy change is anomalous large, and significant larger than reported for bulk: from $\Delta S(x = 1.62) = -82.8 \ \mathrm{J/(K\ mol\ H}_2)$ to $\Delta S(x = 1.79) = -173 \ \mathrm{J/(K}$ $\mathrm{mol\ H}_2)$.[5.8] Consequently, the pressure range in thin films (potential 10 orders of magnitude) is significantly larger than in bulk (5 orders of magnitude). In section 5.5 we discuss the origin of this large entropy change in more detail.

Wavelength Dependence

Up to now we only discussed optical properties of hafnium films with respect to white light. However, the optical properties depend on the wavelength. Using light of the appropriate wavelength may result in a better optical contrast improving the *resolution* (i.e. the minimum pressure change that can be detected optically). This originates from the observation that the transmission of an *as-prepared* film is the most prominent in the red-part of the visual spectrum, while during hydrogenation the transmission the film becomes more color neutral (see figure 5.6).

To investigate the wavelength dependence of the transmission on hydrogenation we studied a Pd-capped hafnium film ($40 \ \mathrm{nm}$) at $120°\mathrm{C}$ by means of hydrogen-spectography, an extension of hydrogenography that enables to measure the transmittance of the film as a function of time for a broad range of wavelengths. Figure 5.7
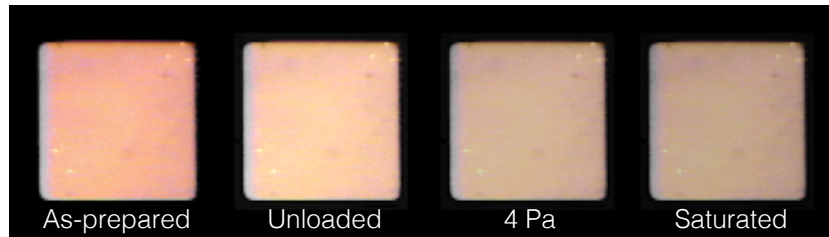
Figure 5.6 | Film Color Change – True color images of the same sample taken at different stages of hydrogenation at $120°\mathrm{C}$. The *as-prepared* state corresponds to the as-deposited sample, the *unloaded* state to the moment the (white light) transmission of the film reaches its maximum, the *4 Pa* state to the equilibrium state of the film reached after the exposure to a $4 \ \mathrm{Pa}$ partial hydrogen pressure, and the *saturated* state to the equilibrium state of the film after an exposure to a partial hydrogen pressure of $10^{+3} \ \mathrm{Pa}$.
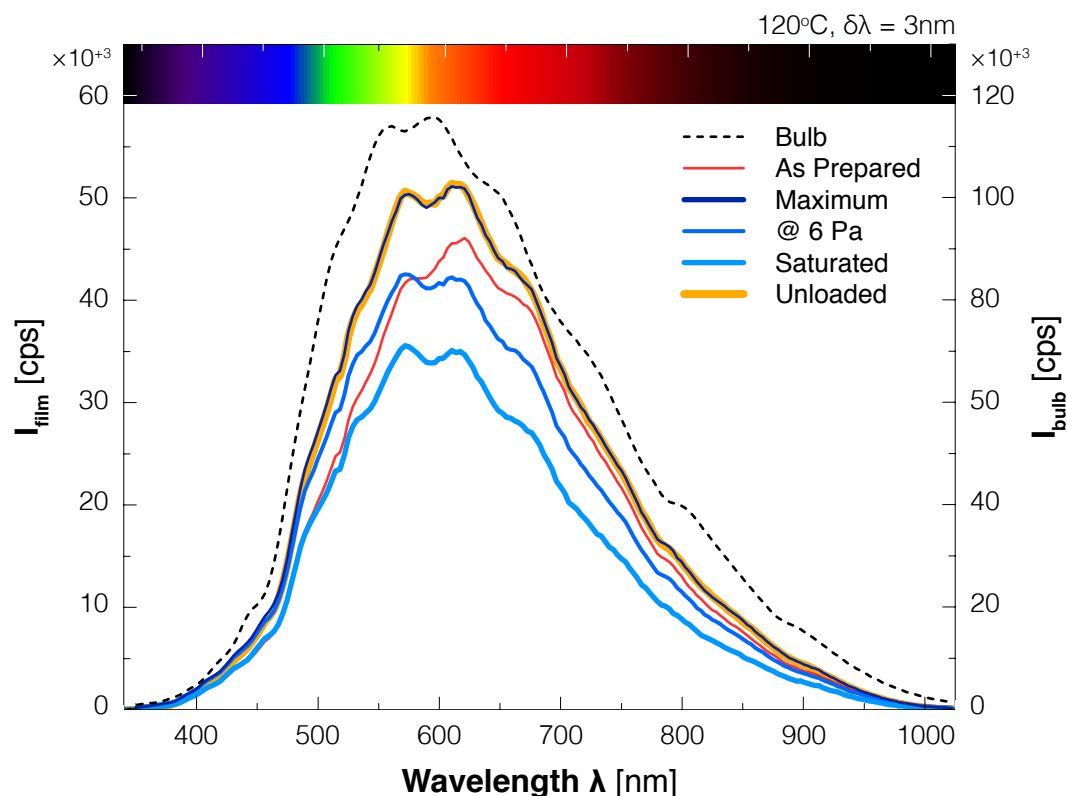
Figure 5.7 | Visual Spectrum – Transmission intensity (counts per second) of a Pd-capped $40\,\mathrm{nm}$ hafnium film as a function of the wavelength at different stages of hydrogenation measured at $120°\mathrm{C}$. The *as-prepared* state (red thin line) corresponds to the film where the film has not been exposed to hydrogen. The *maximum* state (thin darkblue line) corresponds to the moment where the film transmission reached its maximum value, reached after approximately 2 hours of exposure to a partial hydrogen pressure of $6\,\mathrm{Pa}$. The *@ 6 Pa* state (blue line, medium thickness) is an intermediate state, corresponding to state where the transmission reached a stable level when being exposed to a partial hydrogen pressure of $6\,\mathrm{Pa}$ (after approximately 4 hours). The *saturated* state (thick light-blue line) corresponds to the moment when the transmission is stabilized after an exposure to a partial hydrogen pressure of $10^{+3}\,\mathrm{Pa}$. The *unloaded* state (very thick orange line) corresponds to the moment when the film has been exposed to oxygen for 3 days. As reference, the transmission intensity of the halogen bulb (using the same pathway, including the quartz substrate although without Hf and Pd layers) is included (dashed black line). The resolution of the spectra is (after averaging) $\delta\lambda = 3\,\mathrm{nm}$. The left vertical axis corresponds to all film intensities, the left vertical axis to the intensity of the bulb.

shows the transmission of the film as a function of the wavelength at different hydrogenation stages of the film. The behavior of the transmission is similar for all wavelengths: when exposing the film to hydrogen (6 Pa) the transmission first increases from the *as-prepared* state, and then decreases before it reaches a stable level. At each wavelength, an increase to the saturation pressure (10^{+3} Pa) results in a further decrease of the transmission. As observed with white light, exposing the film to oxygen results only in an increase of the transmission for each wavelength. After thee days of exposure to oxygen the spectrum of the film is identical to the spectrum of the film when the transmission reached its *maximum* during the hydrogenation process (see figure 5.7).

The observed true-color change during hydrogenation shown in figure 5.6 is in accordance with the spectra shown in figure 5.7. The red transmission color of the *as-prepared* film is reflected by an intensity peak around 650 nm. At the other stages we observe a second intensity peak (with the same intensity) around 580 nm. The result is a *peak broadening* that is reflected by the shift towards a more neutral color of the film (see figure 5.7). However, the largest transmission change between the *as-prepared* and *unloaded* state (i.e. where the transmission reaches its maximum) of the film is not observed at 580 nm. Instead, we find that the transmission change in the blue part of the visual spectrum is much larger: $\ln(\mathcal{T}_{\text{unl}}/\mathcal{T}_{\text{prep}}) = +0.38$ @ 450 nm *vs.* $\ln(\mathcal{T}_{\text{unl}}/\mathcal{T}_{\text{prep}}) = +0.18$ @ 580 nm. This is visualized in figure 5.8 where, for each wavelength between $350 - 1020 \text{ nm}$, the change of the film transmission $\ln(\mathcal{T}/\mathcal{T}_{\text{prep}})$ is plotted as a function of time. Here we exposed a freshly as-deposited film to two different partial hydrogen pressures: to 6 Pa for the first 5 hours and then to 10^{+3} Pa (saturation pressure) for a few minutes.

While the transition from the *as-prepared* to the *unloaded* state is mainly visible in the blue part of the visual spectrum and hardly visible in the red-part of the visual spectrum $(\ln(\mathcal{T}_{\text{unl}}/\mathcal{T}_{\text{prep}}) = +0.06$ @ $700 \text{ nm})$, the opposite is true for the transition from the *unloaded* to the *saturated* state. Here we find the largest transmission change $(\ln(\mathcal{T}_{\text{sat}}/\mathcal{T}_{\text{unl}}) = -0.32$ @ $700 \text{ nm})$ in the red/infrared-part of the spectrum while in the blue part of the spectrum the transmission hardly changes $(\ln(\mathcal{T}_{\text{sat}}/\mathcal{T}_{\text{unl}}) = -0.13$ @ $450 \text{ nm})$. The largest optical contrast between the *unloaded* to the *saturated* state can therefore be obtained by using monochromatic light with a wavelength around 700 nm. Below we discuss the effect of using monochromatic light on the sensing properties of HfH$_x$ in more detail.
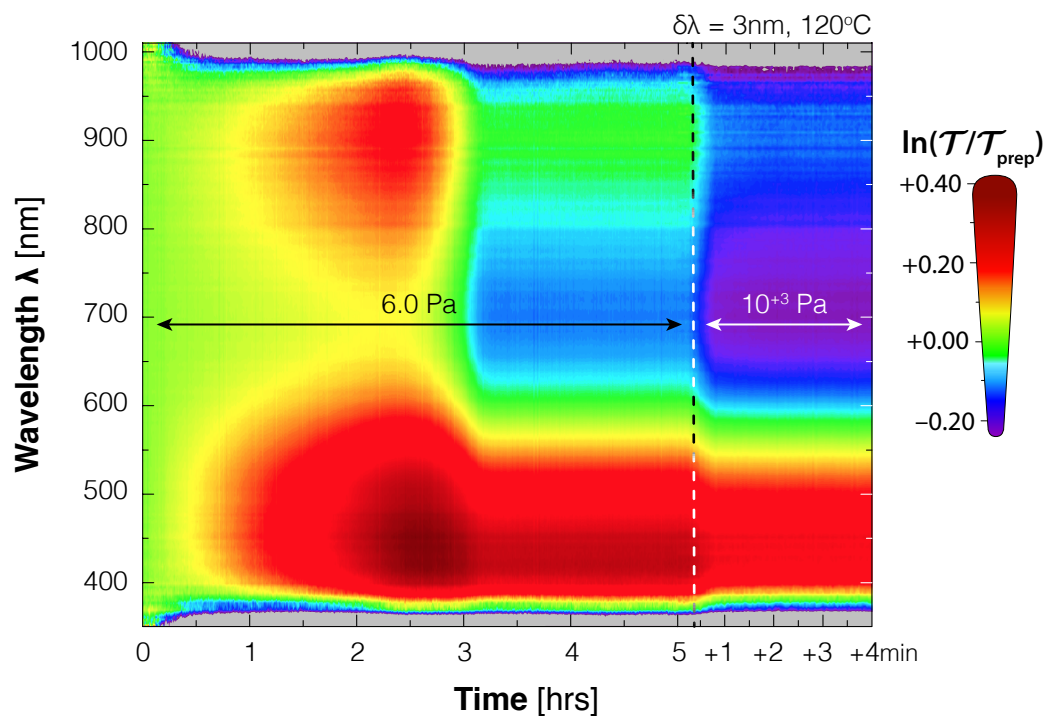
Figure 5.8 | Wavelength Dependence of Transmission Change – Contour plot of the transmission intensity change of a Pd-capped Hf thin film (40 nm) as a function of time for wavelengths between $350 - 1020$ nm (with spatial resolution of $\delta\lambda = 3$ nm). Over time, the film is exposed to two different partial hydrogen pressures at $120°$C: to 6 Pa for the first 5 hours and then to 10^{+3} Pa (saturation pressure) for a few minutes. The spectra are obtained by hydrogenospectrography, with a time-interval of 1 min for the first 5 hours and a time-interval of 5 seconds for the last few minutes.

5.3.1   Sensing Properties

The pressure range of at least 6 and possibly 10 orders of magnitude, the absence of hysteresis, and the linear temperature dependent pressure range make (Pd-capped) HfH$_x$ a very interesting optical hydrogen sensing material. To demonstrate its true potential, we also investigated i) the optical sensitivity, ii) the response time, iii) the optical resolution, and iv) the stability of the films during (de)hydrogenation. Note that we define the optical *resolution* as the smallest possible pressure step that can be detected optically and the optical *sensitivity* as the minimum hydrogen pressure that may be detected optically.

Optical Sensitivity

The optical sensitivity of the films is very high. Although not directly observed, the isotherms shown in figure 5.4 indicate that at $120°$C pressures as low as 2.8×10^{-7} Pa should result in an optical response. Using the corresponding thermodynamics, we predict that at room temperature a hydrogen pressure as low as 2×10^{-11} Pa should be observable. This is at least a factor 10^5 lower than observed with PdH$_x$.[5.3] Since we cannot control pressures below $<10^{-3}$ Pa improving the hydrogenography setup and/or using a different technique is necessary to confirm this low pressure threshold.

Response Time

Our preliminary studies show that the response time of the film is significant longer than that of PdH$_x$. While PdH$_x$ responds within a few seconds to a pressure change within the whole pressure range, the response time of Pd-capped HfH$_x$ thin films varies from a few second to several hours, depending on both the temperature and pressure. Above 1 Pa at $120°$C we find a response time of a few seconds to an increasing pressure step and of half a minute to a decreasing pressure step (see figure 5.9a). Note that the actual response time is probably shorter as it equals the temporal resolution of the pressure step.

At low pressures the response time is significant longer that the temporal resolution of a pressure. As shown in figure 5.9b, at pressures close to 10^{-2} Pa the response time is in the order of minutes to hours. In addition, we observe a delay as the film responds optically only several minutes after the start of the pressure change. The slow kinetics at these low pressures is also reflected when we expose the film in the *unloaded* state to a pressure of 0.4 Pa at $120°$C. It takes roughly 3 hours to reach equilibrium (see figure 5.3). This time is significantly larger at room temperature (see figure 5.10). When we expose the film to a pressure of 1 Pa, it takes roughly 4.2 hrs to obtain 90% of the optical change.
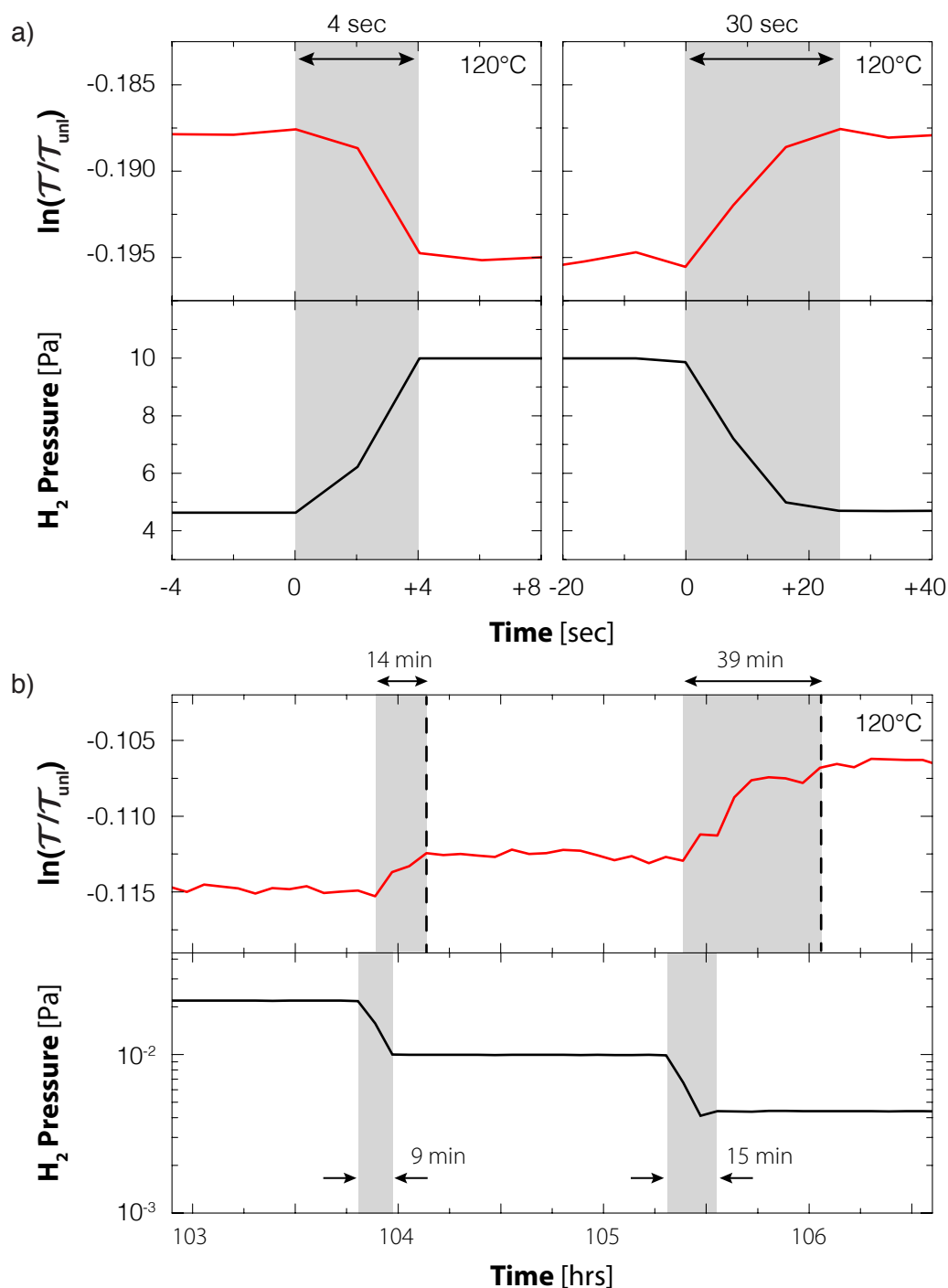
Figure 5.9 | HfH$_x$: Pressure Dependence Kinetics – The optical response of a Pd-capped hafnium film (40 nm) to a pressure change at **a)** high pressures $(4 \leftrightarrow 10\text{ Pa})$ and at **b)** low pressures $(10^{-1} \to 10^{-3}\text{ Pa})$ measured by hydrogenography at $120°\text{C}$.
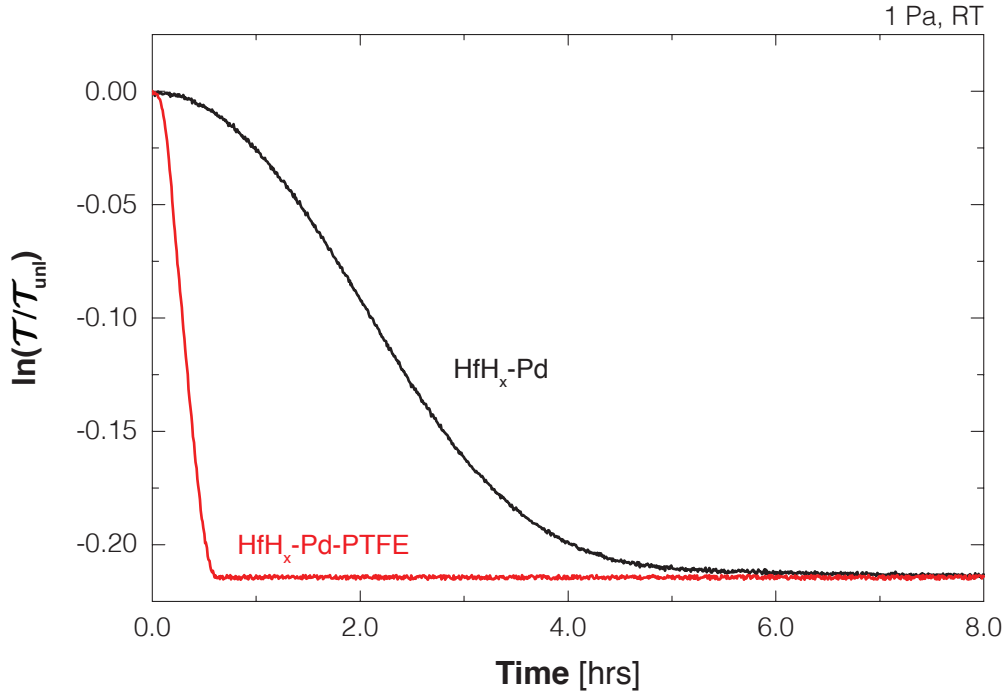
Figure 5.10 | HfH$_x$: Response @ RT – The optical response of two Pd-capped Hf films $(40\,\text{nm})$ to a constant hydrogen pressure of $1\,\text{Pa}$ at room temperature. One film is capped by an additional $30\,\text{nm}$ PTFE layer (red). The optical response of both films is recorded simultaneously with hydrogenography and both films have the same history with respect to hydrogen/oxygen exposures.

To understand the slow response at low pressures and/or at low temperatures, we focus on three processes that defines the response time in the Hf thin films. As illustrated in figure 5.11, these processes are i) the dissociation of the hydrogen molecule at the Pd surface, ii) the (atomic) hydrogen diffusion in the Pd-capping layer, and iii) the (atomic) hydrogen diffusion in the Hf layer. We exclude the hydrogen diffusion in the Pd-capping layer as limiting process, since hydrogen diffuses within $1\,\text{msec}$ through the $10\,\text{nm}$ thick Pd-caplayer (using the diffusion coefficient of $10^{-5}\,\text{cm}^2/\text{sec}$).[5.31] According to bulk data, the hydrogen diffusion in the Hf layer cannot be ignored although alone it cannot not explain the long response times observed. While we observe that it takes multiple hours to hydrogenate a Pd-capped Hf thin film
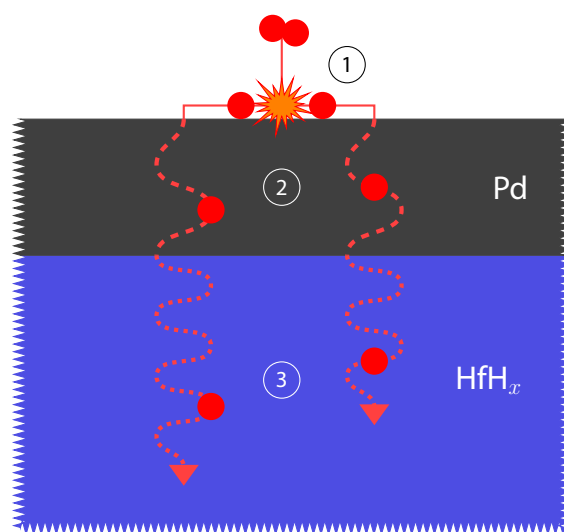
**Figure 5.11 |** **Processes that defines the Response Time** – Illustration of the three processes that determines the response time of a Pd-capped hafnium film: ① the dissociation of the hydrogen molecule at the Pd surface; ② the (atomic) hydrogen diffusion in the Pd-capping layer; ③ the (atomic) hydrogen diffusion in the Hf layer. We find that processes ① and ③ limit the response time of Pd-capped Hf thin films. We can reduce the effect of process ① by adding a PTFE coating-layer.

when exposing it to a hydrogen pressure of $1\,\mathrm{Pa}$ at room temperature, equation 5.1 indicates that the same film should be fully hydrogenated in approximately 5 minutes when we expose it to a hydrogen pressure of $10^{+5}\,\mathrm{Pa}$ at room temperature. Despite the pressure difference of 4 orders of magnitude, $1\,\mathrm{Pa}$ is multiple orders of magnitude above the saturation pressure at room temperature. We therefore expect only an increase of the response time in the order of minutes, not hours.

At room temperature, we find that the response time can significantly be reduced by coating the Pd-caplayer with a thin layer of PTFE $(30\,\mathrm{nm})$. In this way the time to obtain 90% of the optical change reduces from $4.2\,\mathrm{hrs}$ to $32\,\mathrm{min}$. This behavior is in agreement with previous studies that show that dissociative absorption of hydrogen at room temperature can be improved by surface coatings.[5.32 — 5.34] Apparently, the PFTE coating keeps the Pd-surface sites available by adsorbents such as H_2O. Therefore a further reduction of the response time at both room and elevated may be achieved by increasing the dissociative absorption process at the Pd surface through optimizing the coating (e.g. different thickness, other materials). However, this is beyond the scope of this thesis.
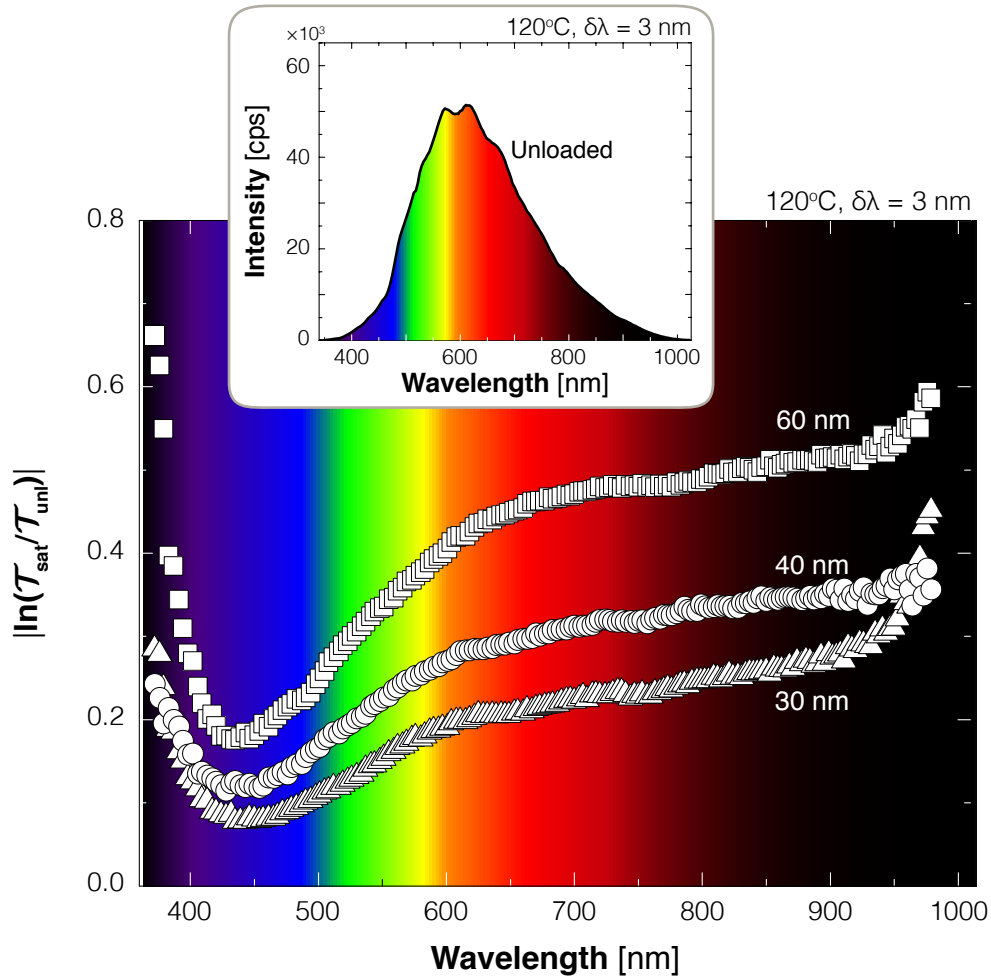
Figure 5.12 | **Wavelength Dependence of Optical Contrast –** The optical contrast or maximum transmission change $|\ln(\mathcal{T}_{sat}/\mathcal{T}_{unl})|$ of Pd-capped hafnium films of various thicknesses ($30\ \mathrm{nm}$ △, $40\ \mathrm{nm}$ ○, and $60\ \mathrm{nm}$ □) as a function of the wavelength. The data are obtained at $120°\mathrm{C}$ and by means of hydrogenspectography (an expansion of hydrogenography) with (after averging) a resolution of $\delta\lambda = 3\ \mathrm{nm}$. The saturated state is obtained by exposing the films to a partial hydrogen pressure of $10^{+3}\ \mathrm{Pa}$. The inset shows the spectrum of the $40\ \mathrm{nm}$ film in the unloaded state.

Optical Resolution

An important parameter for the practical implementation of Hf as hydrogen detection material is its *resolution*, defined as the smallest pressure change (on a logarithmic scale) that can be distinguished optically. We calculate the optical resolution by:

$$\frac{\delta P}{P} = c \times \delta \ln\left(\frac{\mathcal{T}}{\mathcal{T}_{\mathsf{unl}}}\right) \tag{5.3}$$

with

$$c = \frac{\Delta \ln\left(\frac{P}{P_0}\right)}{\Delta \left|\ln\left(\frac{\mathcal{T}}{\mathcal{T}_{\mathsf{unl}}}\right)\right|}. \tag{5.4}$$

Here is $\delta \ln(\mathcal{T}/\mathcal{T}_{\mathsf{unl}})$ defined as the error in $\ln(\mathcal{T}/\mathcal{T}_{\mathsf{unl}})$, while c corresponds to the slope of the linear relation between $\ln(P/P_0)$ and $\ln(\mathcal{T}/\mathcal{T}_{\mathsf{unl}})$ (see figure 5.4). For our improved hydrogenography setup we find that $\delta \ln(\mathcal{T}/\mathcal{T}_0) = 10^{-3}$ (see figures 5.3b or 5.9). From the isotherms plotted in figure 5.4 we find that $c = \ln(10^8)/0.20 = 92.1$. This corresponds to a resolution of $\delta P/P = 9.2 \times 10^{-2}$, which is an order of magnitude smaller than calculated for PdH$_x$ (i.e. $\delta P/P = 5.8 \times 10^{-1}$).[5.6] In addition, this higher resolution is obtained over a much larger pressure range.

The optical resolution can be improved in to ways. First, we can decrease the optical error $\delta \ln(\mathcal{T}/\mathcal{T}_{\mathsf{unl}})$ by using better (read-out) equipment. We demonstrate this with the hydrogenography setup, where, after improvements such as anti-reflection coatings, we were able to reduce the optical error by an order of magnitude to $\delta \ln(\mathcal{T}/\mathcal{T}_{\mathsf{unl}}) = 10^{-3}$. Second, we can increase the optical contrast $\Delta |\ln(\mathcal{T}/\mathcal{T}_{\mathsf{unl}})|$, which results in a smaller slope c. This we may achieve by using light of a single wavelength, as we find that the optical contrast of Pd-capped Hf film (40 nm) strongly depends on the wavelength (see figure 5.12). At wavelengths above $>650 \text{ nm}$ we find an optical contrast of $(|\ln(\mathcal{T}_{\mathsf{sat}}/\mathcal{T}_{\mathsf{unl}})| > 0.30)$, an increase of $\sim 50\%$ compared to white light. This improves the optical resolution to $\delta P/P < 5.9 \times 10^{-2}$.

The optical contrast can also be improved by increasing the thickness of the Hf layer. Figure 5.12 shows that increasing the layer thickness to 60 nm results in a higher optical contrast at all wavelengths, although the largest increase is observed in the red-infrared part of the spectrum. Here we observe a transmission change of $|\ln(\mathcal{T}_{\mathsf{sat}}/\mathcal{T}_{\mathsf{unl}})| \approx 0.50$, more than 200% larger than obtained with a 40 nm thick film and using a white light source. This large transmission change results in a resolution of $\delta P/P = 3.7 \times 10^{-2}$. Increasing the film thickness even more may result in an even better resolution, although effects such as interference and absorption due to a longer pathway may counter this. (see figure 5.2 at p.83 from [5.35])
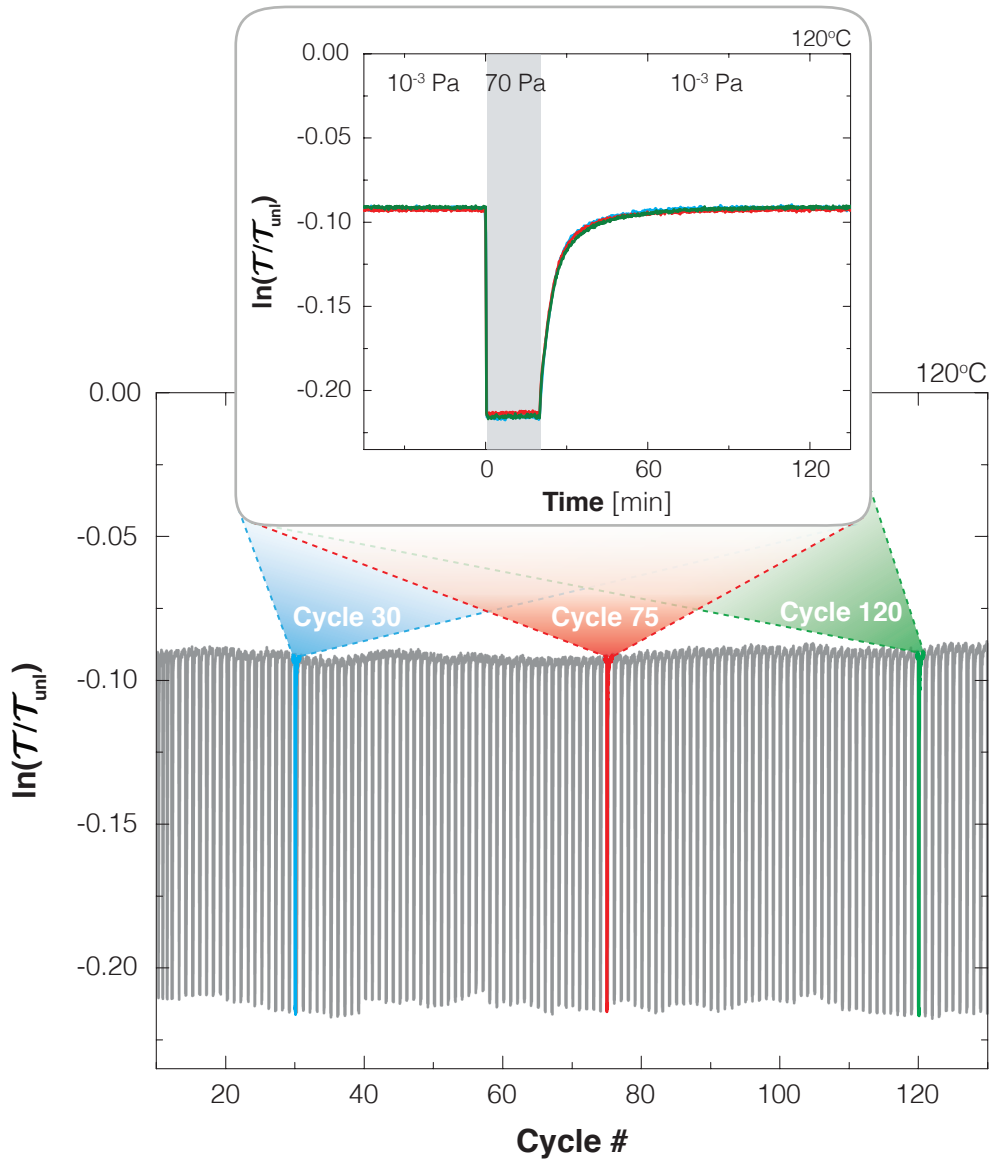
Figure 5.13 | Cycle Stability – The optical response of a Pd-capped hafnium film (40 nm) to 130 cycles of almost complete hydrogenation (70 Pa for 20 min) and partially dehydrogenation (10^{-3} Pa for 160 min) at $120°C$, measured by means of hydrogenography. The shifts in transmission are due to fluctuations in the white light source. The inset shows cycle 30 (blue), cycle 75 (red), and cycle 120 (green) in more detail, where $t = 0$ is defined as the start of each cycle (i.e. the moment the film is (again) exposed to hydrogen).

Stability

We find that the cycle stability of Pd-capped Hf films $(40\,\mathrm{nm})$ is excellent. After cycling the film for more than 100 times between $10^{-3} - 70\,\mathrm{Pa})$ at $120°\mathrm{C}$ we observe no signs of film degradation. Apart from some small oscillations in the minimum and maximum transmittance due to fluctuations in the light source, the cycles are identical (see figure 5.13). We do not observe an increase of the response time with cycling, as shown in the inset of figure 5.13.

The excellent stability of the films is also confirmed by the analysis of structural data (see section 5.4). Despite the volume change of 11% per H upon hydrogenation and in the absence of any intermediate/sticking layers, we do not observe structural differences of a sample that is cycled only once and a sample that cycled more than 100 times. In addition, we do not find any signs for the formation of Hf-Pd alloys. Despite that Hf has a high affinity for oxygen and nitrogen, the structural analysis indicate that the Hf layer is well protected to oxidation or nitridation processes. By means of atomic force microscopy (AFM) we find that the surface roughness of films has not been increased after cycling nor that voids and/or cracks are created (see figure 5.14).

Also after a long exposure to open air, the films still respond optically to hydrogen. Figure 5.15 shows the optical response of a Pd-capped hafnium film $(40\,\mathrm{nm})$ to different hydrogen pressures. Here, the sample has been stored in open air for more than 6 months before we exposed it again to hydrogen. Similar to a freshly prepared sample we observe that each pressure step results in a distinct optical transmission level change without any signs of hysteresis. However, the response time is significantly longer. We now observe response times between a few up to 30 minutes to changing hydrogen pres-
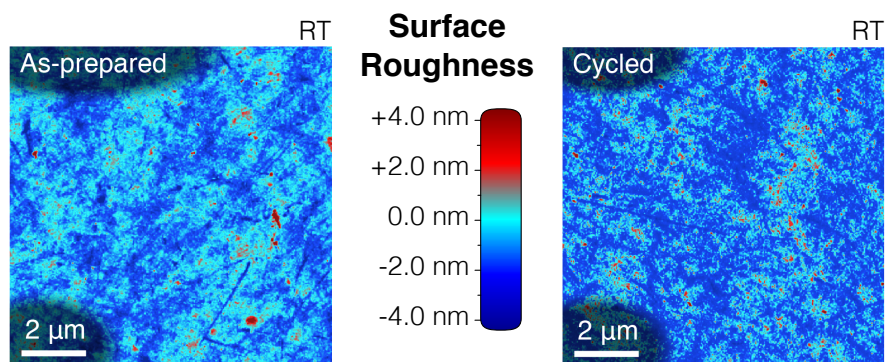
Figure 5.14 | **Surface Roughness of HfH$_x$ thin films** – Atomic force microscopy (AFM) images of a Pd-capped hafnium $(40\,\mathrm{nm})$ thin film on a polished quartz substrate before hydrogenation (left) and after more than 100 hydrogenation cycles (right).

sures (instead of a few minutes). Since the sample is covered by dust (see inset of figure 5.15), we think that the slow response is due to the contamination of the Pd surface. This may be prevented by the use of a protective coating.[5.32 — 5.34]
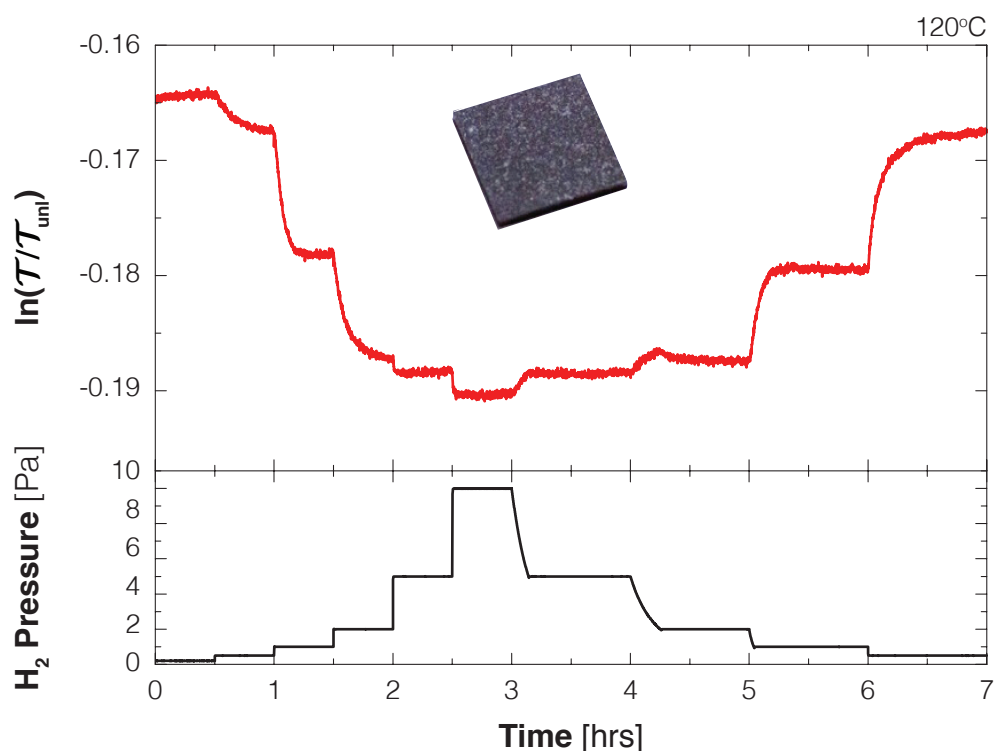
Figure 5.15 | Six Months Reactivation – Optical response of a Pd-capped hafnium film (40 nm) to various hydrogen pressures at $120°C$, after a 6 months exposure to (open) air. The inset shows a photo of the used sample, indicating that the surface is covered by dust particles.

5.4 Structural Properties of HfH$_x$ Thin Films

In the previous section we found that the thermodynamics of Pd-capped HfH$_x$ thin films are similar to bulk. However, the thin film isotherms do no show an inflection at pressures close to the saturation pressure. In bulk this inflection is linked to the incoherent fcc-fct phase transition. The absence of the inflection suggests that the fcc-fct phase transition has a different nature or is even not present. In this section we discuss the structural properties of HfH$_x$ thin films. We studied these properties experimentally by means of *in-situ* x-ray diffraction and *in-situ* neutron reflectometry (see measurement details). With both techniques we were able to use the same multilayer (quartz substrate/Hf $(40\,\mathrm{nm})$/Pd $(10\,\mathrm{nm})$) structure as used with the optical study (see sample preparation). In this way, we can directly link the structural to the optical results.

Discussing the structural properties of Pd-capped HfH$_x$ thin films we use the optical results (see section 5.3) as a guidance. We define three different states:

- **As-prepared** – the state of the film after preparation where the film has never been exposed to hydrogen: $\mathcal{T} = \mathcal{T}_{\mathsf{prep}}$.
- **Saturated** – the state of the film when it is fully saturated with hydrogen: the transmission of the film does not change with pressure: $\mathcal{T} = \mathcal{T}_{\mathsf{sat}}$.
- **Unloaded** – the state of the hydrogenated film when the transmission of the film equals $\mathcal{T} = \mathcal{T}_{\mathsf{unl}}$, usually reached after (a long) exposure to oxygen.

In the discussion below we include also another optical state, defined as $\mathcal{T}_{\mathsf{lin}}$. This point marks the upper limit of the linear (on a log-log scale) relation between the optical transmission $\mathcal{T}$ and the hydrogen pressure P, which defines $\sim 92\%$ of the isotherms.

5.4.1 Distinct Hydride Phases

Figure 5.16 shows the x-ray diffraction patterns corresponding to the different optical states of a Pd-capped hafnium film $(40\,\mathrm{nm})$. We find that each optical state corresponds to a different hydride phase. In the *as-prepared* state we find two intensity peaks. The peaks at $2\theta = 37.43°$ and at $2\theta = 40.96°$ match, respectively, the (100) and the (002) hcp lattice reflections reported for bulk Hf.[5.36] In the *saturated* state, obtained by exposing the film to a partial hydrogen pressure of $10^{+3}\,\mathrm{Pa}$ at $120°\mathrm{C}$, we find one intensity peak at $2\theta = 38.30°$. This position matches the (111) fct lattice reflection reported for bulk HfH$_{1.98}$ $(38.40°)$.[5.36] The *unloaded* state of the film is studied twice. Once after exposing the *saturated* film to open air for $3\,\mathrm{days}$, and a second time after a $6\,\mathrm{months}$ exposure to open air. In both situations we find a single intensity peak (besides the intensity peak corresponding to the Pd-capping layer) at $2\theta \sim 38.4°$, which matches the (111) fcc lattice reflection reported for bulk
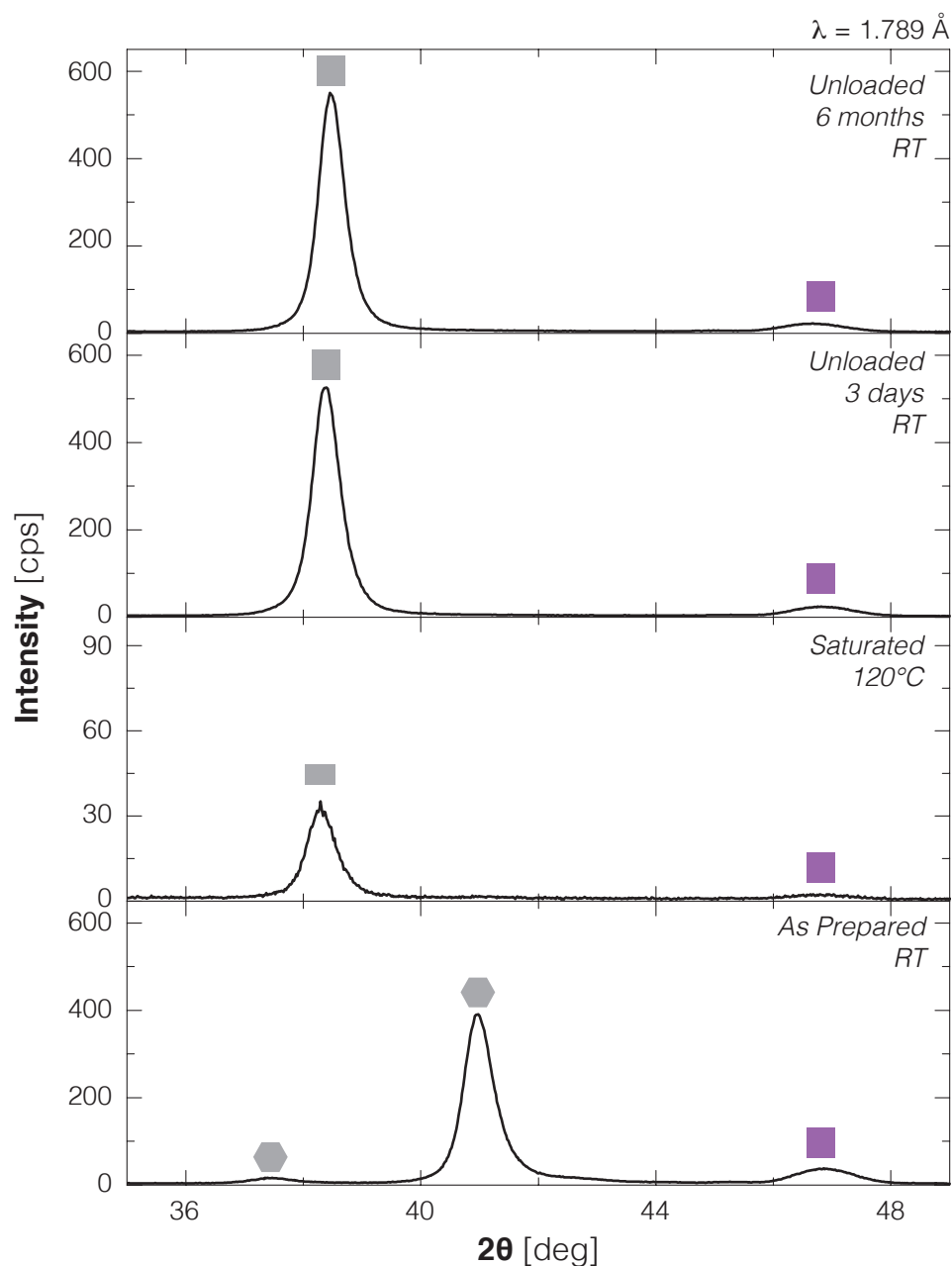
Sample Preparation

The samples used for structural analysis consist of a Hf layer with an uniform thickness of $40\,\mathrm{nm}$ that is capped by a Pd-layer $(10\,\mathrm{nm})$, identical to the samples used for optical measurements. The films are deposited on a substrate by means of an ultra-high vacuum sputter system (base pressure of $10^{-10}\,\mathrm{Pa}$) in 3 $\mu\mathrm{bar}\ \mathrm{Ar}\ (6\mathrm{N})$. The uniform thickness of both layers is obtained by a rotating substrate during sputtering. For *in-situ* x-ray diffraction we used $10 \times 10\,\mathrm{mm}^2$ polished quartz substrates $(1\,\mathrm{mm}$ thick), while for *in-situ* neutron reflectometry we used $3''$ fused quartz wavers $(5\,\mathrm{mm}$ thick). The large substrates are necessary due to the large neutron beam spot size. Also, these substrate have surface roughness of less than $4\,\text{Å}$. This enables a high signal-to-noise ratio. The thickness is determined by means of a sputter-rate, obtained from stylus profilometry (DEKTAK) on bulk samples $(>400\,\mathrm{nm})$.
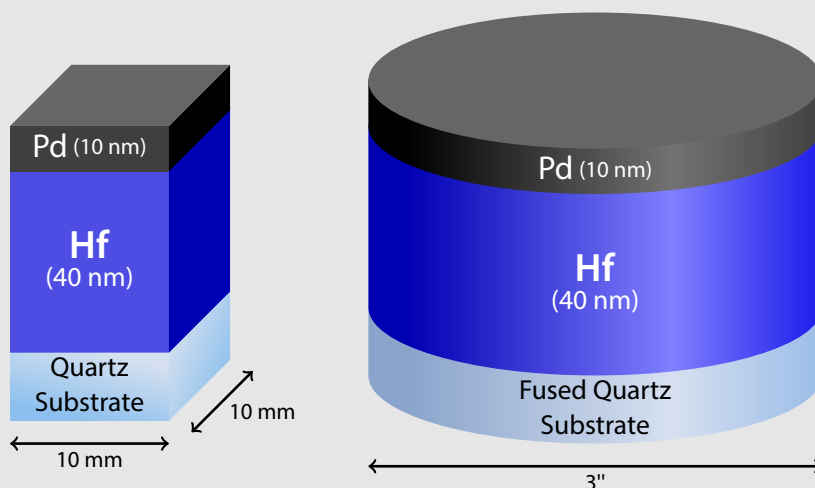
Experimental Details

The x-ray diffraction measurements are performed with a Bruker D8 Advance (Co Kα $\lambda = 1.789\,\text{Å}$), including an Anton Paar XRK 900 reactor chamber to measure in a hydrogen atmosphere. The neutron reflectometry measurements are performed at time-of-flight reflectometer (ROG) of the Reactor Institute Delft (RID). The measurements are performed at one fixed incident angle of $8.5\,\mathrm{mrad}$ resulting in a neutron scattering Q-range between $0.10 - 0.65\,\mathrm{nm}^{-1}$ with a resolution $\Delta Q/Q = 0.04$. Data fitting has been performed with the help of STAR.[5.37] The various hydrogen pressures are obtained by using $0.1\%\ \mathrm{H_2/Ar}$, and $4\%\ \mathrm{H_2/Ar}$ gas mixtures, with a gas flow set to $20\,\mathrm{sccm}$. A typical XRD scan time was $7\,\mathrm{min}$, while a typical neutron reflectometry scan time was $7\,\mathrm{hrs}$. For each technique we assure that the system was in equilibrium by starting a scan at least $30\,\mathrm{min}$ after applying a different pressure. The neutron reflectometry measurements were performed by L. Bannenberg, supervised by A.A. van Well.

Figure 5.16 | X-Ray Diffraction Patterns of HfH$_x$ States – X-ray diffraction patterns of a Pd-capped Hf film $(40\,\mathrm{nm})$ at different (de)hydrogenation states. The *as prepared* state is measured in open air directly after sample preparation and before exposing it to hydrogen. The *saturated* state is measured at $120°\mathrm{C}$ after an exposure to a partial hydrogen pressure of $10^3\,\mathrm{Pa}$ for a few hours. The *unloaded* state is measured after exposing the hydrogenated film to (open) air for 3 days and for 6 months. The symbols indicate the bulk lattice reflections of hcp Hf (●), of fcc HfH$_{1.62}$ (■), fct HfH$_{1.98}$ (■), and fcc Pd (■).

	Structure	Thin Film	Bulk[5.36]
As Prepared (*air, RT*)			
- Hf (100)	⬤ hcp	37.43°	37.71°
- Hf (002)	⬤ hcp	40.96°	41.43°
- Pd (111)	■ fcc	46.84°	46.93°
Saturated (10^{+3} *Pa*, $120°\,C$)			
- Hf$_{1.98}$ (111)	▬ fct	38.30°	38.40°
- Pd (111)	■ fcc	46.74°	46.93°
Unloaded (*3 days in air, RT*)			
- HfH$_{1.43}$ (111)	■ fcc	38.37°	38.67°
- Pd (111)	■ fcc	46.81°	46.93°
Unloaded (*6 months in air, RT*)			
- HfH$_{1.43}$ (111)	■ fcc	38.47°	38.67°
- Pd (111)	■ fcc	46.67°	46.93°

Table 5.1 | HfH$_x$ XRD Lattice Reflections – Comparison of the (2θ) intensity peak positions observed in the XRD patterns shown in figure 5.16 with the reported lattice reflections for bulk HfH$_x$. The symbols ⬤, ■, ▬ (all HfH$_x$) en ■ (Pd) indicates the different structures based on bulk HfH$_x$. The bulk lattice reflections are obtained from the JCPDS database.[5.36] Note that for the *unloaded* state the observed peak positions are compared to the peak position reported for bulk HfH$_{1.62}$.

	Structure	x in HfH$_x$	d (nm)	d/d_prep
As Prepared (*air, RT*)				
	⬤ hcp	0.0	36.1(8)	1
Saturated (10^{+2} *Pa,* $90°\,C$)				
	▬ fct	1.98(2)	43.9(2)	1.22
Unloaded (*1-2 days in air, RT*)				
	■ fcc	1.43(2)	41.4(2)	1.15

Table 5.2 | Neutron Reflectometry on HfH$_x$ – The thickness d and hydrogen fraction x of a Pd-capped HfHx film $(40\ \text{nm})$ measured at different states of the film by means of neutron reflectometry. Each state is measured multiple times to determine whether equilibrium is reached. The number between the brackets indicates the error in the last digit.

HfH$_{1.62}$ ($38.67°$).[5.36] As the position of this intensity peak remains the same after 3 days of exposure to open air, we conclude that the *unloaded* state of the film is structurally stable. A complete overview of the position of the intensity peaks and their identification is given in table 5.1.

The distinct hydride states of the Pd-capped Hf films are also studied by neutron reflectometry (see table 5.2). In this way, we find that after exposing the film to a pressure of 10^{+3} Pa at $120°$C, corresponding to the optical state $\mathcal{T}_{\text{sat}}$, the Hf layer is completely saturated with hydrogen: $x = 1.98 \pm 0.02$. This value matches the maximum hydrogen fraction of $x = 1.96$ reported for bulk.[5.8] From the neutron analysis we deduce that the hydrogen fraction does not reduce to zero when exposing the saturated film to open air. Already after one day we find that the hydrogen fraction only decreases to $x = 1.43 \pm 0.02$. A longer exposure does not result in a further reduction of the hydrogen fraction. As the *unloaded* state corresponds to the same fcc structure as reported for bulk HfH$_{1.62}$,[5.10,5.11] we therefore conclude that the lower fcc phase boundary occurs in thin films at significant lower hydrogen fraction than in bulk.

The neutron data also reflects that the Hf film is clamped. In a clamped metal hydride film, a volume expansion is fully converted in a thickness expansion. The neutron data suggest that the hcp $\rightarrow$ fcc phase transition induces a Hf layer thickness increase of $\sim 16\%$ (see table 5.2), which matches the volume expansion of $\sim 15\%$ obtained from the XRD data.

On the other side, the analysis of the neutron data show that the thickness expansion of the *saturated* Hf layer is much stronger than expected from the XRD data. While the analysis of the XRD data indicates a volume expansion of $\sim 18\%$ with respect to the *as-prepared* state, we find through neutron reflectometry a thickness expansion of $\sim 22\%$ (see table 5.2). This suggests a deformation of the cubic lattice, since the short fct axis should develop along the $[001]$ axis. Unfortunately, the study and the analysis of the out-of-plane diffraction peaks are beyond the scope of this thesis.

5.4.2 Phase Transitions

As the x-ray diffraction analysis indicate that the *as-prepared* state corresponds to the *hcp* hydride phase, the *unloaded* state corresponds to the *fcc* hydride phase, and the *saturated* state corresponds to the *fct* hydride phase, the system should undergo two phase transitions upon hydrogenation: hcp $\rightarrow$ fcc and fcc $\rightarrow$ fct. In bulk both transitions are considered to be incoherent and are reflected in the corresponding isotherms by, respectively, a pressure plateau at low and an inflection at high pressures. In the optical isotherms we do not observe such an inflection nor a kink in the optical transmission at high pressures (see figure 5.4). By means of *in-situ* x-ray

diffraction we studied both phase transition in Pd-capped Hf thin films. The latter has, however, our main focus as Pd-capped Hf thin films show excellent the hydrogen detection properties between the *unloaded* (fcc) and the *saturated* (fct) state. The fcc → fct transition is also studied by means of *in-situ* neutron reflectometry to obtain its effect on the hydrogen fraction and the layer thickness. All *in-situ* measurements are performed at $120°$C, stated otherwise.
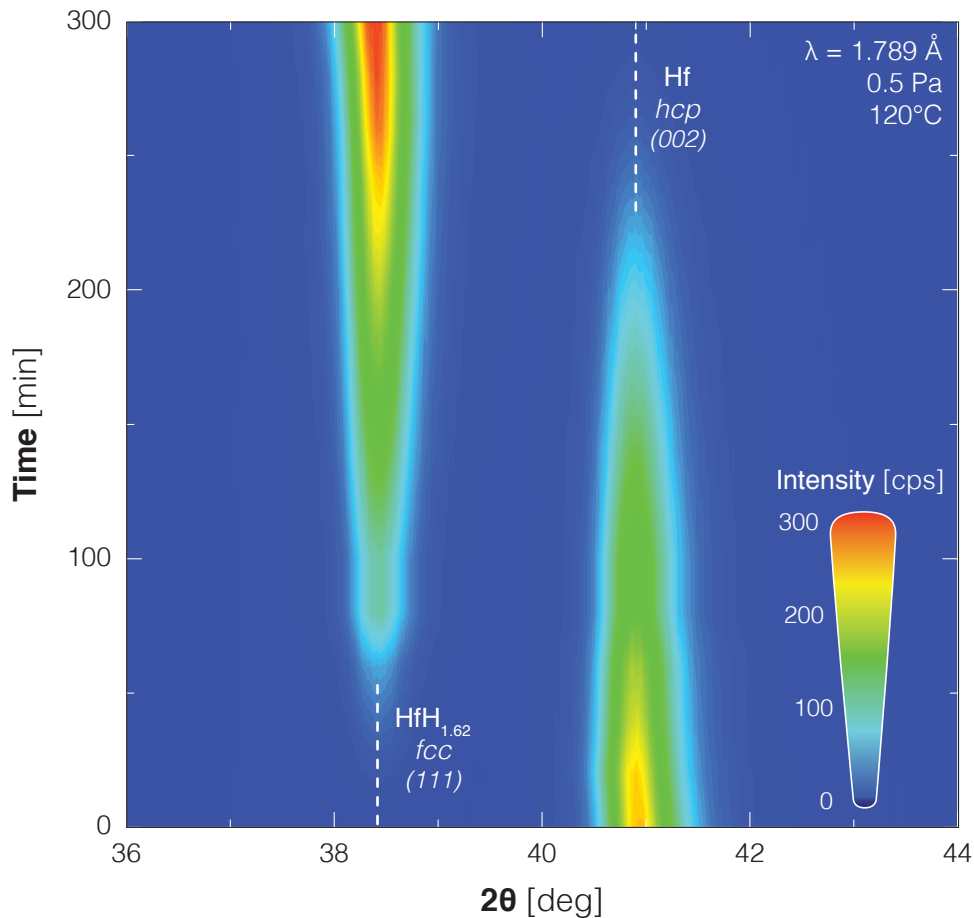
Figure 5.17 | The hcp → fcc Phase Transition – Contour plot of multiple *in-situ* x-ray diffraction (XRD) patterns of the hcp-fcc phase transition in HfH$_x$ upon hydrogenation. Here, red indicates high intensity and blue low intensity. The hcp-fcc phase transition, studied by exposing a Pd capped Hf thin film to 0.5 Pa at $120°$C. The (dashed) white lines indicate the reported reflections of the hcp Hf (002) and the fcc HfH$_{1.62}$ (111) phases for bulk samples.[5.36] Note that in our thin films the *unload* fcc state corresponds to HfH$_{1.43}$.
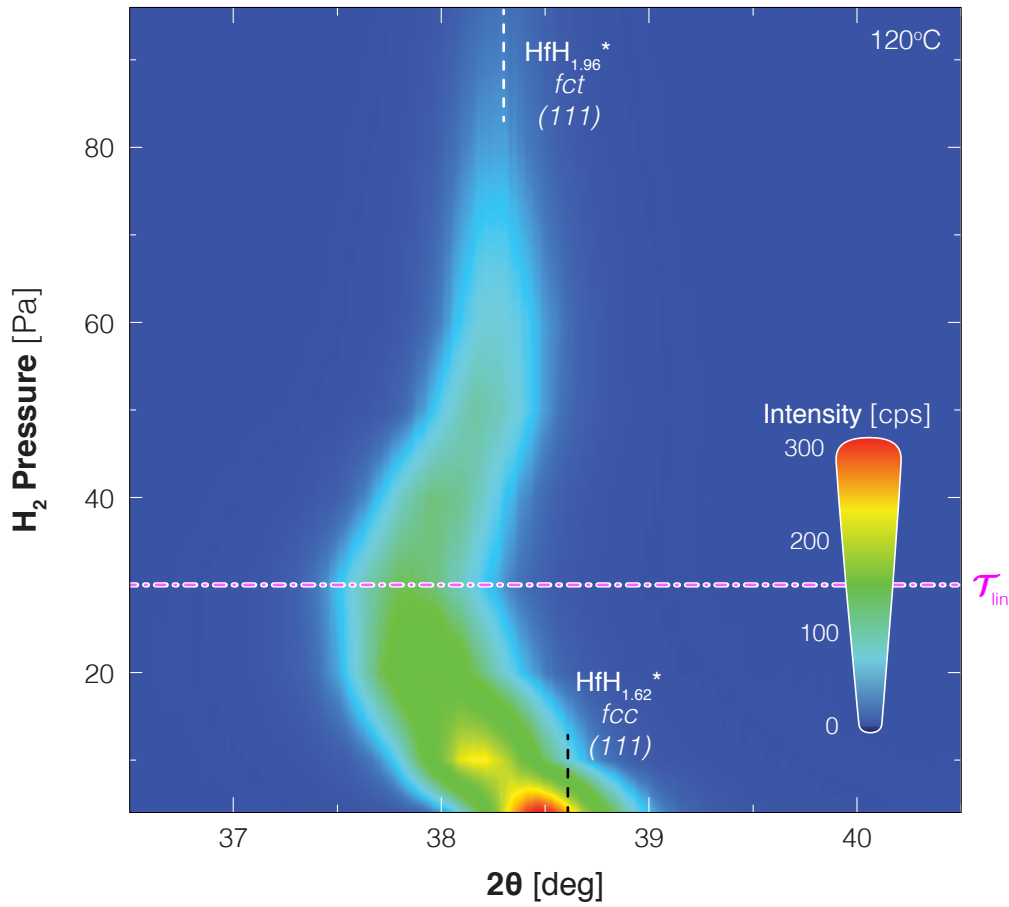
The hcp $\rightarrow$ fcc Phase Transition

Figure 5.17 shows a contour plot of multiple XRD patterns, where each pattern is obtained after a fixed time interval ($10\,\mathrm{min}$) while the Pd capped Hf thin film ($40\,\mathrm{nm}$) is exposed to a constant partial hydrogen pressure of $0.5\,\mathrm{Pa}$ at $120°\mathrm{C}$ for $300\,\mathrm{mins}$. It indicates that the transition from the *as-prepared* Hf to the HfH$_{1.43}$ state is incoherent. Over time we observe that the intensity of the Hf hcp (002) lattice reflection reduces while the HfH$_{1.43}$ fcc lattice reflection emerges and grows in intensity. In the mean time, positions of the lattice reflections do not change. This indicates that the two hydride phases in thin films, similar to bulk, are not elastically coupled.[5.8,5.10,5.11]

The fcc $\rightarrow$ fct Phase Transition

In figure 5.17 we observe after approximately $275\,\mathrm{min.}$, when the hcp structure is completely converted into a fcc structure, the position of the peak intensity (identified as the (111) fcc lattice reflection) starts to reduce. This continues when we, after $300\,\mathrm{min}$, increase the pressure gradually from $4\,\mathrm{Pa}$ to $30\,\mathrm{Pa}$ (see figure 5.18). At this pressure, the shift in 2θ position is almost $1°$. This corresponds to a 2.2% expansion of the d-spacing (see figure 5.19). Above $30\,\mathrm{Pa}$ the position of the intensity peak increases again until it saturates at $60\,\mathrm{Pa}$. At this state the film is saturated with hydrogen (see table 5.2) and the 2θ position of the intensity peak matches the fcc (111) lattice reflection reported for bulk HfH$_{1.98}$ (see table 5.1).

The smooth transition of the 2θ position from the *unloaded* fcc to the *saturated* fct hydride phase indicates the presence of a coherent phase transition wherein the two hydride phases are elastically coupled. This is supported by the observation that the diffraction peaks widens during the transition (see figure 5.19). The fact that (111) lattice spacing shows a maximum at a pressure of $30\,\mathrm{Pa}$ and is 1.7% larger than that of the fct HfH$_{1.98}$ hydride phase at $10^{+3}\,\mathrm{Pa}$ suggests a strong deformation of the cubic lattice. A detailed study of the out-of-plane expansion is necessary to further explore the symmetry of the lattice during the phase transition. This is, however, beyond the scope of this thesis.

The fcc $\rightarrow$ fct phase transition is also studied by *in-situ* neutron reflectometry, where we were able to measure the Hf layer thickness and its hydrogen content as a function of the hydrogen pressure. While the prominent changes in the (111) lattice spacing as measured by XRD occur predominantly between $4-60\,\mathrm{Pa}$, we do not observe any anomalies in the corresponding neutron reflectometry data (see figure 5.20). Instead, we find a gradually increase of the hydrogen fraction between $5-30\,\mathrm{Pa}$. At $30\,\mathrm{Pa}$, where the (111) lattice spacing shows a maximum, we deduce a hydrogen fraction of $x = 1.96$, far above the critical hydrogen fraction reported for the bulk fcc/fct transition ($1.78 < x < 1.86$).[5.8] This suggests that the fcc hydride phase spans a 3 times larger hydrogen fraction range that reported for bulk, while

Figure 5.18 | The fcc → fct Phase Transition – Contour plot of *in-situ* x-ray diffraction (XRD) patterns of a Pd-capped HfH_x thin film $(40\ nm)$ as a function of the applied pressure at $120°C$. Red indicates high intensity and blue low intensity. The horizontal dashed line indicates the optical state $\mathcal{T}_{lin}$, which corresponds to $30\ Pa$ at $120°C$. The vertical lines indicate the reported reflections/d-spacing of bulk $HfH_{1.62}$ and $HfH_{1.96}$. Note that in our thin films these states corresponds to $HfH_{1.43}$ and $HfH_{1.98}$, respectively.

the range of the fct hydride phase is significant smaller ($\sim$10 times) than reported for bulk. Above $30\ Pa$ we observe that the hydrogen fraction saturates at $x = 1.98$.

Also in the analysis of the Hf layer thickness we do not observe any anomalies caused by the fcc → fct phase transition. The results shown in figure 5.20a suggest a gradual layer expansion as a function of the pressure between $10^{-1} - 10^{+3}\ Pa$, although the large signal-to-noise ratio prevent us from determining the exact relation or from determining whether the phase transition causes a change in the relation.
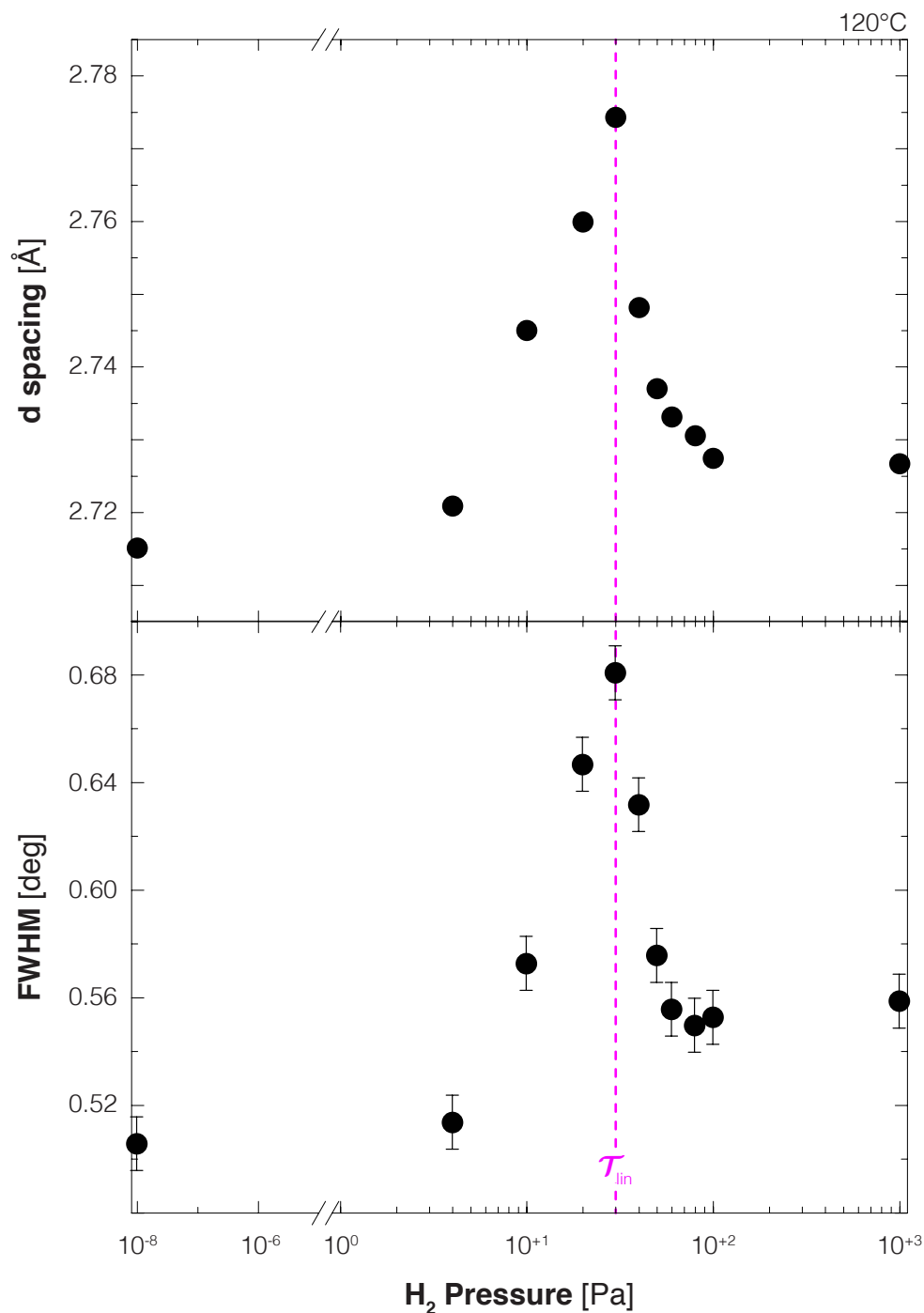
Figure 5.19 | fcc → fct: d-spacing & FWHM – The d-spacing (top) calculated from and the FWHM (bottom) of the intensity peaks as a function of the pressure at $120°C$. The d-spacing is calculated by means is Braggs' law: $2\,d\sin\left(\frac{2\theta}{2}\right) = n\,\lambda$. The plots include the d-spacing and the FWHM of the *unloaded* $(10^{-8}\ \mathrm{Pa})$ and the *saturated* $(10^{+3}\ \mathrm{Pa})$ state. The dashed line indicates the optical state $\mathcal{T}_{\text{lin}}$, which corresponds to $30\ \mathrm{Pa}$ at $120°C$.
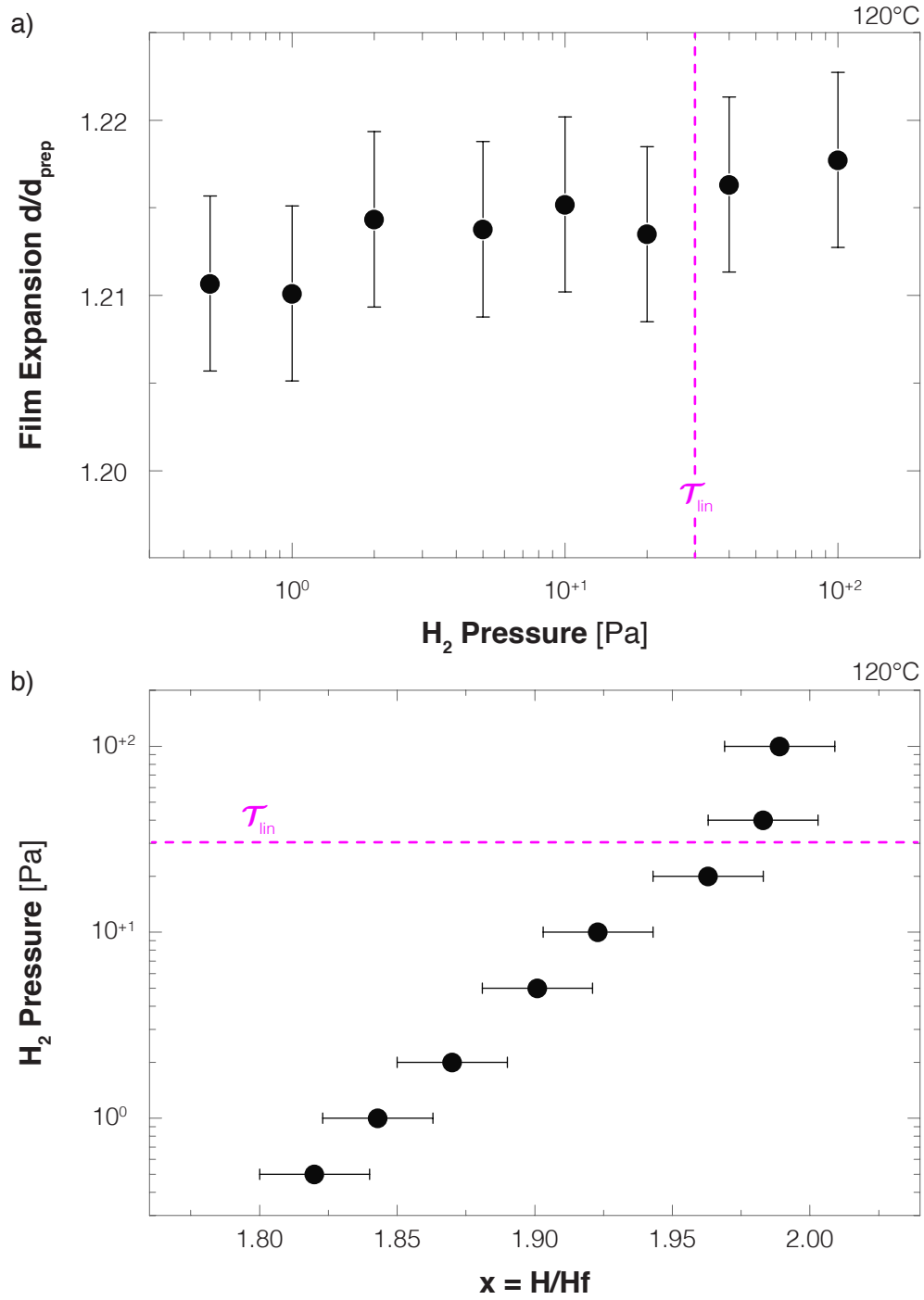
Figure 5.20 | fcc → fct: Neutron Reflectometry – a) The film thickness of a Pd-capped Hf thin film (40 nm) as a function of the hydrogen pressure, measured at $120°\text{C}$ by means of neutron reflectometry. **b)** The hydrogen fraction $x = \text{H/Hf}$ of the same Pd-capped Hf thin film as a function of the hydrogen pressure obtained from the same measurements. The dashed lines indicate the optical state $\mathcal{T}_{\text{lin}}$, corresponding to 30 Pa at $120°\text{C}$.

5.4.3 Link to the Optical Isotherms

Because we used the same sample configuration, we can directly link the structural to the optical results. In this way we find that the optical transmission change, on a logarithmic scale, is linearly related to the hydrogen fraction. As shown in figure 5.21, we find that between $10^{-1} - 10^{+3}$ Pa the neutron data are in excellent agreement with the optical results. Here we plotted both $|\ln(\mathcal{T}/\mathcal{T}_{\mathsf{unl}})|$ and x as a function of the hydrogen pressure where the pressure scale of the optical isotherms measured at $90°$C and $150°$C is converted to the $120°$C pressure scale. For this we assume a
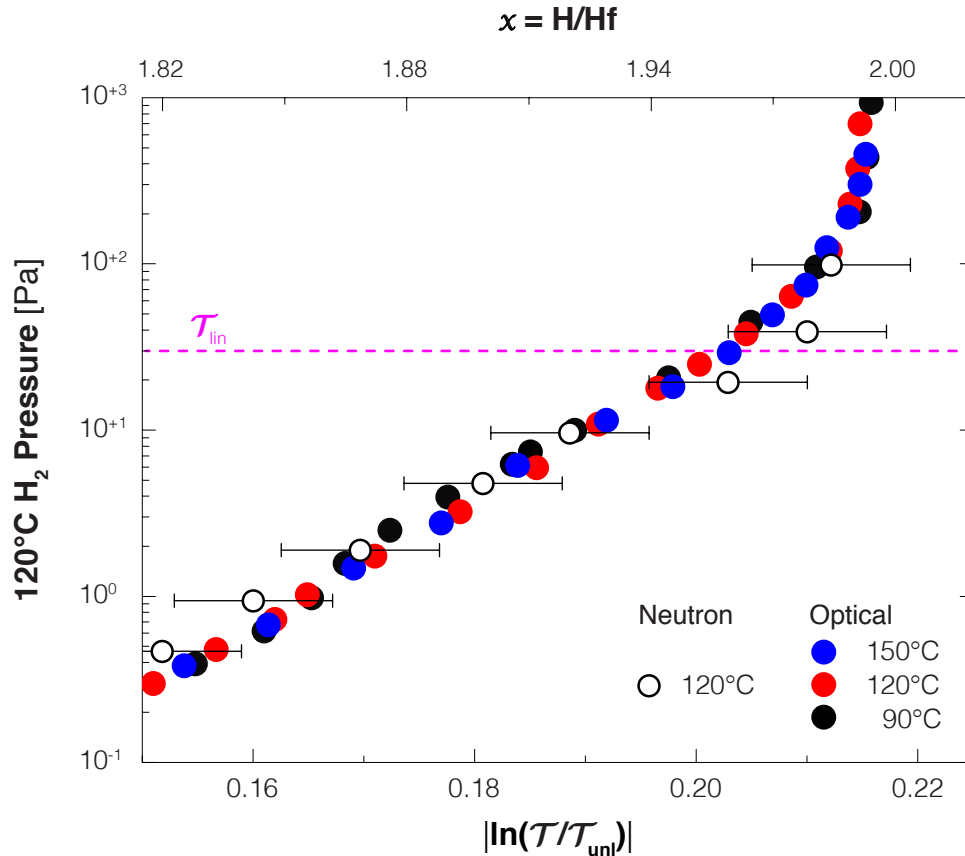
Figure 5.21 | Optical and Hydrogen Fraction Master Curve – Plot where both the optical transmission $|\ln(\mathcal{T}/\mathcal{T}_{\mathsf{unl}})|$ (bottom horizontal axis) and the hydrogen fraction $x = $ H/Hf (top horizontal axis) is plotted as function of the hydrogen pressure between $0.5 - 10^{+3}$ Pa at $120°$C. Here we apply a linear relation between x and $|\ln(\mathcal{T}/\mathcal{T}_{\mathsf{unl}})|$: $x = 1.43 + 2.61 \times |\ln(\mathcal{T}/\mathcal{T}_{\mathsf{unl}})|$. The neutron data is visualized by open symbols: O. The optical isotherms are visualized by closed symbols: ● for $90°$C, ● for $120°$C, and ● for $150°$C. The pressure range of the $90°$C and $150°$C optical isotherms are converted to $120°$C by means of the thermodynamics. The dashed line indicates the optical state $\mathcal{T}_{\mathsf{lin}}$, which corresponds to 30 Pa at $120°$C.

constant $\Delta H = -117.9 \, \text{kJ/mol H}_2$. Because the analysis of the neutron data indicates that x is proportional to $\ln(P/P_0)$ while the analysis of the optical data indicates that $|\ln(\mathcal{T}/\mathcal{T}_{\text{unl}})|$ is proportional to $\ln(P/P_0)$, the combination of both analyses suggests that $|\ln(\mathcal{T}/\mathcal{T}_{\text{unl}})|$ is linearly related to x between $1.8 < x < 2.0$.

The results also suggest that the proportionality between $|\ln(\mathcal{T}/\mathcal{T}_{\text{unl}})|$ and x is also true for $x < 1.8$. The extrapolation to $\mathcal{T} \to \mathcal{T}_{\text{unl}}$ suggests $x \cong 1.43$. This equals the hydrogen content in the dehydrogenated films: $x \cong 1.42$ (see table 5.2). With the definition that $|\ln(\mathcal{T}/\mathcal{T}_{\text{unl}})| = 0$ and the observation that $x \cong 1.43$ at $\mathcal{T} = \mathcal{T}_{\text{unl}}$, we find that

$$|\ln(\mathcal{T}/\mathcal{T}_{\text{unl}})| = \frac{1}{2.61} (x - 1.43) \quad \text{for} \quad |\mathcal{T}| > |\mathcal{T}_{\text{unl}}|. \tag{5.5}$$

Such a relation is not uncommon as it is also observed in other metal hydride systems.[5.29,5.38]

As we find that the optical response is a function of both the wavelength and the layer thickness, so will be equation 5.5. From figures 5.8 and 5.12 we find that the optical transmission change $|\ln(\mathcal{T}/\mathcal{T}_{\text{unl}})|$ is the largest in the (infra)red part and the smallest in the blue part of the spectrum. This behavior is supported by Density Functional Theory (DFT) calculations. Here we calculated the imaginary part ε_i of the dielectric function for fcc $HfH_{1.5}$ and fct HfH_2 as a function of the photon energy or wavelength (see figure 5.22a). We find that there is no difference in ε_i of both hydride phases in the blue part of the spectrum (<550 nm) while the difference increases with increasing wavelength in the red part of the spectrum.

Figure 5.22b indicates that the move from fcc $HfH_{1.5}$ and fct HfH_2 induces a shift in spectral weight below 3 eV below the Fermi level. Excitations that involve these states are, however, too high in energy to affect the visible spectrum. On the other hand, we observe an increase in spectral weight in the first 2 eV above the Fermi level. This leads to an increase in the joined density of states and hence a stronger absorption in the red part of the spectrum. It is noted that in both cases the intra band plasma frequency lies well beyond the optical spectrum.

The optical transmission of a film can be related to the dielectric function by means of the Lambert-Beer law, which states that the optical transmission of a film is the product of the absorption coefficient α and the film thickness d:

$$\mathcal{T} = \mathcal{T}_0 \exp\left[-\alpha(\omega, x) \, d(x)\right]. \tag{5.6}$$

While α is a function of both the hydrogen content x and the wavelength λ through the angular frequency $\omega = 2\pi c/\lambda$ (where c is the speed of light), d is only a function of x. The absorption coefficient is related to the dielectric function:

$$\alpha(x) = \frac{\sqrt{2}\omega}{c} \left(\sqrt{\varepsilon_r^2(x,\omega) + \varepsilon_i^2(x,\omega)} - \varepsilon_r(x,\omega) \right), \tag{5.7}$$

where ε_r and ε_i are, respectively, the real and imaginary part of the dielectric function:

$$\varepsilon(x,\omega) = \varepsilon_r(x,\omega) + i\,\varepsilon_i(x,\omega)\,. \tag{5.8}$$

In other metal hydride systems, such as VH_x, is has been noticed that ε_r is small compared to ε_i.[5.21] For now, we assume that this is also true for HfH_x and we reduce equation 5.7 to

$$\alpha(x,\omega) = \frac{\sqrt{2}\omega}{c}|\varepsilon_i(x,\omega)|. \tag{5.9}$$

We show below that, in order to describe the measured optical transmission change, we cannot neglect ε_r.

Through equation 5.6 and 5.9 we can express the measured optical transmission change between the *unloaded* and the *saturated* Hf layer through a change in α and d. For simplicity, we equal the hydrogen content of the *unloaded* state to $x = 1.5$ and that of the *saturated* state to $x = 2.0$. In this way we find:

$$\ln\left(\frac{\mathcal{T}_{\text{sat}}}{\mathcal{T}_{\text{unl}}}\right) = -\alpha(\omega, x=2.0)\,d(x=2.0) + \alpha(\omega, x=1.5)\,d(x=1.5)$$

$$= -\frac{\sqrt{2}\omega}{c}\left[-|\varepsilon_i(x=2.0,\omega)|d(x=2.0) + |\varepsilon_i(x=1.5,\omega)|d(x=1.5)\right]. \tag{5.10}$$

The analysis of neutron reflectometry data indicate that the hydrogenation of the Hf layer from the *unloaded* to the *saturated* state induces a thickness increases from 15% to 22% with respect to the *as prepared* state of the layer. This means that an *as*

DFT Calculations

The DFT calculations are performed on a $40 \times 40 \times 40$ k-point mesh, reduced to $8 \times 8 \times 8$ for the exchange part of the hybrid exchange correlation functional (HSE06). This mesh, and the choice of the other computational parameters such as the plane wave cutoff $(300\,\text{eV})$ and number of empty states (80), ensures a convergence within 2% for each point of the dielectric function in the optical window. Using the PBE functional we explored the influence of the inclusion of spin orbit corrections and found it to be negligible in the optical window. It is therefore neglected in the hybrid functional calculations. We include both inter-band and intra-band transitions. The first are calculated in the RPA formalism, the latter are added as a Drude contribution obtained from the calculated plasma frequency. For the fcc structures a lattice parameter of $4.7\,\text{Å}$ is used and for the fct structure $a = 4.37\,\text{Å}$ and $c = 4.92\,\text{Å}$. The calculations are performed by M.J. van Setten.

a)

b)
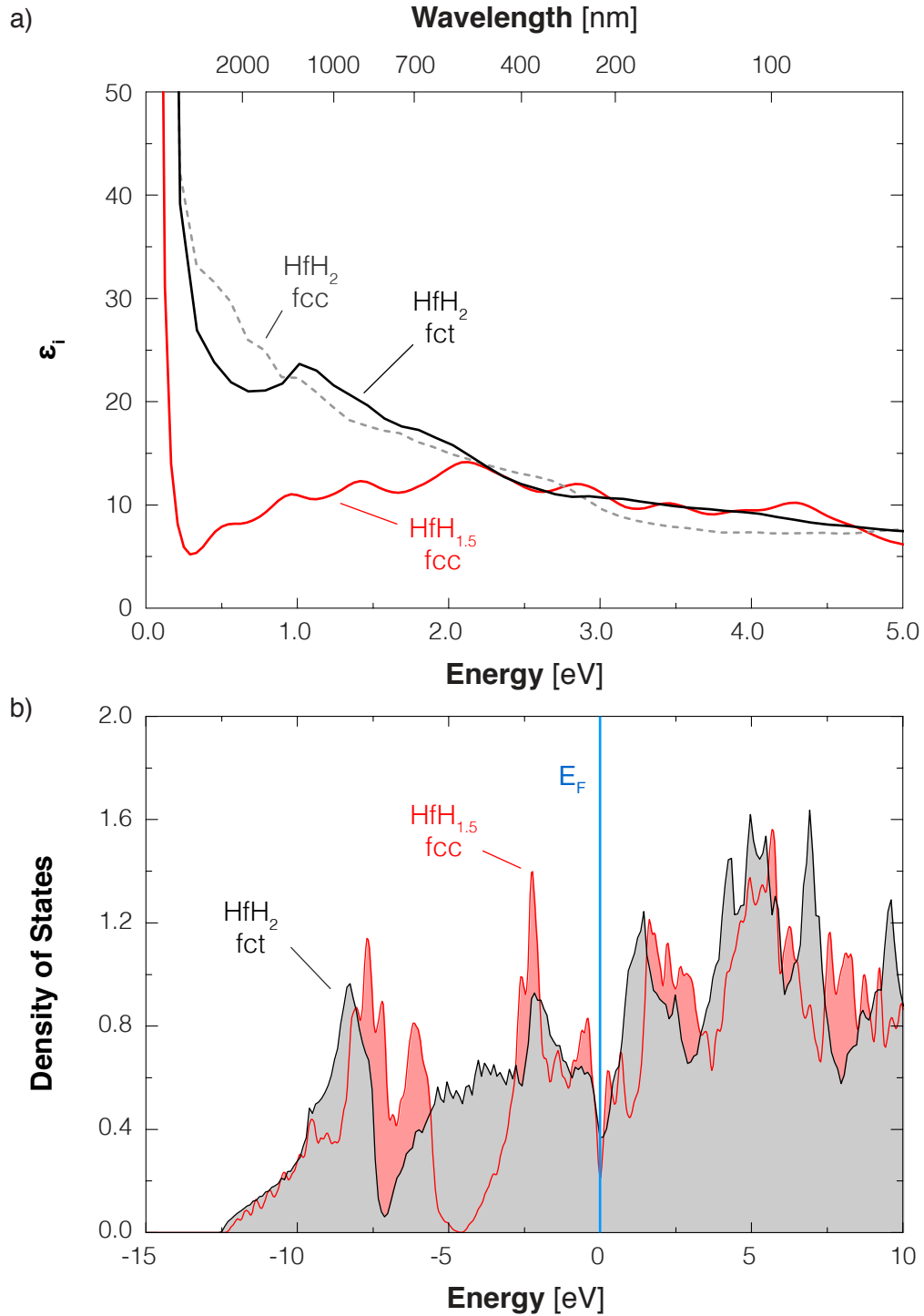
Figure 5.22 | **Density Functional Theory Calculations on HfH$_x$** – **a)** The imaginary part ε_i of the dielectric function calculated for fcc HfH$_{1.5}$ (red) and for HfH$_2$ (black) with either a fct (solid) or a (hypothetical) fcc (dashed line) structure. **b)** Density of States (DoS) calculated for fcc HfH$_{1.5}$ (red) and for fct HfH$_2$ (black), where the photon energy is plotted with respect to the Fermi energy E_F.

prepared Hf layer with a thickness of 40.0 nm shows a thickness increase from 46.0 nm in the *unloaded* state to 48.8 nm in the *saturated* state. In the blue part of the spectrum (450 nm), where the imaginary part of the dielectric function of the fcc $HfH_{1.5}$ and fct HfH_2 are the same and equals $\varepsilon_i = 13.0$ (see figure 5.22a), we calculate that

$$\ln\left(\frac{\mathcal{T}_{\text{sat}}}{\mathcal{T}_{\text{unl}}}\right) = \frac{2\sqrt{2}\pi}{450}\left[-48.8 * 13.0 + 46.0 * 13.0\right] = -0.70 \quad @\ 450\ \text{nm} \tag{5.11}$$

which is 5 times larger than observed with hydrogenspectrography: $\ln(\mathcal{T}_{\text{sat}}/\mathcal{T}_{\text{unl}}) \cong -0.12$ (see figure 5.12). In the red part of the spectrum (700 nm) we find that the imaginary part of the dielectric function changes from $\varepsilon_i = 11.5$ to $\varepsilon_i = 17.5$ between fcc $HfH_{1.5}$ and fct HfH_2 (see figure 5.22a). In this way we calculate that

$$\ln\left(\frac{\mathcal{T}_{\text{sat}}}{\mathcal{T}_{\text{unl}}}\right) = \frac{2\sqrt{2}\pi}{700}\left[-48.8 * 17.5 + 46.0 * 11.5\right] = -4.1 \quad @\ 700\ \text{nm} \tag{5.12}$$

which is more than >12 times larger than observed with hydrogenspectrography: $\ln(\mathcal{T}_{\text{sat}}/\mathcal{T}_{\text{unl}}) \cong -0.31$ (see figure 5.12).

The difference between the calculated and the measured transmission change may be explained through the real part of the dielectric function. Only a small but non-zero change from $\varepsilon_r = -0.6$ to $\varepsilon_r = 0.0$ between fcc $HfH_{1.5}$ and fct HfH_2 is necessary to describe the optical transmission change of $\ln(\mathcal{T}_{\text{sat}}/\mathcal{T}_{\text{unl}}) = -0.127$ measured at 450 nm. At 700 nm a larger difference in ε_r is necessary to describe the measured optical transmission change, $\varepsilon_r = -4.0$ to $\varepsilon_r = +3.0$, although these (absolute) values are still smaller than ε_i. In addition, similar and even larger values for ε_r are calculated for e.g. MgH_2 and PdH_x.[5.39] Note that these calculations do not include the absorption/reflections of the quartz substrate and of the Pd-capping layer. Detailed DFT calculations are necessary to confirm the non-zero changes of the real part of the dielectric function.

Drude Model & Resistivity

Besides additional DFT calculations, the resistivity of the Hf layer may also indicate whether there is a non-zero change of real part of the dielectric function between the *unloaded* and the *saturated* state. This follows from the Drude-Lorentz model. This model describes the transport properties of the free electrons in metals, which are detached from their positively charged ions under influence of other atoms. This creates an electric field that forces the electrons to return to their original position. Because of their inertia, the electrons will oscillate their original position with a characteristic frequency, known as the plasma frequency ω_p, and relaxation time, known as the Drude relaxation time τ. As a result, a oscillating electric field is created which

can be described by the dielectric function given in equation 5.8. The real part of this function can be expressed in terms of ω_p and τ:

$$\varepsilon_r(x, \omega) = \varepsilon_\infty - \frac{\omega_p^2(x) \ \tau^2(x)}{1 + \omega^2 \tau^2(x)} \tag{5.13}$$

where ε_∞ is known as the complex permittivity. The plasma frequency ω_p is proportional to free electrons states N. In Hf, there are $N = 4$ electronic states in the conduction band. However, by forming a metal hydride we expect that free electronic states reduces linearly with the hydrogen fraction. In this way the plasma frequency has the form:

$$\omega_p(x) = \omega_p^0 \sqrt{N - x}. \tag{5.14}$$

Here, ω_p^0 is a constant and calculated from the electron density n in Hf and its atomic mass m:

$$\omega_p^0 = \sqrt{\frac{n \ e^2}{m \ \varepsilon_0}}, \tag{5.15}$$

where e is the elementary charge and ε_0 the permittivity of vacuum. For Hf we find $\omega_p^0 = 3.45 \times 10^{15}$ Hz. The Drude relaxation time τ is given by

$$\tau(x) = \frac{1}{\varepsilon_0 \ \omega_p^2(x) \ \rho(x)}. \tag{5.16}$$

Here ε_0 is the vacuum permittivity and ρ the resistivity. Therefore, by measuring ρ as a function of x we estimate whether we may expect a non-zero change in ε_r.

Figure 5.23 shows the electrical resistivity of a Pd-capped hafnium thin with a PTFE coating as a function of time, where we expose the film to a hydrogen pressure of 10 Pa at room temperature. Simultaneously, the optical reflection intensity at 635 nm is monitored. During the hcp $\rightarrow$ fcc phase transition and in the fct hydride phase, the resistivity hardly changes. However, from the fcc to the fct hydride phase (marked by the increase of the reflection intensity) we observe a strong increase of the electrical resistivity: from $\rho(x \approx 1.5) = 0.086$ mΩ cm to $\rho(x = 2.0) = 0.114$ mΩ cm. By means of equations 5.13 – 5.16 we calculate that the resistivity change induces between the *unloaded* and the *saturated* state a change of the real part of the dielectric of $\Delta\varepsilon_r = \varepsilon_r(x = 2.0) - \varepsilon_r(x = 1.5) = +1.2$ at 400 nm and of $\Delta\varepsilon_r = \varepsilon_r(x = 2.0) - \varepsilon_r(x = 1.5) = +3.5$ at 700 nm. These calculated values are indeed non-zero. Instead, they are, respectively, a factor 2 too large and too small to describe the observed optical transmission change. Possibly, the measured resistivity change may not due to the changing hydrogen content in the Hf layer only. Figure 5.23 shows the resistivity change of the whole sample, including a Pd-capping layer and the PFTE coating. Although we compensate the lower resistivity of Pd (105 nΩ m)
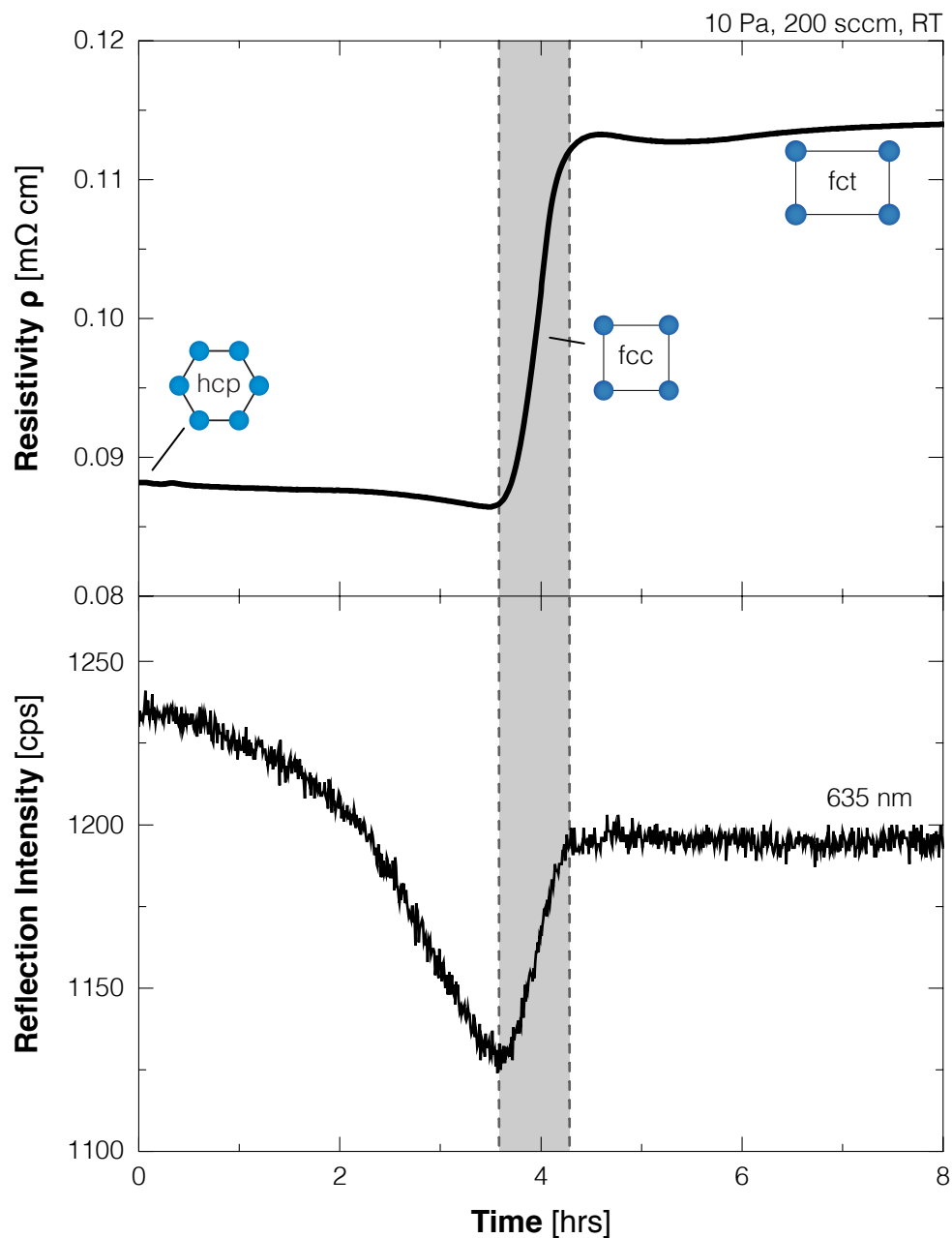
Figure 5.23 | Electrical Resistivity in HfH$_x$ – The electrical resistivity ρ (top) and the optical reflection intensity at 635 nm (bottom) as a function of time of a PTFE coated Pd-capped hafnium thin flim (40 nm). The *as-prepared* film is exposed to a constant hydrogen pressure of 10 Pa with a flow of 200 sccm at room temperature. The gray area indicates the HfH$_x$ fcc phase.

compared to Hf ($303\ \text{n}\Omega\ \text{m}$) by reducing the Pd-capping layer to only $3\ \text{nm}$ and expose the sample to a pressure ($10\ \text{Pa}$) that should not hydrogenate the Pd layer, we cannot rule out that the Pd layer contributes to the measured resistivity change.

The Optical Reflection of the FCC-FCT Phase Transition
One of the main questions resulting from linking the structural to the optical data is *why is the fcc-fct phase transition not reflected in the optical isotherms?* Despite that the maximum (111) lattice spacing coincides with the end of the linear relation between $|\ln(\mathcal{T}/\mathcal{T}_{\text{unl}})|$ and x (indicated by $\mathcal{T}_{\text{lin}}$), figure 5.21 suggests that changing behavior of the optical transmission is the likely to be the result of the same behavior of the hydrogen content in the Hf layer rather than being a consequence of the deformation of the cubic lattice. In addition, we do not observe any optical effect between $10^0 - 30\ \text{Pa}$ where the expansion of the (111) lattice spacing observed is most prominent: no kink or change in slope in optical transmission is observed (see figure 5.4).

In accordance with Lambert-Beer law (see equation 5.6), the thickness d and the absorption coefficient α of the Hf layer are also not affected by the fcc-fct phase transition. As shown in figure 5.20, the analysis of the neutron data suggests that at $\mathcal{T}_{\text{lin}}$ there are no anomalies in the Hf layer thickness. DFT calculations indicate that the fcc-fct phase transition does not induce a significant change in the optical properties of the Hf layer. As shown in figure 5.22 the imaginary part of the dielectric function ε_i calculated for HfH$_2$ with a fct and a (hypothetical) fcc structure are identical between $400 - 750\ \text{nm}$. Assuming that this is also true for the real part of the dielectric function ε_r, equation 5.7 indicates that the absorption coefficient is hardly affected by the fcc-fct phase transition. Nevertheless, the DFT calculations indicate that the fct structure of HfH$_2$ is energetically more favorable than the fcc structure ($\sim 0.5\ \text{eV}$ per 2×1 formula unit).

5.5 Discussion — Entropic Description of the Pressure Range

One of the most characteristic hydrogen detection property of Pd-capped HfH$_x$ thin films is the large pressure range of at least 6 and potentially 10 orders of magnitude. This pressure range is mainly defined by a linear relation between the applied hydrogen pressure and the change of the optical transmission of the film on a log-log scale:

$$\ln\left(\frac{P}{P_0}\right) = \ln\left(\frac{P_{\text{unl}}}{P_0}\right) + c(\lambda, d)\ln\left(\frac{\mathcal{T}}{\mathcal{T}_{\text{unl}}}\right). \tag{5.17}$$

Here P_{unl} equals the equilibrium pressure of the hcp $\rightarrow$ fcc phase transition and c is the slope of the linear relation, which is a function of the wavelength λ and the film thickness d (see figure 5.12). In the previous section we find that this relation only applies to the fcc hydride phase; the transition to the fct hydride phase results in a saturation of the optical transmission. Through neutron reflectometry we find that $\ln(P/P_0)$ is linearly related to x, indicating that also $(\mathcal{T}/\mathcal{T}_{unl})$ is a linear function of x (see figure 5.21 and equation 5.5). This is supported by the fact that the measured optical transmission change between the *unloaded* and the *saturated* state matches the optical transmission change obtained from the dielectric functions calculated for HfH$_{1.5}$ and HfH$_{2.0}$, assuming this linear relation. This leaves us with the question *what induces a pressure increase of at least* 6 *orders of magnitude and appears to be a linear function of* x?

Despite the pressure range is hysteresis free, the solubility range of the fcc hydride phase is too large to be fitted to a classical Sieverts' behavior ($\sqrt{P/P_0} = x/\sqrt{K}$). Furthermore, we find that the pressure range shifts uniformly with temperature, which is contradicts Sieverts' behavior. A Van 't Hoff analysis yields a constant ΔH while the entropy varies and reaches large, seemingly unphysical, values (see figure 5.5). Usually, the entropy change is dominated by the entropy of the hydrogen in the gas phase (-131 J/(K mol H$_2$)). However, to describe the pressure range the move from *unloaded* ($x = 1.43$) to the *saturated* ($x = 1.98$) state should induces change in ΔS from -79.9 J/(K mol H$_2$) to -252 J/(K mol H$_2$). A significant part, from -79.9 J/(K mol H$_2$) to -228 J/(K mol H$_2$), can be assigned to the fcc hydride phase. Below we investigate whether two well-known contributions, the configurational and the vibrational entropy (optical phonos) of dissolved hydrogen in the HfH$_x$ lattice, are large enough to describe the observed entropy change.

In this approach, we mainly focus on the entropy change between $1.80 < x < 1.94$. In this way, we consider only the entropy change in the measured pressure range and disregard any lattice deformations. However, we will consider $x = 1.43$ in order to find whether the contributions can describe the entropy to this extrapolated state. To relate the entropic contributions to the measured ΔS, we describe the dissolved hydrogen in the HfH$_x$ lattice by a lattice gas model. In this way, we ignore the entropy of the Hf host and write:

$$\Delta S(x) = 2\bar{S}_{H_x} - \bar{S}^0_{H_x}, \tag{5.18}$$

where $\bar{S}^0_{H_x}$ is the standard molar entropy of the hydrogen gas (131 J/(K mol H$_2$)). We define the partial molar entropy as the sum of the configurational $\bar{S}_{conf}$ and vibrational $\bar{S}_{vib}$ entropy, which both depend on x:

$$\bar{S}_{H_x} = \bar{S}_{conf}(x) + \bar{S}_{vib}(x). \tag{5.19}$$

5.5.1 Configurational Entropy

The configurational entropy accounts for all possible configurations of the hydrogen atoms in the fcc lattice and the classical model is described by:

$$\bar{S}_{\text{conf}}(x) = -R \ln\left[\frac{x}{r-x}\right]. \tag{5.20}$$

Here, r is the maximum hydrogen fraction within the system. With HfH$_x$ being a tetrahedral system, $r = 2$. In this way we find:

$$\bar{S}_{\text{conf}}(x = 1.43) = -7.65 \text{ J/(K mol H}_2) \tag{5.21a}$$
$$\bar{S}_{\text{conf}}(x = 1.80) = -18.3 \text{ J/(K mol H}_2) \tag{5.21b}$$
$$\bar{S}_{\text{conf}}(x = 1.94) = -29.8 \text{ J/(K mol H}_2) \tag{5.21c}$$

This result in

$$\Delta S(x = 1.43) = 2 \times (-7.61) - 131 = -146 \text{ J/(K mol H}_2)$$
$$\text{exp. -79.9 J/(K mol H}_2) \tag{5.22a}$$
$$\Delta S(x = 1.80) = 2 \times (-18.3) - 131 = -168 \text{ J/(K mol H}_2)$$
$$\text{exp. -180 J/(K mol H}_2) \tag{5.22b}$$
$$\Delta S(x = 1.94) = 2 \times (-29.8) - 131 = -189 \text{ J/(K mol H}_2)$$
$$\text{exp. -228 J/(K mol H}_2) \tag{5.22c}$$

For none of the considered states the calculated ΔS matches the experimental values.

The configurational entropy can be expressed in different ways, depending on the model used.[5.40 — 5.42] For example, Boureau presents a model taking into account the hard-core repulsion between screened protons up to the second nearest neighbor:[5.41]

$$\bar{S}_{\text{conf}}(x) = -R \ln\left[\frac{(6-x)\,x}{(6-4\,x)^2}\right]. \tag{5.23}$$

In this way, we find a much stronger contribution at $x = 1.43$ than at $x = 1.94$:

$$\bar{S}_{\text{conf}}(x = 1.43) = -38.8 \text{ J/(K mol H}_2) \tag{5.24a}$$
$$\bar{S}_{\text{conf}}(x = 1.80) = -13.5 \text{ J/(K mol H}_2) \tag{5.24b}$$
$$\bar{S}_{\text{conf}}(x = 1.94) = -7.76 \text{ J/(K mol H}_2) \tag{5.24c}$$

This means that at $x = 1.43$ ΔS would be more negative than at $x = 1.94$:

$$\Delta S(x = 1.43) = 2 \times (-36.8) - 131 = -205 \text{ J/(K mol H}_2)$$

$$\text{exp. -79.9 J/(K mol H}_2) \tag{5.25a}$$

$$\Delta S(x = 1.80) = 2 \times (-13.5) - 131 = -158 \text{ J/(K mol H}_2)$$

$$\text{exp. -180 J/(K mol H}_2) \tag{5.25b}$$

$$\Delta S(x = 1.94) = 2 \times (-7.76) - 131 = -147 \text{ J/(K mol H}_2)$$

$$\text{exp. -228 J/(K mol H}_2) \tag{5.25c}$$

This is opposite to our observations. In general, we find that the difference in entropy generated by configurational terms is too small to describe the large pressure range where there is a linear relation.

5.5.2 Vibrational Entropy

The vibrational entropy $\bar{S}_{\text{vib}}$ describes the contribution of the vibration of the hydrogen atoms within a lattice and follows from the Einstein model, which defines a single temperature T_E where all vibration modes of the lattice are excited. It is given by

$$\bar{S}_{\text{vib}}(x) = -\frac{3R}{2} \left\{ \ln \left[1 - \exp \left(-\frac{\mathcal{T}}{\mathcal{T}_E(x)} \right) \right] - \frac{\mathcal{T}}{\mathcal{T}_E(x)} \frac{1}{\exp \left(-\frac{\mathcal{T}}{\mathcal{T}_E(x)} \right) - 1} \right\}. \tag{5.26}$$

However, it is known that complex systems like metal hydrides have modes consisting of multiple unique frequencies and therefore results in a higher temperature to excite all frequency modes. This model is known as the Debye Model and does not result in a simple expression for $\bar{S}_{\text{vib}}$. Using a rough simplification and considering only temperatures far above zero Kelvin, the Einstein temperature can be expressed in terms of the Debye temperature T_D by

$$T_E(x) = \sqrt[3]{\frac{\pi}{6}} T_D(x). \tag{5.27}$$

The Debye temperature of different hydrogen contents within the Hf layers is recently calculated by Wang et al.[5.43] From $x = 1.5$ to $x = 1.75$ the Debye temperature reduces from 339 K to 195 K. A linear inter-/extrapolation leads to $T_D(x = 1.43) = 379$ K, $T_D(x = 1.80) = 166$ K, and $T_D(x = 1.94) = 86$ K, or equivalent to $T_E(x = 1.43) = 305$ K, $T_E(x = 1.80) = 134$ K, and $T_E(x = 1.94) = 69$ K. Inserting these temperatures

in equation 5.26, we find that:

$$\bar{S}_{\text{vib}}(x = 1.43) = -14.4 \text{ J/(K mol H}_2) \tag{5.28a}$$

$$\bar{S}_{\text{vib}}(x = 1.80) = -18.0 \text{ J/(K mol H}_2) \tag{5.28b}$$

$$\bar{S}_{\text{vib}}(x = 1.94) = -53.0 \text{ J/(K mol H}_2), \tag{5.28c}$$

which results in:

$$\Delta S(x = 1.43) = 2 \times (-14.4) - 131 = -205 \text{ J/(K mol H}_2)$$
$$\text{exp. -160 J/(K mol H}_2) \tag{5.29a}$$

$$\Delta S(x = 1.80) = 2 \times (-18.0) - 131 = -167 \text{ J/(K mol H}_2)$$
$$\text{exp. -180 J/(K mol H}_2) \tag{5.29b}$$

$$\Delta S(x = 1.94) = 2 \times (-53.0) - 131 = -237 \text{ J/(K mol H}_2)$$
$$\text{exp. -228 J/(K mol H}_2). \tag{5.29c}$$

Again, the calculated values do not match the experimental found values although the vibrational entropy gives a better description than the configurational entropy, especially at $x = 1.80$ and $x = 1.94$.

Even if we combine the configurational and vibrational contributions through equation 5.19 we cannot describe the pressure range found experimentally. This is the case for using the classical model:

$$\Delta S(x = 1.43) = 2 \times (-7.61 - 14.4) - 131 = -175 \text{ J/(K mol H}_2)$$
$$\text{exp. -160 J/(K mol H}_2) \tag{5.30a}$$

$$\Delta S(x = 1.80) = 2 \times (-18.3 - 18.0) - 131 = -225 \text{ J/(K mol H}_2)$$
$$\text{exp. -180 J/(K mol H}_2) \tag{5.30b}$$

$$\Delta S(x = 1.94) = 2 \times (-29.8 - 53.0) - 131 = -295 \text{ J/(K mol H}_2)$$
$$\text{exp. -228 J/(K mol H}_2). \tag{5.30c}$$

as well for using Boureau's model for the configurational entropy:

$$\Delta S(x = 1.43) = 2 \times (-36.8 - 14.4) - 131 = -233 \text{ J/(K mol H}_2)$$
$$\text{exp. -160 J/(K mol H}_2) \tag{5.31a}$$

$$\Delta S(x = 1.80) = 2 \times (-13.5 - 18.0) - 131 = -194 \text{ J/(K mol H}_2)$$
$$\text{exp. -180 J/(K mol H}_2) \tag{5.31b}$$

$$\Delta S(x = 1.94) = 2 \times (-7.8 - 53.0) - 131 = -253 \text{ J/(K mol H}_2)$$
$$\text{exp. -228 J/(K mol H}_2). \tag{5.31c}$$

Other Entropy Contributions

Figure 5.24 shows the contribution of the above described configurational and vibrational entropy to the standard molar entropy $\bar{S}_{H_2}$ as a function of the hydrogen content x. We immediately conclude that Boureau's approach does not describe the experimentally obtained $\bar{S}_{H_2}$, calculated from the observed ΔS and the standard molar entropy of the hydrogen gas $\bar{S}^0_{H_2}$. The main issue with this model is that equation 5.23 shows a singularity at $x = 1.5$, which is well within the fcc hydride phase. A singularity at or close to $x = 2$ should fit the experimentally obtained $\bar{S}_{H_2}$. However, we lack a physical reason to alter equation 5.23 since it successfully describes the configurational entropy of hydrogen in fcc titanium and fcc zirconium.[5.41]

Despite that the values of the (classical) configurational and the vibrational entropy matches the experimentally obtained $\bar{S}_{H_2}$ the best between $1.8 < x < 1.94$, its relation to x does not match. Even combined, the $\bar{S}_{\text{conf}}$ and $\bar{S}_{\text{vib}}$ are not a linear function of x. As a result, there is a significant mismatch at $x = 1.43$. We therefore
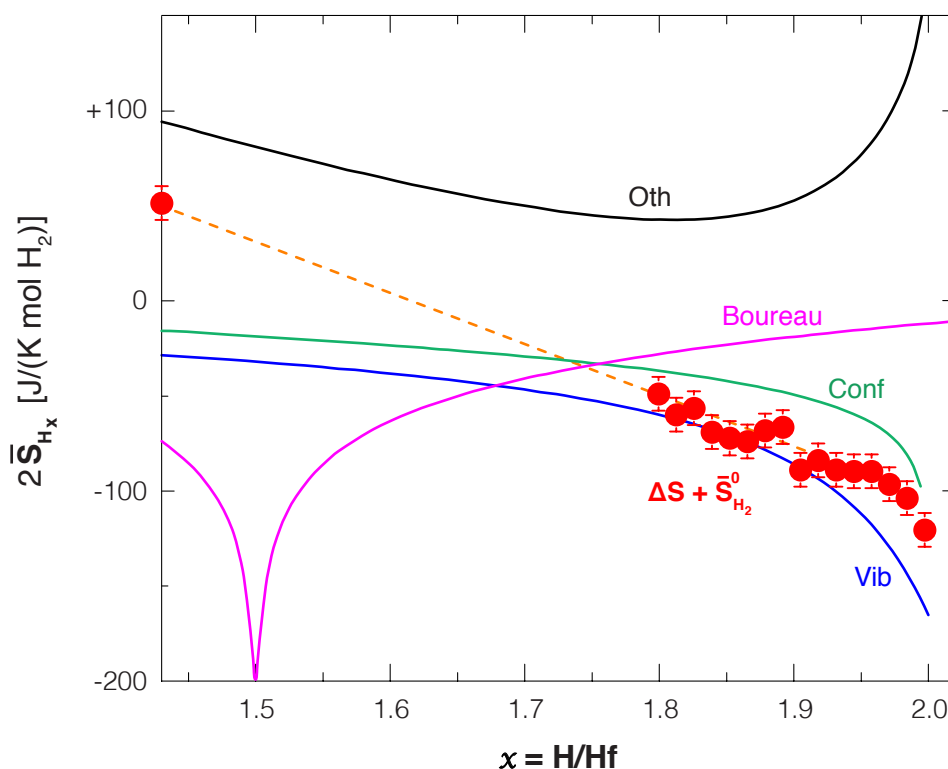
Figure 5.24 | Entropy Contributions to ΔS – The contribution of the vibrational (blue) and the configurational – through the classical (green) and Boureau's (magenta) approach – entropy to the standard molar entropy twice $2\bar{S}_{H_2}$. The black line indicates the entropy needed to match the experimental value $\Delta S + \bar{S}^0_{H_2}$ (red data points), assuming that $\bar{S}_{H_2}$ is at least the sum of the classical configurational and vibrational entropy.

conclude that there must be other contributions that, together with $\bar{S}_{\text{conf}}$ and $\bar{S}_{\text{vib}}$, should add up to a linear relation between $\bar{S}_{\text{conf}}$ and $\bar{S}_{\text{vib}}$ and x. To also describe the experimentally observed entropy at $x > 1.94$ we are looking for contributions that add up to a positive contribution along the whole hydrogen fraction range, with the largest contributions at $x \approx 1.43$ and at $x > 1.94$ (see figure 5.24).

In the search for entropy contributions other than the configurational and the vibrational entropy, we have to keep in mind that they have to have a constant temperature component as the enthalpy remains constant within the fcc hydride phase (see figure 5.5). This means that we can rule out stress as the main other contributor, despite it is known that it can affect the absorption thermodynamics of thin films significantly[5.44 − 5.46] and that we observe a strong expansion of the (111) lattice expansion between 10^{-1} – 30 Pa while the film thickness remains rather constant within this pressure range. However, the stresses σ affect mainly the enthalpy than rather the entropy:

$$\delta H \propto \sum_{j=x,y,z} \sigma_j \epsilon_j, \tag{5.32}$$

where ϵ_i is the strain tensor.

A possible contribution may be found in the enthalpic terms that have a temperature component. An example is the heat capacity C_p, which shows a $\sim 5\%$ increase within the fcc hydride phase and has a strong temperature dependence.[5.7] Being linearly related to the enthalpy ($\delta H \sim C_P \, \delta T$) an enthalpic term could be hidden in the entropy. However, calculations indicate that the contribution to the entropy is too small to be of significance.[5.7]

5.6   New Perspectives

The most characteristic sensing property of HfH$_x$ thin films is the linear optical response to hydrogen over almost at least 6 and possibly 10 orders of magnitude in pressure. We find similar behavior in Pd$_{70}$Au$_{30}$H$_x$[5.47] and nitrogen doped TaH$_x$ (see appendix) thin films, although over a much smaller pressure range. When we plot these results together (see figure 5.25), we find that each material operates in a different pressure range. This means that we can select the pressure range of the sensor by the choice of the appropriate material.

Remarkably, the linear relations of all the three materials plotted in figure 5.25 exhibit the same slope. All three materials are studied by means of white light and the corresponding films have approximately the same thickness (~ 40 nm). Nevertheless, the same slope seems to be a coincidence rather than a general feature. We find that the slope of the linear relation in Pd$_{70}$Au$_{30}$H$_x$ depends strongly on the Au gold concentration,[5.47] while in TaH$_x$ it is a function of the nitrogen concentration

(see appendix). In both cases a different doping level will result in a different optical contrast, and therefore in a different slope.

From the three materials plotted in figure 5.25, we consider HfH_x as the most effective sensing material. First, the fast switching (to an increasing pressure) observed in the $10^{-3} - 10^{-1}$ Pa range is unique.[5.3] Second, the pressure and the transmission can be described by a single relation. This is in contrast to $Pd_{70}Au_{30}H_x$ and (very likely) TaH_x, where we a different relation at low pressures (or at low hydrogen fractions: $x < 0.01$) as for both cases the system is considered to be dilute. As a result,
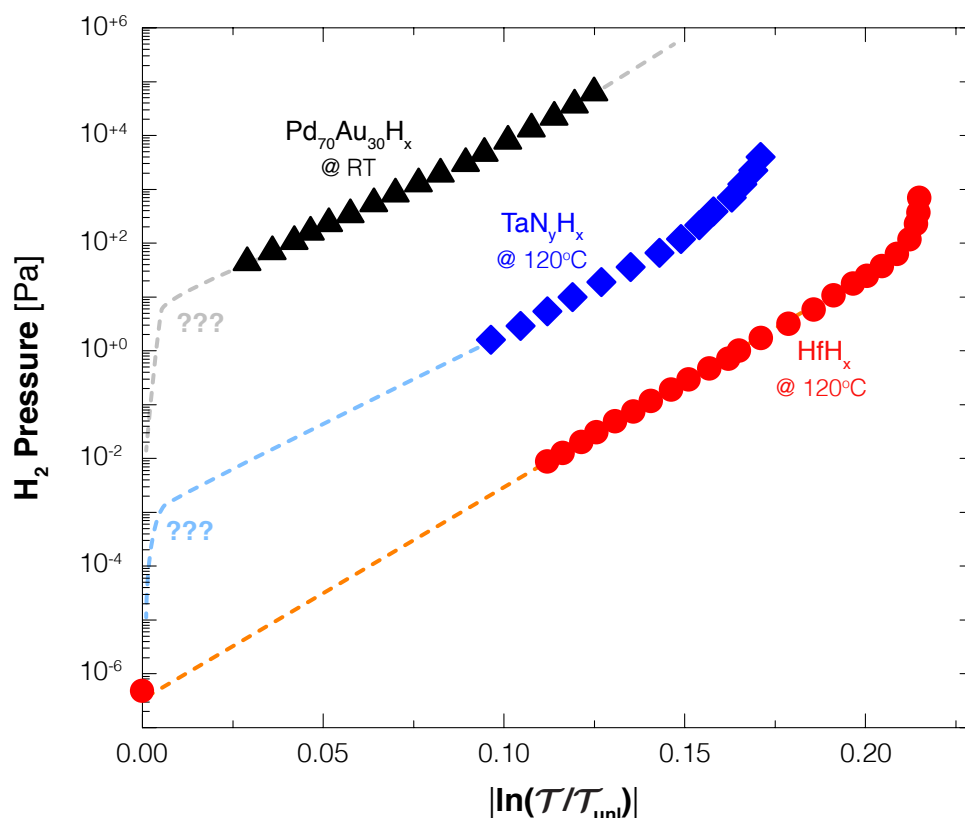
Figure 5.25 | Optical Hydrogen Sensing Materials – The pressure range and optical transmission change of Pd capped HfH_x (red circles, this chapter) and TaN_yH_x (blue diamonds, see appendix) at $120°C$ with respect to the reported transmittance of $Pd_{70}Au_{30}H_x$ (black triangles, adapted from Westerwaal *et al.*).[5.47] The dashed lines are extrapolations based on the behavior close to the unloaded state $\mathcal{T}_{unl}$. The question marks indicates the unknown behavior of TaN_yH_x close to $\mathcal{T}_{unl}$ and the unknown behavior of $Pd_{70}Au_{30}H_x$ above 10^{+5} Pa. Note that the transmission change of HfH_x and TaN_yH_x with increasing pressure is negative, while $Pd_{70}Au_{30}H_x$ shows a positive transmission change.

it should obey Sieverts' law ($\sqrt{P/P_0} \sim x$).[5.4,5.48] We do not find any signs of such a behavior nor are there any reports in bulk that Sieverts' law is observed within the fcc hydride phase.

The discovery of Hf and followed by nitrogen doped TaH$_x$ as optical hydrogen detection materials indicates that transition metal hydrides are perfectly suitable for detecting hydrogen within a large pressure range. Besides being suitable for micro-mirror based sensors, we expect that these materials are also suitable for Local Surface Plasmon Resonance (LSPR) based architecture.[5.49 − 5.51] Using such an architecture could also improve the limited diffusion kinetics at room temperature. HfH$_x$ shows that a hysteresis free pressure ranges can also be found in phases other than those being dilute. It also shows that we can consider systems where a coherent phase transitions occur to be a potential hydrogen detection material. This significantly increases the number of potential hydrogen detection materials.

5.7   Conclusions

We conclude that Pd-capped Hf thin films are perfectly suited to be used as large range optical hydrogen sensors. We find that the material shows a great stability, a good reproducibility, and no hysteresis. The optical sensitivity and resolution are similar to or even better than Pd-based materials, which have so far been considered as the most effective sensing materials. Only the response time (in the order of 40 minutes at room temperature) cannot match that of Pd-based materials. Another great advantage is that the pressure range has natural boundaries. The lower limit is defined by the hcp $\rightarrow$ fcc phase transition at HfH$_{1.43}$ while the upper limit equals the saturation of the hydrogen content at HfH$_{1.98}$. The most characteristic sensing property is, however, the anomalous large pressure range of at least 6 and possibly 10 orders of magnitude, which is also hysteresis free. In addition, a significant part of this pressure range can be described by a simple (linear) relation between the pressure and the optical transmission of the film.

Both structurally and thermodynamically we find that HfH$_x$ thin films show some similarities to bulk. In thin films we find the same hydride phases, while within the fcc hydride phase the enthalpy remains also constant and equals the same value. On the other hand, in thin films the fcc hydride phase spans a much larger hydrogen fraction range ($1.43 < x < 1.94$ vs. $1.62 < x < 1.79$), the fcc-fct phase transition is coherent, and the entropy change within the fcc hydride phase is much larger (within the same x range). Neutron reflectometry shows that both the optical transmission and the pressure (both on a logarithmic scale) are linearly related to x. The latter contradicts studies on bulk, although their results do not exclude such a relation. The large pressure range induces a seemingly unphysically large entropy change within the fcc and fct phase. As a result, the well-known configurational and vibrational

entropy cannot describe such a change. A better understanding of the thermodynamic behavior in HfH$_x$ is essential. Not only to possibly tune the pressure range of HfH$_x$ by nano-scale effects, but also to guide a search for other hydrogen detection materials. Nevertheless, the brief study on HfH$_x$ already changes the current view on hydrogen detection materials and significantly increases the number of potential hydrogen detection materials.

Appendix

In this appendix we briefly discuss three transition-metal-hydrides with respect to their (optical) sensing properties. These materials are TiH_x, ZrH_x, and TaH_x. TiH_x and ZrH_x are, just as HfH_x, group IV hydrides of the periodic table. TaH_x is a group V hydride. This means that electronically TiH_x, ZrH_x, and HfH_x are similar, while TaH_x has one more d-electron. Nevertheless the structural properties of these materials show great similarities. This is reflected in their optical properties on which we focus in this appendix. For TaH_x we also include some preliminary structural results obtained from x-ray diffraction. From this we find that TiH_x, ZrH_x, and also TaH_x have good optical hydrogen sensing properties, although they are not that effective as HfH_x.

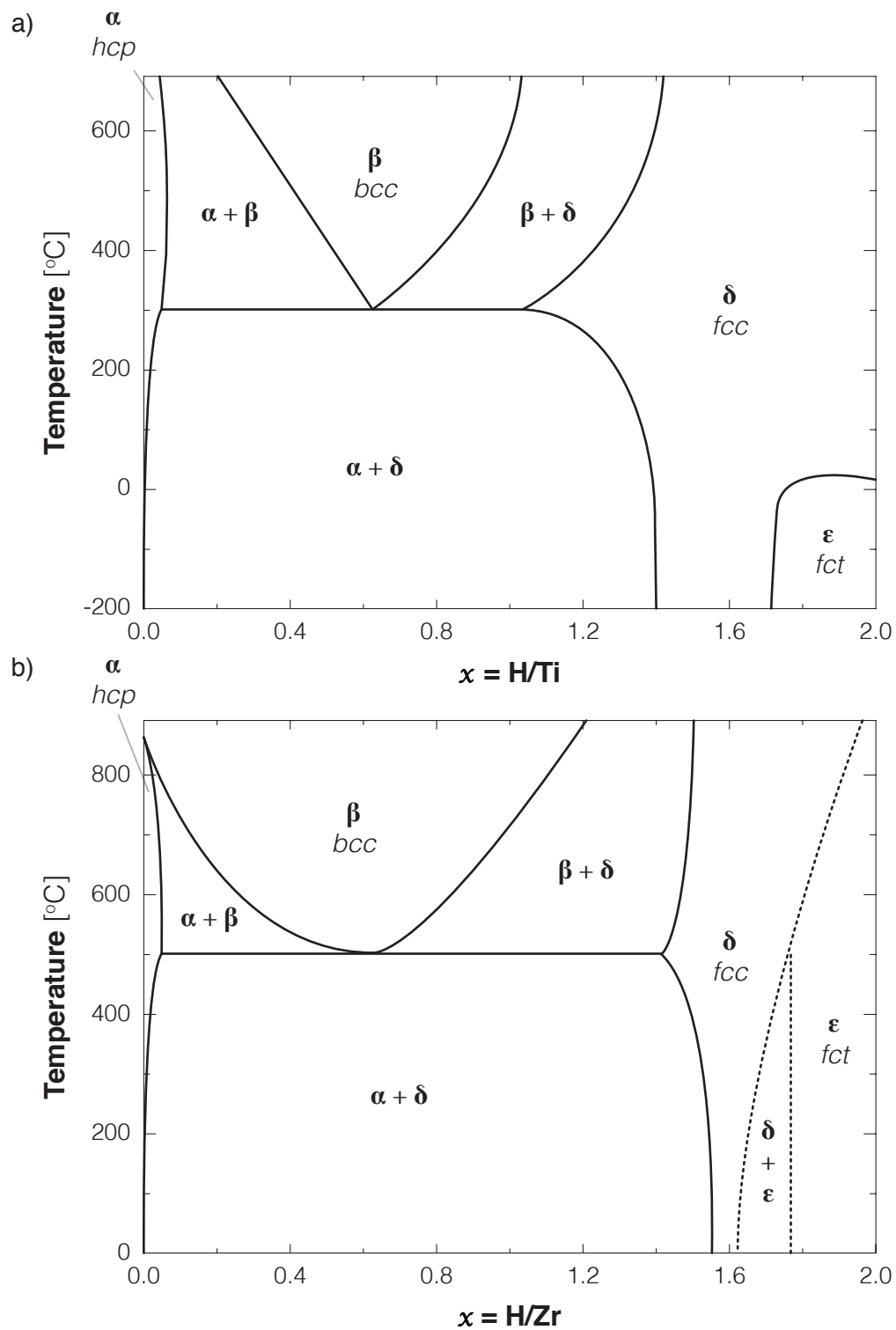## A1 Titanium- & Zirconium-Hydride

A1.1 Background – Bulk

Just as hafnium, titanium and zirconium are both group IV elements of the periodic system. As a result, the phase diagrams of TiH_x and ZrH_x are very similar to that of HfH_x (see figure A1). At low temperatures ($<300°C$ for TiH_x and $<500°C$ for ZrH_x) the same distinct hydride phases are present. There is a dilute hcp hydride phase, a fcc hydride phase and a fct hydride phase. Note that for TiH_x the fct hydride phase is only observed at temperatures below $25°C$.[5.52] Different for each system are the boundaries of the fcc hydride phase. At $120°C$, the fcc hydride phase in TiH_x spans a large hydrogen range ($1.38 \leq x \leq 2$) while in ZrH_x this phase is found between only $1.56 \leq x \leq 1.63$. Note that in HfH_x the fcc hydride phase is found between $1.62 \leq x \leq 1.79$.

In contrast to TiH_x (below $<25°C$), the fcc-fct phase transition in ZrH_x is not well defined. Multiple studies show each a different position of the fcc/fct phase boundary.[5.53 — 5.55] Although the studies show the presence of a coexistence region at low temperatures, it is not clear how large this region is and what the critical temperature is. This may result in a different description of the isotherms at room temperature compared to elevated temperatures.

Thermodynamics

Figure A2 shows the partial pressure-composition-isotherms (PCIs) of (non-powder) bulk TiH_x and ZrH_x measured at high temperatures ($>550°C$). In contrast to the

a)

b)

Figure A1 | Titanium-Hydrogen & Zirconium-Hydrogen Phase Diagrams – Non-isobaric (up to $1\,\mathrm{atm.}$) phase diagrams of **a)** the titanium-hydrogen and **b)** the zirconium-hydrogen (bottom) system adapted from San-Martin *et al.* [5.56] and Zuzek *et al.*, [5.54] respectively. The phase boundaries that are not well-defined are indicated by dashed lines.
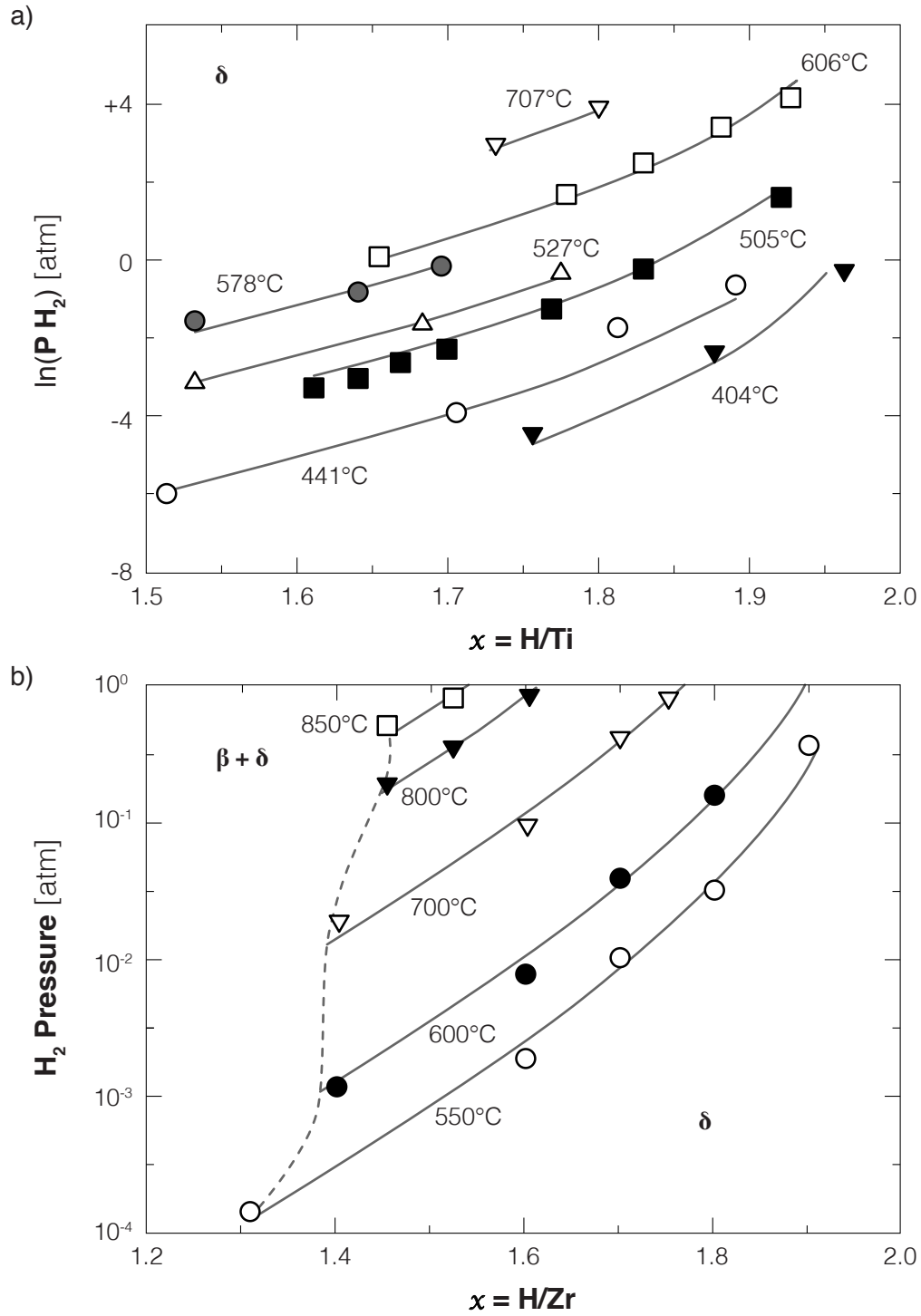
Figure A2 | TiH$_x$ & ZrH$_x$ Isotherms – High temperature partial pressure-composition-isotherms (PCIs) of **a)** bulk titanium and **b)** bulk zirconium adapted from Wang *et al.*[5.57,5.58] De symbols are data points obtained from multiple studies. The solid lines are fits of equation A.3 ($a = 10.65$, $b = 3.65$, and $d = (-17.77 + 0.32\,x) \times 10^3$ for TiH$_x$, $a = 8.01$, $b = 5.21$, and $d = -20.7 \times 10^3$ for ZrH$_x$).

HfH_x isotherms, these isotherms show a strong curvature and therefore only a part can be described by the linear relation between $\ln(P/P_0)$ and $\ln(x/(1+x))$. To describe the full isotherms it is suggested that they can be described a quasi-chemical model.[5.57 − 5.59] This model is of the form

$$\ln\left(\frac{P}{P_0}\right) = \frac{2}{R}\ln\left(\frac{x}{2-x}\right) + a + b\,x + \frac{d}{T} \qquad (A.3)$$

Here the first term on the right-hand side represents the arrangements of hydrogen in the interstitial tetrahedral sites (i.e. configurational entropy), a the vibrational entropy, and $b\,x$ the interaction between nearest neighboring atoms. d is related to the free energy (i.e. ΔH) of hydrogenation. For TiH_x the isotherms can be fitted by equation A.3 with $a = 10.65$, $b = 3.65$, and $d = (-17.77 + 0.32\,x) \times 10^3$, while for ZrH_x $a = 8.01$, $b = 5.21$, and $d = -20.7 \times 10^3$.

The good match between the mathematical form of the quasi-chemical model and the experimental data suggests that the vibrational entropy is not a function of the hydrogen fraction. However, it is reported that the Debye temperature (related to the vibrational entropy by equation 5.26) changes with x, although in ZrH_x the change is small.[5.56,5.60] Also the suggestion that ΔH is constant in ZrH_x is not in agreement with experimental data.[5.54] The use of the model to describe the isotherms in TiH_x can also be questioned as San-Martin *et al.* report that ΔS remains constant within the fcc hydride phase.[5.56] This suggests that the increase of the pressure is due to a change of ΔH, which is not in described by equation A.3.

For the hcp $\rightarrow$ fcc phase transition, the thermodynamic parameters are different for each system. We find that the corresponding enthalpy of formation of ZrH_x is larger than of TiH_x and of HfH_x: $\delta H_{hcp \rightarrow fcc} = -104$ kJ/mol H_2 for TiH_x[5.56] and $\delta H_{hcp \rightarrow fcc} = -199$ kJ/mol H_2 for ZrH_x[5.54] *versus* $\delta H_{hcp \rightarrow fcc} = -112.8$ kJ/mol H_2 for HfH_x. The entropy of formation corresponding to this transition is in ZrH_x also much larger than we find in TiH_x and HfH_x: $\delta S_{hcp \rightarrow fcc} = -92$ J/(K mol H_2) for TiH_x and $\delta S_{hcp \rightarrow fcc} = -171$ J/(K mol H_2) for ZrH_x *versus* $\delta S_{hcp \rightarrow fcc} = -79.9$ J/(K mol H_2) for HfH_x. As a result, the fcc hydride formation pressure at $120°C$ is for TiH_x very similar to that of HfH_x (10^{-6} Pa vs 10^{-7} Pa) while that of ZrH_x is many orders lower (10^{-13} Pa).

Optical Results – Thin Films

Although the properties of bulk TiH_x and ZrH_x suggest that there are some differences with that of HfH_x, preliminary results show that the optical response to hydrogen of Pd-capped TiH_x, ZrH_x, and HfH_x thin films (all 40 nm) is very similar. Figure A3 shows the optical transmission (white light) change of the three systems as a function of time, where – over the time – the hydrogen pressure is (slightly) increased.

As in HfH_x, we find that the optical transmission in TiH_x and ZrH_x also first increases, then decreases until it reaches a stable level (T_{sat}). Again, similar to HfH_x, exposing the films to oxygen results only in partially unloading (not shown). The transmission only increases and converges to the maximum transmission level $\mathcal{T}_{unl}$ reached during the first exposure to hydrogen. Because of the great similarities between the phase diagrams of TiH_x, ZrH_x, and HfH_x, we expect that also in TiH_x and ZrH_x the increase of the optical transmission reflects the hcp $\rightarrow$ fcc phase transition. In addition, the decrease of the optical transmission is expected to be connected to the fcc hydride phase and (possibly) the transition to the fct hydride phase. In addition, we expect that when we expose the hydrogenated films to oxygen the films will return to their fcc hydride phase.

Besides these similarities, the magnitude of the transmission change differs for each system. The positive transmission change of ZrH_x thin films is more than twice
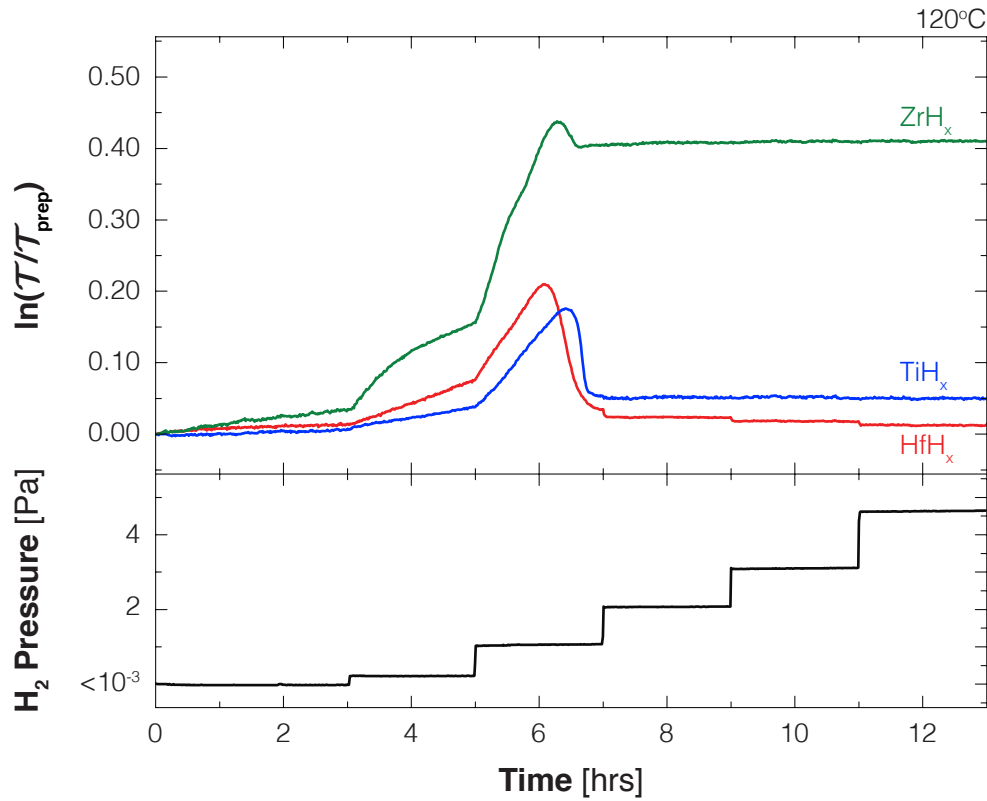
Figure A3 | Titanium & Zirconium Thin Films: Optical Response to Hydrogen – The optical transmission change $\ln(\mathcal{T}/\mathcal{T}_{prep})$ of a Pd-capped Ti and Zr thin film (both $40\ \mathrm{nm}$) as a function of time, where the film is exposed to a different partial hydrogen pressures below $5\ \mathrm{Pa}$ (vacuum) all at $120°\mathrm{C}$. The symbols indicate the structural evolution based on the phase diagrams and the results of HfH_x.

as large as we find with TiH$_x$ or HfH$_x$ thin films (which are similar): $\ln(\mathcal{T}_{unl}/\mathcal{T}_{prep}) = +0.438$ for ZrH$_x$ *versus* $\ln(\mathcal{T}_{unl}/\mathcal{T}_{prep}) = +0.176$ for ZrH$_x$ *versus* $\ln(\mathcal{T}_{unl}/\mathcal{T}_{prep}) = +0.185$ for HfH$_x$. The negative transmission change in ZrH$_x$ is, however, much smaller than observed in TiH$_x$ and HfH$_x$: $\ln(\mathcal{T}_{unl}/\mathcal{T}_{prep}) = -0.036$ for ZrH$_x$ *versus* $\ln(\mathcal{T}_{unl}/\mathcal{T}_{prep}) = -0.125$ for TiH$_x$ *versus* $\ln(\mathcal{T}_{unl}/\mathcal{T}_{prep}) = -0.218$ for HfH$_x$. This means that HfH$_x$ has the largest and ZrH$_x$ the smallest optical contrast within the fcc/fct hydride phase.

Another optical difference is that in ZrH$_x$ the transmission increase is not always linear (see figure A3). Between $3-5\ \mathrm{hrs}$ (applying a constant partial hydrogen pressure of $0.2\ \mathrm{Pa}$) we find that transmission increase reduces over time. A similar effect is observed in the next pressure step (between $5-7\ \mathrm{hrs}$), although less prominent. This effect suggest that the diffusion of hydrogen within the sample is limited. A possible explanation is that the hydrogen diffusion within the fcc hydride phase is significantly slower than in the hcp hydride phase. As a result, the larger the fraction of fcc hydride phase the slower the conversion from the hcp hydride phase will be.

The small negative optical transmission change in ZrH$_x$ thin films can be understand from the small hydrogen fraction range where the system is in the fcc hydride phase. At $120°\mathrm{C}$ this is only $\delta x = 0.07$. As a result, the change of the absorption coefficient will be limited. In TiH$_x$ the fcc hydride phase spans a much larger hydrogen fraction range ($\delta x = 0.62$ at $120°\mathrm{C}$), even larger than HfH$_x$ ($\delta x = 0.17$ at $120°\mathrm{C}$). Nevertheless the negative optical transmission change is in TiH$_x$ smaller than in HfH$_x$. We therefore expect that the film the change of the absorption coefficient (i.e. dielectric function) is significantly smaller than in HfH$_x$.

Outlook

From the preliminary results on Pd-capped TiH$_x$ and ZrH$_x$ thin films we expect that these systems can be used as optical hydrogen sensing materials, although they appear not as effective as Pd-capped HfH$_x$ thin films. First, the pressure range is smaller for TiH$_x$ and ZrH$_x$ given the smaller entropy change per H in compared to HfH$_x$. Second, in TiH$_x$ and ZrH$_x$ the enthalpy of hydrogen formation is not constant, which implies that the relation between the optical transmission of the film and the applied hydrogen pressure changes with temperature. Third, the optical transmission change for both systems is less than observed with HfH$_x$. On the other hand, the different thermodynamics suggest that TiH$_x$ and ZrH$_x$ based sensors are operational in lower pressure range. However, a more detailed study is necessary to confirm the potential of Pd-capped TiH$_x$ and ZrH$_x$ thin films as optical hydrogen sensing materials.

A2 Tantalum-Hydride

A2.1 Background – Bulk

Figure A4 shows the phase diagram of the tantalum-hydrogen system based on bulk samples.[5.48,5.61] The diagram can be divided into two parts. Above $61°C$ only the α hydride phase exists, which corresponds to a disordered solution of hydrogen in a bcc lattice. Below $61°C$ several other distinct hydride phases are observed. All the
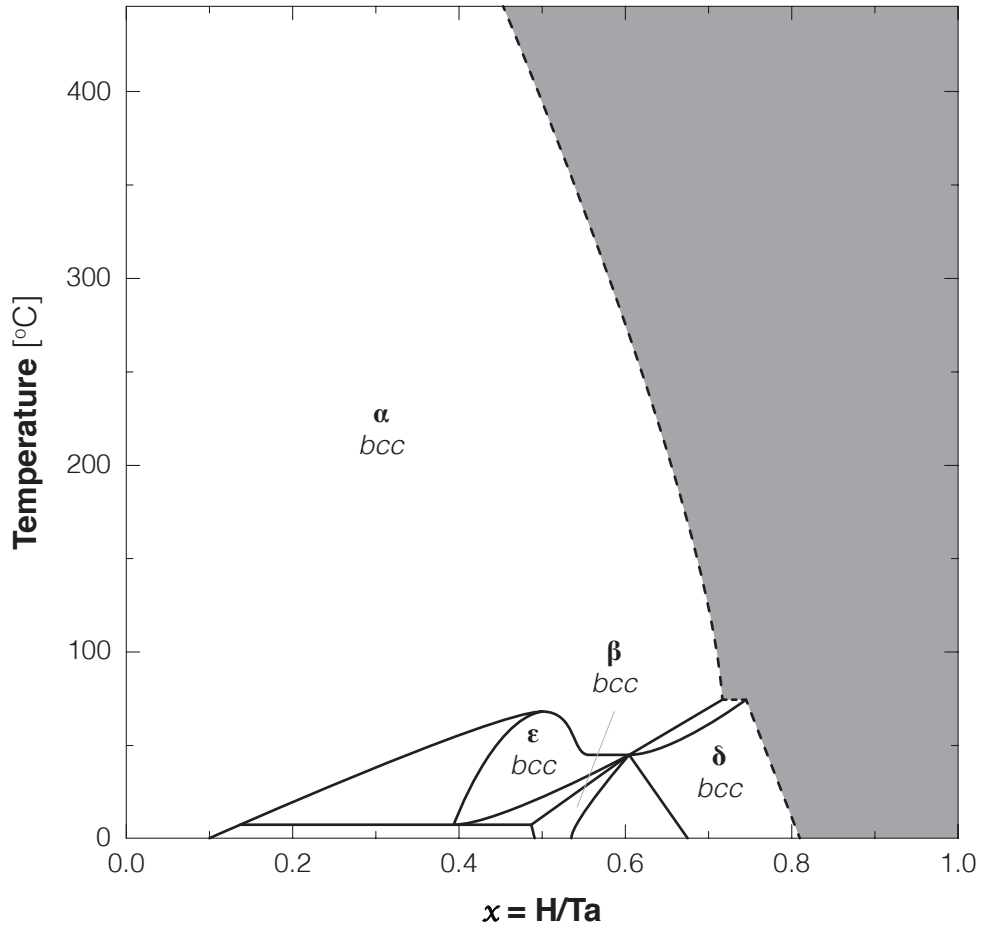
Figure A4 | **Phase Diagram of TaH$_x$** – Non-isobaric (up to $1\,\mathrm{atm}$.) phase diagram of the tantalum-hydrogen system adapted from San-Martin *et al.*[5.61] and Schober.[5.48] The α hydride phase corresponds to a disordered solution of hydrogen in a bcc lattice. The β hydride phase corresponds to an ordered solution of hydrogen in a bcc lattice. The ε hydride phase is a high-temperature modification of the β hydride phase. The α, β, and ε hydride phases describe an orthorhombic crystal structure with an ordered hydrogen solution. The δ hydride phase describes a monoclinic lattice. The shaded area indicates the unexplored region where the hydride formation pressure exceeds $1\,\mathrm{atm}$.

hydride phases have a bcc lattice. The δ hydride phase describes an ordered hydrogen solution in a monoclinic lattice. The β hydride phase describes a fully ordered hydrogen solution in an orthorhombic crystal structure. The ε hydride phase is a (high) temperature modification of the β hydride phase, with a partially ordered hydrogen solution. Between each of these distinct hydride phases there are regions of coexisting phases, implying that the phase transitions are incoherent. Resistivity measurements confirm this.[5.62]

At low hydrogen fractions $x < 0.1$, there is a solution of hydrogen in the bcc lattice. Here, the pressure-composition-isotherms (PCIs) obeys Sieverts' law, which describes a linear relation between the applied pressure $\sqrt{P}$ and x (see figure A5). At higher hydrogen fractions and at high temperatures ($>200°$C) the isotherms obey a different relation. Here, a linear relation between $\ln(x/(1+x))$ and $\ln(P)$ is observed (see figure A6). This behavior is also found in the fcc hydride phase of HfH$_x$, TiH$_x$, and ZrH$_x$. However, at elevated temperatures ($<200°$C) an inflection is observed for $x > 0.1$. This effect is contributed to the ε hydride phase, which has a critical temperature of $T_c = 61°$C.[5.48] As a result, we expect that this inflection becomes more prominent at temperatures closer to this critical temperature.

At high temperatures ($>200°$C) there are no differences between the absorption and desorption isotherms observed.[5.63] This means that the system is considered to be free of hysteresis. High temperature studies show that the thermodynamical
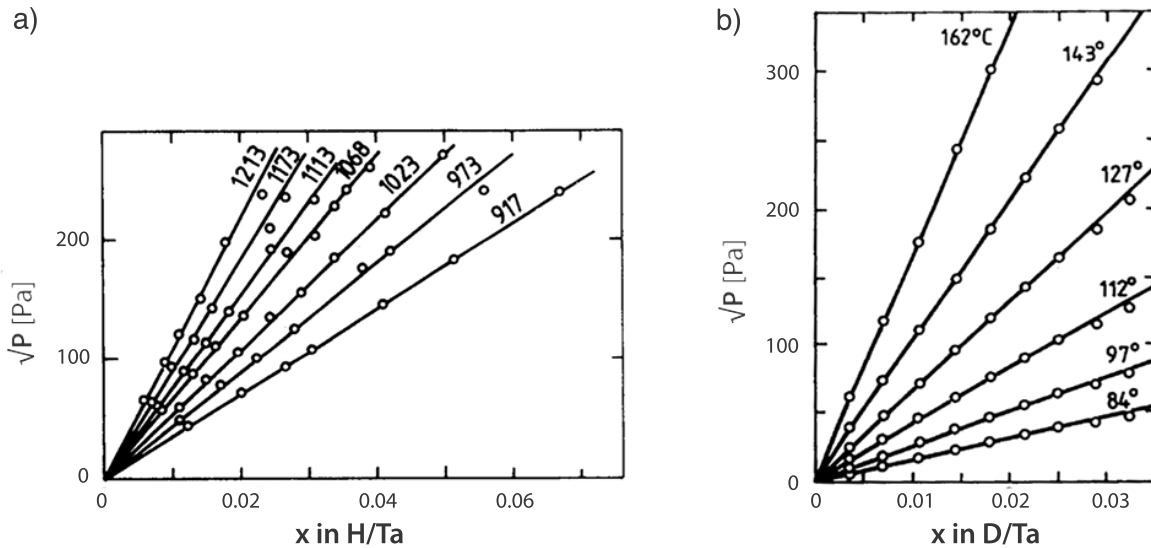
Figure A5 | Sieverts' Behavior in TaH$_x$ – Partial ressure-composition-isotherms (PCIs) of bulk tantalum at **a)** low hydrogen and **b)** low deuterium fractions, both adapted from Schober.[5.48] In both cases Sieverts' behavior ($\sqrt{P} \sim x$) is observed. An (large) isotope effect is not expected.[5.48]

parameters depends on the hydrogen fraction x: both the molar enthalpy and the molar entropy of hydride formation decreases linearly with x.[5.61] ΔH decreases approximately $20 \text{ kJ/mol } H_2$ per H. ΔS decreases approximately $120 \text{ J/(K mol } H_2)$ per
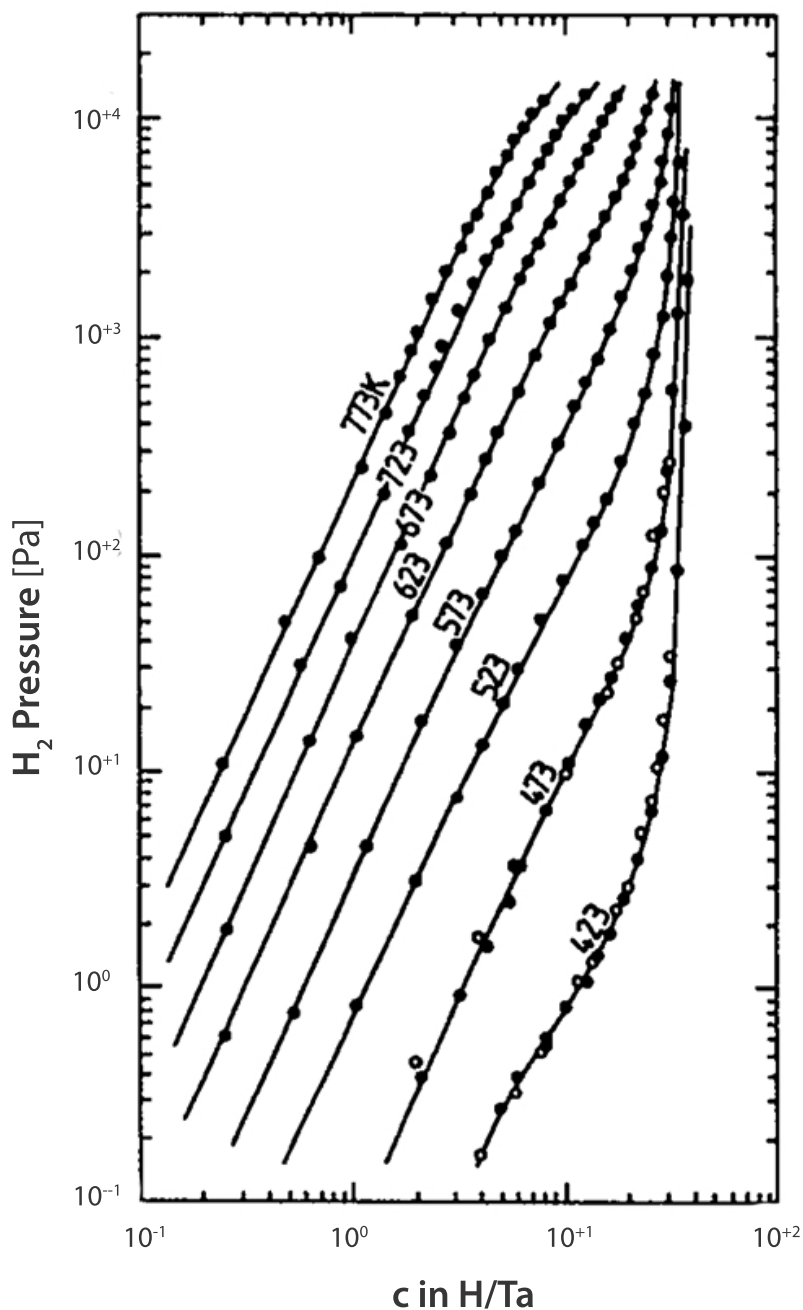
Figure A6 | **Isotherms of bulk TaH$_x$** – High temperature partial pressure-composition-isotherms (PCIs) of bulk tantalum adapted from Schober.[5.48] The hydrogen concentration c is related to the hydrogen fraction x by $c = x / (1 + x)$.

H. As a result of the large entropy change, TaH$_x$ describes a pressure range of many orders of magnitude (see figure A6). This is very similar to HfH$_x$. Below $61°C$ the behavior or the PCIs is not studied in detail. Due to the presence of the incoherent phase transitions, we expect the presence of (several) pressure plateaus.

A2.2   Optical Results – Thin films

In this section we briefly discuss the optical response of a tantalum thin film to hydrogen. Here we distinguish three samples, each with the same sample configuration but prepared after a different target pre-sputter time (see sample preparation for more details). Sample I is prepared after a $1\,\mathrm{hr}$ pre-sputter time. Sample II is prepared after a $>3\,\mathrm{hrs}$ pre-sputter time. Sample III is prepared after a $15\,\mathrm{min}$ pre-sputter time. We find that the optical response of the films on hydrogenation depends strongly on the pre-sputter time. The shorter we pre-sputter the target before sample preparation, the more the films are contaminated by nitrogen. And the more the sample is contaminated by nitrogen, the smaller the transmission change is. Below we discuss the effect of nitrogen contamination in more detail.

Exposing a Pd-capped tantalum thin film (sample I) to hydrogen at $120°C$ results in an immediately decrease of the film transmission. As found in hafnium thin films, varying the pressure stepwise results in distinct steps in the transmission (see fig-

---

Sample Preparation

The tantalum thin films are prepared by means of an ultra-high vacuum sputter system (base pressure of $10^{-10}\,\mathrm{Pa}$) in $3\,\mu\mathrm{bar}$ Ar (6N). For this we used a tantalum target with a purity of 99.9%. The films are deposited on a $10 \times 10\,\mathrm{mm}^2$ polished quartz substrate and are capped by a palladium layer. A $3\,\mathrm{nm}$ adhesion layer is used in order to prevent delamination from the substrate. The Pd layer protects the Hf layer from oxidation and also improves the hydrogen dissociation process.[5.22]   All layers have an uniform thickness, obtained by a rotating substrate during sputtering. The thickness of the tantalum layer is $40\,\mathrm{nm}$, determined by means of a sputter-rate obtained by stylus profilometry (DEKTAK) on bulk samples ($>400\,\mathrm{nm}$). The Pd-capping layer has a thickness of $10\,\mathrm{nm}$ We studied three different samples, each prepared after a different pre-sputter time of the tantalum target. Sample I, sample II, and sample III are prepared after a, respectively, $1\,\mathrm{hr}$, $>3\,\mathrm{hrs}$, and $15\,\mathrm{min}$ pre-sputter time.

Pd (10 nm)

Ta (40 nm)

Ti (3 nm)

Quartz Substrate

10 mm

10 mm
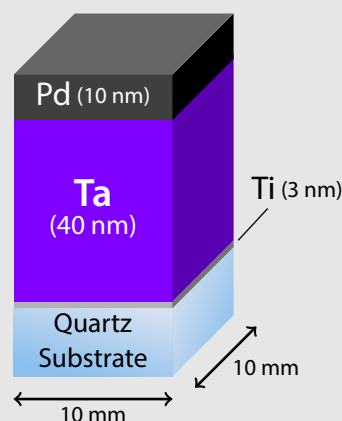
ure A7). We find that this behavior is free of hysteresis. Applying the same pressure from a higher/lower pressure results in the same optical transmission level.

From figure A7 we find that above 10^{+3} Pa the pressure steps become less distinct. This indicates that the film is almost saturated. This becomes more evident when we plot the corresponding isotherm from these steps ($\Diamond$ in figure A8). Here we find a linear relation between $\ln(P/P_0)$ and $\ln(\mathcal{T}/\mathcal{T}_{\text{prep}})$ below $<10^{+2}$ Pa. Above 10^{+2} Pa we find a (slight) deviation from this relation as the optical transmission change reduces per order of magnitude in pressure. By extrapolating this behavior we find a *saturated* transmission level of $\ln(\mathcal{T}_{\text{sat}}/\mathcal{T}_{\text{prep}}) \approx -0.19$. This value is similar to the maximum transmission observed in 40 nm thick HfH$_x$ films (see figure 5.4).

The relation between the applied pressure and the optical transmission of the film is different for each of the three samples we prepared. Sample III, prepared after
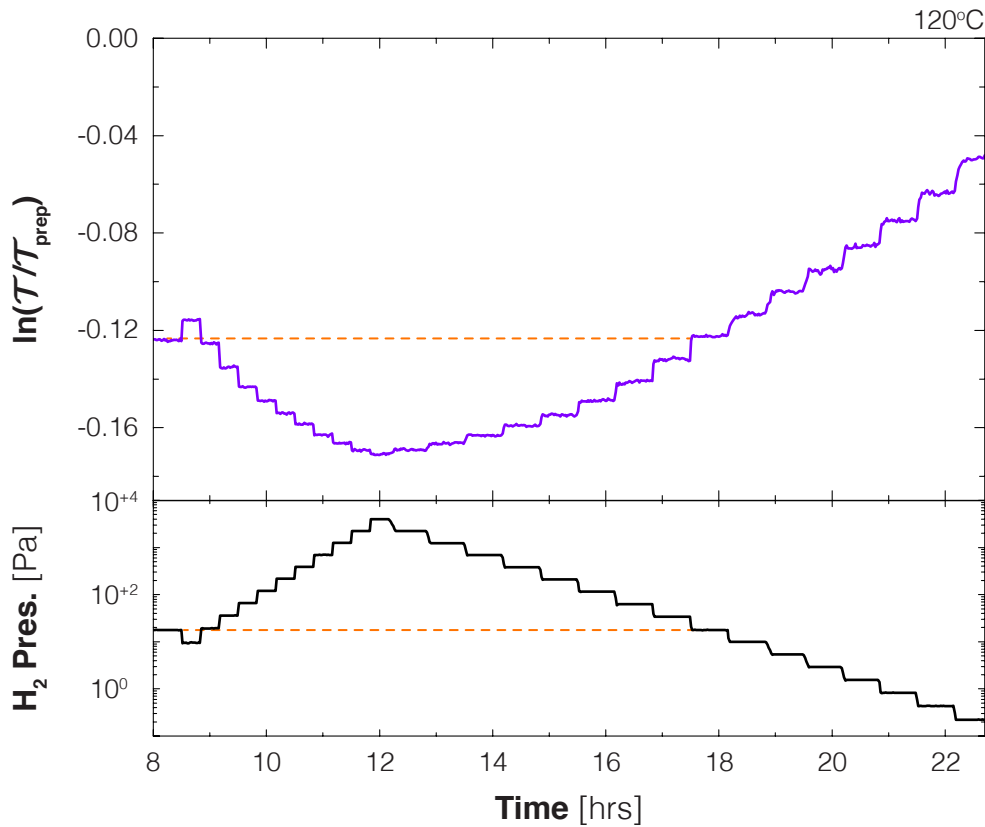
Figure A7 | TaH$_x$: Optical Response to different Hydrogen Pressures – The (white) light optical transmission change $\ln(\mathcal{T}/\mathcal{T}_{\text{prep}})$ of a Pd-capped Ta thin film (40 nm), prepared after a 1 hr pre-sputter of the target (sample I), as a function of time, where the film is exposed to hydrogen pressures between $10^{-1} - 10^{+4}$ Pa at $120°$C. The dashed lines are levels of the same transmission (top panel) and pressure (bottom panel). This indicate the absence of hysteresis.

only $15\,\mathrm{min}$ of pre-sputtering, shows no optical response to hydrogen (△ in figure A8). The samples prepared after a pre-sputtering of more than 3 hours (Sample II) show a large optical transmission change (○ in figure A8). This change is much larger than we find with sample I: $|\ln(\mathcal{T}_{\mathsf{sat}}/\mathcal{T}_{\mathsf{prep}})| \approx 0.8$ (sample II) versus $|\ln(\mathcal{T}_{\mathsf{sat}}/\mathcal{T}_{\mathsf{prep}})| \approx 0.19$ (sample I).

Similar to sample I, we also find with sample II distinct transmission steps when we vary the hydrogen pressure in steps. These transmissions steps are also free of hysteresis. The shape of the corresponding isotherm at $120°\mathrm{C}$ is, however, different. The isotherm of sample II shows a plateau-like behavior between $-0.6 <$ $\ln(\mathcal{T}/\mathcal{T}_{\mathsf{prep}}) < -0.2$ (see figure A8). This is very similar to behavior of the PdH$_x$ isotherms just above the critical temperature of the α-β coexistence region.[5.4] Knowing that the critical temperature of the TaH$_x$ ε hydride phase is $61°\mathrm{C}$, we expect that
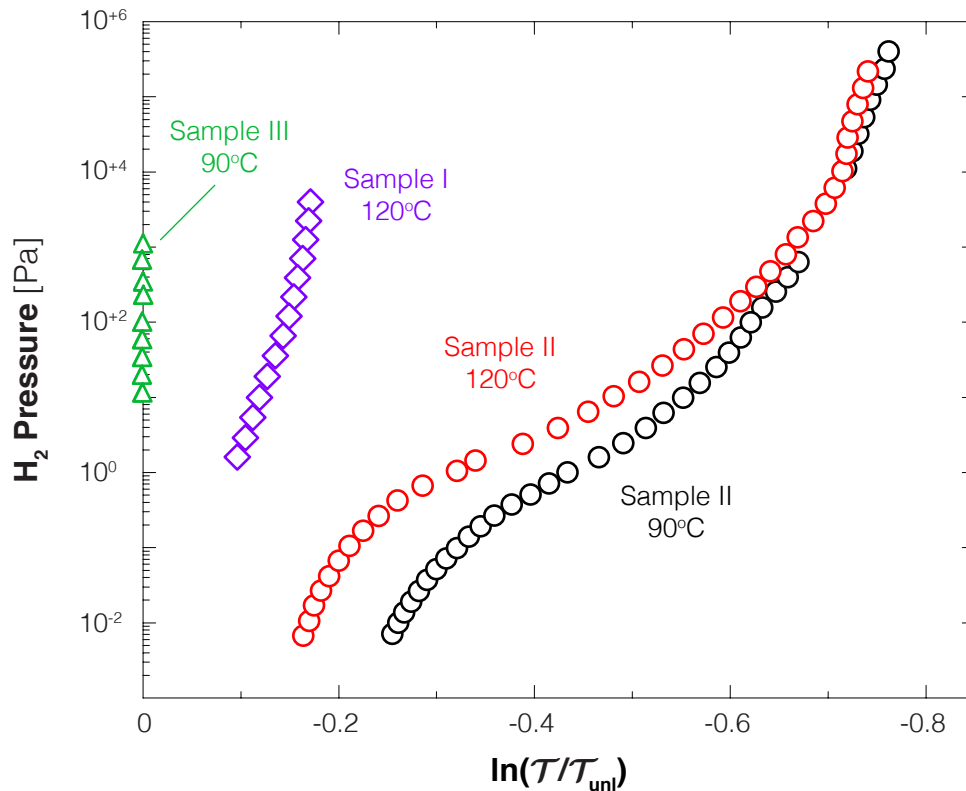
Figure A8 | TaH$_x$ Partial Optical Transmission Isotherms – Partial pressure-optical transmission-isotherms (PTIs) of two Pd-capped hafnium thin films (both $40\,\mathrm{nm}$). Sample I is only measured at $120°\mathrm{C}$ (◇). Sample II is measured at $90°\mathrm{C}$ (○) and $120°\mathrm{C}$ (○). Sample II is measured at only $90°\mathrm{C}$ (△), and shows no optical transmission change. X-ray diffraction shows that sample I contains a larger nitrogen contamination than sample II. All isotherms are the result of one subcycle. **Note that $\ln(\mathcal{T}/\mathcal{T}_{\mathsf{prep}})$ (horizontal axis) decreases from left to right.**

the plateau-like behavior originates from this hydride phase. From a sensor perspective, this behavior is less desirable.

The same behavior (using the same sample II) of the isotherm is found at $90°\text{C}$ (see figure A8). However, there are some peculiarities compared to the $120°\text{C}$ isotherm. Although the maximum optical transmission change is the same, the isotherm is not shifted uniformly in pressure as we found in HfH_x thin films and in bulk Ta at high temperatures. Instead we find a large pressure shift at low optical transmission (i.e. hydrogen fraction) while this difference vanishes at transmission levels close to $\mathcal{T}_{\text{sat}}$. As a result, the plateau-like behavior is smaller and the slope is higher at $90°\text{C}$. This is opposite to what we expect when approaching the critical temperature.

The difference in the behavior of the optical transmission between samples I, II, and III is related to the contamination of nitrogen. X-ray diffraction measurements show the presence of only crystalline Ta_4N in sample III (no optical response), and not of crystalline Ta. Sample II (large optical response) shows, on the other hand, the presence of only crystalline Ta. The x-ray diffraction patterns of sample II (*medium* optical response) show the presence of both crystalline Ta_4N and crystalline Ta. From
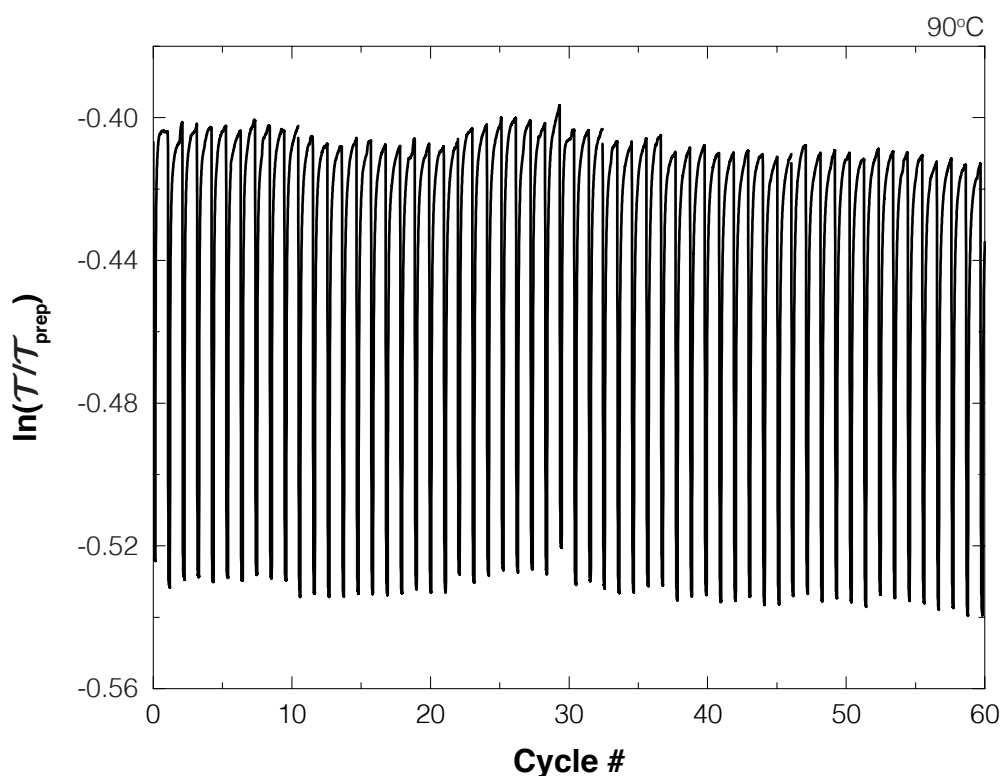
Figure A9 | TaH$_x$: Stability – The optical response of a Pd-capped Ta film (sample II) to (sub)cycles of partial hydrogenation $(80\,\text{Pa})$ and dehydrogenation $(4\,\text{Pa})$ at $90°\text{C}$. The fluctuations in $\ln(\mathcal{T}/\mathcal{T}_{\text{prep}})$ per cycle is the result of fluctuations in the (white) light source.

this we conclude that nitrogen has a large influence on the optical response of the tantalum film. In the next (sub)section we discuss the influence of nitrogen on the structural properties in more detail.

Besides the optical response, we also briefly studied the stability of sample II. Our preliminary results show that this sample exhibits an excellent stability (see figure A9). Within the first 60 (sub)cycles of partially (de)hydrogenation we do not find any film degradation. Note that the use of a Ti adhesion layer is necessary in order to prevent delamination from the substrate.

Below we discuss two other sensing properties in more detail: the wavelength dependence of the optical contrast and the response time.In addition we studied the hydrogen diffusion in Ta films, which is related to the response time. Note that these properties are studied by means of sample II, which shows the largest optical contrast and where we found no evidence of a nitrogen contamination.
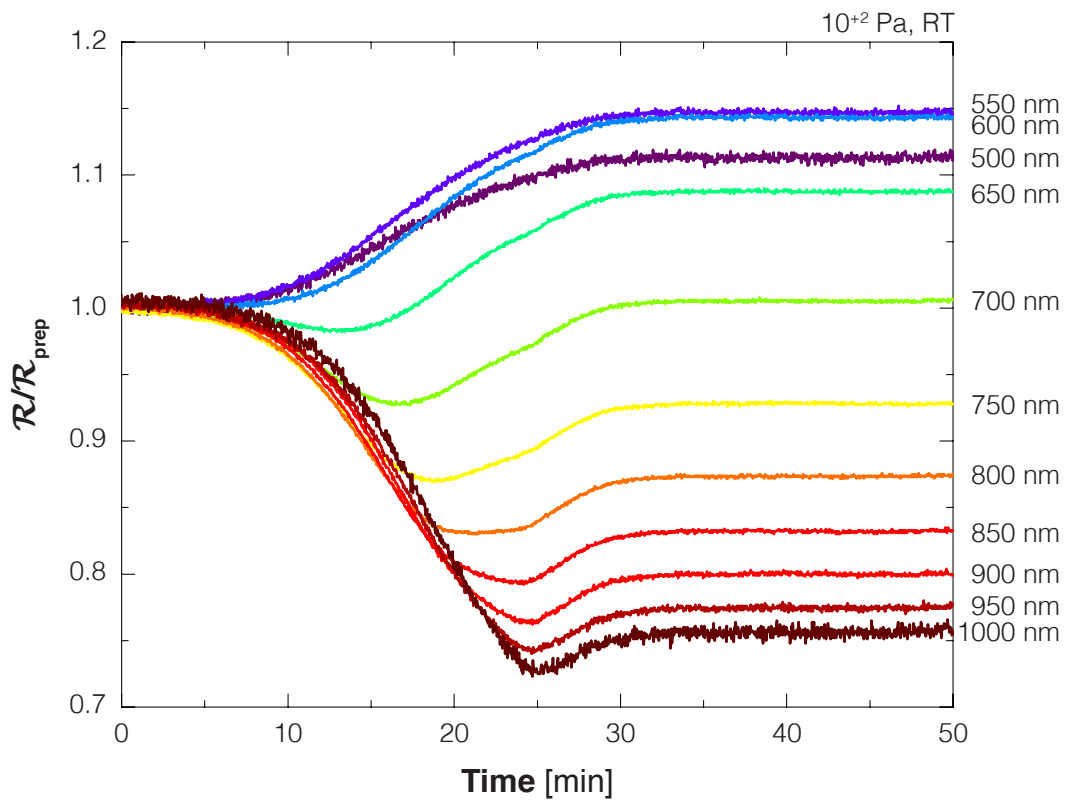
Figure A10 | TaH$_x$: Wavelength Dependence of Optical Reflectance on Hydrogen Exposure – The change of the reflectivity of a Pd-capped TaH$_x$ $(40\,\mathrm{nm})$ thin film plotted as a function of time for different wavelengths between $500 - 1000\,\mathrm{nm}$. The film is exposed to a constant partial hydrogen pressure $10^{+2}\,\mathrm{Pa}$ at room temperature.

Wavelength Dependence

In HfH$_x$ thin films we found that the optical properties strongly depend on the wavelength of the light. This is also true for TaH$_x$ thin films (sample II). Figure A10 shows the change of the optical reflection of a Pd-capped Ta thin film $(40\,\text{nm})$ as a function of time, where we exposed the film to a constant partial hydrogen pressure of $100\,\text{Pa}$ at room temperature. Note that, ignoring interference effects, the optical reflection change of the film is opposite to that of the optical transmission.

The wavelength dependence of the reflection change suggests that we cannot ignore interference effects in TaH$_x$ thin films. First we find in the blue part of the spectrum $(<700\,\text{nm})$ that the reflection increases during the hydrogenation. However, in the red part of the spectrum $(>700\,\text{nm})$ the reflection decreases during the hydrogenation. In addition, this reflection decrease is much stronger than the reflection increase. This is not expected from the optical transmission measurements. Here we find a strong transmission decrease, which implies a strong reflection increase. Second, we find particular behavior as a function of time. Except for the blue part of the spectrum, the reflection shows a (local) minimum. After a period of decrease, the reflection increases. The ratio of the decrease/increase magnitude depends on the wavelength: above $>700\,\text{nm}$ the ratio is greater than one (>1), while below $<700\,\text{nm}$ the ratio is smaller than one (<1). Figure A10 shows that also the time to reach the local minimum scales with this ratio. The larger the ratio is the more time it takes to reach the (local) minimum. A detailed study on the wavelength dependence of the film transmission change (similar to HfH$_x$) is necessary to quantify the interference effects.

Response Time

As in HfH$_x$, we find that the response time of TaH$_x$ thin films depends strongly on the applied pressure. The response time is in the same order as we find with a Pd-capped HfH$_x$ thin film. This is shown in figure A11, where the optical transmission change is plotted as a function of time when we expose the Pd-capped Ta film to different hydrogen pressures at $90°\text{C}$. Between each applied pressure, we reduced the pressure to $10^{-3}\,\text{Pa}$ to partially unload the film. We find that only when applying high pressures the films respond quickly, although it is still in the order in minutes. When we apply a pressure as low as $0.5\,\text{Pa}$ it takes several hours to reach a stable optical level. Also the desorption is slow. Even after 3 hours the film has not reached a stable optical transmission level when we reduced the pressure to $10^{-3}\,\text{Pa}$. This is independent of the starting pressure.

Adding a PTFE coating on top of the Pd-surface reduces the response time significantly. The films reaches within minutes a stable level when exposing the films to hydrogen. Only at low hydrogen pressures $(<0.5\,\text{Pa})$ the response time to an in-
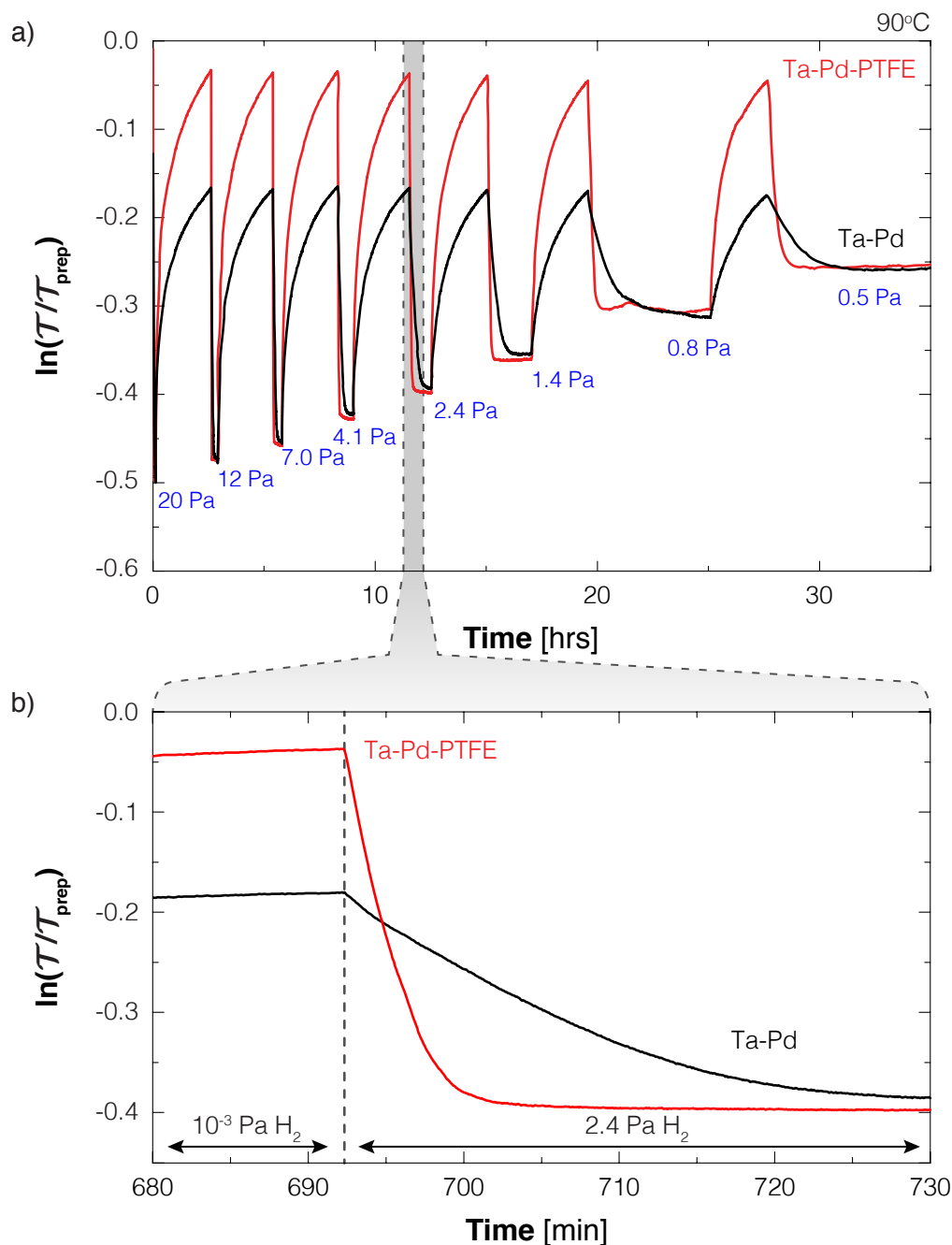
Figure A11 | TaH$_x$: Response Time – a) the optical response of a Pd-capped Ta film (sample II) with (red) and without (black) a PTFE-capping layer to different hydrogen pressures as a function of time. Between each (hydrogenation) pressure, the films are for several hours exposed to a partial hydrogen pressure of 10^{-3} Pa. **b)** Close-up of the optical response between $680 - 730$ min. After 692 min we apply a hydrogen pressure of 2.4 Pa.

creasing hydrogen pressure is still in the order of one hour. Also the response time to a decreasing hydrogen pressure is significantly reduced by adding a PTFE coating. Although the film does not reach a stable optical level within 3 hours, the optical transmission reduction is much higher than observed with films without a PTFE coating (see figure A11). This suggests that the low response time is partially an intrinsic property of Ta.

Hydrogen Diffusion

To test whether the slow response is an intrinsic property of Ta, we studied the diffusion of hydrogen in a Ta film by means of an optical technique. This technique has already been used by de Man *et al.* and Westerwaal *et al.* to study the hydrogen permeability of Pd-based membranes.[5.31,5.64] In order to use this technique, we prepared a special sample configuration that is schematically shown in figure A12. Here, a thick $(270\,\text{mm})$ Ta film is covered by an yttrium layer $(60\,\text{nm})$. The yttrium is partially covered by Pd dots $(10\,\text{nm}$ thick, $0.9\,\text{mm}$ in diameter), which are equally spaced. By exposing the sample to air, the uncovered yttrium layer will be partially oxidized cre-
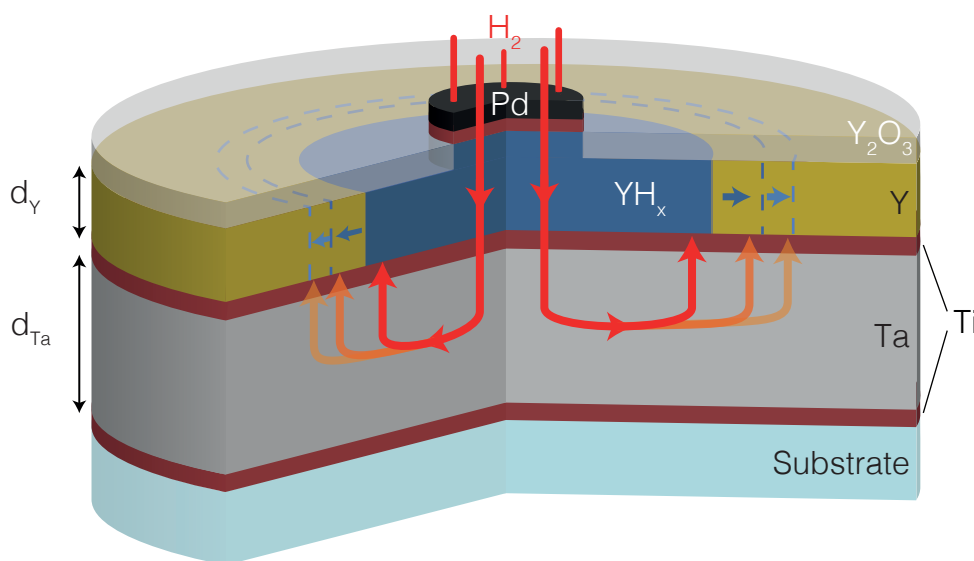
Figure A12 | TaH$_x$ Diffusion Sample Configuration – Sample configuration used for monitor the hydrogen diffusion in a TaH$_x$ film. The sample consist of a $270\,\text{nm}$ tantalum layer, a $60\,\text{nm}$ yttrium indicator layer of which $\sim 15\,\text{nm}$ is partially oxidized and partially coverd by Pd dots (10 nm thick, $0.9\,\text{mm}$ in diameter). In order to prevent mixing of Ta/Y and Y/Pd, and in order to avoid clamping to the substrate, Ti ($3\,\text{nm}$) adhesion/intermediate layers are used. Note that the actual sample is a $3''$ quartz waver and it consists of many Pd dots in a hexagonal pattern (the distance between the dots is $10\,\text{mm}$).

ating a ~ 15 nm layer that is impermeable to hydrogen. In order to prevent mixing of Ta/Y and Y/Pd, and in order to avoid clamping to the substrate, Ti (3 nm) adhesion/intermediate layers are used.

The yttrium layer is used as an indication layer. When we expose the sample to hydrogen gas, hydrogen can only enter the film through the Pd dots. Because the diffusion through yttrium is supposed to be much slower $(10^{-11} \text{ cm}^2/\text{sec})$,[5.65] the diffusion takes only place in the tantalum layer. While the hydrogen diffuses laterally through the Ta layer, the affinity of Y to hydrogen is so large that it will hy-
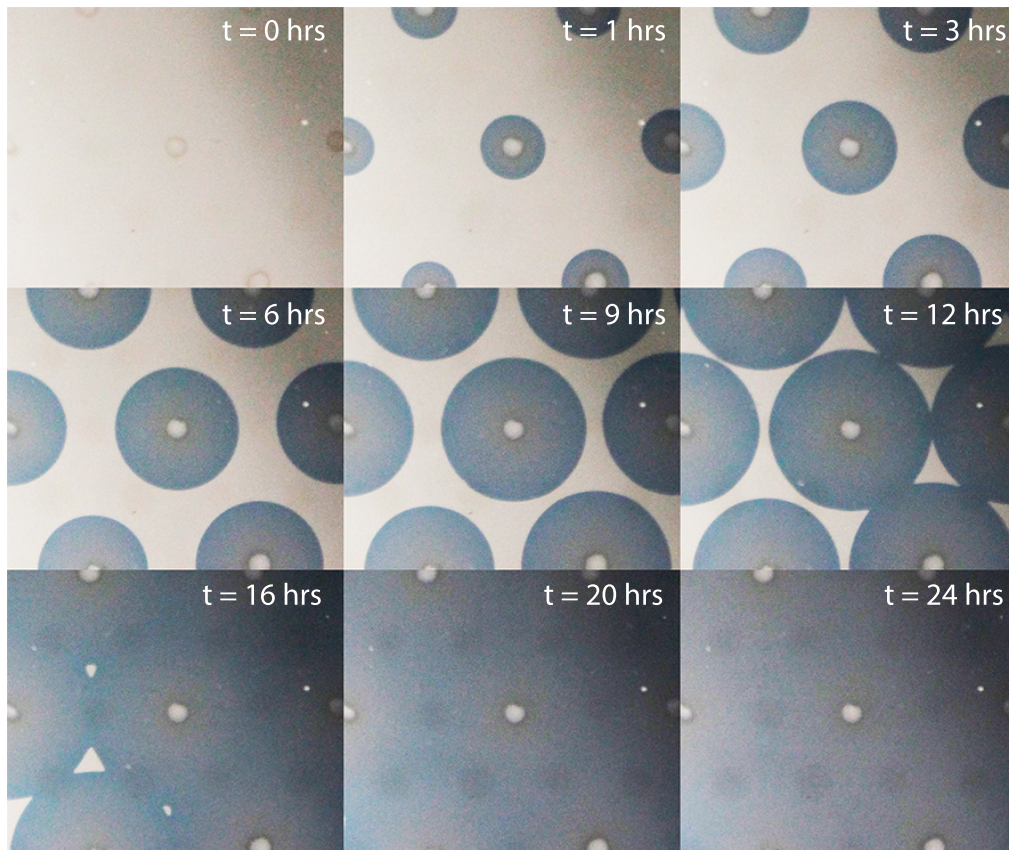
Figure A13 | **Hydrogen Diffusion in TaH$_x$** – Images of a selected area of a TaH$_x$ (270 nm) film (see figure A12 for sample configuration) taken at different times when we expose the film to a constant partial hydrogen pressure of $1.6 \times 10^{+3}$ Pa at $90°$C. The images show the same area of the film. The darkgray circles mark the position of the Pd dots $(1 \text{ mm}$ diameter). The (growing) blue circles indicate the parts of the sample that are hydrogenated. We find that the corresponding diffusion coefficient (at these conditions) is $1.6 \times 10^{-6} \text{ cm}^2/\text{sec}.$

drogenate the yttrium layer above it (the hydrogenation pressure of Y is 10^{-27} bar at room temperature).[5.66] As a result the diffusion from in the Ta layer is reflected by the hydrogenated area of the yttrium layer. Because the hydrogenation of yttrium results in color shift from a neutral to a dark blue color, we monitor the diffusion through Ta optically by means of a high-resolution camera (12 megapixel). Note that we assume that the 3 nm Ti layers are too thin to influence the growing diffusion front. In order to avoid phase transitions, we studied the diffusion in Ta only at 90°C.

Figure A13 shows pictures of the sample (focussed on the same Pd-dot) taken at different times. Here we expose the sample to a constant partial hydrogen pressure of $1.6 \times 10^{+3}$ Pa for more than 24 hrs. We find that the radius of the hydrogenated area (dark blue) around the Pd-dot grows over time. Around $t \approx 12$ hrs we find that the hydrogenated areas of neighbouring Pd-dots contact each other. After $t \approx 20$ hrs the whole sample has been hydrogenated. Knowing that the distance between the Pd-dots is 10 mm, we can calculate from the pictures shown in figure A13 the hydrogenated area as a function of time. From this we calculate that the diffusion coefficient equals 1.6×10^{-6} cm²/sec. Note this diffusion coefficient corresponds to the condition when we apply a pressure of $1.6 \times 10^{+3}$ Pa at 90°C. It will be different when we apply a different pressure at a different temperature. Extrapolating this to a film of 40 nm means that it should be hydrogenated within a second when we apply a pressure of $1.6 \times 10^{+3}$ Pa at 90°C. This means that only when the diffusion is significantly lower at lower pressures the slow response time can be considered as an intrinsic property of Ta.

Instead of the diffusion coefficient, in the field of membranes often the hydrogen permeability is used. The hydrogen permeability κ_{Ta} also relates the radius r_f of the diffusion front to the time after exposure. In addition, it corrects for the layer thicknesses and the applied hydrogen pressure. The hydrogen permeability is given by

$$ t = \frac{1}{8} \frac{d_{\mathsf{Ta}}}{d_{\mathsf{Y}}} \frac{c_{\mathsf{Y}}}{\sqrt{P}} \frac{R_{\mathsf{Pd}}^2}{\kappa_{\mathsf{Ta}}} \left[2 \left(\frac{r_f}{R_{\mathsf{Pd}}} \right)^2 \left(ln \left(\frac{r_f}{R_{\mathsf{Pd}}} \right) - \frac{1}{2} \right) + 1 \right]. \tag{A.4} $$

Here d_{Ta} is the thickness of the Ta film (270 nm), d_{Y} the thickness of the (non-oxidized) Y film (45 nm), c_{Y} the hydrogen concentration in the yttrium layer (0.18 mol/cm³), P the applied hydrogen pressure ($1.6 \times 10^{+3}$ Pa), and R_{Pd} is the radius of the Pd-dot (0.9 mm). The diffusion results can be described by equation A.4 (see figure A14). From the resulting fit we find that $\kappa_{\mathsf{Ta}} = 2.6 \times 10^{-7}$ mol/(m sec Pa$^{0.5}$) at 90°C. This value matches the reported bulk value.[5.67]
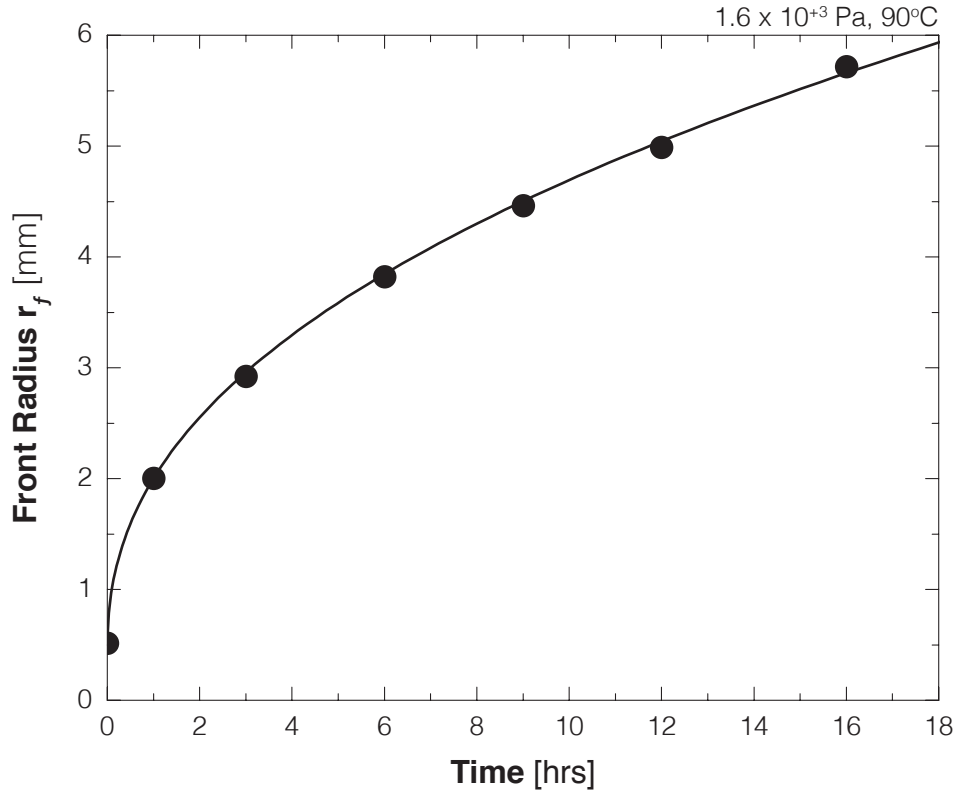
Figure A14 │ Time Dependence of Diffusion Front in TaH$_x$ – Plot of the hydrogen diffusion front radius r_f as a function of time when we expose a TaH$_x$ $(270\,\mathrm{nm})$ film (see figure A12 for sample configuration) to a constant partial hydrogen pressure of $1.6 \times 10^{+3}\,\mathrm{Pa}$ at $90°\mathrm{C}$. The solid line represents the fit of equation A.4 to the data points. From this we find that the hydrogen permeability in Ta equals $2.6 \times 10^{-7}\,\mathrm{mol/(m\ sec\ Pa^{0.5})}$. We therefore conclude that the diffusion of hydrogen in a thin film is the same as in bulk.

A2.3   Structural Results – Thin films

The optical results of three samples each prepared after a different pre-sputter time indicate that there are structural differences between the samples. X-ray diffraction measurements confirm this. Figure A15 shows the x-ray diffraction patterns of the three different samples in their as-prepared state. Sample II (large optical contrast) shows a lattice reflection at $44.5°$, which we identify as the (110) reflection of bcc Ta. Sample I (medium optical contrast) shows a two lattice reflections. One at $44.1°$, which we identify as the (110) reflection of bcc Ta although with a larger lattice constant, and one at $39.2°$. This last lattice reflection coincides with the (110) reflection of Ta$_4$N (also with a bcc structure). The suggestion that the optical contrast is affected by a nitrogen contamination is supported by the x-ray diffraction pattern of sample III (no optical contrast). Here we find only one although a strong lattice reflection

λ = 1.789 Å, RT
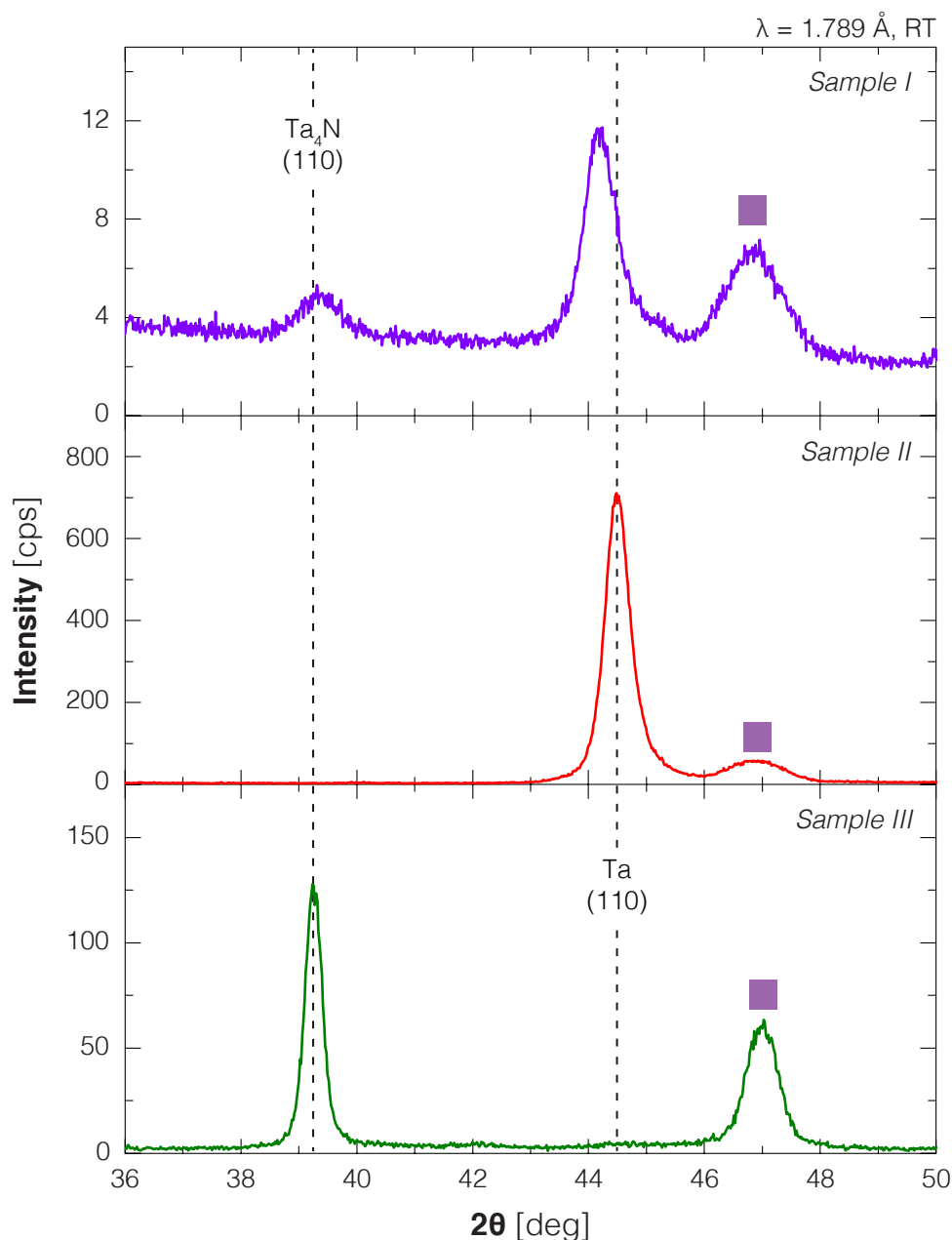
Figure A15 | X-ray Diffraction Patterns of different Ta Samples – X-ray diffraction patterns of the *as-prepared* state of three samples prepared at different times measured at room temperature. Each sample has the same configuration and consist of a Pd-capped Ta thin film $(40\ \mathrm{nm})$ including a $3\ \mathrm{nm}$ Ti adhesion layer. Sample I shows a medium, sample II a large, and sample II no optical contrast. The dashed lines indicate the (110) plane reflection of Ta_4N $(39.2°)$ and Ta $(44.5°)$. The intensity peak at $46.9°$ (■) corresponds to the (111) lattice reflection of Pd. Note that the samples are obtained with different settings (e.g. time constants).
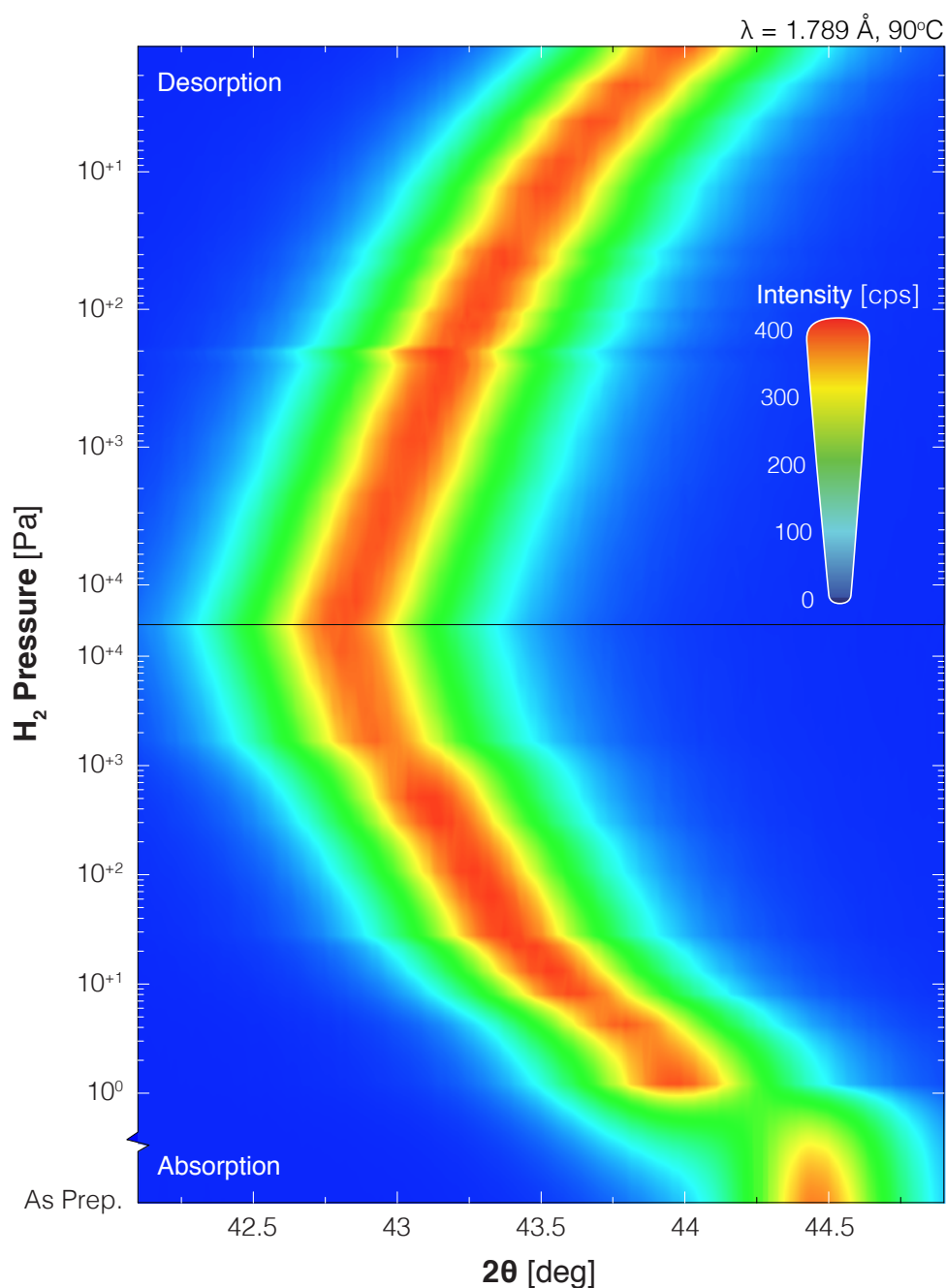
Figure A16 | In-situ X-ray Diffraction Patterns of TaH$_x$ – Contour plot of multiple in-situ x-ray diffraction patterns obtained from a Pd-capped TaH$_x$ (40 nm) thin film (sample II) during the first hydrogenation cycle at 90°C. The bottom and top panel corresponds, respectively, to the absorption and the desorption part of the first cycle. Here, red indicates a high intensity and blue a low intensity.

at $39.2°$, which is most likely originated from Ta$_4$N. Note that we do not observe any TaO$_x$ peaks.

The nitrogen contamination is most likely originated from the sputter target. This because the presence (and the amount) of Ta$_4$N depends only on the pre-sputter time. It also means that the affinity for nitrogen is very high, and higher than that for hydrogen. Several studies show that this is indeed the case: $\Delta H = -106\,\mathrm{kJ/mol}$ N$_2$[5.68] versus $\Delta H = -80\,\mathrm{kJ/mol}$ H$_2$.[5.48] The fact that we do not observe an oxygen contamination despite the much higher affinity $(\Delta H = -200\,\mathrm{kJ/mol}$ O$_2)$ can be understood from the diffusion coefficients. The diffusion of nitrogen in tantalum $(6 \times 10^{-3}\,\mathrm{cm^2/sec}$ between $300 - 660°C)$ is orders of magnitude larger than the diffusion of oxygen $(<10^{-8}\,\mathrm{cm^2/sec}$ within the same temperature range).[5.69] Therefore only a thin surface layer will be oxidized. This oxidation layer is easily removed during a short pre-sputtering of the target.

TaH$_x$: In-situ XRD

The absence of phase transitions at temperatures above $61°C$ is confirmed by in-situ x-ray diffraction. Figure A16 shows the contour plots of the XRD patterns obtained from a Pd-capped tantalum thin film (Sample II) at different pressures at $61°C$. as a function of the pressure we find a shift of the (110) Ta lattice reflection without a reduction of reflection intensity. This suggests that the crystallinity of the (bcc) lattice does not change during (de)hydrogenation.

Figure A16 indicates that also structurally the films are free of hysteresis. There are only marginal differences in the peak shift as a function of the pressure during the first hydrogenation compared to the first dehydrogenation. The absence of hysteresis is becomes more evident when we plot the corresponding (110) d-spacing as a function of the applied pressure (see figure A17). Only at pressures above $>10^{+3}\,\mathrm{Pa}$ (at $90°C$) we find some differences between the absorption and desorption curves. We think that this is a first-cycle effect as it is not present in the $120°C$ data.

Comparing the d-spacing as a function of the pressure between $90°C$ and $120°C$ shown in figure A17 with the optical isotherms shown in figure A8 give rise to some questions. This because the shift of the d-spacing from $90°C$ to $120°C$ is uniform for all pressures (on a logarithmic scale). On the other hand, the optical isotherms do not share this uniform shift when we increase the temperature from $90°C$ and $120°C$. As mentioned above, the $90°C$ and $120°C$ optical isotherms coincides above $10^{+3}\,\mathrm{Pa}$. A more detailed study is necessary to determine whether the difference can be explained by means of a particular behavior of the absorption coefficient (see equation 5.6) or that it is a consequence of a sample artefact.
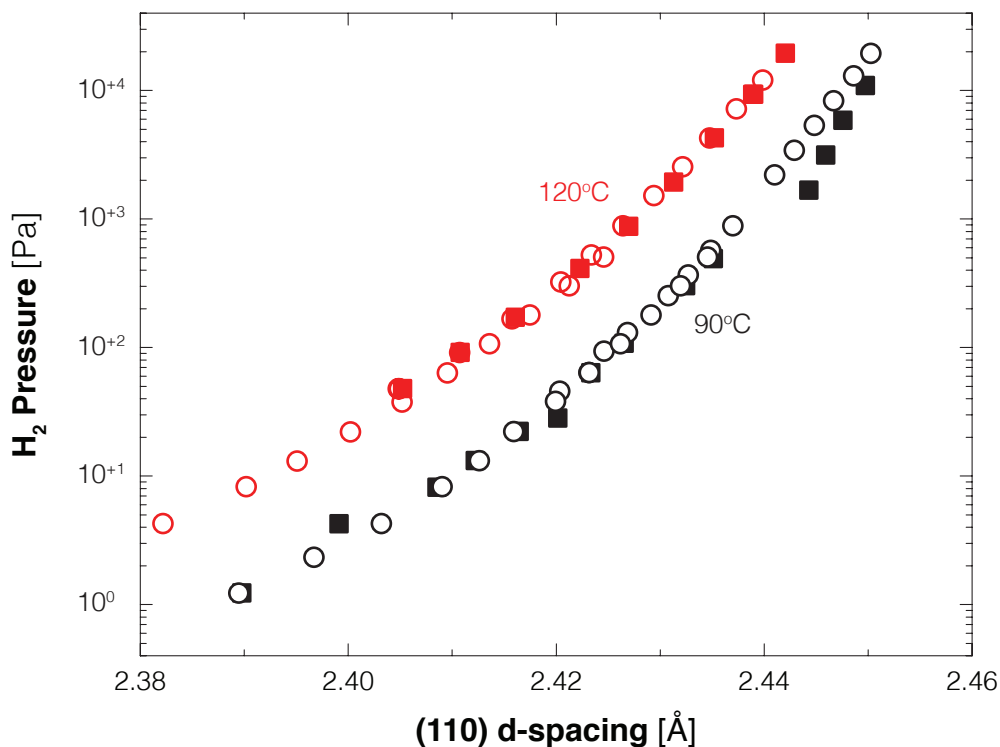
Figure A17 | Expansion of the (110) d-Spacing in TaH$_x$ – The (110) d-spacing in TaH$_x$ (assuming a bcc-structure) as a function of the pressure at $90°$C and $120°$C. The closed square symbols correspond to the absorption measurements where we increase the hydrogen pressure, the open circles correspond to the desorption measurements where we decrease the hydrogen pressure. All the data are obtained from the same Pd-capped TaH$_x$ $(40\,\text{nm})$ thin film (sample II). The $90°$C data corresponds to the first cycle, the $120°$C data corresponds to the third cycle.

A2.4 Outlook

We find that HfH$_x$ is not unique as a(n) (optical) hydrogen sensing material. TaH$_x$ describes also a large hydrogen sensing range that finds its origin in a large entropy change. In addition, it is without hysteresis and the film shows a good (sub)cycle stability. The response time is in the same order of Hf (i.e. slower than PdH$_x$), although it may be improved by using a PTFE coating.

However, there are some drawbacks with respect to its sensing properties. Although the sensing range is determined by natural boundaries (i.e. the unloaded/as-prepared and the saturated state), it is very likely that the pressure range of TaH$_x$ is described by two relations. At low hydrogen pressures we expect Sieverts' behavior ($\sqrt{P} \propto x$), while at higher pressures we expect the same relation as observed in bulk Ta and in Hf: $\ln(P) \propto \ln(x/(1+x))$. With a ΔH that depends on the hydro-

gen fraction, it is much more complex to describe the relation between the pressure and the optical response (transmission/reflection) in TaH$_x$ than in HfH$_x$ thin films. In addition, the plateau-like behavior we find in the optical isotherms at temperatures around $100°$C is not desirable.

Also the large impact of nitrogen on the optical response is important to take into account. A large nitrogen contamination makes the material unusable for hydrogen sensing. However, the preliminary results show that we can turn this also into an opportunity. By control the nitrogen contamination in the films the relation between the pressure and the optical response can be controlled. In addition, the plateau-like behavior of the optical isotherms can be avoided. The loss of optical contrast can be compensated by selecting a proper wavelength and (possibly) by increasing the film thickness.

References

[5.1] *C. Perrotton, N. Javahiraly, A. Kazemi, and P. Meyrueis.* **Review of optical fiber sensor technologies for hydrogen leak detection in hydrogen energy storage.** SPIE Proceedings **8026**, 802605 (2011).

[5.2] *S.F. Silva, L. Coelho, O. Frazao, J.L. Santos, and F.X. Malcata.* **A review of palladium-based fiber-optic sensors for molecular hydrogen detection.** Sensor Journals **12**, 93 – 102 (2014).

[5.3] *N. Javahiraly and C. Perrotton.* **Hydrogen leak detection: a comparison between fiber optic sensors based on different designs.** SPIE Proceedings **9202**, 920206 (2014).

[5.4] *F.A. Lewis, K. Kandasamy, and X.Q. Tong.* **Palladium-hydrogen system.** Solid State Phenomena **73 – 75**, 268 – 502 (2000).

[5.5] *R. Gremaud, M. Slaman, H. Schreuders, B. Dam, and R. Griessen.* **An optical combinatorial method to determine the thermodynamics of hydrogen absorption and desorption in metals.** Applied Physics Letters **91**, 231916 (2007).

[5.6] *R. Gremaud.* **Hydrogenography. A thin film optical combinatorial study of hydrogen storage materials.** Doctoral thesis. VU University Amsterdam. ISBN/EAN 978-90-9023439-7 (2008).

[5.7] *H. Wang and K. Konashi.* **Investigation on electronic, mechanical and thermal properties of Hf-Hd system.** Journal of Nuclear Materials **443**, 99 – 106 (2013).

[5.8] *M.H. Mintz.* **Hafnium-hydrogen.** Solid State Phenomena **49 – 50**, 331-356 (1996).

[5.9] *R.K. Edwards and E. Veleckis.* **Thermodynamic properties and phase relations in the system hydrogen-hafnium.** Journal of Physical Chemistry **66**, 1657 – 1661 (1962).

[5.10] *S.S. Sidhu and J.C. McGuire.* **An x-ray diffraction study of the hafnium-hydrogen system.** Journal of Applied Physics **23**, 1257 – 1261 (1952).

[5.11] *S.S. Sidhu.* **The effect on metal-metal bonds of increased concentration of hydrogen in hafnium dihydride.** Acta Crystallographica **7**(5), 447 – 449 (1954).

[5.12] *C. Korn.* **NMR study comparing the electronic structures of ZrHx and TiHx.** Physical Review B **28**(1), 95 – 111 (1983).

[5.13] *R. Quijano, R. de Coss, and D.J. Singh.* **Electronic structure and energetics of the tetragonal distortion for TiH2, ZrH2, and HfH2: A first-principles study.** Physical Review B **80**(18), 184103 1 – 8 (2009).

[5.14] *N.I. Kulikov, V.N. Borzunov, and A.D. Zvonkov.* **Electronic band-structure and inter-atomic in nickel and titanium hydrides.** Physica Status Solidi **86**, 83 – 91 (1978).

[5.15] *S.E. Kul`kova, O.N. Muryzhnikova, and I.I. Naumov.* **Electronic structure and lattice stability in the dihydrides of titanium, zirconium, and hafnium.** Physics of the Solid State **41**(11), 1763 – 1770 (1999).

[5.16] *Y. Levitin, J. Bloch, and M.H. Mintz.* **Kinetic study of the hafnium-hydrogen reaction.** Journal of the Less-Common Metals **175**, 219 – 234 (1991).

[5.17] *J.N. Huiberts, R. Griessen, J.H. Rector, R.J. Wijngaarden, J.P. Dekker, D.G. Groot, and N.J. Koeman.* **Yttrium and lanthanum hydride films with switchable optical properties.** Nature **380**, 231 – 234 (1996).

[5.18] *K. Von Rottkay, M. Rubin, F. Michalak, and R. Armitage.* **Effect of hydrogen insertion on the optical properties of Pd-coated magnesium lanthanides.** Electrochimica Acta **44**, 3093 – 3100 (1999).

[5.19] *R. Griessen.* **Switchable mirrors.** Europhysics News (2001).

[5.20] *I.A.M.E. Giebels.* **Shining light on magnesium based switchable mirrors.** Doctoral thesis. VU University Amsterdam. ISBN 90-9018547-X (2004).

[5.21] *D.E. Azofeifa, N. Clark, W.E. Vargas, H. Solós, G.K. Sólis, and B. Hjörvarsson.* **Temperature- and hydrogen-induced changes in the optical properties of Pd capped V thin films.** Physica Scripta **86**, 065702 1 – 11 (2012).

[5.22] *M.A. Pick, J.W. Davenport, M. Strongin, and G.J. Dienes.* **Enhancement of hydrogen uptake rates for Nb and Ta by thin surface overlayers.** Physical Review Letters **43**(4), 286 – 289 (1979).

[5.23] *T.B. Flanagan and W.A. Oates.* **The palladium-hydrogen system.** Annual Review of Materials Science **21**, 269 – 304 (1991).

[5.24] *F.D. Manchester, A. San-Martin, and J.M. Pitre..* **The H-Pd (hydrogen-palladium) system.** Journal of Phase Equilibria **15**(1), 62 – 83 (1994).

[5.25] *R. Griessen, J.N. Huiberts, M. Kremers, A.T.M. van Gogh, N.J. Koeman, J.P. Dekker, and P.H.L Notten.* **Yttrium and lanthanum hydride films with switchable optical properties.** Journal of Alloys and Compounds **253**, 44 – 50 (1997).

[5.26] *M. Kremers, N.J. Koeman, R. Griessen, P.H.L. Notten, R. Tolboom, P.J. Kelly, and P.A. Duine.* **Optical transmission spectroscopy of switchable yttrium hydride films.** Physical Review B **57**(8), 4943 – 4949 (1998).

[5.27] *E.S. Kooij, A.T.M van Gogh, and R. Griessen.* **In-situ resistivity measurements and optical transmission and reflection spectroscopy of electrochemical loaded switchable YHx films.** Journal of The Electrochemical Society **146**(8), 2990 – 2994 (1997).

[5.28] *P. Ngene, T. Radeva, M. Slaman, R.J. Westerwaal, H. Schreuders, and B. Dam.* **Seeing hydrogen in colors: low-cost and highly sensitive eye readable hydrogen detectors.** Advanced Functional Materials **24**(16), 2374 – 2382 (2014).

[5.29] *D.E. Azofeifa, N. Clark, W.E. Vargas, H. Solís, G.K. Pálsson, and B. Hörvarsson.* **Hydrogen induced changes in the optical properties of Pd capped V thin films.** Journal of Alloys and Compounds **580**, S114 – S118 (2013).

[5.30] *T.B. Flanagan and W.A. Oates.* **Thermodynamics of intermetallic compound-hydrogen systems.** **Hydrogen in Intermetallic Compounds I Vol. 63**, Springer Berlin Heidelberg. ISBN 0-387-18333-7 49 – 85 (2005).

[5.31] *R.J. Westerwaal, E.A. Bouman, W.G. Haije, H. Schreuders, S. Dutta, M.Y. Wu, C. Boelsma, P. Ngene, S. Basak, and B. Dam.* **The hydrogen permeability of Pd-Cu based thin film membranes in relation to their structure: a combinatorial approach.** International Journal of Hydrogen Energy **40**(10), 3932 – 3943 (2015).

[5.32] *M. Slaman, R.J. Westerwaal, H. Schreuders, and B. Dam.* **Optical hydrogen sensors based on metal-hydrides.** SPIE Proceedings **8368**, 836805 (2012).

[5.33] *P.A. Szilagyi, R.J. Westerwaal, R. van de Krol, H. Geerlings, and B. Dam.* **Metal-organic framework thin films for protective coating of Pd-based optical hydrogen sensors.** Journal of Materials Chemistry C **1**, 8146 – 8155 (2013).

[5.34] *P. Ngene, R.J. Westerwaal, S. Sachdeva, W.G. Haije, L.C.P.M. de Smet, and B. Dam.* **Polymer-induced surface modifications of Pd-based thin films leading to improved kinetics in hydrogen sensing and energy storage applications.** Angewandte Chemie International Edition **53**, 12081 – 12085 (2014).

[5.35] *R.J. Westerwaal.* **Growth, microstructure and hydrogenation of Pd-catalyzed complex metal hydride thin films.** Doctoral Thesis. VU University Amsterdam ISBN 978-90-8659071-1 (2007).

[5.36] **JCPDS-International Centre for Diffraction Data** (1998).

[5.37] *R.W.E. van der Kruijs.* **Specular and off-specular reflection of polarized neutrons from magnetic thin films and multilayers (Doctoral Thesis).** Doctoral Thesis. Delft University Press. ISBN 978-90-4072309-4 (2002).

[5.38] *A. Borgschulte, R.J. Westerwaal, J.H. Rector, B. Dam, and R. Griessen.* **Hydrogen sorption mechanism of oxidized nickel clusters.** Applied Physics Letters **85**(21), 4884 – 4886 (2004).

[5.39] *J. Isidorsson, I. Giebels, H. Arwin, and R. Griessen.* **Optical properties of MgH2 measured in situ by ellipsometry and spectrophotometry.** Physical Review B **68**, 115112 1 – 13 (2003).

[5.40] *R. Speiser and J. Spretnak.* **Thermodynamics of binary interstitial solid solutions.** Transactions of the American Society for Metals **47**, 493 – 507 (1955).

[5.41] *G. Boureau.* **A simple method of calculation of the configurational entropy for interstitial solutions with short range repulsive interactions.** Journal of Physics and Chemistry of Solids **42**(9), 743 – 748 (1981).

[5.42] *M. O'Keeffe and S.A. Steward.* **The configurational entropy of hydrogen in body-centered cubic metals.** Journal of Physics and Chemistry of Solids **43**(12), 1181 (1982).

[5.43] *F. Wang, C.P. Liang, and H.R. Gong.* **Effects of spin-orbit coupling on various properties of hafnium dihydride.** Materials Chemistry and Physics **139**(1), 139 – 146 (2013).

[5.44] *A. Baldi, M. Gonzalez-Silveira, V. Palmisano, and B. Dam.* **Destabilization of the Mg-H system through elastic constraints.** Physical Review Letters **102**, 226102 1 – 4 (2009).

[5.45] *A. Baldi, G.K. Pálsson, M. Gonzalez-Silveira, H. Schreuders, M. Slaman, J.H. Rector, G. Krishnan, B.J. Kooi, G.S. Walker, M.W. Fay, B. Hjörvarsson, R.J. Wijngaarden, B. Dam, and R. Griessen.* **Mg/Ti multilayers: Structural and hydrogen absorption properties.** Physical Review B **81**(22), 224203 1 – 10 (2010).

[5.46] *Y. Pivak, H. Schreuders, M. Slaman, R. Griessen, and B. Dam.* **Thermodynamics, stress release and hysteresis behavior in highly adhesive Pd-H films.** International Journal of Hydrogen Energy **36**(6), 4056 – 4067 (2011).

[5.47] *R.J. Westerwaal, J.S.A. Rooijmans, I. Leclercq, D.G. Gheorge, T. Radeva, L.P.A. Mooij, T. Mak, L. Polak, M. Slaman, B. Dam, and T. Rasing.* **Nanostructured Pd-Au based fiber optic sensors for probing hydrogen concentrations in gas mixtures.** International Journal of Hydrogen Energy **38**, 4201 – 4212 (2013).

[5.48] *T. Schober.* **Vanadium-, niobium-, tantalum-hydrogen.** Solid State Phenomena **49 – 50**, 357 – 442 (1996).

[5.49] *C. Wadell, S. Syrenova, and C. Langhammer.* **Plasmonic hydrogen sensing with nanostructured metal hydrides.** ACS Nano **8**(12), 11925 – 11940 (2014).

[5.50] *C. Wadell, F.A.A Nugroho, E. Lidstrom, B. Iandolo, J.B. Wagner, and C. Langhammer.* **Hysteresis-Free Nanoplasmonic Pd-Au Alloy Hydrogen Sensors.** Nano Letters **15**, 3563 – 3570 (2015).

[5.51] *C. Perrotton, R.J. Westerwaal, N. Javahiraly, M. Slaman, H. Schreuders, B. Dam, and P.A. Meyreuis.* **Reliable, sensitive and fast optical fiber hydrogen sensor based on surface plasmon resonance.** Optics Express **21**, 382 – 390 (2013).

[5.52] *I. Lewkowicz.* **Titanium-hydrogen.** Solid State Phenomena **49 – 50**, 239 – 280 (1996).

[5.53] *A. Aladjem.* **Zirconium-hydrogen.** Solid State Phenomena **49 – 50**, 281 – 330 (1996).

[5.54] *E. Zuzek, J.P. Abriata, A. San-Martin, and F.D. Manchester.* **The H-Zr (hydrogen-zirconium) system.** Bulletin of Alloy Phase Diagrams **11**(4), 385 – 395 (1990).

[5.55] *G.G. Libowitz.* **The zirconium-hydrogen system at high hydrogen contents.** Divison of Technical Information Extension, U.S. Atomic Energy Commission (1960).

[5.56] *A. San-Martin and F.D. Manchester.* **The H-Ti (hydrogen-titanium) system.** Bulletin of Alloy Phase Diagrams **8**(1), 30 – 42 (1987).

[5.57] *W.E. Wang.* **Thermodynamic evaluation of the titanium-hydrogen system.** Journal of Alloys and Compounds **238**, 6 – 12 (1996).

[5.58] *W.E. Wang and D.R. Olander.* **Thermodynamics of the Zr-H system.** Journal of the American Ceramic Society **78**(12), 3323 – 3328 (1995).

[5.59] *M. Arita, K. Shimizu, and Y. Ichinose.* **Thermodynamics of the Ti-H system.** Metallurgical Transactions A **13**(8), 1329 – 1336 (1982).

[5.60] *S. Yamanaka, K. Yamada, K. Kurosaki, M. Uno, K. Takeda, H. Anada, T. Matsuda, and S. Kobayashi.* **Thermal properties of zirconium hydride.** Journal of Nuclear Materials **294**, 94 – 98 (2001).

[5.61] *A. San-Martin and F.D. Manchester.* **The H-Ta (hydrogen-tantalum) system.** Journal of Phase Equilibria **12**(3), 332 – 343 (1991).

[5.62] *J.A. Pryde and I.S.T. Tsong.* **A theory of the resistivity of high-concentration interstitial alloys with application to the tantalum-hydrogen and tantalum-deuterium systems.** Acta Metallurgica **19**, 1333 – 1338 (1971).

[5.63] *E. Veleckis and R.K. Edwards.* **Thermodynamic properties in the systems vanadium-hydrogen, niobium-hydrogen, and tantalum-hydrogen.** Journal of Physical Chemistry **73**(3), 683 – 692 (1969).

[5.64] *S. de Man, M. Gonzalez-Silveira, D. Visser, R. Bakker, H. Schreuders, A. Baldi, B. Dam, and R. Griessen.* **Combinatorial method for direct measurements of the intrinsic hydrogen permeability of separation membrane materials.** Journal of Membrane Science **444**, 70 – 76 (2013).

[5.65] *M. Di Vece and J.J. Kelly.* **Electrochemical study of hydrogen diffusion in yttrium hydride switchable mirrors.** Journal of Alloys and Compounds **356 – 357**, 156 – 159 (2003).

[5.66] *P.H.L. Notten, M. Kremers, and R. Griessen.* **Optical switching of Y-hydride thin film electrodes - a remarkable electrochromic phenomenon.** Journal of The Electrochemical Society **143**, 3348 – 3353 (1996).

[5.67] *K.S. Rothenberger, B.H. Howard, R.P. Killineyer, A.V. Cugini, R.M. Enick, F. Bustamante, M.V. Ciocco, B.D. Morreale, and R.E. Buxbaum.* **Evaluation of tantalum-based materials for hydrogen separation at elevated temperatures and pressures.** Journal of Membrane Science **218**, 19 – 37 (2003).

[5.68] *C. Stampfl and A.J. Freeman.* **Stable and metastable structures of the multi-phase tantalum nitride system.** Physical Review B **71**, 204111 1 – 5 (2005).

[5.69] *N.L. Peterson.* **Diffusion in refractory metals.** Report. Advanced Metals Research Corporation (1960).

Summary

Hydrogen (gas) plays, besides in scientific research, also an essential role in many sectors of the industry. For example, hydrogen is necessary to produce ammonia, it can be used to determine the quality of products (hydrogen is produced during food ageing), or it can result in medical diagnostics (e.g. lactose intolerance). As hydrogen will play an important role as an energy carrier in a sustainable economy, hydrogen detection is essential.

Hydrogen is a colorless, odorless, and tasteless gas with a low ignition energy combined with a high energy output. Hydrogen detection is therefore essential. The most common approach to detect hydrogen is based on the change of the resistivity of a material as a function of the hydrogen concentration. These detectors are, however, bulky, expensive when being used in large quantities, and the sensing-unit contains electric wires. Sparks can therefore lead to unsafe situations. These disadvantages can be tackled by using optical fibers. Optical fibers are based on the changing optical reflection of a material when it absorbs hydrogen (switchable mirrors). By placing this material on the tip of the optical fiber, the sensing unit and the read-out equipment (including all electronics) can be separated by hundreds of meters. Other advantages of optical fibers are that they are small, flexible, and easy to combine to do multiple probe measurements. Thin film metal hydrides are extremely suitable for optical hydrogen detection.

In the first part of this thesis we show that the thermodynamics of metal hydrides plays a crucial role in the definition, calibration, and the adjustment of the operational pressure range of a (optical) hydrogen detector. The enthalpy of hydrogenation determines the strength of the temperature dependence of the pressure range, while the entropy determines its offset. By changing one - or both - parameters we can change the pressure range and, possible, also its temperature dependence. We find this when we, for example, focus on the equilibrium pressure of the absorption of a thin Mg (magnesium) hydride film, which is sandwiched between two Ti (titanium) hydride layers. The equilibrium pressure of a Mg film with a thickness of 10 nanometer is almost 1 order of magnitude lower than obtained with a Mg film of 2 nanometer. A similar effect is observed using Mg dots of different sizes, although the results are less evident. It is, however, unclear whether this pressure difference is the consequence of the interface energy between the Mg and Ti layers or due to plastic deformations.

While studying the thermodynamics of metal hydrides, we encountered a special phenomenon. To increase the pressure range of a thin Mg film by alloying it with Ti, we find that a simultaneous change of both the enthalpy and the entropy. In fact, we find that the change in enthalpy linear related is to the change in entropy. In literature, this phenomenon is known as enthalpy-entropy compensation and it is characterized by the compensation temperature T_{comp}. Although this phenomenon has been studied for decades and is observed in many different (chemical, biological, and solid-state physical) processes, its origin is unknown. In literature, there is even no consensus whether this effect has a physical nature. Instead, published models, including our own, shows that it is possible to obtain a compensation temperature within the experimental temperature range using only statistical conditions. From this, many authors conclude that when one obtain a compensation temperature within the temperature range, one can only conclude that the corresponding compensation effect must have a statistical origin. As the compensation effect in the Mg/Ti metal hydride system we found experimentally satisfy this condition, it should mean that it has to have a statistical nature. However, we disprove this by means of a mathematical deduction. We conclude that the published models do not include an important aspect: ordering. We show that it is possible to obtain the same compensation temperature from both a sorted and a random system, each with a different basis. A random system has a statistical basis, while a sorted system is associated with a physical basis. To distinguish both situations an additional characterization parameter is necessary: the order coefficient. In this way, we exclude the possibility that the enthalpy-entropy compensation observed in Mg/Ti, which is constructed from a sorted system, has a statistical nature. We therefore conclude it must have a physical nature.

Besides our research on changing the thermodynamics of metal hydrides, we also discovered that two (thin film) metal hydride exhibit excellent hydrogen sensing properties (both resulting in a patent application). For some properties, these materials outperform the current most efficient system, which is based on Pd (palladium) hydride. By alloying Mg with Zr (zirconium) we find, for specific ratios, a pressure range of almost 4 orders of magnitude. Unfortunately, this is accompanied with hysteresis, which means that the path of increasing pressure and the path of decreasing pressure are not the same. This means that (small) fluctuations in the pressure cannot be measured. Many metal hydride systems show hysteresis. Therefore, it surprised us that Hf (hafnium) hydride shows an optical change within an extremely large pressure range (at least 6 orders, possibly 10) without hysteresis. In addition, it shows excellent stability (more than hundred cycles) and fast response times (within seconds at high pressures). Compared to other metal hydride systems the properties of the Hf-H system within the pressure range are extraordinary. First, the hydrogen fraction increases significantly ($+40\%$). Second, the system undergoes

a phase transition. It is therefore remarkable that we find a well-defined and a simple relation between the pressure and the optical properties of the Hf hydride. In addition, the phase transition has little influence on this relation and does not introduce a hysteresis. We also find that, within the pressure range, the enthalpy of the system does not change. This does not only mean that the temperature dependence of the pressure range is constant (which simplifies the calibration), it also means that the pressure range must be fully described by a seemingly unphysically large entropy change. Unfortunately, the origin of this entropy change is not known as it cannot be described by known contribution such as the configurational and vibrational entropy. Preliminary results show that also nitrogen doped Ta (tantalum) and possibly also Ti and Zr hydrides are suitable for hydrogen detection, although their pressure ranges are smaller than in Hf hydride.

As a general conclusion, we find that thin film metal hydrides are extremely suitable for hydrogen detection. The optical change combined with the possibility to change the pressure range by means of changing the layer thickness, the interfaces, or the alloy fraction indicate the large flexibility to adjust the sensing properties to the safety requirements. In addition, the discovery of the hydrogen sensing properties of Mg-Zr-H and, in particular, Hf-H shows that there are still many new sensor-possibilities available to explore.

Samenvatting

Waterstof (gas) heeft, behalve in wetenschappelijk onderzoek, ook een prominente rol in vele takken van de industrie. Waterstof is nodig bij de productie van ammonia, kan gebruikt worden in de kwaliteitscontrole van producten (waterstof productie is een teken van afbraak), of kan gebruikt worden voor het verkrijgen van medisch diagnoses (bijv. lactose-intolerantie). Gezien het feit dat waterstof verder een belangrijke rol zal spelen als energiedrager in een duurzame economie, is waterstofdetectie van het grootste belang.

Waterstof is een kleurloos, geurloos, en een smaakloos gas met een lage ontbrandingsenergie gecombineerd met een hoge energie-inhoud. Waterstofdetectie is daarom essentieel. De voornaamste methode om waterstof detecteren is gebaseerd op de verandering van de weerstand van een materiaal als een functie van de waterstof concentratie. Deze detectoren hebben als nadeel dat ze groot van formaat zijn, duur zijn voor gebruik in grote hoeveelheden, en bestaan uit elektrische koppelingen binnen de meet-capsule. Dit kan leiden onveilige omstandigheden bij kortsluiting. Deze nadelen kunnen voorkomen worden door het gebruik van optische fibers. Hier wordt gebruik gemaakt van de veranderende optische reflectie van een materiaal wanneer deze waterstof absorbeert (schakelbare spiegels). Doordat dit materiaal op het uiteinde van een optische fiber geplaatst wordt, kan de meet-capsule vele honderden meters verwijderd worden van de uitleesapparatuur en andere elektronica. Andere voordelen van optische fibers zijn dat ze klein (van formaat), flexibel, en makkelijk op te schalen zijn voor meerpuntsmetingen. Dunne film metaal hydriden zijn uiterst geschikt voor optische waterstof detectie.

In het eerste gedeelte van dit proefschrift laten we zien dat de thermodynamica van metaal hydriden een cruciale rol speelt in het definiëren, de calibratie en het aanpassen van het detectiebereik van een (optische) waterstof detector. De enthalpie van hydrogenatie bepaalt hoe sterk de temperatuur afhankelijkheid van het bereik is, terwijl de entropie de offset bepaalt. Door een - of beide - parameters te veranderen kan het drukbereik en mogelijk ook de temperatuur afhankelijkheid van de detector veranderd worden. Dit zien we bijvoorbeeld als we kijken naar de evenwichtsdruk van de belading een dunne Mg (magnesium) hydride film welke is ingeklemd door twee titanium(hydride) lagen. Een Mg film met een dikte van 10 nanometer belaadt bij een waterstof druk die bijna 1 orde (een factor 10) lager ligt

dan een 2 nanometer dikke Mg film. Een soort gelijk effect zien we in Mg eilandjes met verschillende doorsnedes, maar deze resultaten zijn minder evident dan die verkregen met de dunne films. Het is echter onduidelijk of dit verschil een direct gevolg is van de grensvlak energie tussen de Mg en Ti lagen of van een plastische deformatie.

Tijdens onze studie van de thermodynamica van metaal hybriden, stuitten wij op een bijzonder fenomeen. In een poging om het drukbereik van een Mg dunne film aan te passen door het te legeren met Ti, vinden we dat de enthalpie en de entropie gelijktijdig veranderen. In feite vinden we dat de verandering in de enthalpie lineair gerelateerd is aan de verandering in de entropie. Dit fenomeen is in literatuur bekend als enthalpie-entropie compensatie en wordt gekarakteriseerd door de compensatie temperatuur T_{comp}. Ondanks het feit dat dit fenomeen al veelvuldig is geobserveerd in vele verschillende (chemische, biologische en vaste-stof fysische) processen, is de oorsprong van dit effect onbekend. In literatuur wordt er zelfs getwijfeld of dit fenomeen daadwerkelijk een fysisch effect is. In plaats hiervan laten verschillende gepubliceerde modellen, inclusief een door ons nieuw ontwikkeld model, zien dat het mogelijk is om een compensatietemperatuur binnen het experimentele temperatuurbereik te krijgen uit statische voorwaarden. In literatuur wordt hieruit geconcludeerd dat wanneer een compensatietemperatuur binnen de gemeten temperatuur bereik valt, de corresponderende enthalpie-entropie compensatie een statistische aard moet hebben. Gezien het door ons gevonden compensatie effect in het Mg/Ti metaal hydride systeem voldoet aan deze conditie, zou dat moeten betekenen dat het geobserveerde enthalpie-entropie compensatie effect van statistische aard moet zijn. Wij laten aan de hand van een mathematische deductie zien dat dit niet het geval is. De sleutel tot onze conclusie is dat de gepubliceerde modellen een belangrijk aspect niet meenemen: ordening. Het is mogelijk om dezelfde compensatietemperatuur te verkrijgen uit zowel een geordend en een ongeordend systeem, dit terwijl de basis van beide systemen compleet anders is. Een ongeordend systeem heeft een statistische achtergrond (willekeurige fluctuaties), terwijl een geordend systeem juist geassocieerd kan worden met een fysische achtergrond. Om het onderscheid te maken tussen een geordend en een ongeordend systeem is de definitie van een extra karakteriserende parameter noodzakelijk: de order coëfficiënt. Hiermee sluiten wij uit dat de enthalpie-entropie compensatie in Mg/Ti, welk is opgebouwd uit een geordend systeem, een statische aard kan hebben, en laten daarmee zien dat het effect een fysische basis moet hebben.

Naast ons onderzoek naar de thermodynamica ontdekten wij dat twee (dunne film) metaal hydride systemen uiterst geschikt zijn voor optische waterstofdetectie (beide resulterend in een patentaanvraag) en in sommige eigenschappen beter presteren dan het meest efficiënte geacht systeem, welke op Pd (palladium) hydride is gebaseerd. Door Mg te legeren met Zr (zirkonium) vinden wij bij bepaalde Zr/Mg

verhoudingen dat we de waterstofdruk kunnen meten over een drukbereik van bijna 4 orders van grootte. Dit gaat helaas gepaard met hysterese, wat inhoudt dat een toenemende druk en een afnemende druk niet hetzelfde optische pad volgt. Dit betekent dat (kleine) fluctuaties in de druk niet gevolgd kan worden. Hysterese is een veelvoorkomend effect in de (de)hydrogenatie van metaal hydriden. Mede daardoor is het verrassend dat Hf (hafnium) hydride een optische verandering over zeer groot drukbereik (tenminste 6 orders, mogelijk 10) laat zien zonder hysterese. Bovendien gaat dit gepaard met uitmuntende stabiliteit (meer dan honderd cycli) en snelle reactietijden (in orde van seconden bij hoge drukken). Ten opzichte van vele andere metaal hydriden zijn de eigenschappen van het Hf-H systeem binnen het drukbereik erg bijzonder. Niet alleen neemt de waterstof fractie binnen Hf enorm toeneemt $(+40\%)$, er vindt ook nog een faseovergang plaatsvindt. Desondanks vinden wij een zeer goed gedefinieerde en eenvoudige relatie tussen de druk en de verandering van de optische eigenschappen over het gehele drukbereik. De faseovergang heeft nauwelijks een invloed op deze relatie en veroorzaakt ook geen hysterese. Bovendien vinden wij dat de enthalpie van het systeem niet veranderd. Dit betekent niet alleen dat temperatuur afhankelijkheid van het druk-bereik constant is (wat de calibratie eenvoudig maakt) maar ook dat de druk-bereik volledig toe te schrijven is aan een grote verandering van de entropie. Helaas is de oorsprong van deze entropie verandering nog onbekend gezien deze niet toegeschreven kan worden aan contributies zoals de configurationele en de vibrationele entropie. Een eerste analyse laat zien dat ook stikstof verontreinigd Ta (tantaal) en mogelijk ook Ti en Zr hydriden geschikt zijn voor waterstof detectie, al hoewel het drukbereik kleiner is dan in Hf hydride.

Als algemene conclusie stellen wij dat dunne film metaal hydriden uiterst geschikt zijn voor waterstof detectie. De optische verandering gecombineerd met de mogelijkheid om het drukbereik te veranderen aan de hand van laagdikte, interfaces, en legeringen resulteert in een grote flexibiliteit om de sensor eigenschappen aan te passen aan de veiligheidsbehoefte. Bovendien laat de ontdekking van de waterstof eigenschappen van Mg-Zr-H en van met name Hf-H laat zien dat er in dit veld nog veel nieuwe sensor-mogelijkheden te exploreren zijn.

Acknowledgements

I would like to start to thank my supervisor, Bernard Dam. He gave me the possibility and the freedom to evolve myself in many aspects. His support to focus on hydrogen sensors in the second part of my Ph.D. project was a great and welcome impulse for me. Also, thanks to him I was able to visit some beautiful places around the world by attending some conferences (see the insides of the cover). In addition, it took a while to breach my closed personality but, as a result of his thoroughness, we made an enormous progress on both a scientific and a personal level in the last few years.

Furthermore, I want to thank Bernard, Heleen (thank you for the beautiful flowers!), and the rest of the MECS group for their support and freedom to, for one year, take care of my father, to visit him as much as possible, and to process his passing. I really appreciate all your support!

Some special thanks to Ruud and Peter, with whom I worked on hydrogen sensors with great pleasure. I also want to give my roommates, Lennard, Kohta, Steffen, and finally Nienke and Fahimey some *warm* words. It was great to talk about many (non-scientific) topics and I am also glad that you all survived my preference for cold temperatures. In addition, I want to mention that it was a great pleasure to guide Willy, Evelien, Arjen, and Sara during their bachelor projects.

It was great for being part of the MECS group for more than 5 years. My gratitude goes out to Herman and Joost for their technical support and for the great time during the coffee breaks and lunches. In this context, I also want to thank Wilson, Wim, Hans, Roel, Fokko, Sarmila, Moreno, Bartek, Digda, Ming, Jicheng, Petra, Arjan, Eline, Mercedes, Maartje, and many other people for the excellent time. I also enjoyed the collaboration with Lars and Ad with respect to the neutron measurements, and with Ronald, to unravel the mystery of enthalpy-entropy compensation.

Also, I want to thank all strawberry farmers around the world to make it possible to start the second half of each day with a fresh box of strawberries. I am sorry for all manufactures and sellers of coats. In my opinion your profession is unnecessary as you can easily survive the winters in the Netherlands without a coat.

Tenslotte wil ik graag mijn enorme dankbaarheid uiten aan mijn familie. De afgelopen vijf jaar waren niet de eenvoudigste maar jullie steun, warmte, en alle leuke uitjes waardeer ik enorm. Ik hoop dat onze band net zo hecht blijft zoals deze nu is. Bedankt!

List of

Publications

(2017)   *C. Boelsma, L.J. Bannenberg, M.J. van Setten, A.A. van Well, and B. Dam.* **Hafnium: An optical hydrogen sensor spanning 6 orders in pressure.** Under review.

(2017)   *C. Boelsma, R. Griessen, H. Schreuders, and B. Dam.* **Verification of the enthalpy–entropy compensation effect.** Under review.

(2016)   *A. Molinari, F. D'Amico, M. Calizzi, Y. Zheng, C. Boelsma, L.P.A. Mooij, Y. Lei, L. Polak, H. Hahn, B. Dam and L. Pasquini.* **Interface and strain effects on the H-sorption thermodynamics of size-selected Mg nanodots.** International Journal of Hydrogen Energy **41**, 9841 – 9851.

(2015)   *K. Asano, R.J. Westerwaal, A. Anastaspol, L.P.A. Mooij, C. Boelsma, P. Ngene, H. Schreuders, S.W.H. Eijt, and B. Dam.* **Destabilization of Mg hydride by self-organized nanoclusters in the immiscible Mg–Ti system.** Journal of Physical Chemistry C **119**, 12157 – 12164.

(2015)   *R.J. Westerwaal, E.A. Bouman, W.G. Haije, H. Schreuders, S. Dutta, M.Y. Wu, C. Boelsma, P. Ngene, S. Basak, and B. Dam.* **The hydrogen permeability of Pd–Cu based thin films membranes in relation to their structure: a combinatorial approach.** International Journal of Hydrogen Energy **40**(10), 3932 – 3943.

(2014)   *T. Mak, R.J. Westerwaal, M. Slaman, H. Schreuders, A.W. Vugt, M. Victoria, C. Boelsma, and B. Dam.* **Optical fiber sensor for the continuous monitoring of hydrogen in oil.** Sensors and Actuators B **190**, 982 – 989.

(2014)   *L. Pasquini, M. Sacchi, M. Brighi, C. Boelsma, S. Bals, T. Perkisas, and B. Dam.* **Hydride destabilization in core–shell nanoparticles.** International Journal of Hydrogen Energy **39**, 2115 – 2123.

(2011)   *L.P.A Mooij, A. Baldi, C. Boelsma, K. Shen, M. Wagemaker, Y. Pivak, H. Schreuders, R. Griessen, and B. Dam.* **Interface energy controlled thermodynamics of nanoscale metal hydrides.** Advanced Energy Materials **1**, 754 – 758.

Patent Applications:

(2015)   *C. Boelsma and B. Dam.* **Single element hydrogen sensing material.** PCT Patent. Application number: PCT/NL2015/050200. Publication number: WO2015152712 A1. Filling date: 30 Mar. 2015. Publication date: 8 Oct. 2015

(2014)   *C. Boelsma and B. Dam.* **Large pressure range hydrogen sensor.** PCT Patent. Application number: PCT/NL2014/050805. Publication number: WO2015080577 A1. Filling date: 27 Nov. 2014. Publication date: 4 Jun. 2015

Curriculum Vitae

Christiaan Boelsma was born on 4 May 1985 in Heer-
hugowaard, the Netherlands. From 1997 to 2004 he
followed pre-university education at the Han Fort-
mann College in Heerhugowaard. After this, he pur-
sued his passion for physics by finishing a BSc in
Physics and Astronomy at VU University in Amster-
dam. He received his degree in 2008. In the mean-
time, he started a Master in Physics, also at VU Uni-
versity in Amsterdam. During his master project, he
encountered for the first time the world of metal
hydrides. This project was conducted in the Con-
densed Matter Physics group under supervision of
prof. dr. Bernard Dam and prof. dr. Ronald Griessen.
After completion, he was offered by prof. dr. Bernard
Dam to continue his work on metal hydrides in the form of a Ph.D. position. He grate-
fully accepted this offer and he started this new part of his career in August 2011 in
the Materials for Energy Conversion and Storage group at Delft University of Tech-
nology, headed by prof. dr. Bernard Dam. The results of his research project are
described in this thesis.